

<https://doi.org/10.15388/vu.thesis.105>  
<https://orcid.org/0000-0001-8529-3436>

VILNIUS UNIVERSITY  
CENTER FOR PHYSICAL SCIENCES AND TECHNOLOGY

Vytautas  
JANONIS

# Development of terahertz diffractive optics and plasmon-phonon polaritonics components

**DOCTORAL DISSERTATION**

Technological Sciences  
Materials Engineering (T 008)

---

VILNIUS 2020

This dissertation was written between 2015 and 2019 at the Center for Physical Sciences and Technology.

The research was supported by the Research Council of Lithuania with grants for academic achievements: DOK-16551, P-DAP-19-408, and mobility funding: P-DOC-17-202, P-DAK-18-228.

**Scientific supervisor: Dr. Irmantas Kašalynas** (Center for Physical Sciences and Technology, Natural Sciences, Physics – N 002).

This doctoral dissertation will be defended in a public meeting of the Dissertation Defence Panel:

**Chairman – Prof. Habil. Dr. Jūras Banys** (Vilnius University, Natural Sciences, Physics – N 002).

**Members:**

**Dr. Ramūnas Aleksiejūnas** (Center for Physical Sciences and Technology, Technological Sciences, Materials Engineering – T 008);

**Dr. Renata Karpič** (Vilnius University, Natural Sciences, Physics – N 002);

**Prof. Dr. Piotr Perlin** (Institute of High Pressure Physics, Technological Sciences, Materials Engineering – T 008);

**Dr. Roland Tomašiūnas** (Vilnius University, Technological Sciences, Materials Engineering – T 008).

The dissertation shall be defended at a public meeting of the Dissertation Defence Panel at 3 p. m. on the 20<sup>th</sup> November 2020 in room A101 of the Center for Physical Sciences and Technology.

Address: 3 Saulėtekio Ave., Vilnius, Lithuania. Phone No.: +370 5 264 8884; email: office@ftmc.lt.

The text of this dissertation can be accessed at the libraries of Center for Physical Sciences and Technology and Vilnius University, as well as on the website of Vilnius University: [www.vu.lt/lt/naujienos/ivykiu-kalendorius](http://www.vu.lt/lt/naujienos/ivykiu-kalendorius)

<https://doi.org/10.15388/vu.thesis.105>  
<https://orcid.org/0000-0001-8529-3436>

VILNIUS UNIVERSITETAS  
FIZINIŲ IR TECHNOLOGIJOS MOKSLŲ CENTRAS

Vytautas  
JANONIS

# Terahercinės difrakcinės optikos ir plazmon-fonon-poliaritonikos komponentų kūrimas

**DAKTARO DISERTACIJA**

Technologijos mokslai  
Medžiagų inžinerija (T 008)

---

VILNIUS 2020

Disertacija rengta 2015–2019 metais Fizinių ir technologijos mokslų centre.

Mokslinius tyrimus rėmė Lietuvos mokslo taryba – skyrė paramą už akademinis pasiekimus DOK-16551 ir P-DAP-19-408 bei paramą akademinėms išvykoms P-DOC-17-202 ir P-DAK-18-228.

**Mokslinis vadovas – dr. Irmantas Kašalynas** (Fizinių ir technologijos mokslų centras, gamtos mokslai, fizika – N 002).

Gynimo taryba:

**pirmininkas – prof. habil. dr. Jūras Banys** (Vilniaus universitetas, gamtos mokslai, fizika – N 002).

**Nariai:**

**dr. Ramūnas Aleksiejūnas** (Vilniaus universitetas, technologijos mokslai, medžiagų inžinerija – T 008);

**dr. Renata Karpič** (Fizinių ir technologijos mokslų centras, gamtos mokslai, fizika – N 002);

**prof. dr. Piotr Perlin** (Didelių slėgių fizikos institutas, Varšuva, Lenkija, technologijos mokslai, medžiagų inžinerija – T 008);

**dr. Roland Tomašiūnas** (Vilniaus universitetas, technologijos mokslai, medžiagų inžinerija – T 008).

Disertacija ginama viešame Gynimo tarybos posėdyje 2020 m. lapkričio 20 d. 15 val. Fizinių ir technologijos mokslų centro A101 auditorijoje. Adresas: Saulėtekio al. 3, Vilnius, tel. +370 5 264 8884; el. paštas: office@ftmc.lt .

Disertaciją galima peržiūrėti Fizinių ir technologijos mokslų centro bei VU bibliotekose ir VU interneto svetainėje adresu:

<https://www.vu.lt/naujienos/ivykiu-kalendorius>.

# ACKNOWLEDGEMENTS

First of all I would like to express my gratitude towards my supervisor Dr. Irmantas Kašalynas for his continuous support and help during my PhD studies and associated research as well as helpful ideas and my continuing education into the scientific method.

I thank Dr. Linas Minkevičius, Dr. Bogdan Voisiat and Dr. Simonas Indrišiūnas for their design and manufacturing of diffractive optical components, and result analysis.

I thank my colleagues at UNIPRESS, Warsaw, Poland, Dr. Pawel Prystawko, Dr. Jacek Kacperski and others for my fruitful stay in their institution, supply of materials and help in manufacturing polaritonic component samples. I thank Dr. Saulius Tumėnas for discussions and measurements of the polaritonic component angular reflectivity spectra, also Dr. Linas Minkevičius and Dr. Ignas Grigelionis for the development of the polaritonic emission measurement setup and its automation, also Dr. Vadym Korotieiev for his theoretical work.

I would also like to acknowledge members of the THz photonics lab of the Center for Physical Sciences and Technology: Dr. Ignas Grigelionis, Dr. Linas Minkevičius, Dr. Mindaugas Karaliūnas, Dr. Vytautas Jakštas, Rusnė Ivaškevičiūtė-Povilauskienė, Justinas Jorūdas, Domas Jokubauskis and others. I thank you all for the delightful work environment and patient replies to my questions in every aspect of academic and *not-so-much* life as well as fruitful discussions and refreshing coffee breaks.

Lastly, and most importantly, I wish to thank my family, especially my wife **Agnė** and daughter **Ūla**, for my continuous emotional growth towards being a better person, never-ending support, recuperation, and great patience during these trying times.

# TABLE OF CONTENTS

<b>Acknowledgments</b>	<b>5</b>
<b>Table of Contents</b>	<b>8</b>
<b>Abbreviations</b>	<b>10</b>
<b>1 INTRODUCTION</b>	<b>11</b>
1.1 Major Goal . . . . .	15
1.2 Tasks of this Work . . . . .	15
1.3 Scientific Novelty . . . . .	15
1.4 Statements of Defence . . . . .	17
1.5 Contribution of the Author . . . . .	18
1.6 Co-authors Contribution . . . . .	18
1.7 Publications . . . . .	20
1.8 Participation in Projects . . . . .	24
<b>2 LITERATURE OVERVIEW</b>	<b>26</b>
2.1 Diffractive Optics . . . . .	26
2.1.1 Materials in THz Range . . . . .	27
2.1.2 Refractive Lenses . . . . .	31
2.1.3 Metal Mirrors . . . . .	32
2.1.4 Diffractive Optical Elements . . . . .	33
2.1.5 Zone Plates . . . . .	34
2.1.6 Metamaterial Lenses . . . . .	38
2.1.7 Main Parameters of a Lens . . . . .	39
2.1.8 Aberrations of a Lens . . . . .	41
2.1.9 Fabrication Methods for Fresnel Lenses . . . . .	43
2.1.10 Direct Laser Ablation of Optical Components . . . . .	44
2.2 Polaritonics . . . . .	45
2.2.1 Theory of SP Dispersion . . . . .	46
2.2.2 Plasmon Polaritons . . . . .	49
2.2.3 Phonon Polaritons . . . . .	52
2.2.4 Plasmon-Phonon Interaction . . . . .	55
2.2.5 Polariton Coupling . . . . .	57

2.2.6	Theory of a Grating Coupler . . . . .	61
2.2.7	Narrowband Thermal Radiation . . . . .	61
<b>3</b>	<b>METHODS</b>	<b>64</b>
3.1	Finite Difference Time Domain . . . . .	64
3.2	MPFL Characterization Setups . . . . .	66
3.3	Rigorous Coupled Wave Analysis . . . . .	67
3.4	Fourier Transform Infrared Spectroscopy . . . . .	71
<b>4</b>	<b>RESULTS</b>	<b>77</b>
4.1	Diffractive Lenses . . . . .	77
4.1.1	Multilevel Phase Fresnel Lenses . . . . .	77
4.1.2	0.6 THz DOE Samples . . . . .	77
4.1.3	4.7 THz DOE Samples . . . . .	81
4.1.4	Performance of DOEs for 0.6 THz Frequency . . . . .	85
4.1.5	DOE for 0.6 THz Summary . . . . .	95
4.1.6	Performance of the DOEs for 4.7 THz Frequency . . . . .	97
4.2	Surface Relief Grating Couplers for SPP <sub>h</sub> P Excitation . . . . .	103
4.2.1	Surface Relief Grating Samples . . . . .	103
4.2.2	<i>n</i> -GaN Substrate Reflectivity . . . . .	105
4.2.3	Design of the SRG Coupler . . . . .	106
4.2.4	Calculation of <i>n</i> -GaN SPP <sub>h</sub> P Dispersion . . . . .	108
4.2.5	SRG-1 Reflectivity at Fixed Incidence Angle . . . . .	112
4.2.6	SRG Reflectivity on the Incidence Angle . . . . .	114
4.2.7	Emission from <i>n</i> -GaN SRG . . . . .	116
4.2.8	Coherence of <i>n</i> -GaN SRG Emission . . . . .	122
4.2.9	Power of <i>n</i> -GaN SRG Emission . . . . .	126
4.3	Reflectivity of Metal Grating Coupled Heterostructures . . . . .	128
4.3.1	Metal Grating Coupled Heterostructure Samples . . . . .	128
4.3.2	Unpatterned Sample Reflectivity . . . . .	130
4.3.3	MGC Reflectivity Dispersion . . . . .	132
4.3.4	Experimental Investigation of MGC Reflectivity Spectra . . . . .	134
4.3.5	Field Plots . . . . .	137
<b>5</b>	<b>MAIN RESULTS AND CONCLUSIONS</b>	<b>143</b>

<b>6</b>	<b>SANTRAUKA</b>	<b>145</b>
6.1	Paveikslų Sąrašas . . . . .	145
6.2	Įvadas . . . . .	150
6.2.1	Darbo tikslas . . . . .	153
6.2.2	Išsikelti uždaviniai . . . . .	153
6.2.3	Naujumas . . . . .	153
6.2.4	Ginamieji teiginiai . . . . .	155
6.2.5	Publikacijos ir asmeninis indėlis . . . . .	155
6.2.6	Dalyvavimas projektuose . . . . .	156
6.3	Teorinis įvadas . . . . .	157
6.3.1	Difrakciniai elementai . . . . .	157
6.3.2	Poliaritonika . . . . .	159
6.4	Metodai . . . . .	162
6.4.1	Difrakcinė optika . . . . .	162
6.4.2	Poliaritonika . . . . .	163
6.5	Rezultatai . . . . .	165
6.5.1	Difrakcinė optika 0,58 THz dažniui . . . . .	165
6.5.2	Difrakcinė optika 4,7 THz dažniui . . . . .	169
6.5.3	$n$ -GaN paviršinių gardelių tyrimas . . . . .	172
6.5.4	Heterostruktūrų su paviršinėmis metalinėmis gardelėmis tyrimas . . . . .	178
6.5.5	Išvados . . . . .	184
	<b>REFERENCES</b>	<b>186</b>
<b>7</b>	<b>CURRICULUM VITAE</b>	<b>200</b>



# ABBREVIATIONS

Abbreviation	Meaning
ABS	Acrylonitrile Butadiene Styrene
AFM	Atomic Force Microscope
AMC	Amplification Multiplication Chain
BBR	Black Body Radiation
DLA	Direct Laser Ablation
DOE	Diffraction Optical Element
FDTD	Finite Difference Time Domain
FIR	Far Infrared
FMM	Fourier Modal Method
FTIR	Fourier Transform Infrared
FWHM	Full Width at Half Maximum
HDPE	High Density Polyethylene
LIPSS	Laser Induced Periodic Surface Structures
LO	Longitudinal Optical
LOPC	Longitudinal Phonon Plasmon Coupling
MGC	Metal Grating Coupler
MIR	Mid Infrared
MPFL	Multilevel Phase Fresnel Lens
OAP	Off-Axis Parabolic
PE	Polyethylene
PFL	Phase Fresnel Lens
PLA	Polyactic Acid
POE	Passive Optical Element
PQL	Phase Quantisation Level (p)
PTFE	Polytetrafluoroethylene

QCL	Quantum Cascade Laser
RB	Reststrahlen Band (also known as Residual radiation region)
RCWA	Rigorous Coupled Wave Analysis
RIE	Reactive Ion Etching
SEM	Scanning Electron Microscope
SI	Semi Insulating
SNOM	Scanning Near Field Optical Microscope
SNR	Signal to Noise Ratio
SNR	Signal to Noise Ratio
SP	Surface Polariton
SPhP	Surface Phonon Polariton
SPP	Surface Plasmon Polariton
SPPhP	Surface Plasmon Phonon Polariton
SRG	Surface Relief Grating
SZPL	Soret Zone Plate Lens
TE	Transverse Electric
THz	Terahertz
TM	Transverse Magnetic
TO	Transverse Optical
TPX	Polymethylpentene

# 1. INTRODUCTION

Terahertz (THz) range corresponds to the frequency range between 0.1 and 10 THz and currently receives a large amount of research interest. Research into THz frequencies is pushed by the uniquely large number of its possible applications. Due to the low quantum energies and therefore a non-ionizing nature, its usefulness in healthcare for non x-ray based methods of scanning teeth, cancerous, epidermal layers, and other tissues had been demonstrated [1,2]. Due to strong dielectric media penetration, THz frequency based systems had been developed for fabrication and industry quality control [3]. Security applications for parcel screening, drug and explosive identification [4], and even security screening of hidden objects on people at airports or other places of interest [5] had been demonstrated. The use of THz in the scientific field of astrophysics has long been known, as THz frequency-based telescopes gather information about the chemical composition of distant objects and universal superstructures in satellite and aerial telescopes [6,7]. Maybe even more pressing is the need for THz application for ultra high data rate information transmission. Due to inevitable exponential increase of everyday internet bandwidth needs, even emerging 5G technology is predicted to be insufficient to carry enough data in several years [4,8,9]. Significant increase in bandwidth is expected with introduction of THz frequency data transmission systems. Proof of principle setups are already able to carry several GB/s data rates in point to point over-the-air transmission systems [10].

All of the mentioned applications require three main components: emitters, transmission or beam profiling optics, and detectors. Preferably all of these components should be compact, efficient, and have easy and low cost fabrication process. Active THz components (emitters and

detectors) commonly suffer from a technological phenomenon known as the "Terahertz gap" [11]. This phenomenon entails that neither electronic nor optical elements work particularly well in this frequency range requiring novel solutions. THz frequencies are too high for efficient operation of electronic circuits from the side of radio frequencies while the quantum energy is typically at or below  $kT$  of 24 meV preventing room temperature optical devices from operating. Due to this fact novel ideas for THz generation and detection are continuously brought forth and investigated.

While emitters and detectors are obviously of high importance and are strongly investigated, operation of a whole data transfer or scanning system can only be achieved by efficiently controlling the radiation between these elements. The **first part of this thesis** deals with the development of compact, lightweight and easily fabricated passive beamforming components. Namely, the multilevel phase Fresnel lenses (MPFLs) and Soret zone plates (SZPs) are designed for the application of focusing 0.6 and 4.7 THz frequency radiation. The elements are designed, modelled and then fabricated using fast, relatively simple and cost effective method of direct laser ablation (DLA). DLA demonstrates superior versatility for fast and iterative component fabrication in comparison to mechanical methods as well as much easier application and lower cost as compared to optical lithography based fabrication. Successful characterisation of manufactured components and their state of the art performance demonstrated the applicability of this fabrication method in quick iterative component development stage and use of the fabricated elements for THz beamforming.

If one turns attention to energies above the THz range, one has to shift their viewpoint from frequency scale, common to electronics, to wavelengths, which is common to optics. THz frequency range is also called Far Infrared (FIR) by the optical society. Above THz (or FIR) range lies Mid infrared (MIR), spanning from  $3\ \mu\text{m}$  to  $50\ \mu\text{m}$  (or around  $200\ \text{cm}^{-1}$  to  $3000\ \text{cm}^{-1}$ ), according to *ISO 20473:2007*. This frequency range is usually dominated by thermal emission of black/grey bodies of near room temperature and is most often characterised by broadband and omnidirectional black body like emission profiles. Even though MIR range is quite well understood novel applications beyond classi-

cal thermal radiators still emerge. Use of specifically designed thermal emitters for daytime radiative cooling had been demonstrated [12, 13]. A recent suggestion of using narrowband thermal emission by waste heat from a CPU to power nanophotonic circuitry had been made [14].

Polaritonics are long shown to be a capable method for light confinement as well as designing the radiative properties of an element [15, 16]. Surface phonon polaritons (SPhPs) are shown to be of great promise in designing optical components in THz and MIR range due to their characteristic frequencies and low inherent losses. High quality excitations and subwavelength light confinement are used for material property investigation, as well as various sensors and emitters [12, 13, 17]. One of emerging device examples is a polaritonic laser which has been developed in InGaAs/AlInAs material system based quantum cascade structures [18].

**The second part** of this thesis mainly concerns the investigation of polaritonic excitations in surface grating coupled polar semiconductors, and their interaction with light. Even though this topic seems to be distant from the THz beamforming components in the first chapter, the devices under investigation are based on the same diffraction phenomena. In this case, a grating is used for coupling the far field light to the surface polariton (SP) excitations of semiconductor structures.

A coherent (narrowband and strongly directional) excitation of SPs has been demonstrated in first modelled and then experimentally fabricated samples of surface relief grating coupled  $n$ -GaN. Variable frequency coherent emission in the range of  $560\text{ cm}^{-1}$  to  $1000\text{ cm}^{-1}$  has been demonstrated. Frequency variation was achieved via changing incidence angle or surface grating geometry with spatial coherence lengths reaching over  $50\lambda$ . Interaction of metal grating coupled GaN/GaN and GaN/AlN/SiC heterostructures with incoming radiation was also investigated by modelling and measuring the reflectivity spectra. Reflectivity dip lines associated with polaritons on sample surface, within the heterostructure as well as epsilon near zero modes were identified and their frequency variability was demonstrated via modelling of the reflectivity spectra.

As the underlying physics of the Fresnel optics and the polaritonic phenomena are freely scaleable in the frequency space with the

proper selection of materials according their dielectric properties, this thesis is believed to pave a way in design and fabrication for novel emission/beam profiling devices.

## 1.1 Major Goal

The development of diffractive lenses, grating couplers, and surface plasmon-phonon-polaritonic structures for spectroscopic imaging systems and THz-IR applications.

## 1.2 Tasks of this Work

- To investigate silicon- and metal foil-based diffractive lenses for application in imaging systems at 0.6 THz and 4.7 THz frequencies;
- To investigate the dispersion characteristics of surface plasmon-phonon-polaritons in the Reststrahlen band of polar semiconductors;
- To investigate *n*-type gallium nitride grating for application in coherent thermal sources;
- To investigate metal grating couplers for AlGaN/GaN/SiC heterostructures in the region of the Reststrahlen band.

## 1.3 Scientific Novelty

- Multilevel phase corrected Fresnel lenses with different numbers of phase quantisation levels, working at 0.6 THz frequencies, were fabricated using the direct laser ablation method for the first time. Their focusing properties were investigated and application in commercial uses was demonstrated as feasible using an imaging/quality control setup.
- Free standing metal Soret zone plate lens and silicon multilevel phase Fresnel lens were developed via direct laser ablation method for focusing record high 4.7 THz frequency. Fabricated elements were characterised and their focusing properties were investigated.

- Investigation of polariton excitation in *n*-GaN surface relief gratings was carried out theoretically and experimentally. Thorough investigation of reflectivity spectra dependence on the grating periodicity and incidence angle of IR radiation revealed that the experimental results closely matched the theoretical predictions. Therefore, applicability of the modelling method for designing elements as well as applicability of polaritonic *n*-GaN elements themselves for tailored reflectivity with narrowband features were confirmed.
- The coherence properties of thermally excited polaritonic emission from *n*-GaN surface relief gratings were demonstrated for the first time. Narrowband features in the order of  $10\text{ cm}^{-1}$  were observed and spatial coherence length in the order of  $50\lambda$  was achieved demonstrating applicability of *n*-GaN SRGS in the fields of tailored narrowband thermal emission as well as coherent signal transfer.
- Reflectivity spectra of metal grating coupled GaN/GaN and GaN/AlN/SiC heterostructures were investigated for the first time. Heterostructures were demonstrated to be successfully used in broadening the operational range of surface phonon polaritons. A metal grating coupler was successfully used for the confinement of light within the heterostructure layers.



## 1.4 Statements of Defence

- Direct laser ablation is suitable for the fabrication of multilevel phase Fresnel lenses working at 0.6 THz frequency, and these components can be used in THz imaging applications.
- The direct laser ablation method is advantageous for the development of metal Soret Zone plates and silicon multilevel phase Fresnel lenses for 4.7 THz and higher frequency radiation.
- Surface plasmon-phonon polaritons are optically excited in the  $n$ -GaN surface relief gratings in the frequency range of 560-1000  $\text{cm}^{-1}$ , defined by the hybrid plasmon phonon mode frequencies.
- Surface plasmon phonon polaritons, thermally excited in the emission spectra of  $n$ -GaN gratings, demonstrate coherent, variable frequency radiation in the Reststrahlen band of a heavily doped semiconductor.
- Metal grating coupled GaN/GaN and GaN/AlN/SiC heterostructures are suitable for the development of infrared optical components with custom designed features in the reflectivity spectrum.

## 1.5 Contribution of the Author

The author carried out characterisation experiments for the Fresnel optics at 0.6 THz frequencies, designed and carried out the transmission experiments as well as application demonstration by scanning the circuitry containing plastic card. Author also took part in the result analysis of the 4.7 THz focusing optics and the preparation for publications.

All of the calculations using the rigorous coupled wave analysis method were carried out by the author. He also designed and fabricated the surface relief grating structures, as well as carried out most of the characterisation measurements. The author analysed all experimental and theoretical results for surface gratings, prepared and presented the results in the publications as well as in the conference reports with the help of the co-authors.

The author of the dissertation also carried out work in fields not directly related to the thesis. This involved spectroscopy of 2D electron gas plasmons, where preparation for experiments, part of data analysis and preparation for publishing was carried out [P8,P9,P12,P13]. In the investigation of electroluminescence of AlGa<sub>N</sub>/Ga<sub>N</sub> heterostructure impurities, sample preparation and part of the result analysis was done by the author [P10,P11]. Calculations or theoretical reflectivity spectra for result analysis of Al<sub>2</sub>O<sub>3</sub> surface structure reflectivity were also carried out [P14].

## 1.6 Co-authors Contribution

Experiments, methodology, and research vectors were lead by Dr. Irmantas Kašalynas. The wafers of *n*-Ga<sub>N</sub>, Ga<sub>N</sub>/Ga<sub>N</sub> and Ga<sub>N</sub>/SiC were kindly provided by the Institute of High Pressure Physics PAS, Warsaw, Poland. The *n*-Ga<sub>N</sub> surface relief gratings were fabricated in the Institute of High Pressure Physics PAS, Warsaw, Poland with valuable help from Dr. Pawel Prystawko, Dr. Piotr Kruszcwski, Dr. Jacek Kacperski and Krzysztof Gibasiewicz. The polariton dispersion was analytically calculated by Dr. Vadym Korotyeyev. The design and development of heating-rotation stage as well as automated angular emission measurements were carried out by Dr. Linas Minkevičius and Dr. Ignas Grige-

lionis. Angular reflectivity in the Bruker spectrometer was measured in close collaborator with Dr. Saulius Tumėnas. The diffractive lenses have been designed by Dr. Irmantas Kašalynas and Dr. Linas Minkevičius, while they were laser-processed by Dr. Simonas Indrišiūnas and Dr. Bogdan Voisiat in the Department of Laser Technologies, FTMC, Lithuania. Experimental characterisation of the diffractive lenses was carried out in part by Dr. Linas Minkevičius at FTMC, Lithuania, and by Dr. Ignas Grigelionis and Dr. Heiko Richter at the Institute of Optical Sensor Systems, DLR-Berlin, Germany.

## 1.7 Publications

The main results of the dissertation were published in 7 scientific publications and 18 conference reports.

### Scientific Publications

#### Publications directly related to thesis:

- P1 L. Minkevičius, S. Indrišiūnas, R. Šniaukas, B. Voisiat, **V. Janonis**, V. Tamošiūnas, I. Kašalynas, G. Račiukaitis, G. Valušis, “Terahertz multilevel phase Fresnel lenses fabricated by laser patterning of silicon,” *Opt. Lett.*, vol. 42, no. 10, p. 1875-1878, 2017. <https://doi.org/10.1364/OL.42.001875>.
- P2 L. Minkevičius, S. Indrišiūnas, R. Šniaukas, G. Račiukaitis, **V. Janonis**, V. Tamošiūnas, I. Kašalynas, G. Valušis, “Compact diffractive optics for THz imaging,” *Lith. J. Phys.*, vol. 58, no. 1, pp. 99–107, 2018. <https://doi.org/10.3952/physics.v58i1.3655>.
- P3 S. Indrišiūnas, H. Richter, I. Grigelionis, **V. Janonis**, L. Minkevičius, G. Valušis, G. Račiukaitis, T. Hagelschuer, H. W. Hübers, I. Kašalynas, “Laser-processed diffractive lenses for the frequency range of 47 THz,” *Opt. Lett.*, vol. 44, no. 5, pp. 1210-1213, 2019. <https://doi.org/10.1364/OL.44.001210>
- P4 **V. Janonis**, S. Tumėnas, P. Prystawko, J. Kacperski, and I. Kašalynas, “Investigation of  $n$ -type gallium nitride grating for applications in coherent thermal sources,” *Appl. Phys. Lett.*, vol. 116, no. 11, p. 112103, 2020. <https://doi.org/10.1063/1.5143220>.
- P5 V. V. Korotyeyev, **V. Janonis**, and I. Kašalynas, “Description of the wavevector dispersion of surface plasmon-phonon-polaritons,” arXiv:2002.05473, 2020. <https://arxiv.org/abs/2002.05473>
- P6 **V. Janonis**, V. Jakštas, I. Kašalynas, P. Prystawko, and P. Kruszewski, “Reflectivity of Plasmon-Phonon Modes in Grating-Coupled Al-GaN/GaN Heterostructures Grown on SiC and GaN Substrates,” *Phys. status solidi B*, vol. 255, p. 1870118, 2018. <https://doi.org/10.1002/pssb.201870118>.
- P7 **V. Janonis**, D. Pashnev, I. Grigelionis, V. V. Korotyeyev, R. Balagula, L. Minkevičius, J. Jorudas, et al., “Electrically-Pumped THz Emitters Based on Plasma Waves Excitation in III-Nitride Structures” In Proceedings of

SPIE. Vol. 1149909. SPIE. 2020. <https://doi.org/10.1117/12.2569261>.

**Publications during the doctorate studies not directly related to the thesis:**

- P8 D. Pashnev, T. Kaplas, V. Korotyeyev, **V. Janonis**, A. Urbanowicz, J. Jorudas, I. Kašalynas, “Terahertz Time-Domain Spectroscopy of Two-Dimensional Plasmons in AlGa<sub>N</sub>/Ga<sub>N</sub> Heterostructures.” *Applied Physics Letters*, vol. 117, no. 5, p. 51105, 2020. <https://doi.org/10.1063/5.0014977>.
- P9 D. Pashnev, V. Korotyeyev, **V. Janonis**, J. Jorūdas, T. Kaplas, A. Urbanowicz, I. Kašalynas, Experimental evidence of temperature dependent effective mass in AlGa<sub>N</sub>/Ga<sub>N</sub> heterostructures observed via THz spectroscopy of 2D plasmons. Under preparation.
- P10 I. Grigelionis, J. Jorudas, V. Jakštas, **V. Janonis**, I. Kašalynas, P. Prystawko, P. Kruszewski, M. Leszczyński, “Terahertz electroluminescence of shallow impurities in AlGa<sub>N</sub>/Ga<sub>N</sub> heterostructures at 20 K and 110 K temperature,” *Mater. Sci. Semicond. Process.*, vol. 93, pp. 280–283, 2019.
- P11 I. Grigelionis, V. Jakštas, **V. Janonis**, I. Kašalynas, P. Prystawko, P. Kruszewski, M. Leszczyński, “Terahertz Electroluminescence of Shallow Impurities in AlGa<sub>N</sub>/Ga<sub>N</sub> Heterostructures at Temperatures above 80 K,” *Phys. status solidi*, vol. 255, no. 5, p. 1700421, 2018.
- P12 V. Jakštas, J. Jorudas, **V. Janonis**, L. Minkevičius, I. Kašalynas, P. Prystawko, M. Leszczyński, “Development of AlGa<sub>N</sub>/Ga<sub>N</sub>/SiC high-electron-mobility transistors for THz detection,” *Lith. J. Phys.*, vol. 58, no. 2, 2018.
- P13 V. Jakštas, I. Grigelionis, **V. Janonis**, G. Valušis, I. Kašalynas, G. Seniutinas, S. Juodkazis, P. Prystawko, M. Leszczyński, “Electrically driven terahertz radiation of 2DEG plasmons in AlGa<sub>N</sub>/Ga<sub>N</sub> structures at 110 K temperature,” *Appl. Phys. Lett.*, vol. 110, no. 20, 2017.
- P14 X. Wang, G. Seniutinas, A. Balčytis, I. Kašalynas, V. Jakštas, **V. Janonis**, R. Venckevičius, R. Buividas, D. Appadoo, G. Valušis, S. Juodkazis, “Laser structuring for control of coupling between THz light and phonon modes,” *J. Laser Micro Nanoeng.*, vol. 11, no. 3, pp. 377–380, 2016.

## Conference Reports

**Conference reports directly related to thesis (presenters name underlined):**

- C1 **V. Janonis**, P. Prystawko, K. Gibasiewicz, J. Kacperski, I. Kašalynas, Investigation of the reflectivity spectra of n-type GaN semiconductor with surface relief grating // 44rd International conference on infrared, millimeter and terahertz waves (IRMMW THz-2019) : 1-6 September 2019, Paris, France. ISBN 9781538682852. DOI: 10.1109/IRMMW-THz.2019.8873926.[Poster]
- C2 **V. Janonis**, V. Jakštas, P. Prystawko, I. Kašalynas, Light coupling with the periodical structures processed on GaN and GaN/SiC semiconductors French-German THz Conference 2019, Kaiserslautern 02.-05. April 2019. [Oral presentation]
- C3 **V. Janonis**, P. Prystawko, I. Kašalynas, n-GaN puslaidininkių su paviršinėmis gardelėmis atspindžio spektrų tyrimas // 43-oji Lietuvos nacionalinė fizikos konferencija, 2019 m. spalio 3-5 d., Kaunas : pranešimų medžiaga. Kaunas : Kauno technologijos universitetas, 2019. eISBN 9786090216385. [Oral presentation]
- C4 **V. Janonis**, I. Kašalynas, S. Indrišiūnas, P. Prystawko, Reflectivity spectra of doped GaN with periodic deep surface structures // 34th International conference on the physics of semiconductors ICPS2018: July 29th – August 3rd, 2018, Montpellier, France. [Poster]
- C5 **V. Janonis**, S. Indrišiūnas, P. Prystawko, I. Kašalynas, Investigation of reflectivity spectrum of GaN with periodic apertures on the surface // 16th International conference on Advanced properties and processes in optoelectronics materials and systems (Apropos 16) : October 10-12, 2018, Vilnius, Lithuania. ISBN 9786099551159. [Oral presentation]
- C6 **V. Janonis**, V. Jakštas, I. Grigelionis, I. Kašalynas, P. Prystawko, P. Kruszewski, J. Leszczyński, Reflectivity of plasmon–phonon modes in grating-coupled AlGa<sub>N</sub>/Ga<sub>N</sub> heterostructures grown on SiC and GaN substrates // 12th international conference on nitride semiconductors (ICNS12) : 24th-28th July, 2017, Strasbourg, France.[Poster]
- C7 **V. Janonis**, V. Jakštas, I. Kašalynas, Prystawko, Pawel. Investigation of reflectivity of plasmon–phonon modes in grating-coupled AlGa<sub>N</sub>/Ga<sub>N</sub> heterostructures grown on SiC and GaN substrates // Open readings

- 2017 : 60th international conference for students of physics and natural sciences : March 14-17, 2017, Vilnius, Lithuania. ISSN 2029-4425. [Poster]
- C8 **V. Janonis**, V. Jakštas, I. Kašalynas, P. Prystawko, M. Leszczynski, Reflectivity of plasmon–phonon modes in grating-coupled AlGa<sub>N</sub>/Ga<sub>N</sub> heterostructures grown on SiC and Ga<sub>N</sub> substrates // 46th international school & conference on the physics of semiconductors (Jaszowiec 2017) : Szczyrk, Poland, June 17th – 23rd, 2017. [Poster]
- C9 **V. Janonis**, V. Jakštas, I. Grigelionis, I. Kašalynas, Investigation of thermal and plasmonic emission from grating-gated Ga<sub>N</sub>/AlGa<sub>N</sub> high electron mobility transistors // 45th international school & conference on the physics of semiconductors "Jaszowiec 2016", Szczyrk, Poland, June 18-24, 2016. [Poster]
- C10 **V. Janonis**, V. Jakštas, I. Grigelionis, I. Kašalynas, Pirminis plazmoninių Ga<sub>N</sub>/AlGa<sub>N</sub> emiterių charakterizavimas Furje spektroskopijos metodika ir tyrimo metodo įvertinimas // FizTeCh: 6-oji Fizinių ir technologijos mokslų centro doktorantų ir jaunųjų mokslininkų konferencija, 2016 spalio 26-27 d. Vilnius. [Poster]
- C11 **V. Janonis**, V. Jakštas, I. Kašalynas, Investigation of thermal and plasmonic emission from Ga<sub>N</sub>/AlGa<sub>N</sub> grating gated high electron mobility transistors // Open readings. 2016 Vilnius, Lithuania. ISSN 2029-4425. [Poster]
- C12 L. Minkevičius, D. Jokubauskis, **V. Janonis**, S. Indrišiūnas, G. Račiukaitis, V. Tamošiūnas, I. Kašalynas, G. Valušis, High numerical aperture diffractive optics for imaging applications at 0.6 THz frequency // 43rd International conference on infrared, millimeter and terahertz waves (IRMMW THz-2018) : 9-14 September 2018, Nagoya, Japan. ISBN 9781538638095. DOI: 10.1109/IRMMW-THz.2018.8510393.
- C13 D. Jokubauskis, L. Minkevičius, S. Indrišiūnas, M. Karaliūnas, V. Tamošiūnas, **V. Janonis**, I. Kašalynas, G. Račiukaitis, G. Valušis, Silicon diffractive optics for terahertz beam manipulation & application for terahertz imaging // 7th Russia-Japan-USA-Europe symposium on fundamental & applied problems of terahertz devices & technologies & 4th TERAMIR international laboratory workshop : September 17-21, 2018, Warsaw, Poland.
- C14 L. Minkevičius, D. Jokubauskis, S. Indrišiūnas, **V. Janonis**, V. Tamošiūnas, I. Kašalynas, G. Račiukaitis, G. Valušis, Silicon based diffractive

optics for imaging applications at sub-THz frequencies // 16th International conference on Advanced properties and processes in optoelectronics materials and systems (Apropos 16) : October 10-12, 2018, Vilnius, Lithuania. ISBN 9786099551159.

- C15 L. Minkevičius, S. Indrišiūnas, B. Voisiat, G. Račiukaitis, **V. Janonis**, V. Tamošiūnas, I. Kašalynas, G. Valušis, Compact diffractive optics for THz imaging // 28th international symposium on space terahertz technology (ISSTT 2017) : March 13-15, 2017, Cologne, Germany.
- C16 I. Kašalynas, R. Venckevičius, L. Minkevičius, F. Wahaia, **V. Janonis**, V. Tamošiūnas, D. Seliuta, G. Valušis, A. Sešek, J. Trontelj, S. C. D. Carvalho, High spatial resolution terahertz imaging of carcinoma tissues at 0.6 THz frequencies // 41st International conference on infrared, millimeter, and terahertz waves (IRMMW-THz 2016) : 25-30 September, 2016, Copenhagen, Denmark. DOI: 10.1109/IRMMW-THz.2016.7758885.
- C17 I. Kašalynas, R. Venckevičius, V. Jakštas, **V. Janonis**, J. Laužadis, G. Seniutinas, E. Širmulis, G. Valušis, K. Požela, S. Juodkazis, P. Prystawko, J. Leszczyński, THz emission from grating-coupled AlGa<sub>N</sub>/Ga<sub>N</sub> heterostructures: comparison between plasmonic and thermal emission // 40th international conference on infrared, millimeter, and terahertz waves (IRMMW-THz2015) : 23 - 28 August 2015, Chinese University of Hong Kong. ISSN 2162-2027. DOI: 10.1109/IRMMW-THz.2015.7327829.
- C18 I. Kašalynas, V. Jakštas, **V. Janonis**, J. Laužadis, E. Širmulis, R. Venckevičius, G. Valušis, K. Požela, P. Prystawko, M. Leszczynski, Investigation of plasmonic and thermal THz emission from grating-coupled Al-GaN/GaN high mobility electron transistors // 51st international conference on microelectronics, devices and materials and the workshop on terahertz and microwave systems (MIDEM) : September 23-25 2015, Bled, Slovenia. Ljubljana. ISBN 9789619293355.

**Additionally, during the doctorate studies, 22 conference reports not directly related to the thesis, were co-authored.**

## 1.8 Participation in Projects

The research was performed while working in projects:

1. Research Council of Lithuania NMP "Toward future technologies," „Kompaktiški integriniai THz komponentai ir spektroskopinio THz vaizdinimo sistemos“ (KITKAS), LAT-04/2016;



2. Research Council of Lithuania, „Kompaktiški terahercinės spinduliuotės plazmoniniai emiteriai.“ (KOTERA-PLAZA), 01.2.2-LMT-K-718-01-0047;
3. European Space Agency, "Directive transistor-based THz detectors" (THzFET), 3500-T41;
4. Research Council of Lithuania, "Terahertz plasma wave instabilities in GaN/AlGaN nanowires" (TERAGANWIRE), S-LL-19-1.

## 2. LITERATURE OVERVIEW

### 2.1 Diffractive Optics

Refractive and reflective THz optical elements are widely used in scientific laboratory setups. Their use in modern handheld optoelectronics or micro to pico-satellite systems [19], however, is strongly hindered by their large size and weight. The need for compact integrated THz optics solutions is even more relevant with the global tendencies of device miniaturization and optimization [20]. There is a notable need for THz optics for astronomical applications, as many molecular emission lines are based in this frequency range, allowing for the use of THz spectroscopy for the chemical analysis of astronomical objects [6], observation of thermal emission from cold molecular clouds or control of quantum cascade laser based detection systems [21]. Cosmological observations are sometimes carried out in nano-satellites, which are under rapid development and face restrictions on component weight and size.

Diffractive optical elements (DOEs) are mostly implemented as multilevel Fresnel lenses or Soret zone plates produced from different materials like metals, plastics and crystals. However DOEs also offer much wider application possibilities, as formation of Bessel [22, 23], Fibonacci [24] and other types of beams has been demonstrated. Various processing technologies are implemented for lens fabrication, from mechanical milling, 3D printing and laser processing to UV lithographic and reactive ion etching (RIE).

THz DOEs are mostly used in experimental setups with specific element requirements. For example, cryogenic spectroscopic laboratory systems based on MCT point detectors require robust and easy-integration optical beamforming components. Here, diffractive

optics could prove superior to commonly used refractive lenses.

Commercial THz DOE applications also emerge as implementation of these elements is demonstrated in linear conveyor package scanning systems, where large area DOE are used to transform radiation from a point source into a THz sheet [25]. Even some commercial offers can nowadays be found for security or quality control scanning applications [26, 27]. At the moment, the interest in widespread THz device integration may be further illustrated by the first implementation of the SOLI radar, working at 0.06 THz frequency in commercial *Google Pixel 4* phones in 2019, without use of additional optics.

A lot of DOEs are fabricated from plastics, metals and even paper for the sub-THz spectral region. While this range is interesting for data transfer and communications, higher frequencies are needed for spectroscopic material characterisation, imaging, and astronomy applications [4]. DOEs at frequencies above 1 THz are scarcely reported on due to difficulties associated with finding appropriate materials as well as higher requirements on fabrication precision, cost, complexity, and scalability [28]. Some of works include ion etched multilevel Si lenses working up to 1.5 THz [29], 2.5 THz [30] or laser processed binary lens for 2.1 THz [31].

### 2.1.1 Materials in THz Range

The first step in the development of an optical element is the selection of a material having properties tailored for the specific application. In cases when DOEs are designed for transmission geometry, the main requirements for materials are small absorption losses and a high refractive index for effective phase retardation. On the practical note, the material should be cheap, easy to process and offer constant quality ensuring repeatability in component fabrication. The main properties and challenges in selecting a material for the fabrication of a THz range optical component are analysed in this section.

Standard visual range materials such as glass are not suitable for the THz range. The transmission coefficient of glass drops dramatically due to increased absorption between 0.5 and 100 THz [4, 32] with the exact range varying according to specific type of glass. Crystalline z-cut

quartz is an exception. This material is transparent in optical as well as THz regions; nevertheless, a high absorption band is still observed between 4 and 70 THz limiting its possible operational bandwidth. Another problem with z-quartz is its high price [33].

Some polymer-based materials offer up to 90% transmission and a refractive index of about 1.5, making them reasonably attractive in the manufacturing of refractive lenses for the sub-THz region [33–35]. Available transparent materials such as Polyethylene (PE), high density polyethylene (HDPE), Polymethylpentene (TPX) or Polytetrafluoroethylene (PTFE) also are easy to process by milling [36] or even 3D-printing [37] thus making the production of optical components fast and simple. The ease of use for these materials also allows for quick iterative complex component fabrication by simply printing out modeled structures [38]. Custom, 3D-printed plastic components had been shown to be applicable in vortex beam generation [39], forming Gaussian beams into sheet ones [25], as well as for holographic image forming [40] in addition to simply focusing Gaussian beams [41,42], waveguiding and producing diffractive gratings or prisms for the sub-THz region [40].

Low refractive index of the polymers used in the making of passive elements gives advantage of small reflective losses as  $R = ((n - 1)/(n + 1))^2$  according to Fresnel equations. However the low refractive index also introduces a disadvantage as the polymer based components must have high enough thickness to sufficiently modify the optical path. Increase of optical absorption losses as well as scattering from inhomogeneities in the bulk of a polymer are also observed with the increase of material thickness [34,43]. Due to its polymeric (large molecule) nature, plastics also show increase in absorption with the increase of the frequency commonly above 0.5 THz, as it nears the characteristic absorption lines of the vibrational modes of the polymer as seen in **Fig. 2.1**.

For the softer, thermoplastic 3D printable materials (Acrylonitrile butadiene styrene (ABS), Polyactic acid (PLA), Nylon, Bendlay and Polystyrene) absorption losses were shown to become large even below 1 THz frequency [37]. For harder, millable materials such as PP and HDPE, absorption starts to be prominent at around 1.5 THz. The highest operational window (for polymeric materials) is exhibited by TPX,

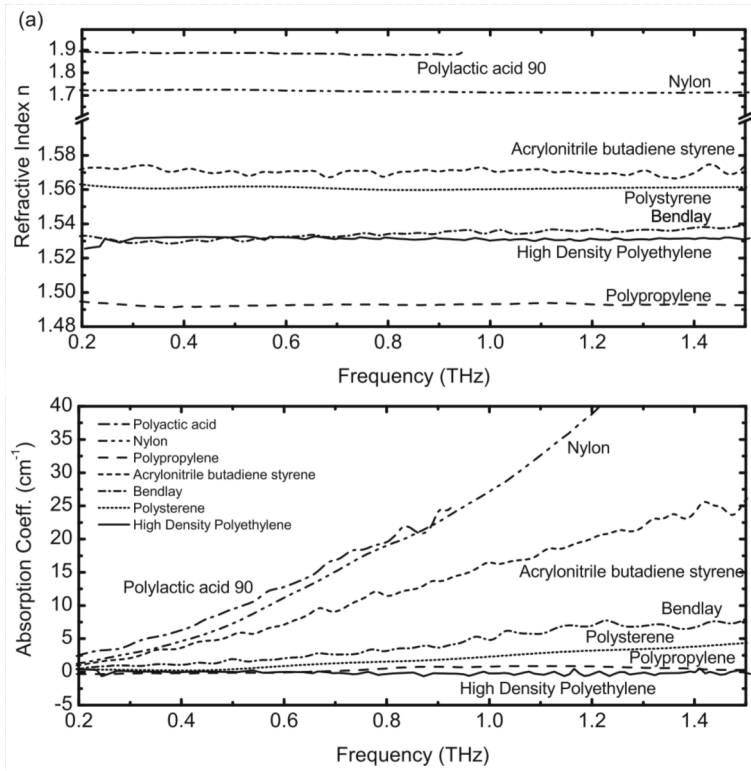


**Figure 2.1:** Refractive index and absorption coefficient spectra of polymeric materials commonly used for THz optics [37].

nevertheless its transmission also starts to be inconsistent (increased absorption lines start appearing) above 1 THz and drops drastically at 4 THz [33,34].

Material of choice for the passive THz element fabrication is crystal based. There are many crystalline materials suitable for the manufacturing of optical THz components. It is important to note that specific spectral features associated with Reststrahlen band (RB), impurities and free-carrier absorption, must be considered in thoroughly designing a specific optical component. Crystalline materials met in THz component design are Si, Ge, SiC, sapphire and diamond [34]. Nevertheless, in view of practical application, silicon is probably the most promising one. High resistivity silicon exhibits an almost flat 50% transmission characteristic up to 12 THz (25  $\mu\text{m}$ ), (see transmission spectra in Fig. 2.2). Silicon is even more attractive for the use in rapid prototyping and fabrication for its relatively low price, as well as famously

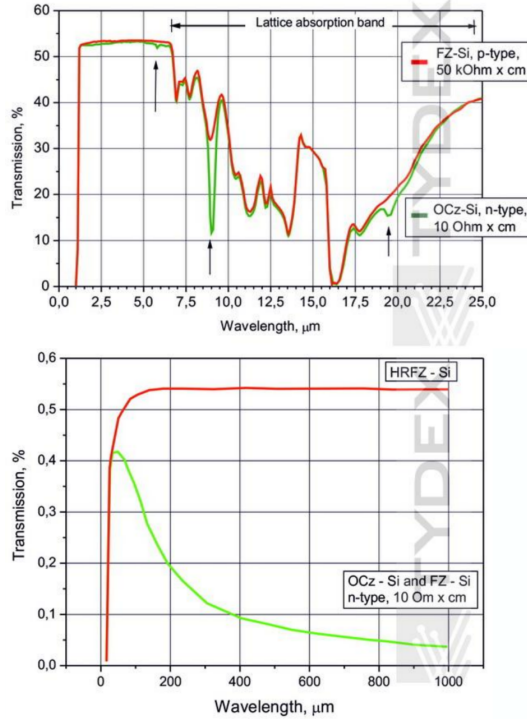


**Figure 2.2:** Transmission spectra of high resistance floating zone and *n*-type doped Si. **a)** shows the short wavelength region of IR to visual range, with lattice absorption region prominent and accordingly marked. **b)** shows the long wavelength region with prominent difference between transmissions of high resistance and doped Si due to free carrier absorption [33].

mature processing technology. The technological maturity of silicon offers abundance of processing options and also an unique possibility for integration of fabricated DOEs into conventional electronics.

In respect to THz optical properties silicon offers a relatively high index of refraction (around 3.4) with low dispersion in the THz range. While the high refractive index of silicon increases the light bending/phase retardation efficiency of the components, it also increases the reflective Fresnel losses. Nevertheless, reflective losses may be suppressed by the application of antireflective coatings with transmission losses being limited to 6% by parylene coating for the frequency range of 0.8 to 0.9 THz [44]. Antireflective periodical surface structures were also produced by dicing and etching resulting in transmission losses below 1% [44] or, more recently, laser processing resulting in transmission coefficient  $T = 90\%$  at a designed, specific frequency. [9]

The main optical losses in crystalline materials are caused by free carriers and phonons of the material. The former are well controlled by using high-resistance floating zone silicon (resistivity typically in the range of 10 k $\Omega$ cm) with negligible free carrier concentration and therefore, very low absorption with values below 0.5 cm<sup>-1</sup> in the frequency range of 0.1 to 2 THz (see **Fig. 2.2 b**) The phonon (or vibrational) losses in Si are prominent in the band of 13 THz to 50 THz (see **Fig. 2.2**) defining the main limitation of possible operational range of the fabricated devices.

Low absorption losses and high refractive index of silicon together with high quality processing cause high efficiency of fabricated optical elements as compared to ones made from plastic components or metal zone plate based devices. These facts make Si an optimal choice for fabrication of THz optical components.

### 2.1.2 Refractive Lenses

Classical refractive THz elements can be fabricated by carefully selecting materials for respective application frequencies. The operation of refractive elements relies on phase retardation within a material and its operational range limitations are only associated with the dielectric properties of the material. For example, a refractive lens fabricated from HDPE (with the refractive index of around 1.5) can be used to effectively manipulate radiation at subterahertz frequencies. HDPE elements are often met in practice due to ease of fabrication, even though they suffer from inherent drawbacks of the material like large bulk and increased absorption losses. Polymer refractive lenses are also unsuitable for compact setups, as the the properties of the materials prohibit fabrication of low  $f/D$  (focal distance to element diameter) ratio components. Plastic lenses benefit from relatively simple fabrication via milling/polishing [43], 3D printing [41] or compression moulding [45].

A wideband performance may be achieved using classical Si lenses, which is in fact unparalleled by other beam-shaping techniques [46]. Performance can be maintained from sub-THz to several THz frequencies, by ensuring high fabrication quality as fabrication imperfection tolerances scale proportionally with the wavelength of the radiation. There

are drawbacks, as refractive Si optics is bulky and also exhibits high reflective losses. Even though reflective losses, can be negated by the application of antireflective coatings, the process of coating or patterning of a curved lens surface can become increasingly complicated. Application of refractive Si elements in semi-integrated optics has been demonstrated by the use of hemispherical lens which focuses incident radiation to a detector or emitter placed on the lens base [36,47]. Unfortunately bulk Si hemisphere has a large footprint (height approximately equal to the radius) and mass. Even more, the large thickness of hemispherical lens is known to introduce notable geometrical aberrations also affecting the performance of the system [41].

There are, however attempts to overcome the material and size requirements of refractive THz optical elements. Application of a HDPE-based double sided multi-spherical achromatic Fresnel lens has been demonstrated as having high efficiency at 0.5 THz [36]. Several HDPE Fresnel lens designs had been investigated for the wideband use in 0.15 to 0.6 THz operational range [48]. A Si Fresnel lens fabrication method has been suggested using grey scale lithography and reactive ion etching [49]. Taking all of this into account it can be seen that another path must be taken in order to attain truly compact, efficient and integration ready THz optics elements.

### 2.1.3 Metal Mirrors

In order to avoid the material absorption and scattering losses while also achieving wideband operation, reflective metal based passive optical elements (POEs) may be used. As the plasma frequency in metals is usually located in visible or even UV spectral range, metals tend to maintain near 100% reflectivity in all sub-THz to NIR optical range ensuring extremely almost lossless operation [50].

Probably the most widely spread laboratory grade reflective POEs are the spherical and off-axis parabolic (OAP) mirrors named after their respective surface geometries. While the spherical mirrors with large curvature radius are used for slight alteration of a diverging beam, the OAP is most often met in focusing a collimated beam to a point or collimating the radiation emitted from a point source. In most labora-



tory applications the  $90^\circ$  OAP has proven to be most versatile and most commonly applied. The off axis geometry allows one to place the detectors or emitters outside of the initial optical path and avoid shadowing (for example from detector housing) in order to collect maximum amount of radiation.

At its basis, the reflective elements rely on metal coated surfaces, interacting with the wavefront of radiation, with high efficiency due to the lack of absorption losses [50]. Metallic mirrors require high precision milling and polishing of curved faces in order to work in a wide frequency range. They are used in different applications from laboratory and industrial laser systems to astronomy [51]. Requirement of high manufacturing precision increases the price of such optical components [52]. Due to the off-axis geometry orientation of OAPs in the optical axis is a non trivial task [50,53]. In addition the use of metal mirrors in commercial applications is also hindered by their large size and mass. Another drawback of gold plated mirrors is their low mechanical robustness due to the softness of gold, which requires additional design and application of dielectric coatings for efficient use of the element. On a practical note, OAP elements cannot even be cleaned for the most part (apart from dry-air blowing [52]).

To conclude this section, in order to apply THz optics in small and lightweight systems, another beamforming solution must be found.

### 2.1.4 Diffractive Optical Elements

Diffractive optical elements (DOEs) are widely investigated upon [20, 54, 55], even though research is still needed until full commercial integration is achieved. In some cases using DOEs is the only viable solution, for example in the case of free electron laser beam manipulation [56]. Here compact and cooled diffraction based lenses proved superior to any other beam manipulation element. In the case of THz range achieving small focal length of the optical element which is needed for various applications is also virtually unobtainable without DOEs [29] or the use of bulky spherical silicon lenses.

Due to fundamental wave diffraction nature these elements may be fabricated for radio, millimetre, THz, IR [57] visible and even acoustic

waves [58]. DOEs are already quite widely investigated. Their main advantages are small size and mass with the efficiency also theoretically higher than their classical reflective or refractive counterparts [43, 57]. Generation of complex beam patterns becomes possible even when using a single DOE. This was demonstrated, for example, by generating THz vortex beams with singular 3D-printed diffractive element [39].

Even though diffractive optics of the visible range are met in nature [59], its fabrication in practice is complicated due to the nm scale resolution requirement [60]. In THz region, with the wavelengths of microns and millimetres diffractive optics become much more easy to fabricate. Therefore DOEs are much more competitive in respect to the conventional refractive lenses.

Semiconductor wafers have an additional benefit of being highly robust to environmental conditions which is a very important factor in practical applications. The diameter of the DOEs maybe large while keeping the focal length small thus allowing for very compact optics with small  $f/D$  ratio components [43]. DOEs offer to increase the spread of THz based optoelectronics such as gas sensors [61] or 4K data transmission [10] in applications ranging from mobile phones to satellites. DOEs are essential in beyond 5G data transfer technologies as THz pulses might be used for signal carrying with sufficient speed, while THz DOEs would ensure directive and efficient point to point data transfer [9]. DOEs have also been demonstrated in application for multi pixel cameras, as diffractive lenses were used for increase of SNR and decrease of crosstalk in separate pixels [41, 62].

All in all it can be seen that small, lightweight and integrated THz optics components can be based on diffractive optical elements with their small dimensions, high efficiency, design flexibility and capability of integration with modern electronics.

### 2.1.5 Zone Plates

Refractive lenses (shown in **Fig. 2.3 a**) have a homogeneous curved surface which achieves an uniform phase change for the radiation [43, 57]. In this case the lowest thickness of the element must be at least in the range of  $n \times \lambda$  and in most cases, at the centre of the element, much

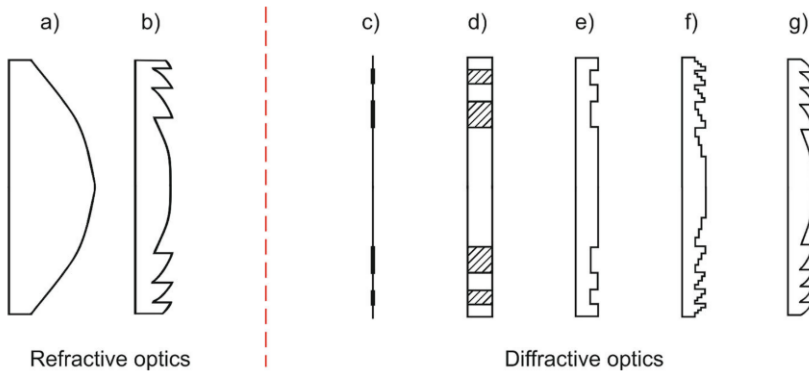


**Figure 2.3:** Crosssections of different design lenses. **a)** and **b)** show conventional and Fresnel refractive lenses, respectively. **c)** Fresnel or Soret zone plate. **d)** Planar dielectric zone plate. **e)** Phase reversing zone plate. **f)** Multilevel phase Fresnel lens with 4 phase quantisation levels. **g)** Kinoform MPFL with infinite number of phase quantisation levels (Phase Fresnel Lens), difference from the conventional Fresnel lens in **b)**, is single phase relation between different lens zones. [43]

more than that [20,57].

In order to reduce the amount of the material the continuously shaped (curved) surface (**Fig. 2.3 a**) may be cut in step-wise fashion and translated back while still keeping the overall surface shape (**Fig. 2.3 b**). This was most widely observed in practice in lighthouse optics where the required small focal length would be unobtainable with classical lenses still having acceptable mass. The surface curvature is kept for the most part, while the amount of required material is substantially cut. Due to the radii of the concentric circles being still much larger than the operational wavelengths, these elements exhibit a wideband operation with small chromatic aberrations.

Next step in the optimization of the optical elements was the Phase Fresnel Lens (PFL). In order to further reduce the dimensions and increase the efficiency, wideband operation must be sacrificed, limiting the elements performance to a single frequency. The widths of the zones of PFL are chosen in a way that each zone would encompass continuous wave phases from  $\phi$  to  $\phi + 2\pi$ . The phase difference of  $2\pi$  is therefore maintained in equivalent points of two adjacent zones virtually maintaining the phase map of a conventional lens at the operational frequency [29,57]. The frequency limitation becomes obvious, because for a different frequency (wavelength) the phase relation will not be

preserved, and strong chromatic aberrations will be observed. It is evident from the **Fig. 2.3** that PFLs further reduce the amount of the material needed for operational component. Width of the element is reduced from many wavelengths related to the diameter of an element to  $n \times \lambda$  in a PFL. PFL thickness is limited only by the refractive index of the material and the ability of a wafer to physically support itself [36,57].

PFLs structure zone widths and heights are in the range of the wavelength and therefore the fabrication accuracy must be much greater than in the case of polished classical refractive lens. Nevertheless, when properly fabricated, PFLs should offer up to 100% focusing efficiency with small  $f/D$  and low physical thickness [43,63].

The fabrication of continuous (kinoform) PFLs is too complicated for practical applications. Step like approximation is therefore commonly used. Certain number ( $p$ ) of subzones (or phase quantisation levels (PQLs)) in the profile of the multilevel phase Fresnel lens (MPFL) is introduced (see **Fig. 2.3 f**).

Physics and derivation of MPFL geometry were properly described by Hristov [57]. Soret was the first one to build a diffractive element from alternating opaque and transmissive circular zones (Soret zone plate lens SZPL). This lens concept is illustrated in **Fig. 2.3 c**. Later on, after a suggestion from Lord Rayleigh, Wood showed that the focusing power could be increased four times by changing opaque zones with transmissive ones using an additional phase shift of  $\pi$ , causing constructive light interference at the focal spot.

Here, without the derivation of well known optics, the main geometrical parameters of the PFL can be summarized as follows. The radii of the zones are governed by the  $2\pi$  phase quantisation condition. In the case of SZPL these can be written as [57]:

$$b_w = \sqrt{\lambda f n + \left(\frac{n\lambda}{2}\right)^2} \quad (2.1)$$

where  $w = 1, 2, \dots, W$  is an integer and  $W$  is the number of full-wave zones in the Fresnel lens,  $f$  is the focal length and  $\lambda$  is the resonant wavelength (frequency) for the lens. Here, the main limitation for the PFLs becomes evident. The design is calculated for a single frequency resulting in large

chromatic aberrations for other wavelengths in contrast to continuously curved surfaces which perform well for a very large wavelength range.

The Soret zone plate is the ultimate case of the width reduction as it may be fabricated from an extremely thin metal foil (tens of microns in thickness), the mechanical support of this foil becoming the main challenge in the use of extremely thin SZPLs. Integration of the SZPL on a chip [64] and with band pass filters [65,66] has been demonstrated. Main requirement for SZPL is the binary structures of alternating transmissive and opaque zones. Optimal transmission modulation, of course, is shown in zones fabricated from metal [43, 54, 57], nevertheless DOEs fabricated from graphite [66] or even paper [67] have also been demonstrated. Even though the dimensions of SZPL in the propagation direction is in the subwavelength dimensions the trade-off here comes from focusing efficiency, limited to around 10% [57].

The efficiency of a zone plate is increased 4 times (up to 40%) when instead of opaque zone, phase reversed zone is introduced. This is achieved by etching a groove in the surface of the zone plate, depth of which is selected as to retard the radiation phase by  $\pi$ , resulting in two phase quantisation levels of  $\phi = 0$  and  $\phi = \pi$ . The efficiency of DOE climbs asymptotically to 100% if increasing number of PQLs are introduced into the profile of the MPFL. With the number of subzones (PQLs) being  $p$ , the phase difference of  $2\pi/p$  between neighbouring subzones must be maintained. This leads to the outer radii of the subzones ( $b_s$ ) being governed by the equation [57]:

$$b_s = \sqrt{\frac{2s(f+w/2)\lambda_0}{p} + \left(\frac{n\lambda_0}{p}\right)^2} \quad (2.2)$$

where  $s = 1, 2, \dots, S$ ;  $S = qN$ ,  $N$  is the number of zones and  $w$  is the thickness of the plate (groove depth). The thickness of the plate is most commonly much lower than the focal distance, therefore  $w$  may often be neglected.

The zone heights are governed by the optical path of radiation within the material. Therefore it can be calculated as:

$$t_s = \frac{\lambda_0}{p(n-1)} \quad (2.3)$$

where  $n$  is the refractive index of the lens material. For example, in the case of silicon diffractive lens, designed for 1 THz frequency the depth for  $\pi$  phase change is  $124 \mu\text{m}$  [28].

ZPs can be relatively easily designed to work when manufactured on various arbitrary form surfaces, easing their integration into devices with specific geometrical restrictions [57].

### 2.1.6 Metamaterial Lenses

A metamaterial lens incorporates the low thickness of metallic Soret zone plate with an increased efficiency of a multilevel phase Fresnel lens. In this case instead of blocking or modulation of optical path, phase of the wave is being manipulated by a metamaterial structure on the surface of a supporting wafer. Metallic (or other conductive) elements are commonly used to incrementally retard the wave phase. When these elements are arranged in a circular geometrical pattern lensing is achieved with radiation constructively interfering in the focal spot [20]. Some examples of these elements, include V (illustrated in **Fig. 2.4**) or C-shaped apertures or bars made of gold, on the surface of Si with different angles in the case of V-shape or gap size in the C structure for the incremental phase change [20, 43, 46]. These metal structures still suffer from the notable reflective losses of metal surfaces of the element, limiting typical efficiencies to 30-40% [46]. An interesting implementation of an emitting metamaterial lens fabricated from U-shape meta atoms working in pulsed NIR excitation setup was also demonstrated [68]. In this case the light amplification at metal plasmon modes of meta atoms and the nonlinearity of strong field excitation transfers energy from NIR source excitation to broadband THz radiation, which is then focused according to the lens geometry.

Metamaterial lenses commonly contain a substrate and a complex pattern of flat metal meta-atoms on its surface (see **Fig. 2.4**). First of all, the fabrication of these elements is relatively complex, often needing metal evaporation, UV lithography and etching processing, limiting the possibilities of fast iterative device prototyping. Now the cost of a mass produced metamaterial lens is expected to be low due to fabrication compatibility with Si CMOS technology. Metamaterials are still not

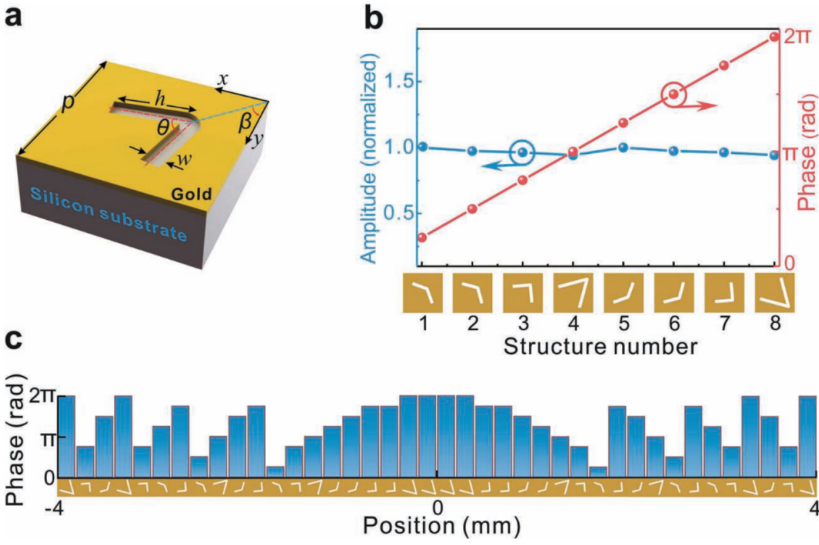


**Figure 2.4:** a) Metamaterial lens unit cell, otherwise known as meta-atom. In the illustrated case "v" shaped aperture on gold film coated Si substrate is used to change the phase of transmitted radiation. b) Phase and amplitude change as a function of the geometry of "v" shaped aperture. c) Phase map of a cross-section of a metamaterial lens. [20]

sufficiently well developed for widespread applications and prototyping purposes. Multilevel Fresnel lenses and zone plates are, therefore, researched and developed in this work.

### 2.1.7 Main Parameters of a Lens

It is important to note the basic parameters of a lens. **Focusing gain** is defined as the squared ratio between the focused field in the focal spot  $E_f$  and the field at the same spot without the lens present  $E_0$ . In the case of Soret zone plate it is approximated as [57]:

$$G_f = \left( \frac{E_f}{E_0} \right)^2 = N_0^2 + 1 = \left( \frac{a_0^2}{\lambda_0 f_1} \right)^2 \quad (2.4)$$

In this expression,  $N_0$  is the number of open zones,  $a_0$  is the radius of the lens and  $f_1$  is the primary focal distance. It is well established in classical works that the focusing gain for single Fresnel zone lens would be 4 times (or 6 dB). [57] In the first approximation, with each zone demonstrating the same  $G_f$ , Soret demonstrated that a multizone plate would have the focusing gain as  $G_f = N_0^2$ . It was also shown, that for

an ideal lens (Fresnel or classical refractive) of the same diameter and focal distance, the focusing gain would be  $\pi^2$  times larger. Even though theoretically Eq. 2.4 suggests that there is no limitation to the number of zones and therefore the focusing gain, an optimum number exists, as axial spherical aberrations are introduced for an increasing number of zones (increasing zone distance from the optical axis), reducing the efficiency of the component.

**Focusing efficiency** ( $e_f$ ) is defined as a squared ratio between the focused field intensity in the focal spot of a lens under investigation and an ideal lens. In the case of Soret zone plate the efficiency, of course is small, due to only half of the surface (open) area is used. This greatly increases reflective/absorptive losses according to lens type. It was shown theoretically that the efficiency of SZPL is limited to  $e_f = 1/\pi^2$  i.e. to 10% [57]. The efficiency can be increased to some extent by the use of reflector behind the zone plate, using multilevel design and the usage of more complex 3D lenses [57].

In the case of multi level phase corrected zone plate (or MPFL), the efficiency of the lens depends on the number of PQLs,  $p$ . In the case of phase reversal zone plate, the number of active (transmissive) zones is twice as large as in the SZPL, increasing the field intensity twice, and the power in the focal spot by 4 times. Therefore, the focusing gain as well as efficiency increases 4 times in respect to the SZPL. On the other hand, due to the step-like approximation of the lens surface (the phase front), phase Fresnel lenses inherently have a smaller efficiency in respect to an ideal curved lens. The efficiency of a theoretical MPFL can also be approximated to be a function of the phase step ( $\Delta\Phi = 2\pi/p$ ) between the subzones (and effectively the subzone number) as [57]:

$$e_f = \frac{\sin^2(\Delta\Phi/2)}{(\Delta\Phi/2)^2} \quad (2.5)$$

The calculated function is shown in the **Fig. 2.5**. It was shown that for the cases of 2, 4, and 8 subzones (phase steps of  $180^\circ$ ,  $90^\circ$ , and  $45^\circ$ ) the corresponding efficiencies would be 40.5, 81, and 90.5% demonstrating an asymptotic behaviour with the increase of subzone number [57]. It is important to note, that reflective and absorptive optical losses reduce the focusing gain and efficiency.



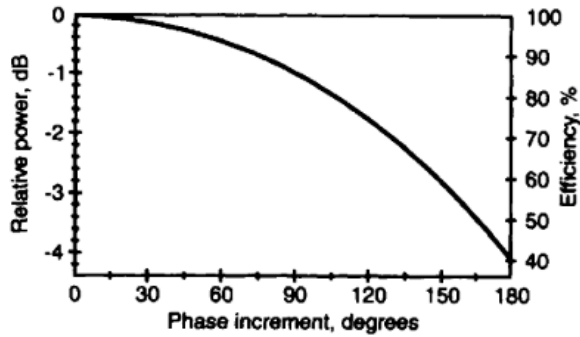


**Figure 2.5:** Theoretical relative focussing gain and focussing efficiency function on the phase increment of a multilevel phase Fresnel lens. [57]

### 2.1.8 Aberrations of a Lens

In the case of an ideal lens, a monochromatic wave is being manipulated and perfectly focused on a focal spot. For example, a spherical diverging wave front can be transformed to a spherical converging wave front or vice versa. In reality distortions of the wave front are introduced, preventing the perfect focusing performance. The distortion of the wavefront is known as lens aberration. In the case of diffractive optics the axial-spherical, off axis and frequency (or chromatic) aberrations are the most prominent ones.

**Axial spherical aberration** is caused by the optical path difference of the wave coming from the zones closer to the centre point ( $O$ ) of the lens and the peripheral zones ( $Q_n$ ). It can be seen from **Fig. 2.6** that spherical waves originating from different points on the radius of the lens intersect optical axis at different points  $P'$  and  $P$ . This difference of interference points causes the focal spot of the lens to be elongated in the propagation direction  $z$  proportional to the lens diameter.

It was shown in classical works that this aberration theoretically becomes essential when

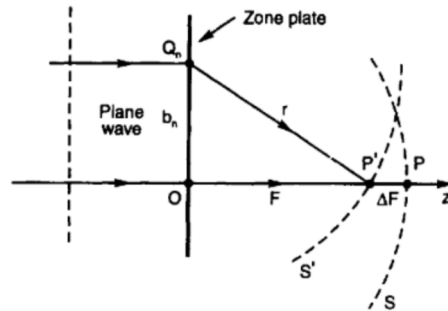


**Figure 2.6:** Schematic illustration of an axial spherical aberration. [57]

the number of zones in a plate ( $N$ ) is larger than [57]:

$$n_a = \sqrt{\frac{2f}{\lambda}} \quad (2.6)$$

For example, at the wavelength of 0.5 mm (600 GHz) and a focal length of 10 mm  $n_a$  is around 6 zones. With more zones in the lens, an elongation of focal spot would be observed. In practice, however, a few wavelengths of axial spherical aberration is met and widely considered as acceptable. Axial spherical aberrations may be minimized by fabricating the zone plate on a surface of a sphere with the centre point in the focal spot, but the fabrication complexity and the dimensions of the lens would then increase substantially. In practice axial spherical aberration in Eq. 2.6 effectively describes the optimal number of MPFL zones and the lens diameter.

**Off axis aberration** is observed when the wave hits the lens at an angle to the optical axis. The maximum theoretical angle at which the off axis aberration would be negligible is approximated as [57]:

$$\left| \pm \sqrt{2\lambda NF} \frac{n\lambda}{F} \sin \varphi_{Max} - N\lambda \sin^2 \varphi_{Max} \right| < \frac{\lambda}{4} \quad (2.7)$$

In the case of Si lens with 6 zones and  $F = 10$  the maximum angle without notable off axis aberration would be around  $3^\circ$ , while for  $N = 9$  and  $F = 5$  it would be reduced to  $1.2^\circ$ . Off axis aberration in essence describes the precision of positioning of a DOE in an optical system. With very small max angle values very precise positioning is needed.

**Frequency aberration** is seen from the zone radii equation 2.1, as for given geometry  $b$ , the focal distance  $F$  is inversely proportional to the wavelength of the radiation. Most real radiation sources are quasi monochromatic, meaning that instead of a single wavelength radiation, a line with a notable frequency width is produced. In the case of non monochromatic source, shorter wavelength part of the line would be focussed further from the lens while the longer wavelengths would be focused closer, resulting, in an elongation of the focal spot. In the case

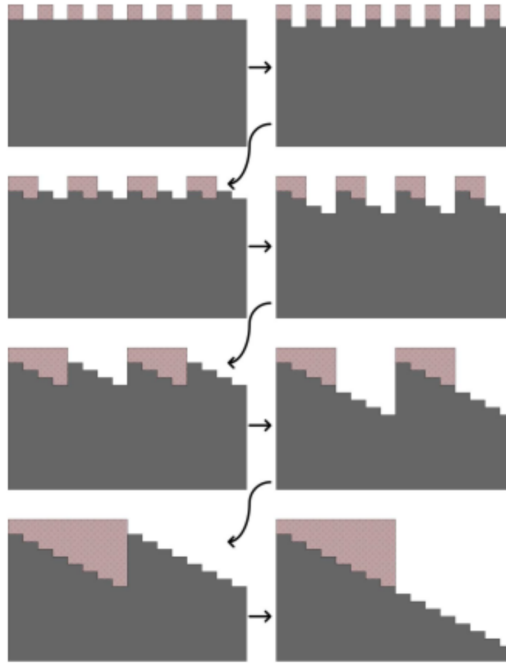


**Figure 2.7:** Fabrication steps for the lithographic processing of a multilevel phase Fresnel lens. [30]

of a Soret zone plate, the bandwidth may be approximated as:

$$\frac{2\Delta\omega}{\omega_0} \approx \frac{1}{N} 100\% \quad (2.8)$$

This means that the operational bandwidth of 0.6 THz lens with 10 zones would be around 10%, or  $0.6 \pm 0.06$  THz.

### 2.1.9 Fabrication Methods for Fresnel Lenses

The main fabrication techniques for the PFLs mainly depend on the target wavelength. At sub-THz frequencies the wavelength of radiation is large and it cannot “feel” the manufacturing imperfections in tens or even hundreds of microns in size. At these frequencies mechanical milling [36] or 3D printing [41, 42] may be used providing acceptable performance of the devices. With the reduction of wavelength below  $10 \mu\text{m}$  different fabrication method of lithography together with wet or reactive-ion etching is employed [28–30, 69].

This fabrication method, while achieving much smaller defect

sizes in nanometer range, requires multiple runs of mask alignment, photolithography, and etching procedures. Illustration of multiple step photolithography of a MPFL is shown in **Fig. 2.7** [30]. Fabrication becomes complicated and results in a costly investigated element [28], especially in the case of iterative development stage where each unique design would require setting up of full processing procedure. Another limitation here comes from the required etch depth reaching, for example 50  $\mu\text{m}$  for Si lens designed for 2.5 THz. This depth is hard to achieve without special techniques. In addition, sacrificial layers are needed in order to remove photoresists [30].

In the intermediate range of 0.1 THz to 5 THz completely different method of fabrication must be used which could produce micrometer sized defects while keeping the process relatively simple and the cost of fabricated element low. The method of choice for accomplishing these criteria may be direct laser ablation [70,71]. This versatility in addition to free raster designing of fabrication pattern allows for the method to be used for fast iterative processing of different structures (for example THz metal zone plates and semiconductor based PFLs) for new device prototypes.

### 2.1.10 Direct Laser Ablation of Optical Components

Direct Laser Ablation (DLA) (also known as direct laser writing) is based on the ablation of substrate material with ultrashort high intensity laser pulses. When properly optimized, in this regime the light is being absorbed in a very limited area at the material surface [72]. Very high amount of energy is being absorbed by the material during DLA, therefore material evaporates from solid state directly to vapour with a minimal amount of thermal transfer and damage to the remaining substrate. Evaporated material is then carried away from the processing area with the help of technical gall flow [72,73]. Due to applicability of ablation process to any material DLA has been widely used in structuring various materials ranging from ultrahard materials [74] to metals [54,64], semiconductors [75,76], to even soft polymer materials [77], wood or paper [66].

In DLA the laser beam of most commonly IR wavelength (for ex-

ample 1064 nm supplied by diode-pumped solid state laser) is being raster scanned on the surface of the sample [71]. Raster scanning with overlapping laser spots is used ensuring the smoothness of processed surface. Raster scanning process is very versatile in the sense that the processing geometry is freely chosen. This means that, while unit price of a component might be larger than in other mass processing techniques (for example photolithography), the price of a single unique design component becomes substantially lower. Main raster scanning limitations are associated with the digital mapping of processing profile.

From the technical point of view, scanning, speed is directly related to the processing cost and design process duration in element processing. The manipulation of the beam in the 2 dimensions of the sample plane is quite challenging task, increasing the cost of the fabrication system, and decreasing the speed of the fabrication. Therefore a system consisting of a polygon mirror based scanner is utilized in this work. The beam was rapidly scanned in one direction and the sample itself was mounted on precision travelling stage to scan in the other.

DLA fabrication method has already demonstrated great results for THz science in the fabrication of binary phase lenses on silicon as well as metal phase plates, and diffractive optics with integrated band pass filters [54,64,65]. Antireflective coatings were also demonstrated for minimising the reflective losses associated with comparatively large semiconductor refractive indices [9,75].

## 2.2 Polaritonics

Surface plasmon polariton (SPP) based nanophotonics are widely used in order to achieve subwavelength light confinement, waveguiding, extraordinary aperture transmission as well as light amplification phenomena [78]. Even though plasmons were described already in 1900s, exploration and application of novel excitation systems and materials is still ongoing whether its investigation of different metal nanoparticles, voids, sheets or even more exotic 2D materials or 2D electron gas in HEMT structures [12,15].

Surface phonon polaritons (SPhPs) are emerging as a viable alter-

native to plasmonics in THz to MIR spectral range due to restrictions associated with plasmon damping present for this spectral range. Modern material engineering and fabrication techniques allowed SPhP observation in a number of different semiconductor materials including:  $\alpha$ -quartz [79], GaP [80], GaN [81], SiC [82,83], 2D materials as BP [84], Graphene [85,86], BN [85] as well as many others.

Excitation of SPs has many applications in chemical sensors and even photonic circuitry, ultrafast optical computing systems [87]. Light localisation and amplification at SP resonances allow for excitation of non linear processes using relatively low incoming light intensities [87]. While non linear processes in SPs are famously used for surface enhanced Raman scattering and second harmonic generation, non-linearities of SPhPs are not widely reported yet.

SPs are also an excellent platform for applications in custom design thermal emitters due to their low losses and ability to specify the emission spectra. SP based emitters have been demonstrated in applications for thermophotovoltaics and radiative cooling [88], IR and chemical sensing [89,90], biosensing [91] and others. Recently a SP based cooling-photonic circuitry feeding system powered by computer processor waste heat has even been suggested [14].

All of these applications require narrowband, custom design IR sources. With severe IR band efficiency limitations of conventional LED devices and highly complicated QCL fabrication and cost polaritonic devices might become a viable and attractive solution for integrated systems [89].

### 2.2.1 Theory of SP Dispersion

SP dispersion may be described in a 2D system containing two semi-infinite material layers arranged in  $z$  direction. The layers, namely an open space and a substrate are shown in (**Fig. 2.8**). In order to support surface polaritons, the substrate must be characterized by a negative real part of dielectric permittivity function  $\epsilon_1$ . If one considers a p-polarized (TM-polarization) beam incident to the interface with a component in the  $x$  direction, the field in the open space (characterised by dielectric function  $\epsilon_2$ ) and substrate medium (characterised by dielectric function

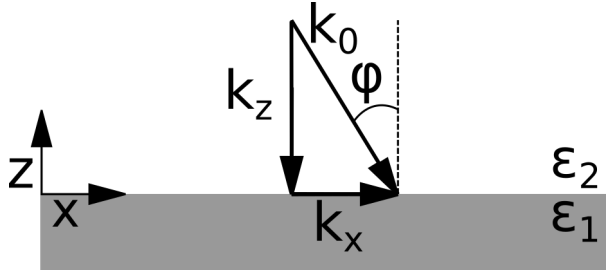


**Figure 2.8:** Basic surface polariton excitation geometry. A far field beam with wavevector  $k_0$  is incident onto a flat boundary between a substrate material ( $\epsilon_1$ ) and open space ( $\epsilon_0$ ) at the incidence angle of  $\phi$ . The components of  $k_0$  in  $x$  (surface) and  $z$  (surface normal directions) are marked as  $k_x$  and  $k_z$ .)

$\epsilon_1$ ) may be described as [92]:

$$\mathbf{H}_1 = (0, H_{y1,0}, 0) \exp i(k_{x1}x - k_{z1}z - vt) \quad (2.9)$$

$$\mathbf{E}_1 = (E_{x1}, 0, E_{z1}) \exp i(k_{x1}x - k_{z1}z - vt) \quad (2.10)$$

$$\mathbf{H}_2 = (0, H_{y2,0}, 0) \exp i(k_{x2}x + k_{z2}z - vt) \quad (2.11)$$

$$\mathbf{E}_2 = (E_{x2}, 0, E_{z2}) \exp i(k_{x2}x + k_{z2}z - vt) \quad (2.12)$$

Here,  $k_{xi}$  is the component of complex SP wavevector in the plane of the surface of either the substrate ( $i = 1$ ) or the open space ( $i = 2$ ),  $v$  is the real frequency of incoming radiation. The electromagnetic fields, naturally, are governed by Maxwell equations:

$$\text{rot}\mathbf{H}_i = \epsilon_i \frac{1}{c} \frac{\delta \mathbf{E}_i}{\delta t} \quad (2.13)$$

$$\text{rot}\mathbf{E}_i = -\frac{1}{c} \frac{\delta \mathbf{H}_i}{\delta t} \quad (2.14)$$

$$\text{div}\epsilon_i \mathbf{E}_i = 0 \quad (2.15)$$

$$\text{div}\mathbf{H}_i = 0 \quad (2.16)$$

In these expressions  $\epsilon_i$  stand for the complex dielectric permittivities of the respective layers. In order to obtain the transmitted and reflected fields, one has to also take into account the field continuity condition at the dielectric boundary as:

$$E_{x1} = E_{x2} \quad (2.17)$$

$$H_{y1} = H_{y2} \quad (2.18)$$

$$\varepsilon_1 E_{z1} = \varepsilon_2 E_{z2} \quad (2.19)$$

Equations 2.17 and 2.18 directly result in:

$$k_{x1} = k_{x2} = k_x \quad (2.20)$$

At the same time, equation 2.13 results in:

$$\frac{\delta H_{yi}}{\delta z} = -\varepsilon_i E_{xi} k_0, \text{ resulting in:} \quad (2.21)$$

$$+k_{z1} H_{y1} = +k_0 \varepsilon_1 E_{x1} \quad (2.22)$$

$$+k_{z2} H_{y2} = -k_0 \varepsilon_2 E_{x2} \quad (2.23)$$

Equations 2.22, 2.23, 2.17 and 2.18 result in a system:

$$H_{y1} - H_{y2} = 0 \quad (2.24)$$

$$\frac{k_{z1}}{\varepsilon_1} H_{y1} + \frac{k_{z2}}{\varepsilon_2} H_{y2} = 0 \quad (2.25)$$

In order to have a solution, the determinant  $D_0$  of Eq. 2.24-2.25 system must be 0, providing the dispersion relation:

$$D_0 = \frac{k_{z1}}{\varepsilon_1} + \frac{k_{z2}}{\varepsilon_2} = 0 \quad (2.26)$$

Further, by taking into account equations 2.13, 2.14 and 2.22, 2.23 dispersion is obtained as:

$$k_x^2 + k_{zi}^2 = \varepsilon_i (k_0)^2 \quad (2.27)$$

Finally the latter two expressions give the well known equation for SP dispersion as:

$$k_x = k_0 \sqrt{\frac{\varepsilon_1 \varepsilon_2}{\varepsilon_1 + \varepsilon_2}} \quad (2.28)$$

An important notice in this expression is the momentum mismatch between the  $k_x$  of the SP and  $k_0$  of far field radiation as the square root member of Eq. 2.28 is non equal to unity. This mismatch prevents the



polariton interaction with the light in the far field. Therefore, instead of coupling to the far field, polaritons exist as evanescent waves (non radiative fluctuations) propagating along the surface of the material (real  $k_x$ ) and exhibiting exponentially decaying electromagnetic fields in the  $z$  direction normal to the material surface (imaginary  $k_z$ ) [12,92]. In order to couple SPs to the far field radiation one has to design a coupling mechanism for the alleviation of the mismatch, which is studied in more detail in section 2.2.5.

Another implication of the Eq. 2.28 is found by investigating the dielectric function of a material which would be supporting SPs. If one takes the case of air/material interface, the  $\epsilon_2$  may be approximated as its real part-  $\epsilon'_2 = 1$  and imaginary part-  $\epsilon''_2 = 0$ . Now, upon looking closely at Eq. 2.28, and taking into consideration the negative real part of the permittivity required for the SP supporting material, one can note that in order to obtain real  $k_x$  ( $k'_x \neq 0$ ) and therefore excite propagating polariton modes, one has to have some limitations to the dielectric functions of the interface. Namely, the dielectric permittivity of the substrate must be of negative real part ( $\epsilon'_1 < 0$ ) and magnitude larger than  $\epsilon'_2$  ( $|\epsilon'_1| > |\epsilon'_2| = 1$ ). This condition is known to be strongly pronounced for plasmons (collective oscillation of free electrons in a material) in the frequency range of  $0 < \nu < \nu_p$  therefore allowing for surface plasmon polariton excitation (section 2.2.2). It may also be pronounced in polar semiconductors, within the so called Reststrahlen band (section 2.2.2). Specifying the spectral region of  $|\epsilon'_1| > \epsilon'_1 = 2$  allows to specify the operational range of an surface polariton based device.

## 2.2.2 Plasmon Polaritons

Historically, the investigation of surface polaritons was most often carried out in metal based structures via the excitation of SPPs. Plasmons are charge density fluctuations of free carriers within a conductive material [87,92].

SPP is a quasiparticle comprised of a photon that interacts with the propagating plasmon wave at the material interface. As such SPPs were first observed and most commonly applied in metal structures containing huge amounts of free carriers (in the order of  $10^{23}\text{cm}^{-3}$ ). The char-

characteristic bulk plasmon frequency  $\nu_P$  is governed by the density  $n$  and effective mass  $m^*$  as:

$$\nu_P = \frac{1}{2\pi} \sqrt{\frac{ne^2}{m^* \epsilon_\infty \epsilon_0}} \quad (2.29)$$

Here  $e$  is the electron charge,  $\epsilon_\infty$  and  $\epsilon_0$  are the high frequency permittivity of the material and vacuum permittivity, respectively. Characteristic plasmon energy (frequency  $\nu_P$ ) in a metal is in the range of 10 eV i.e. in the UV wavelength range i.e. far from THz range. In the case of doped materials, the free carrier contribution to the dielectric function is limited to a  $\nu_P$  value at much lower frequencies due to the much smaller carrier densities as illustrated in **Fig. 2.9**. For example if we take GaN material with a relatively strong doping (a case relevant to this work) of  $1.55 \times 10^{19} \text{ cm}^{-3}$  the plasmon frequency is around  $1100 \text{ cm}^{-1}$  or 136 meV. Lower electron density may be beneficial in fabricating devices for THz and IR spectral range, nevertheless in this case the issue of comparatively strong plasmon damping and high associated losses must be taken into account [78,93].

In the case of surface waves, Maxwell's theory demonstrates that surface plasmon oscillations are observed in the frequency range from 0 to  $\nu_{SP} = \nu_P/\sqrt{2}$ , known as the surface plasmon frequency [92]. Plasmonic response results in strong and wideband reflectivity of most metals as plasmons excitation (electrons polarisability) by incident electromagnetic radiation is highly effective in a wide spectral range [12,78]. The extremely wide range of plasmon observation/operation is highly welcome as plasmonic devices can be created from NIR to VIS to even UV frequency ranges. Strong reflectivity of free electrons is used for development of wideband reflective optics - metal mirrors of, for example, parabolic or spherical shape section 2.1.3.

In order to predict the behaviour of SPPs, one must describe the dielectric function of the electrons. Dielectric function of the free electron plasma follows the Drude law and is expressed as [78,94]:

$$\epsilon_{fc} = \epsilon_\infty - \frac{\nu_P^2}{\nu^2 + i\nu\gamma_P} \quad (2.30)$$

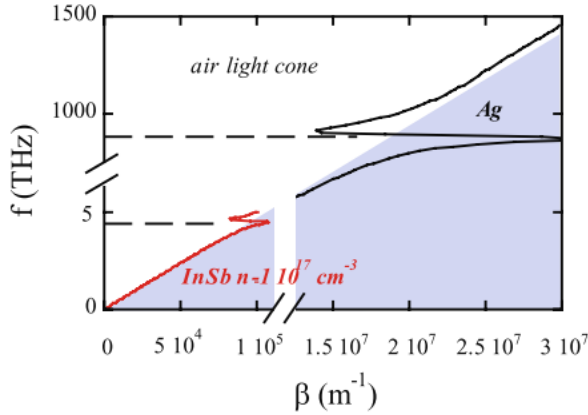


**Figure 2.9:** Example of an SPP dispersion in the air/Ag and air/n-InSb interfaces. Dashed lines illustrate the SPP frequencies of respective materials [78].

Here  $\epsilon_\infty$  is the high frequency dielectric constant of the material and  $\gamma_p$  is the plasmon damping factor, representing the optical losses of the modes. The  $\gamma_p$  represents internal losses associated with free-carrier scattering [93]. SPP losses are usually in the order of hundreds or even thousands of inverse centimetres (scattering times in the order of hundreds to tens of femtoseconds) in metals. Drude like dielectric contribution of free electrons and its reflectivity spectrum in the case of doped GaN are illustrated in the section 2.2.3.

Due to the high electron densities metals support strongly localized SPPs only in UV to NIR spectral range. Use of PPs at (relatively) low frequencies of THz to MIR becomes complicated due to high electron scattering losses and decreased PP localisation. In this spectral range, metal SPPs resemble almost homogenous EM field and are known as *Sommerfeld-Zenneck* waves [78]. In order to obtain SP features in THz to MIR range, doped semiconductor structures can be utilised. Semiconductor SPPs have the advantage of its frequency being tuned via the charge density of material doping (Fig. 2.9) [78]. Nevertheless, strong carrier damping results in large feature linewidths. The PP linewidth being in the order of the working frequency (hundred of inverse centimetres) makes the SPP use for THz to mid-IR complicated [93,95].

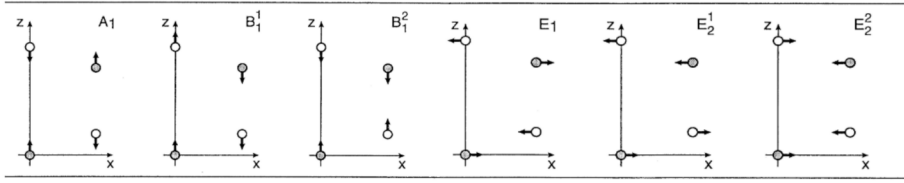


**Figure 2.10:** Vibration geometries of different longitudinal optical phonon modes in polar wurtzite crystal structure. [12]

### 2.2.3 Phonon Polaritons

Surface Phonon Polaritons (SPhPs) are considered as a viable alternative for the design of components in THz and MIR frequencies. Use of polar semiconductors was suggested due to their unique properties in this spectral range. In the case of undoped polar semiconductors in MIR spectral range, the optical phonons govern the electromagnetic response of the material and enable the SPhP excitation. Vibrating charged lattice ions provide charge dipoles in a resonant frequency range called the Reststrahlen band (RB). The RB is the spectral determined by transverse optical (TO) and longitudinal optical (LO) phonon modes. Optical phonon modes correspond to lattice ion vibrations with  $k$ -vectors aligned parallel (LO) and perpendicular (TO) to the incident field. Positively and negatively charged ions move coherently with and against the direction of the electric field respectively. In the case of wurtzite crystal, there are a number of optical phonon modes corresponding to the atom vibrations in different configurations illustrated in **Fig. 2.10**. Out of these modes some are active in Raman experiments ( $E_2$ ,  $A_1$  and  $E_1$ ) and some are active in IR experiments ( $A_1$  and  $E_1$ ) and some are silent ( $B_2$  modes).

Dispersion of SPhPs is governed by the Eq. 2.28, where phonon behaviour is described by a Lorentz-like oscillator model governing the permittivity function  $\epsilon_s$  [12, 96, 97]:

$$\epsilon_s = \epsilon_\infty \left( \frac{\nu_{LO}^2 - \nu^2 - i\nu\gamma_{LO}}{\nu_{TO}^2 - \nu^2 - i\nu\gamma_{TO}} \right) \quad (2.31)$$

Here,  $\epsilon_\infty$  is the high frequency dielectric constant of the semiconductor,  $\nu_{TO}$ ,  $\nu_{LO}$ ,  $\gamma_{TO}$  and  $\gamma_{LO}$  stand for the resonant frequencies and damping factors of TO and LO phonons. One has to take note that the Eq. (2.31) takes in to account an isotropic model with single TO-LO mode.

Meanwhile, in many semiconductors many TO-LO phonon modes exist as, for example there are 4 active modes in sapphire. [P14]. Even in the case of GaN, anisotropy of hexagonal crystal with  $A_1$  and  $E_1$  vibrational modes is needed to be accounted for [94]. Nevertheless, as it had been demonstrated previously, in some cases isotropic model is sufficient and can be used to describe behaviour of a semiconductor with good accuracy [81, 98]. This is especially true in the case of hexagonal GaN reflectometry. Here,  $A_1$  and  $E_1$  IR active modes specify the dielectric function, nevertheless it was shown that in a reflectometry setup only  $E_1$  TO and  $A_1$  LO modes can be excited resulting in single TO-LO mode behaviour [81, 99].

Due to the intrinsic properties of phonons, their optical losses (damping constants) are around an order of magnitude lower than those of their plasmonic counterparts [12]. The PhP based devices, therefore, demonstrate quality factors ( $Q = FWHM/\nu_0$ ) in the order of 100 [82]. The quality factor of a resonance is associated with the losses in the material and can be estimated from optical constants as:

$$Q = \frac{\nu \frac{d\text{Re}(\epsilon)}{d\nu}}{2\text{Im}(\epsilon)} \approx \frac{\nu}{\gamma} \quad (2.32)$$

This approximation is accurate when  $\gamma \ll \nu$ , where  $\gamma$  is the reciprocal of the excitation lifetime and  $\nu$  is the excitation frequency [12].  $Q$  is therefore seen to be inversely proportional to the optical losses. Reduction in optical losses (use of low loss phonon excitation), therefore, can increase  $Q$  to theoretically reach values of 250 for SiC structures [82]. It is worth to note that Eq. 2.32 describes upper bound of excitation for single particles. It does not account for number of effects as near field coupling, Fano interference or other array induced effects which could lead to further  $Q$  improvements. It has been shown that  $Q$  of the fabricated structures far exceed even the theoretical quality factors of their plasmonic counterparts [82, 100]. Hillenbrand et al. demonstrated in their work that in SiC structures SPhP field enhancement would exceed the one attainable by gold structures by 20 times (**Fig. 2.11**). Theoretical quality factors estimated for spherical particles excitations of different materials is demonstrated in **Fig. 2.12**. Supreme quality factors in po-

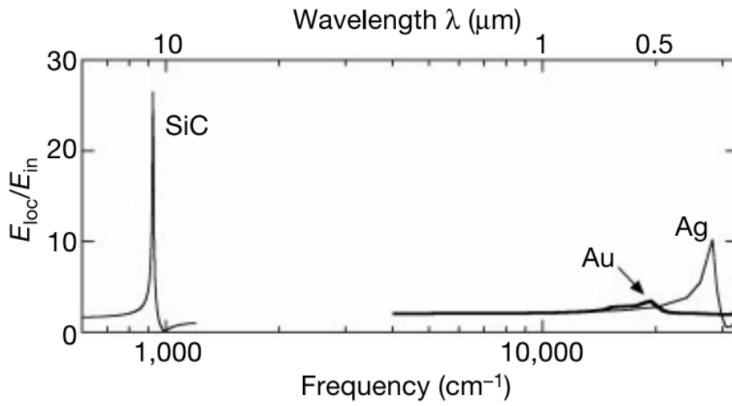


**Figure 2.11:** Typical field enhancement factors of gold and silver SPP structures compared to the case of SiC SPhPs. [100]

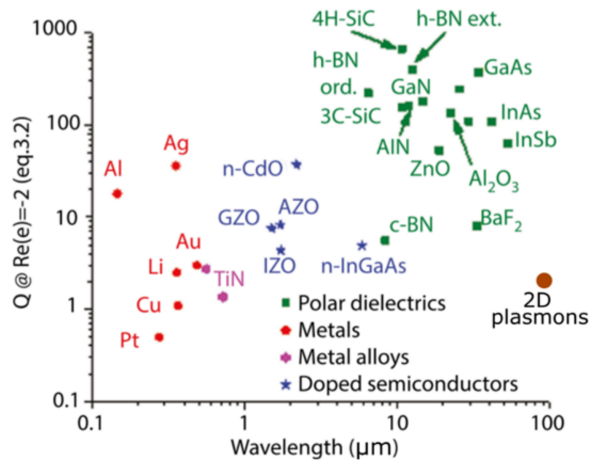


**Figure 2.12:** Theoretical quality factor estimations for different material nanoparticle excitations. Adapted after Ref. [12]

lar semiconductor excitations is clearly shown. High quality excitations with a nanometre scale spatial resolution were shown to be very promising for applications in high density, read-only optical memory or a very sensitive dielectric function/tension/defect probing used in material research applications [100].

The main limitation of SPhP devices as compared to the SPP is the operational bandwidth limited to the RB of the semiconductor. Devices fabricated from GaN and SiC (most commonly reported SPhP materials) possess some of the broadest RB regions among other semiconductors. Optical reflectivity of undoped semiconductor is high inside and

low outside of the RB, respectively. Combination materials with different RBs allows to artificially expand the region of SPhP operation by using several layers heterostructures [101]. In this example, stacked semiconductor layers were used to combine the RBs of wurtzite type GaN ( $560\text{-}736\text{ cm}^{-1}$ ) and SiC ( $797\text{-}973\text{ cm}^{-1}$ ) [12]. A wideband reflector was demonstrated with a combined reflectivity region of  $560\text{-}970\text{ cm}^{-1}$  as the result [101].

Another way of improving the bandwidth of semiconductor based polaritonic devices is the introduction of doping [101]. More detailed analysis on doped semiconductor properties will be carried out in the section 2.2.4.

To conclude, SPhP-based devices can be fabricated in the THz to NIR range with exceptionally high quality features. The operational bandwidth limitation can be artificially modified by thoughtful material engineering.

## 2.2.4 Plasmon-Phonon Interaction

Plasmons and phonons in a doped semiconductor form coupled hybrid modes called in literature LO phonon-plasmon coupled modes (LPP) [94], plasmon coupled with surface phonon (PCSP) [102] or LO phonon-plasmon coupling (LOPC) [93, 95, 103, 104] modes. The dielectric function of the doped semiconductor is governed by [94]:

$$\epsilon_s = \epsilon_\infty \left( \frac{v_{LO}^2 - v^2 - iv\gamma_{LO}}{v_{TO}^2 - v^2 - iv\gamma_{TO}} - \frac{v_p^2}{v^2 + iv\gamma_p} \right) \quad (2.33)$$

Real and Imaginary parts of dielectric function were calculated using equation 2.33 for the case relevant to experimental results of this work (see **Table 4.2** in section 4.2.2). Dielectric permittivity functions were calculated for separate inputs of phonons (undoped material), plasmons (free carriers) and phonons + plasmons (doped semiconductor) are shown in **Fig. 2.13 a** and **b**. Respective reflectivity spectra are also shown in **Fig. 2.13 c**. It can be seen that the region of negative real part of dielectric function ( $\epsilon_1 < 0$ ) spans from  $v = 0$  to plasmon frequency  $v_p$  of around  $1100\text{ cm}^{-1}$  in the case of free carriers and from  $v_{TO}$  to  $v_{LO}$  in the case if undoped GaN. Doped semiconductor demonstrates

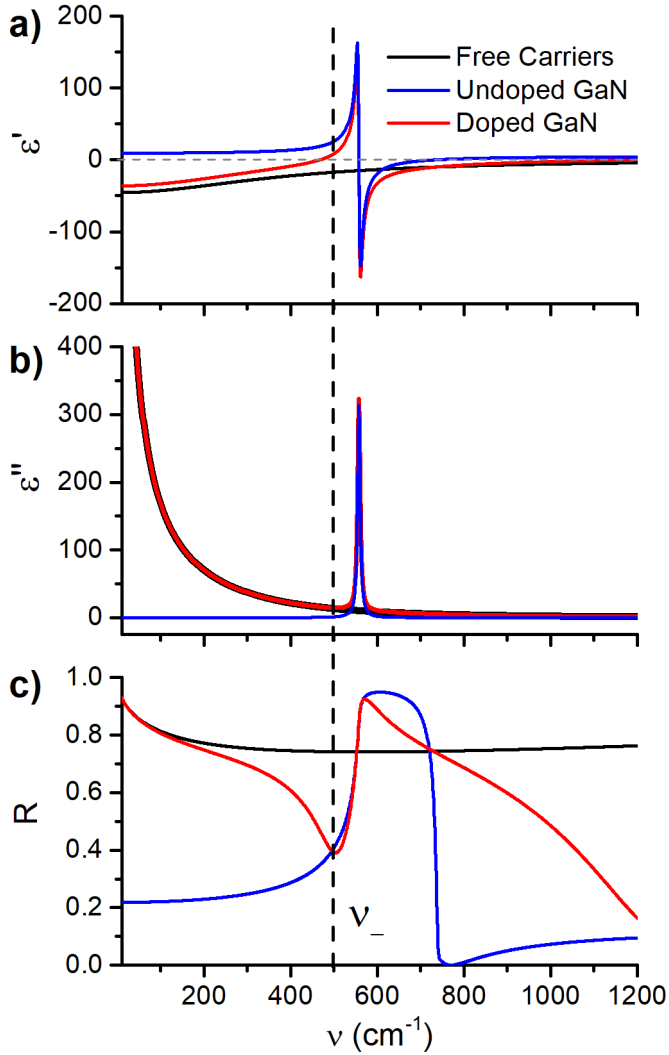


**Figure 2.13:** a) real and b) imaginary parts of free carrier plasmonic contribution, phononic lattice contribution and hybrid case of doped  $n$ -GaN complex dielectric function. c) Reflectivity calculated using the complex dielectric function of a and b. Parameters relevant to the case of experimental  $n$ -GaN wafer described in the section 4.2.2 were used. Dashed line demonstrates the hybrid mode frequency  $\nu_-$  at around  $500 \text{ cm}^{-1}$  while  $\nu_+$  is located above the plot scale at  $1260 \text{ cm}^{-1}$ .



a hybrid phonon-plasmon behaviour, with a region of the negative real part of the permittivity spanning almost whole region below plasmon frequency of around  $1100 \text{ cm}^{-1}$  with an exception of narrow region near the TO pole at  $560 \text{ cm}^{-1}$ .

Real part of the dielectric function of a doped semiconductor crosses the 0 at two points (without counting the pole at TO frequency), resulting in the two regions where strong GaN reflectivity drops (reflectivity minima) are observed. In the low  $k$  approximation the  $v_{LO}$  hybridizes into two modes  $v_-$  and  $v_+$  governed by the expression:

$$v_{\pm} = \left( \frac{v_{LO}^2 + v_P^2 \pm \sqrt{(v_{LO}^2 + v_P^2)^2 - 4v_P^2 v_{TO}^2}}{2} \right)^{1/2} \quad (2.34)$$

The frequencies of reflectivity minima are seen to be dependent on the carrier density (plasmon frequency); therefore, their spectral position can sometimes be used to specify the doping level of a material [102, 103, 105]. However its dependency on the damping factor (or the carrier mobility) may influence accuracy of the evaluation. [104] The LOPC modes were demonstrated in various doped materials including  $\alpha$ -GaN by IRSE ellipsometry [94], 4H-SiC by Raman spectroscopy [104], GaN epilayers [103] and GaAs as well as AlGaAs by IR reflectometry [102]. In the later, resonant absorption and selective thermal emission of doped GaAs and AlGaAs layers was also demonstrated for the application of tailored thermal emission.

### 2.2.5 Polariton Coupling

Incoming radiation cannot couple to the SPs on a flat surface due to the momentum mismatch (see Eq. 2.28). It is worth to note that due to fundamentally same physics, coupling of SPPs, SPhPs or hybrid modes is similar, with differences arising only due to different resonant frequencies and the material processing.

Momentum mismatch is alleviated by exploiting two main methods. The first one relies on the effect of photon tunnelling in Kretschmann and Otto configurations, also called attenuated total reflection geometry (**Fig. 2.14 a-c**). The other method relies on wave diffraction from probes

(**Fig. 2.14 d**) or various surface structures (**Fig. 2.14 e, f**) [12,87]. In the former a prism coupler is used (**Fig. 2.14 a-c**), where the  $k_x$  component of light is controlled with the permittivity value of the prism material and the angle of incidence [103]. At a certain configuration, where the  $k_x$  components of the light and the SP become equal, resonant photon tunnelling takes place and the SPs are coupled to the incoming radiation.

A prism coupler allows for the investigation of flat material surfaces while maintaining the pristine surface geometry. Nevertheless use of additional components and the need for precise positioning would significantly increase the complexity of a device. Due to pristine surface of the sample, this method is mostly useful in material property testing, for example, between fabrication steps.

In the diffraction based excitation, instead of arranging the light incidence geometry of the setup for the wavevectors to match, momentum conservation is achieved by supplying the missing value using diffraction from surface structures or probes (**Fig. 2.14 d-f**). In fact any irregularities of a surface cause light diffraction, therefore SP excitation by using different means had been demonstrated. Even a randomly rough surfaces are able to couple light to SPs due to wide range of possible wavevectors within it, although the efficiency of coupling and quality of the resonance are very low in these kinds of structures.[P14] Couplers do not strictly require periodicity as single whiskers on the surface of SiC had also been shown to demonstrate polarized thermal SPhP emission coupling [106].

A local SPP [87], SPhP [100], or even an SPP-SPhP hybrid mode [84] excitations were demonstrated using a Scanning Near-field Optical Microscope (SNOM) or Atomic Force Microscope (AFM) like tips positioned in the near field area of the sample surface. The near field (SNOM or AFM) tip in this case is positioned near a surface of SP material and SPs are excited in a specific location with nanometre precision by illuminating the tip with a strong optical beam. Theoretically, the SP excitation via SNOM tip can be treated either as a diffraction from a sub-wavelength tip aperture or as a photon tunnelling phenomenon as in the case of prism coupler [87]. Excitation based on SNOM setups allowed for the observation of SPP and SPhP excitation, propagation dynamics

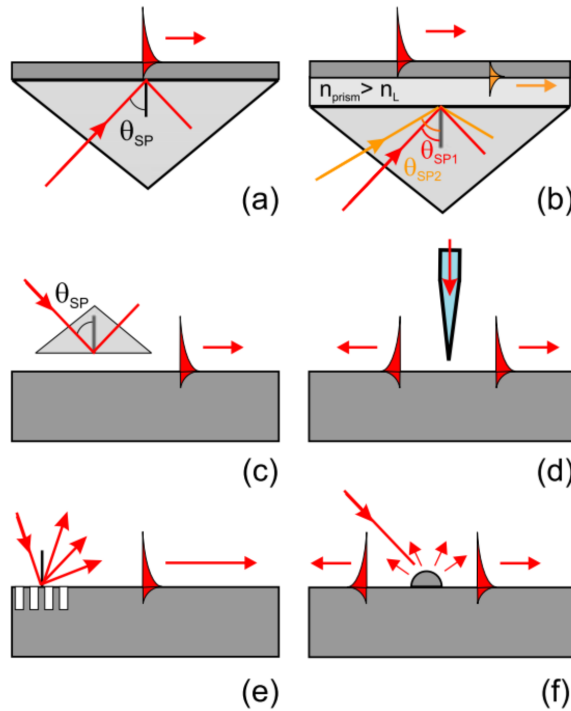


**Figure 2.14:** Main techniques of surface polariton coupling: by using prisms (a-c), probes (d), surface relief gratings (e) or surface irregularities (f). [87]

and even their manipulation, for example focussing [12, 85]. This excitation offers a very high precision, and sensitivity for various sensing or even optical memory applications [84, 87, 100], s-SNOM can be applied for IR vibration absorption spectroscopy of chemical composition [107] and THz mobile carrier contrast in doped semiconductors [108]. Obviously, SNOM is not scaleable and therefore not suitable for fabrication of macroscopic scale optical components.

SPhPs excitation was demonstrated by coupling light to SPhPs using surface relief gratings (SRGs) [83, 109, 110]. A grating coupler can be used to fabricate scaleable large area optical components with high coupling efficiency and quality factors of SP features. One of the first implementations of one dimensional SRGs for SPhP excitation was demonstrated by Greffet et. al. [83, 109]. Note that in diffraction geometry the geometrical parameters of the grating are of great importance therefore careful design and sufficient fabrication quality must be assured [111].

High quality SRGs formed on the surface of SiC showed sharp SPhP features, where strong reflectivity drop as well as thermal

emission from SPhP decay could be observed. The narrowband and highly directional thermal SPhP emission suggested the coherence of SPhPs [13, 96]. The coherence length over 60 wavelengths realizing a locally coherent thermal emitter has been demonstrated in a SRG on SiC surface [83].

Later SPhP/SPP excitation and emission from one dimensional grating on doped GaN epilayer in non equilibrium conditions under pulsed electric field excitation was demonstrated [110]. In this case SPP excitation and emission were investigated in cryogenic conditions, therefore limiting the possible experiment geometries and the excitation efficiency by the cryo-equipment. Directly following these results SPPPhPs in strongly doped GaAs were demonstrated, under pulsed electrical excitation in cryogenic conditions [112]. In both cases weak and wide emission signal was observed, which was limited by high angular aperture beams used for experiments.

Two dimensional gratings have also been demonstrated as series of SiC nanopillars demonstrating exceptional subwavelength confinement in FTIR and Raman studies with  $Q = 40-135$  due to long lifetimes of phonons [82]. Tuning of the SPhP feature frequency over  $60 \text{ cm}^{-1}$  via change of the SiC nanopillar filling factor with sustained quality factor of around 300 has been demonstrated [17]. Even more, active SPhP modulation via photocarrier injection was shown for InP and SiC SPhPs [95]. In these works narrow linewidths are achieved due to long phonon lifetimes (small damping factors) of localized phonon polaritons. On the other hand, localized polariton nature dictates that low spatial coherence and non directional emission was achieved, which required additional optics to direct the radiation into a single far field mode.

In conclusion of this section and in view of this work, the best choice for the fabrication of THz-IR optical components, would be a one dimensional grating coupler. Such a component would offer easy scalability, fast prototyping, robustness and operation without the additional optical components or highly complex setups. An SRG coupler on a semiconductor surface had already been used in several previous works. Nevertheless, no in-depth SPPPhP investigation by tuning of SP excitation in different geometries in the doped GaN-based

system for the continuous operation of an optical component had been yet demonstrated.

## 2.2.6 Theory of a Grating Coupler

In order to design a surface grating coupled surface polariton device, a description of the theory behind a grating coupler is needed. The purpose of any electromagnetic wave coupler is the coupling of near field radiation of a certain mode to the light in the far field. In the case under question SP is the near field exhibiting mode, which cannot interact with the far-field light due to momentum mismatch according to Eq. 2.28. A one dimensional SRG on the material surface provides a certain wavevector value  $k_G$ . At a properly selected frequency and incidence angle, momentum conservation law can be fulfilled as:

$$k_{SPPhP} = k_0 \sin \varphi + Mk_G \quad (2.35)$$

Here  $\varphi$  is the incidence angle of the light,  $M$  is an integer representing the diffraction order of the light ( $M = 0; \pm 1; \pm 2; \dots$ ) Together with 2.28 and 2.33, the equation 2.35 forms the system of equations which, when solved allows to analytically specify the SP frequency dispersion and losses[P5]. As can be seen from Eq. 2.35, tuning of the polariton coupling frequency in a given material system is possible via the geometric parameters of grating period and incidence angle.

Note, that Eq. 2.35 does not contain any information of specific grating geometry (as height, filling factor, grating form) or fabrication quality. Therefore, the true dispersion would be slightly shifted from the analytically predicted values and therefore strictly analytical solution fails to describe exact behaviour of a real grating coupler. In order to design an efficient coupler, one must numerically calculate the dependence of SPPhP behaviour on the SRG shape, filling factor, period fluctuations, groove height and particularities experimental setup [113].

## 2.2.7 Narrowband Thermal Radiation

Objects with temperatures above absolute 0K exhibit random motion of its constituting particles - electrons and atomic nuclei. Motion of

charge carrying particles results in random currents within the material causing electromagnetic emission in a wide spectral range - Black Body Radiation (BBR). In theoretical point of view thermal emission was explained thoroughly by the Planck's law of thermal radiation [13]. It states that an ideal black body characterized by its perfect absorption over the whole electromagnetic spectrum also emits a broad spectrum radiation determined by the black bodies temperature (strength of particle motion). Increase in the temperature causes increase in the emission intensity and blue shift of the spectral position of peak emissivity. A fundamental property of thermal emission is described by Kirchoff's law of thermal radiation in which emissivity ( $E$ ) of every object is shown to be directly related to its optical absorptivity ( $A$ ) as  $E = A$ .

The application thermal emitters, narrowband absorbers or other optical elements in modern applications, beyond basic incandescent light bulbs or cooling radiators, often requires the tuning of emission/absorption/reflection spectra. Thermal absorption and emission are linked to the time reversibility principle of the microscopic processes, engineering of temporal and spacial coherence is possible by judicious material selection and patterning [13]. Temporal and spatial coherence of any radiation source correspond to the ability to preserve phase of wave oscillation in time or space respectively.

In the design of radiation spectra, the temporal coherence time corresponds to the linewidth of the emission via the Fourier transform relation. Coherence time can be essentially described by the lifetime of the collective oscillation resulting in the emission [96].

One should note that maximum intensity of thermal emitter is limited by the Planck's law. Narrow linewidth of a selective thermal emitter is achieved by modulating the emissivity function of the element. By suppressing thermal emission in the vicinity of a feature narrow linewidth emission may be achieved. In the case of SPP emission suppression is observed due to the nature of Reststrahlen band. Reduction of the emission linewidth, therefore, also causes a reduction in integrated emission power of the emitter [13].

Spatial coherence is characterized by its length  $L_{SC}$ . This is the maximum distance at which the light emitted from a point  $x$  on a source is still able to interfere with the light from a point  $x + L_{SC}$ . In view

of SPPPhPs this can be understood as the distance of SPPPhP propagation. Spatial coherence is also associated with the directivity of the emitted light via the Fourier transform relation (Wiener-Khinchin theorem [96]), similarly to the case of temporal coherence being associated with the feature linewidth. While extremely small ( $\delta$ -type) spatial coherence of a random thermal source leads to isotropic emission, a pronounced spatial coherence leads to highly directive radiation profile [13, 83]. Highly pronounced coherence has been demonstrated in semiconductor SRGs [83] where simple estimation of coherence length (valid for many types of sources) was estimated as  $L_{SC} \approx \lambda/\Theta$  to be around  $60\lambda$  high. It should be noted that in the case of semiconductor gratings emission of light is directional only at certain frequencies, with radiation pattern exhibiting a rainbow-type emission with each frequency at a slightly different angle according to the grating equation 2.35. The coherence of SPhP emission was nicely explained by Le Gall as follows. "The presence of angular peaks in the thermal emission can be understood as the result of interference between the light scattered by different ridges illuminated by the same surface-phonon polariton propagating along the interface" [96].

While the term of coherent thermal source is often met controversially, there are many ways of engineering the spatial and temporal coherence of thermal sources. High spatial as well as temporal coherence may be simultaneously and relatively simply achieved by using polar semiconductor SRG structures. This way narrowband and strongly directional thermal emission has been demonstrated to be possible [83]. While the temporal coherence in this case is governed by the long lifetimes (low damping) of optical phonon excitations (material properties), the spatial directivity may be achieved by an SRG (geometrical surface structuring) exhibiting coherence length many times that the radiation wavelength [13, 83].

## 3. METHODS

### 3.1 Finite Difference Time Domain

The Finite-Difference Time-Domain (FDTD) method relies on the discretization of an arbitrary body into a matrix of points and subsequent iterative solution of finite difference Maxwell equations [114]. Even though FDTD typically requires a lot of computational resources, its efficiency further deteriorates when the discretization steps are much smaller or much larger than the wavelength of investigated radiation. The ability to model arbitrary structures with high degree of precision produces great results, as testified by its widespread use in EM modelling.

The basic operation of FDTD method is defined in the original publication [114] as well as in modern tutorials [115]. The modelled area is discretized into spatial points, with finite distances and electric as well as magnetic field components described in the unit cells of respective points as shown in the **Fig. 3.1**. Here each point of defined electric field is surrounded by 4 points of magnetic field and vice versa forming a network of coupled contours. The arbitrary object is defined by the dielectric properties at the points coinciding with its geometry. Correct formulation of finite difference  $E$  and  $H$  equations allows to form a set of equations where magnetic field values at any point in time depend only on electric field values of adjacent points at a previous point in time and vice versa. The calculation of magnetic fields, followed by electric field solution, is carried out in successive time steps (leap-frog method). By stating that at the time point of  $t = 0$  a radiation source of specific frequency is turned on (for example a plane wave appears at the border of simulated space) and selecting a small time step, the evolution of the



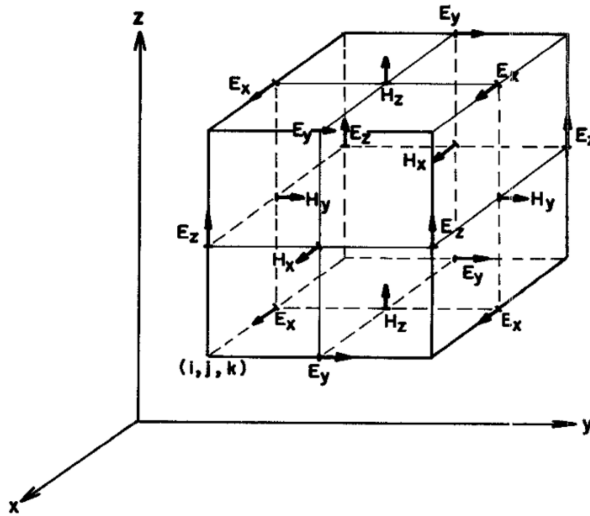


**Figure 3.1:** FDTD calculation unit cell with represented points of electric and magnetic field component definitions. [114]

E-M field is simulated within a given system. Calculations are run until a steady state solution is obtained and the final field distribution is defined. Being a time domain method, FDTD is capable of a solution for a wide frequency range of radiation.

In order to obtain an accurate solution while keeping the required system resources to manageable levels a tradeoff in the spatial and temporal discretization steps must be carefully maintained. For example the spatial discretization steps should be smaller than the shortest wavelength of investigated radiation. At the same time to small discretization steps increase the calculation resources without increasing the calculation accuracy. Accordingly optimal time discretization steps must be chosen. The boundary conditions of the simulated space must also be correctly defined, as the discretization lattice must be truncated in a specific way in order to not introduce reflections which could distort the steady state solution.

While the interaction of simple and well defined scatterers as a sphere or cylinder may be defined by analytical equations, this is impossible for complex arbitrary structures [114]. Even though an MPFL may be seen as a set of cylinders, it falls under the category of an arbitrary objects due to large number of zones and subzones of different height preventing the analytical formulation of the device.

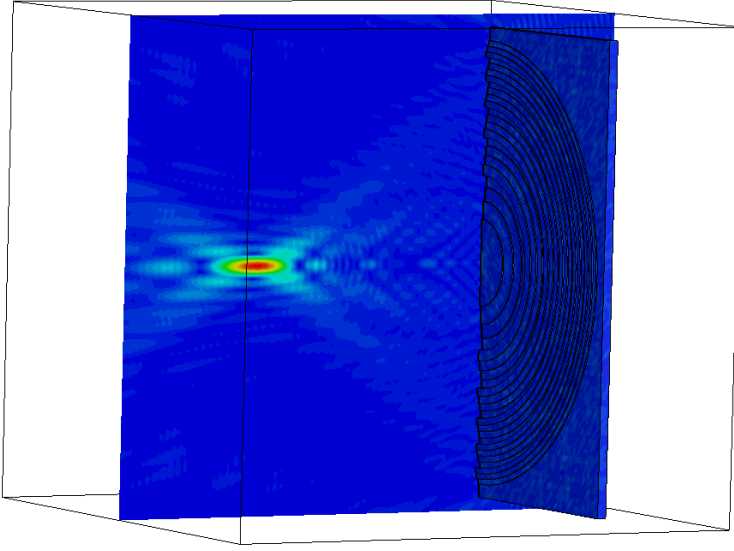


**Figure 3.2:** A typical example of FDTD calculation result for an MPFL with 8 phase quantisation levels.

The FDTD method has been used for DOE investigation with great success in multitude of previous works [23, 54, 62, 65, 116]. Within this work a commercial software package CST was used for the calculation of DOE performance.

## 3.2 MPFL Characterization Setups

The performance of MPFLs was explored experimentally using the setup shown in **Fig. 3.3**. Schottky diode AMC (Amplification Multiplication Chain) from Virginia Diodes Inc. (VDI AMC 346 (VDI MC156) [70]) was used as the THz source. The initial 12.083 GHz Radio Frequency signal was supplied by the Agilent E8257D generator and the frequency then multiplied 48 times ( $6 \times 2 \times 2 \times 2$ ) to 580 GHz by the AMC. The 580 GHz frequency radiation was then out-coupled from AMC output waveguide via horn antenna (VDI WR 1.5). The resulting output power was around  $800 \mu\text{W}$ .

The radiation from the source was a diverging Gaussian beam. The beam was collimated using conventional refractive HDPE lens and guided via flat gold mirror to the sample. The MPFL focusing performance was estimated by microbolometer detector at the focal

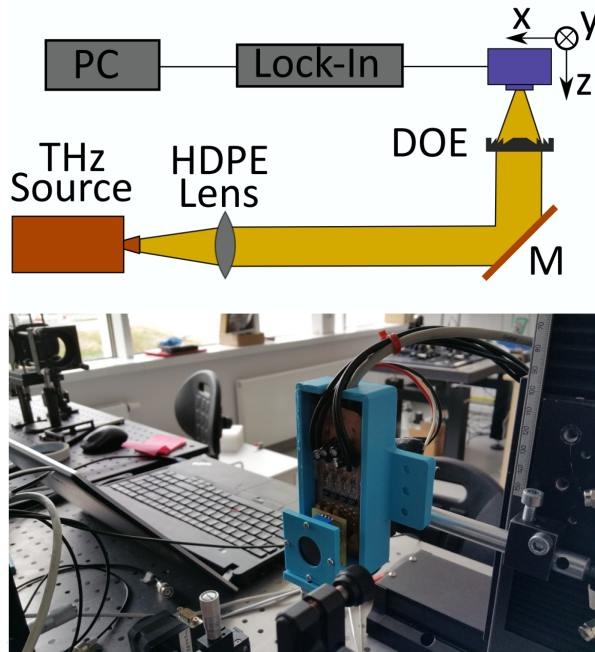


**Figure 3.3:** Schematic representation and a photo of the MPFL characterisation setup. Collimated THz beam is directed at the MPFL using flat mirror M and the focussed beam profile is measured using 3D articulated point detector.

plane [1]. Detector signal was measured using a Lock In amplifier. Single pixel detector was placed on an automated manipulation system consisting of 3 precision travelling stages. The detector was scanned in xy directions in the focal plane of the sample as well as in the focal depth in xz directions. Information about the signal amplitude at the focal spot, focal spots diameter, position as well as symmetry of focused beam was obtained.

Setup, schematically represented in **Fig. 3.4** was used for the THz Imaging experiment. In this case, an imaging target was attached to a 2D manipulation stage and placed in the focal spot of a MPFL. Transmitted signal at each target position was registered using a point detector. Images were recorded at  $0.1 \times 0.1 \text{ mm}^2$  resolution.

### 3.3 Rigorous Coupled Wave Analysis

Several methods are implemented in order to calculate the behaviour of surface polaritons. Calculations are carried out by FDTD,

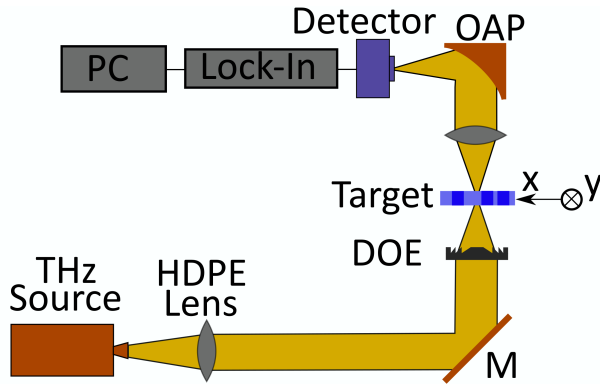


**Figure 3.4:** Schematic representation of the MPFL Imaging setup. Collimated THz beam is directed at the lens (DOE) using flat mirror M. In the focal plane of the lens imaging target is positioned and scanned in the xy plane. Transmitted beam is collimated using a second HDPE lens and directed to the stationary point detector D using off axis parabolic mirror OAP.

full wave 3D simulation in commercial software. Even though this method allows for very accurate modelling, it requires a large amount of computation time and resources. Surface structure behaviour is calculated using L-C circuit calculations in deep grating structures, yet this method is unable to describe shallow, diffraction based gratings [117]. The transfer matrix method also allows to obtain transmission and reflection spectra of certain interface structures, yet it does not allow for the electromagnetic field distribution calculation. Many calculation methods including effective medium theory, FDTD, transfer matrix method and RCWA have been described in the dissertation of Han, Katherine M. 2014 [118].

Rigorous Coupled Wave Analysis (RCWA) offers relatively simple means to describe the optical performance of periodic structures. In this work, 1D-periodic gratings were investigated, even though RCWA (also called Fourier Modal Method - FMM) has been demonstrated to work well with 2D-periodic gratings [119–121]. In investigated case, the is described by 2D crosssection consisting of a an open space region of incoming radiation, the 1D-periodic grating region and the substrate region. This structure is schematically shown in **Fig. 3.5**. Structures of arbitrary geometry may be investigated by using many sub-layers with arbitrary positions and widths. Each layer is described by its thickness and the dielectric function of the material. The grating region is expanded in

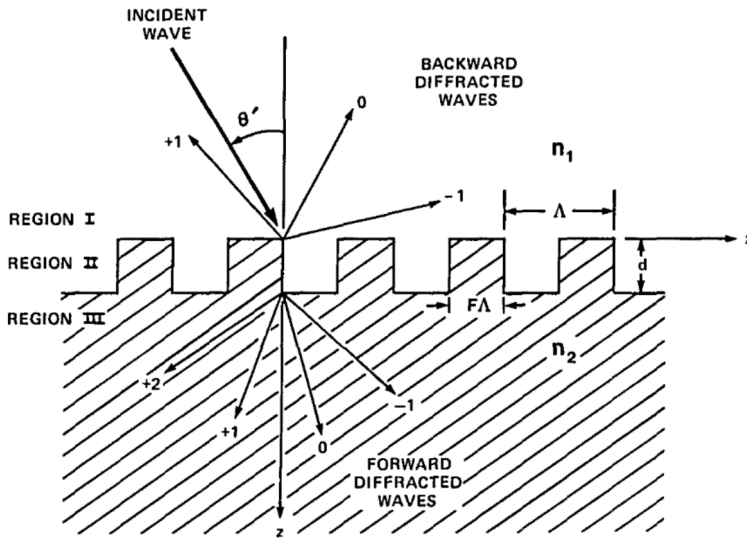


**Figure 3.5:** One-dimensional grating representation in RCWA calculations. Region I is the superstrate in most cases it is air or open space. Region II is the periodic grating layer with certain geometric parameters. Region III is the substrate. Incident wave at an angle  $\Theta$  is being diffracted into certain number of forward (transmitted) and backward (reflected) diffracted waves. [123]

its Fourier series and together with the Floquet condition represent the grating as having infinite periodicity. Through the Fourier expansion, the system of partial differential Maxwell equations is transformed into a system of ordinary differential equations. These are further reduced to a set of linear equations by using the boundary conditions of continuous tangential components of  $E$  and  $H$  fields at the layer boundaries. By truncating the number of Fourier components (diffraction orders  $N$ ), the infinite equation system is limited to a finite one, which can then be solved numerically as a matrix formulation. The calculations are run for one specific frequency and diffraction efficiencies for transmitted and reflected waves as well as field distributions are obtained. [118,122,123]. By summing up the diffraction efficiencies and running the calculation for a set of frequencies the reflection  $R$ , transmission  $T$  and absorption  $A = 1 - T - R$  spectra are obtained.

In RCWA, the solution of Maxwell equations is rigorous, i.e. no common simplifications or assumptions are implemented. These would include the neglect of second derivatives, neglect of boundary effects, neglect of higher-order waves, neglect of dephasing from the Bragg angle,

or small grating modulation [123]. In an ideal case the solution of the system would take an infinite number of Fourier series orders  $N_{max} = \infty$ , and hence infinite calculation resources are not attainable for practical application. In reality, the truncation of Fourier series is used by limiting the maximum number of orders  $N_{max}$  used in the calculation and therefore cutting down the required resources and achieving an sufficient level of accuracy. Selection of the  $N_{max}$  depends on the specific investigated structure. It is advisable to run the calculations with increasing number of Fourier series to see the optimal convergence point for each calculated structure. This implies running a long calculation of high precision with a high number of Fourier orders to specify the converged solution condition and then finding the lowest number of Fourier components which satisfy the set convergence condition.

The derivation and optimization of the RCWA method has been described elsewhere [122,123]. This work concerns with its use for calculation of surface gratings. Matlab code was used for the calculation of SRG performance. Initial code was taken from an open source, which had already been validated in IR to VIS range in various publications [124]. Adaptation of the code was carried out in order to incorporate the dielectric permittivity functions of polar semiconductors in THZ to NIR spectral range (Eq. 2.33) and specific structure geometries relevant to this work. The code was validated by fitting measured spectra of various samples.

Input parameters included the polarization of radiation (TM or TE), angle of incidence, frequency of the radiation, period and width of the grating, dielectric function parameters of grating and substrate layers, their thicknesses and number of Fourier orders. The field plots had each of the layers further divided into 50 to 500 sublayers to increase the precision of calculations and avoid divergence of the result. Calculation of a single reflectivity spectrum or a field plot with a high precision took below 10 minutes, while the reflectivity contour plot calculations took up to several hours.

### 3.4 Fourier Transform Infrared Spectroscopy

Fourier transform infrared (FTIR) spectroscopy measurements were carried out using commercial Nicolet 8700 spectrometer for the measurements at a set incidence angle. It was also used for the measurements of sample emission spectra. A vacuumable Bruker V70 spectrometer system was used for the angular measurements of reflectivity spectra. Basic scheme of a FTIR spectrometer is shown in **Fig. 3.6 a**.

Collimated radiation from internal source is directed into the Michelson's interferometer (see **Fig. 3.6 a**). Beam is then directed from the interferometer into a OAP-1 mirror, which focuses the beam to a spot in the sample compartment. After spreading out again, the radiation is directed into the pyroelectric Deuterated Lanthanum m Alanine doped TriGlycine Sulphate (DLaTGS) detector by OAP-2 mirror.

Incoming beam is split into two secondary beams with the help of KBr beamsplitter in the case of MIR spectral range. Beams are then reflected back into the beamsplitter from the stationary and moving mirrors. Interference of the secondary beams is achieved. By scanning the moving mirror in certain distance  $L$ , the interferogram (interference signal as a function of the optical path) is recorded at discrete distance steps  $\Delta L$ . The interferogram holds the information on radiation power of different wavelengths as the interference condition is obtained for a singular wavelength at each mirror position. Power spectrum as a function of frequency  $P(\nu)$  is obtained by calculating the Fourier transform of the interferogram. It is worth to note that Fourier transform relation also shows that the width of obtained power spectrum is inversely proportional to the optical path step  $\Delta L$  while the spectral resolution is respectively related to the scanning distance  $L$ .

In transmission geometry, when no sample is placed in the FTIR beam path, the power spectrum  $P_{0T}(\nu)$  contains the information about the spectrum of the source  $F_{Src}$ , spectrometer optics  $F_{Opt}$  and detector  $F_{Det}$  as well as atmospheric transmission information  $T_{Atm}$ . In the case when a polariser is used it may also contain the polariser transmission function  $T_{Pol}$ . Resulting reference power spectrum may be expressed as:

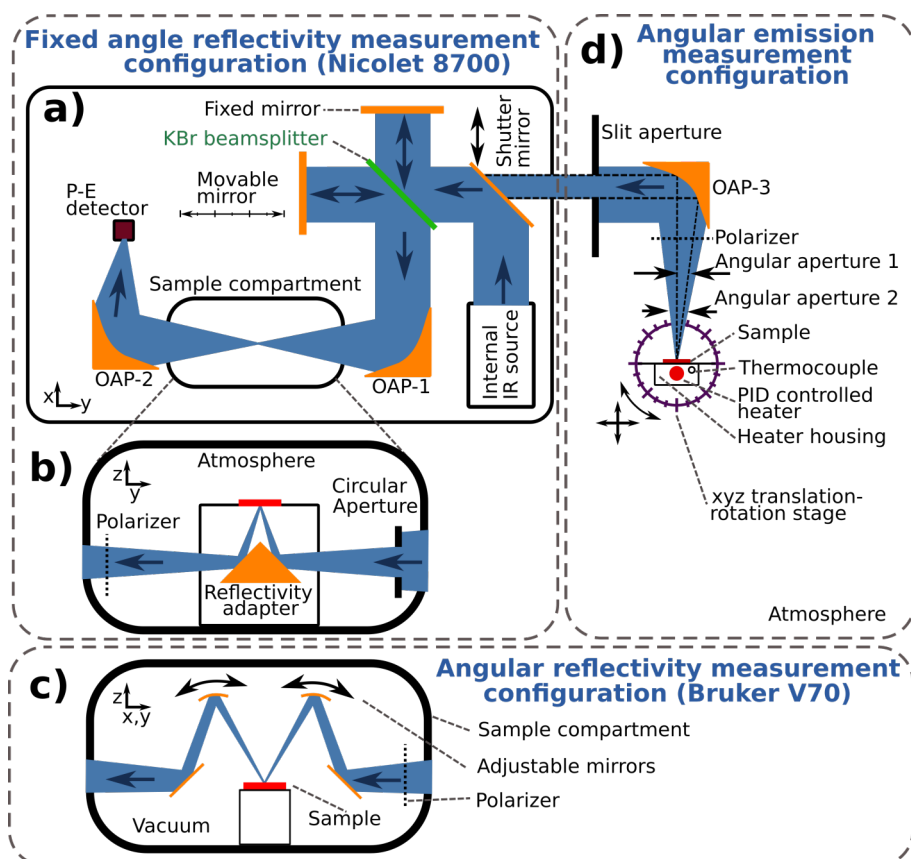


**Figure 3.6:** Schematic representation of the FTIR setup. **a)** Standard configuration of Nicolet 8700 used for transmission spectroscopy illustrating the FTIR operation principle. Internal source (typically a glowbar and associated optics) is used to generate the collimated IR beam. **b)** Sample compartment of the spectrometer with a reflectivity adapter in polarized, limited angular aperture reflectivity measurement configuration. In this configuration a circular aperture may be used to limit the incidence angles of the beam. **c)** Sample compartment representation of the Bruker V70 FTIR spectrometer with angular reflectivity measurement adapter with two movable mirrors used to direct and collect radiation from the sample area at different incidence angles. **d)** External radiation source configuration used for the angular emission measurement.



$$P_{0T} = F_{Src}F_{Opt}F_{Det}T_{Atm}T_{Pol} \quad (3.1)$$

When the sample is placed in the transmission geometry, the power spectrum contains additional information about the sample transmission  $T_S$  resulting in a sample transmission power spectrum:

$$P_{ST} = F_{Src}F_{Opt}F_{Det}T_{Atm}T_{Pol}T_S \quad (3.2)$$

By dividing these spectra sample transmission function is obtained:

$$\frac{P_{ST}}{P_{0T}} = T_S \quad (3.3)$$

Sample reflection  $P_{RS}$  and reference reflective surface  $P_{0R}$  (for example a mirror) spectra must be obtained as:

$$P_{0R} = F_{Src}F_{Opt}F_{Det}T_{Atm}T_{Pol}R_0 \quad (3.4)$$

and

$$P_{SR} = F_{Src}F_{Opt}F_{Det}T_{Atm}T_{Pol}R_S \quad (3.5)$$

Reflection spectrum is therefore calculated as ratio:

$$\frac{P_{SR}}{P_{0R}} = \frac{R_S}{R_0} \approx R_S \quad (3.6)$$

The final approximation is valid in the case when the reflection of the reference is almost unitary, which is obtained by measuring the reflectivity of a gold mirror.

In the case of emission measurements the internal FTIR IR source ( $F_{Src}$ ) switched with an external sample with emission function as  $E_S$ . Spectra in different polarizations were measured. Spectra polarized in TE configuration contained the information about incoherent wafer emission  $E_{S0}$  as SPs and could not be out-coupled in this configuration. Spectra in TM polarization contained information about coherent SP radiation  $E_{SCoh}$  as well as incoherent radiation of the wafer  $E_{S0}$ . Polariser displayed distinct spectral features their transmission functions had to be taken into account as  $T_{PolTM}$  and  $T_{PolTE}$ . The measured polariser transmission spectra are depicted in **Fig. 3.7**. Resulting emission power

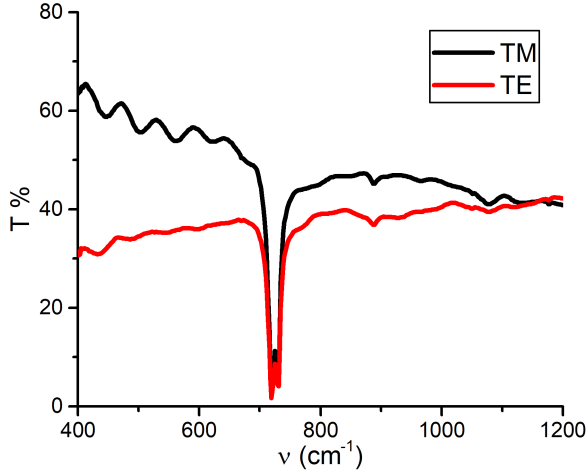


**Figure 3.7:** Polariser transmission functions in TM and TE configurations.

spectra could be approximated as:

$$P_{ETE} = F_{Opt}F_{Det}T_{Atm}T_{PolTE}E_{S0} \quad (3.7)$$

and

$$P_{ETM} = F_{Opt}F_{Det}T_{Atm}T_{PolTM}(E_{S0} + E_{SCoh}) \quad (3.8)$$

Power spectra were investigated by taking into account the polariser transmission functions as:

$$P_{ETM} - P_{ETE} = \frac{F_{Spect}T_{PolTM}(E_{S0} + E_{SCoh})}{T_{PolTM}} - \frac{F_{Spect}T_{PolTE}E_{S0}}{T_{PolTE}} = F_{Spect}E_{SCoh} \quad (3.9)$$

here spectrometer function is denoted as  $F_{Spect} = F_{Opt}F_{Det}T_{Atm}$ .

This function is not specified quantitatively, therefore spectra in arbitrary units are obtained.

The basic configuration of **Fig. 3.6 a** was used to specify the transmission spectra of the polariser. In an ideal case the transmission spectra of a polariser should not have any features and demonstrate a flat almost 50% transmission. The polariser transmission spectra in TM and TE configurations is shown in **Fig. 3.7**. Note that in this specific case the polariser exhibited complex transmission features. In the case of reflectivity measurement the reflectivity of the sample was compared to the spectrum of an optical mirror in the same polariser configuration.

The reflectivity spectra at a fixed incidence angle were measured with a Nicolet spectrometer employing an adapter optimized for measurements at  $20^\circ$  (in the case of metal grating measurements) or  $26^\circ$  (in the case of  $n$ -GaN SRG measurements). Modification of the experimental setup for this case is shown in **Fig. 3.6 b**. The reflectivity adapter consisted of a prism mirror, directing the radiation to an aperture upon which the sample was positioned. The sample aperture was of 5 mm diameter for SRG measurements. Sample aperture was of 1 and 2 mm diameters for MGC-1 and MGC-2 sample measurements respectively. Circular aperture of 7 mm diameter was used at around 10 cm optical path distance from the sample to limit the angular aperture of the experiment to around  $4^\circ$  in the case of  $n$ -GaN SRG sample measurements, no aperture was used in metal grating coupled sample measurements.

Reflectivity angular dispersions were measured using a Bruker V70 FTIR spectrometer, and its simplified beam incidence configuration is demonstrated in **Fig. 3.6 c**. The internal scheme of the Bruker V70 spectrometer differed significantly from the Nicolet spectrometer, but as it used the same principle operation, no additional scheme is illustrated. An automatically rotatable mirror system was used to obtain the reflectivity spectra within the range of  $14^\circ$  to  $45^\circ$  incidence angles. Measurements in TE and TM polarizations were carried out using a grid polariser. The results obtained for either gold, or TE polarization were used as the reference in this case in order to remove the influence of phononic features and observe more pronounced polaritonic input.

Emission experiments were carried out using the Nicolet 8700 FTIR spectrometer in the external radiation source configuration shown in **Fig. 3.6 d**. In order to realize the external emission measurements OAP-3 mirror was used to collimate the radiation from the source to the spectrometer. Collimated beam is obtained by placing the investigated emitter in the focal spot of a 10 cm focal distance OAP-3 mirror. The sample as well as OAP-3 mirror are placed on  $xyz$  adjustable translation stages for precise adjustment. Sample was attached to a custom built heater consisting of a massive (in comparison to the sample) heater-housing, temperature of which was controlled using a thermocouple and a PID temperature controller. Temperature was stabilized with better than  $\pm 1^\circ\text{C}$  precision. The heater setup with the sample were placed on a ro-

tation stage, which was controlled via personal computer. Angular reflection spectra dependency was measured with a  $2^\circ$  precision in manual mode and  $0.25^\circ$  resolution in automated mode. In order to limit angular aperture  $\varphi_1$ , a slit aperture of 2 mm was placed in the collimated beam near the entrance port of the spectrometer. The angular aperture was therefore limited to the angle of around  $1.1^\circ$ . With the further decrease of the aperture the SNR dropped below acceptable levels distorting the measurement results. Each presented data point was obtained by averaging 60 measurements.

## 4. RESULTS

### 4.1 Diffractive Lenses

#### 4.1.1 Multilevel Phase Fresnel Lenses

In this chapter, the design and fabrication of THz MPFLs are described. The structures were fabricated by laser patterning of either monocrystalline silicon wafers or molybdenum foil in order to develop MPFLs and SZPLs, respectively. The focusing performance was investigated both theoretically and experimentally.

In the beginning of this chapter, MPFLs for 0.58 THz frequency are described. Elements with different numbers of phase quantisation levels  $p$  were investigated in order to determine the dependency of focusing power on the design complexity ( $p$  number) of the element fabricated by direct laser ablation. A large area MPFL was additionally fabricated and its application in an imaging experiment was demonstrated. In order to test the frequency limitations of laser processed diffractive elements, three lenses were designed and fabricated to work at 4.7 THz frequency. Performance of Si 4.7 THz MPFLs with binary ( $p = 2$ ) and octal ( $p = 8$ ) phase quantization levels and a SZPL were tested. Applicability of DLA method for the fabrication of DOEs in THz frequency range was confirmed.

#### 4.1.2 0.6 THz DOE Samples

The components described in this section were fabricated for the operational frequency of 0.58 THz (wavelength of 0.517 mm). Sample designs starting with two zones ( $p = 2$ ) and ending with almost kinoform shape ( $p > 1000$ , representing the case of a continuous Fresnel

lens) were chosen. Two sets of the samples were developed for the focusing THz beam at the focal distances of 5 and 10 mm, respectively. The manufacturing tolerances were also checked in terms of the surface roughness of the processed subzones.

The samples under investigation were fabricated in the Department of Laser Technology at the Centre for Physical Sciences and Technology. A silicon wafer of 460  $\mu\text{m}$  thickness,  $(110)\pm 0.5^\circ$  crystal orientation was used for the fabrication. The wafer was also  $p$ -doped with boron and had the resistance of  $10\text{-}25 \Omega \times \text{cm}$ . It had the refractive index of 3.48 and the absorption coefficient of  $2 \text{ cm}^{-1}$  at the working frequency of 0.58 THz.

The wafer was patterned by a industrial-scale laser direct writing system using a 1064 nm wavelength laser (Atlantic 60 from Ekspla Ltd.). Pulses of 13 ps duration and repetition rate of 1 MHz with peak energy of 60  $\mu\text{J}$  were used for the patterning.

The patterning was carried out by scanning the optical beam in one direction on the sample surface using a high speed polygon scanner (LSE170 from Next Scan Technology) and translating the sample using single axis translation stage (PR0115 from Aerotech) [125]. A spot diameter of about 44  $\mu\text{m}$  was achieved and a spot overlap of 50% at a scan speed of 50 m/s was used during processing scan. An average of 86 nm thick layer of the silicon was ablated in single scan. This allowed to maintain precise control over the shape profile of the lens with the material removal rate in the spot area of about 1.4  $\mu\text{m}/\text{min}$ .

The MPFLs had the diameter of 17.5 mm. The 5 mm focal length MPFLs consisted of  $N = 9$  main zones, while the ones with 10 mm focal length had  $N = 6$ . The theoretical  $n_a$  (Eq. 2.6) for the corresponding lenses was of 4.4 and 6.2. This meant that the MPFLs with  $f = 5$  mm possessed small axial aberrations full optimisation of which was not on the purpose of this work. The requirement of  $N \ll n_a$  was not completely fulfilled; however, good focusing performance was still expected for selected MPFL designs.

Each of the focal length groups consisted of 5 samples. For the  $f = 5$  mm focal length group,  $p$  was of 4, 8, 16, 32 and 1643 (latter one also called the kinoform shape). For the  $f = 10$  mm focal length group,  $p$  was of 2, 4, 8, 16 and 1643. In the limiting cases,  $p = 2$  design corre-

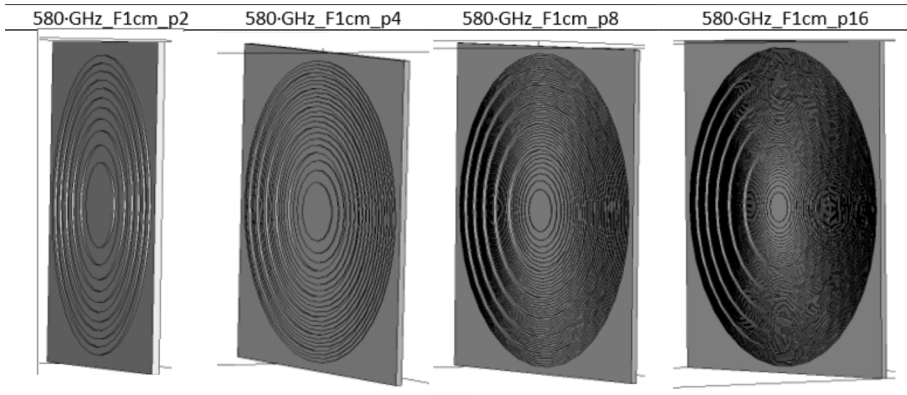


**Figure 4.1:** Designs of  $f = 10$  mm MPFLs with  $p = 2, 4, 8$  and  $16$  subzones. Images were taken from the modelling software interface.

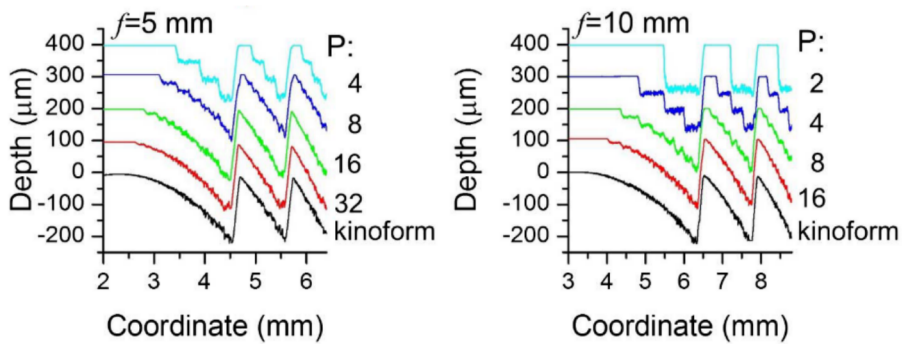


**Figure 4.2:** Step profilometer measurement results for fabricated MPFL cross sections with  $f = 5$  mm and  $f = 10$  mm focal distances. Adapted after Ref. [P1].

sponded to a phase inverting zone plate, while  $p = 1643$  design was expected to reproduce the surface of a continuous Phase Fresnel Lens. Selected sample design visualisations taken from modelling interface are demonstrated in **Fig. 4.1**.

Surface morphologies for centre zones of all of the fabricated samples are shown in the **Fig. 4.2**. It can be seen that phase quantitation steps are clearly observed for up to 8 PQLs. When  $p$  is further increased, the width of a subzone becomes smaller than the laser spot and thus the subsequent overlap smooths the whole surface of the MPFL. Structures with the larger  $p$  are believed to perform slightly differently due to differences of the leftover unprocessed area. This is clearly observed in the case of the first (centre) subzone diameters of  $p = 4$  and  $p = 32$  MPFLs

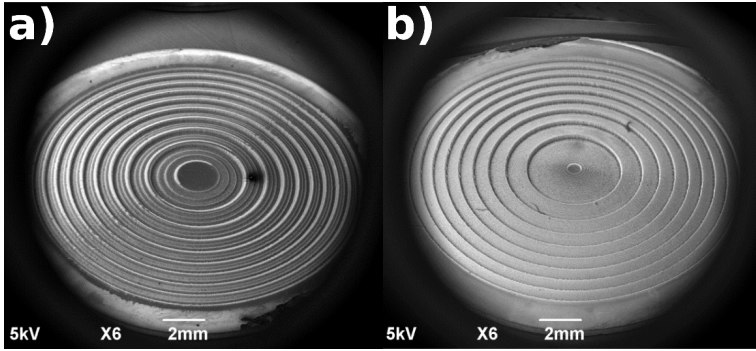


**Figure 4.3:** SEM images of fabricated MPFLs with  $f = 5$  mm and subzone numbers of a)  $p = 4$  and b)  $p = 32$  MPFLs.

SEM images of which are shown in **Fig. 4.3**. Here  $p = 4$  sample has comparatively large unprocessed centre area as well as top rings at each of the zones, while in the case of  $p = 32$  MPFL almost all surface area is processed.

It can be seen in the step profiler results as well as in the SEM images in that there were no notable fabrication defects for the lenses. Nevertheless, there was a notable increase of the surface roughness in the laser processed areas seen in magnified SEM images in **Fig. 4.4**. This roughness is attributed to the formation of LIPSS (Laser Induced Periodic Surface Structures) which are widely known and investigated in the field of laser processing [126, 127]. LIPSS are known to form even at relatively low laser exposure as nano-scale structures self-form due to hydrodynamic processes in the affected area. Each pass of the laser exposure increases the LIPSS height in addition to ablating the processed surface. In the case of MPFL structures, formation of columnar morphology of increasing height was observed with the increased laser exposure. In the case of the of 4 PQL MPFL the depths of LIPSS at each processed subzone were  $5.5 (\pm 1)$ ,  $6 (\pm 1.5)$  and  $11 (\pm 3.4)$   $\mu\text{m}$  with corresponding widths of:  $19.6 (\pm 6)$ ,  $20 (\pm 2.2)$  and  $23 (\pm 3.7)$   $\mu\text{m}$ . The SEM images of these zone surfaces are given in **Fig.4.4** insets 1, 2 and 3 respectively.

The characteristic dimensions of surface roughness features were much smaller than the wavelength of  $517 \mu\text{m}$  of the operational 0.58 THz frequency thus scattering from surface roughness was expected to be negligible in the fabricated MPFLs. Nevertheless it had already been shown that laser ablation of silicon surface affects the



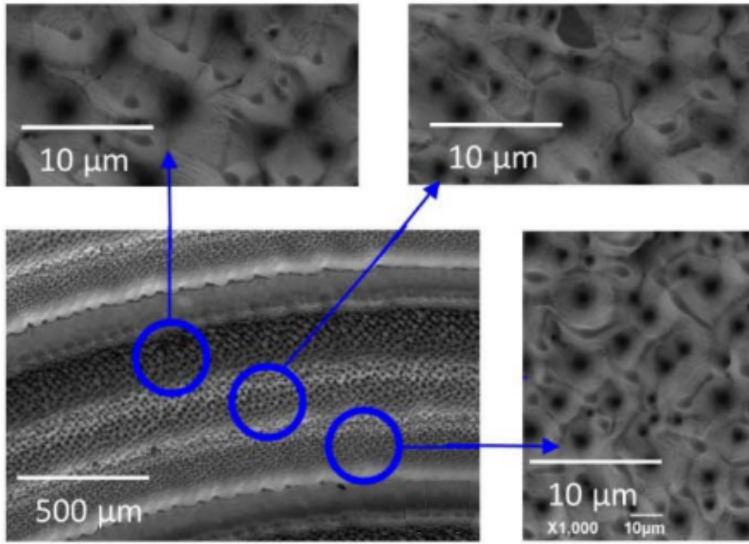


**Figure 4.4:** SEM photographs of  $f = 5$  mm focal distance lens with  $p = 4$  sub-zones. Insets show magnified surface view at different subzones. Adapted after Ref.[ P1].

THz properties of fabricated samples through the increased optical losses in the ablated structures and/or formation of a black silicon layer [73,128].

A large area MPFL was designed and fabricated for the use of the device with larger beamwidth systems.[P2] A MPFL with the 50 mm diameter,  $p = 16$  number of phase quantisation levels and the focal length  $F = 30$  mm was fabricated and shown in **Fig. 4.5**.

#### 4.1.3 4.7 THz DOE Samples

Two kinds of samples were fabricated for the focusing of 4.7 THz radiation. The first one was the Soret zone plate (also known as binary metal zone plate) with open zones fabricated by DLA. Openings in the form of concentric rings with support beams were formed in opaque metal foil. The sample and its magnified centre zone view are shown in the microscope photos in **Fig. 4.6**. The second kind was the MPFLs fabricated on high resistivity silicon using the DLA process. Sample designs with 2 and 8 subzones were chosen.

The same lens parameters were chosen for all of the focusing elements. The diameter  $D = 25$  mm and the focal depth  $f = 50$  mm, leading

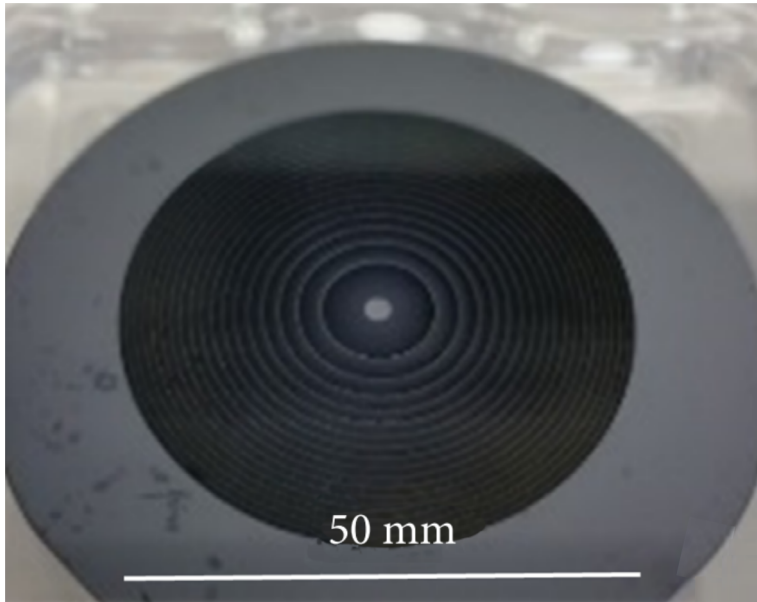


**Figure 4.5:** Optical photograph of 5 cm diameter MPFL with 16 PQLs and 3 cm focal depth. Adapted after Ref. [P2].

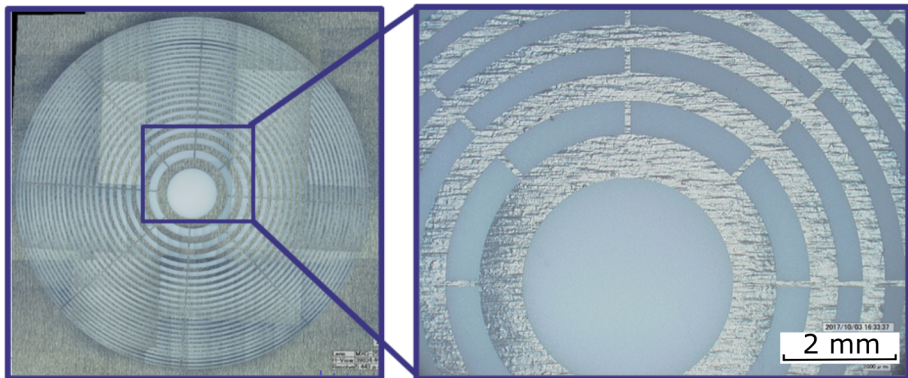


**Figure 4.6:** Microscope image of the fabricated Soret zone plate.

to an F-number of  $\approx 0.5$ , were selected as the initial design parameters for the research. An operational frequency of 4.745 THz ( $\lambda = 63.18 \mu\text{m}$ ) was chosen. This frequency is important for the measurement of oxygen absorption line using QCL THz sources in astronomical telescopes. The QCL used for characterisation was a laboratory version of GREAT spectrometer on board of SOFIA telescope [6].

A theoretical estimation of the chosen designs predicted the numerical aperture of the focusing elements to be of 0.243, focusing spot size of around  $300 \mu\text{m}$ , Gaussian beam waist of  $2 \times w_0 = 164 \mu\text{m}$  and the Rayleigh range (distance from the focal plane to  $z$  coordinate where the beamwidth is doubled) of 1.1 mm. Focusing gain  $G_f$  was predicted to be of 28 dB (630 times) in the case of SZPL and 32 dB (over 1500 times) in the case of  $p = 8$  PQL MPFL.

The SZPL was fabricated of a  $16.5 \pm 2.2 \mu\text{m}$  thick molybdenum foil. The chosen metal foil had already exhibited an adequate mechanical stability, which was needed to support itself in the previously reported research [54, 129, 130]. The thickness of a free standing metal foil was confirmed to be suitable for the development of efficient diffractive optics for the THz range. The samples were fabricated employing a second-harmonic beam of the femtosecond laser Pharos from Light Conversion (300 fs, 100 kHz, 515 nm) focused with a 10 mm focal length objective and scanned with a linear two-axis positioning stage from Aerotech. Smooth-cut lines were achieved using a spot size of  $5.6 \mu\text{m}$ , a pulse density of 40 000 pulses/mm, and a fluence of  $17.9 \text{ J/cm}^2$ , and by repeating each scan five times.

The MPFL samples were patterned on a  $500 \pm 25 \mu\text{m}$  thick and double-side polished high resistivity float zone silicon wafer with (100) orientation. The Si demonstrated a resistivity of  $100 \text{ k}\Omega\text{cm}$ , a refractive index of 3.46. Negligible absorption coefficient and high refractive index caused an average transmission of 50%, limited mainly by reflective losses for the unprocessed wafer at the target wavelength.

A two-level (binary plate) lens was chosen as having the simplest design and processing. The second design consisted of 8 PQL-MPFL. This design was chosen as having optimal performance and production time/complexity as indicated by the results in section 4.1.4.

For the fabrication of MPFLs, different laser processing parameters

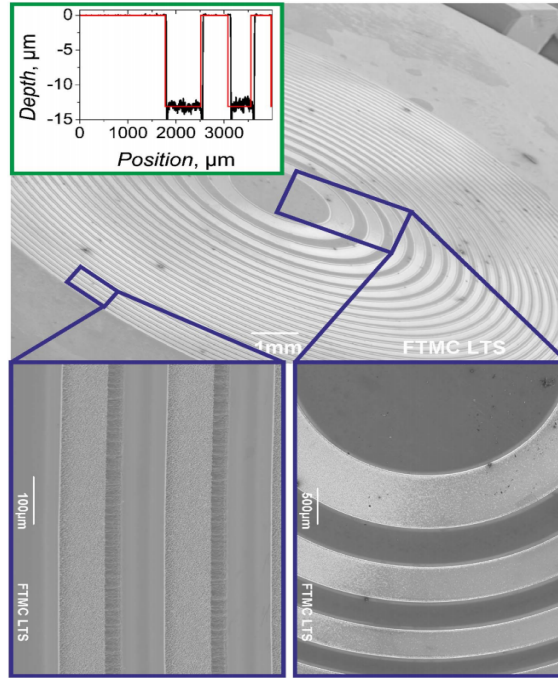


**Figure 4.7:** SEM images of the fabricated binary phase Fresnel lens. Inset shows the profilometer scan of fabricated MPFL as compared to the designed profile. Adapted after Ref. [P3].

were chosen than in the case of SZPL due to difference in material. A beam of the picosecond laser Atlantic-60 from "Ekspla" (13 ps, 100 kHz, 532 nm) focused with the telecentric 80 mm focal length objective was scanned using a "hurrySCAN" 14 scanner from "SCANLAB". Samples with eight (MPFL8) and two (MPFL2) phase quantisation levels were patterned with a beam spot size of about 28 and 13  $\mu\text{m}$ , respectively. It is worth noting that the MPFL8 sample consisted of 200 subzones smallest of which had the width of about 32  $\mu\text{m}$ . The minimal zone width was still larger than the beam width, avoiding possible laser overlap of different subzones. This allowed for better accordance between the theoretical design and the fabricated sample geometry. The material removal rate of 300 nm in a single scan was obtained for MPFL processing with the laser parameters of: 4 J/cm<sup>2</sup> fluence and 65% pulse overlap for the MPFL2 sample, and 1.6 J/cm<sup>2</sup> and 82% for the MPFL8 sample, respectively.

A stylus profiler (Dektak 150) and scanning electron microscope (SEM, JEOL JSM) were used to characterize the morphology of 4.7 THz

MPFL samples. The SEM images of the sample and the step-profile scanned in the centre are shown in **Fig. 4.7**. The surface roughness ( $R_a$ ) after laser patterning of the silicon was below 500 nm, which was over 120 times smaller than the 63  $\mu\text{m}$  wavelength of the radiation. Negligible scattering losses were therefore expected to be observed in the fabricated structures.

#### 4.1.4 Performance of DOEs for 0.6 THz Frequency

The focused beam intensity distribution in the focal plane ( $xy$  plane) and focal depth ( $xz$  plane) of the MPFLs were measured. Results for kinoform MPFLs with 5 and 10 mm focal distances are shown in the **Fig. 4.8** as they are indicative of the results obtained for other geometries also.

Similar maximum focused beam intensities were obtained for both focal distance lenses at around 1.7 V detector signal. Symmetric focal spots were observed in the  $xy$  scans at the focal distances of respective lenses in **Fig. 4.8 a** and **b** with a smaller spot diameter obtained for 5 mm focal distance lens. cross sections of the focused beam intensity in the  $x$  direction in logarithmic scale are shown in **Fig. 4.8 e**. Results reveal the existence of secondary airy disks around the central focal spot. Asymmetry is observed for secondary rings. This attributed to either slight misalignment of the MPFL within the sample holder and optical axis of the experiment or a deviation of the subzone depth in the fabrication process. The latter variation was also seen in the step profiler measurements in various directions along the MPFL centre. The overall focusing gain of over 20 dB for the produced MPFLs was similar to the result of 17 dB obtained for SZPL, indicating some possible problems in the design and fabrication processes of the MPFLs [1].

Scans in  $xz$  plane were carried out and results for the kinoform lenses are shown in **Fig. 4.8 c** and **d**. The results revealed an elongation of the focal spot, as well as formation of signal ripples in the  $z$  direction. Ripples were attributed to the formation of standing waves between the sample and emitter/detector. Note that in these plots the  $z$  coordinate is arbitrary, starting at an arbitrary point and are not directly related or indicative of the exact focal distance. Arbitrary  $z$  scan start position is

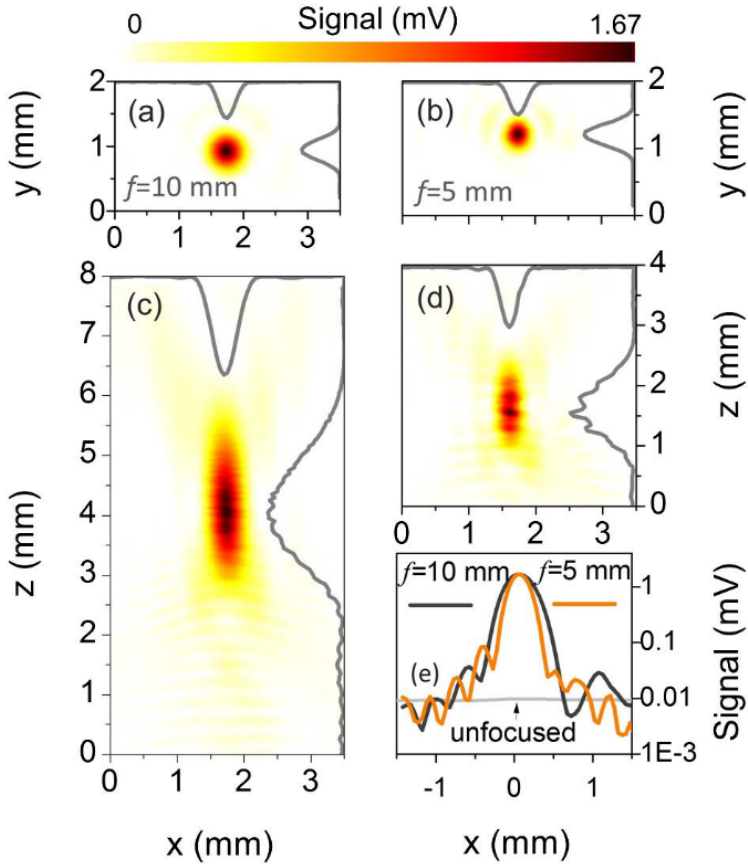


**Figure 4.8:** Experimental 2D beam profiles for the kinoform MPFLs with the focal lengths  $f=10$  mm and  $f=5$  mm. **a)** and **b)** Respective lens results in the focal  $xy$  plane. **c)** and **d)** The results in the focal depth ( $xz$  plane). The beam cross section at maximum intensity is presented in linear scale as a solid line for each case. **e)** Comparison of focusing performance for two kinoform lenses. Note the log scale of intensity. Adapted after Ref. [P1].

caused by the geometry of the detector as it could not be positioned at the exact surface of the lens due to possible detector damage upon direct contact. Nevertheless the focal distances of the fabricated devices coincided well with the initial designs of 5 and 10 mm. Smaller standing wave formation was observed for MPFLs as compared to previously reported SZPLs [1].

Focused beam intensity on the number of subzones was plotted in the **Fig. 4.9**. The intensity of the beam increased with increasing PQL number and saturated at  $p > 8$  subzones. This dependency closely matched the theoretical result as given by Eq. 2.5 [63] and shown in **Fig. 4.9**. It is seen that asymptotic focusing power of MPFL on the  $p$  comes not only from the fabrication, where the laser beam overlap smooths the surface of the steps, but is a fundamental in nature of MPFL operation. Further improvement of laser ablation resolution is not needed as higher number of discrete PQLs would not improve the operation of the lens. It illustrates that optimal performance of MPFLs in current design was achieved.

At closer inspection, the kinoform MPFLs showed a slightly smaller signal than the one containing 16 PQLs. This was attributed to slight defects in the fabricated samples due to processing tolerances. Further optimization of DLA and sample design could further improve the efficiency of MPFLs.

It is worth noting that in the case of MPFL with  $f = 5$  cm and  $P = 16$  there was a significant signal drop from the expected value. This was attributed to a deviation in the fabrication of the sample as the groove depth mismatch from the designed values was found under closer inspection.

A cross section of focused beam intensity in the  $z$  axis direction is shown in **Fig. 4.10 a**. The measured results, where the plane surface is facing the detector, were fitted with Gaussian function, and the FWHM values of 0.55 and 0.43 mm were obtained for MPFLs with  $F = 10$  and 5 mm focal lengths respectively. FWHM values of the focussed beam in the  $x$  direction were calculated from the  $xz$  scan for each detector - lens distance  $z$  and are shown in **Fig. 4.10 b**. Average values of beam waist were calculated to be of 0.47 mm and 0.37 mm and the focal depth of 3 mm and 1.3 mm for the groups of  $f = 10$  and 5 mm MPFLs respec-

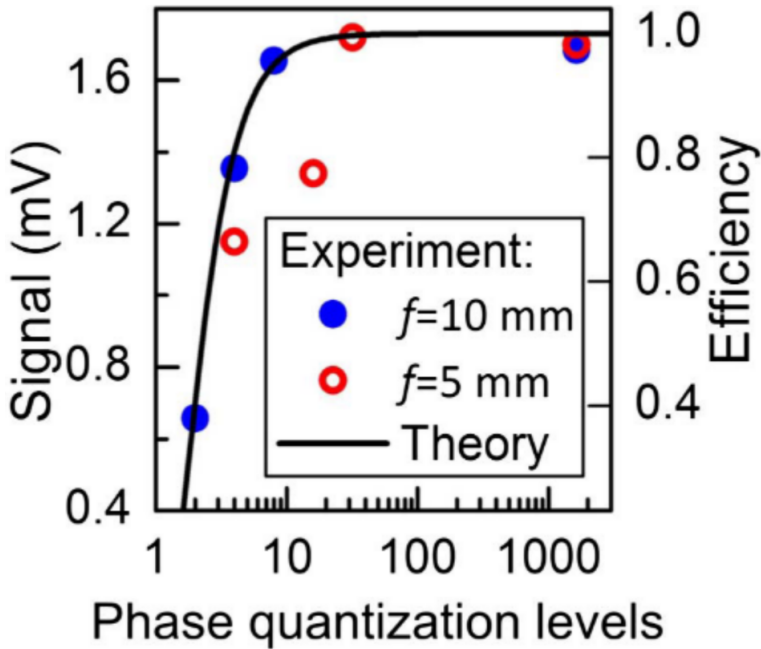


**Figure 4.9:** Dependence of experimental peak signal of the focused beam on the number of phase quantisation levels of a MPFL presented in dots. Line shows the dependence of theoretical diffraction efficiency on the number of phase quantization levels (Eq. 2.5). Adapted after Ref. [P1].

tively. The obtained values of beam waist were close to the operational wavelength of  $517 \mu\text{m}$ . Abbe diffraction limit for the operational wavelength and lens geometries given as  $d_A = \lambda/2NA$  was, respectively,  $0.4$  and  $0.3 \mu\text{m}$ . Therefore it can be stated that near diffraction limited performance is achieved using current sample geometries and only around 20% reduction in the focal spot diameter is possible with further optimisation of design and fabrication. The focused spot parameters for separate lenses are listed in **Fig. 4.18**.

Fringes were observed in the  $z$  scan in **Fig. 4.10** when the ablated surface was facing the emitter. Fringes were attributed to the formation of standing cavity waves formed between (semi) reflective detector and flat Si surface. To check this assumption, the experimental setup was changed and the MPFL was rotated in order to face the ablated zone toward THz detector. In this case, much weaker fringes were observed as the ablated surface of the MPFL scattered the radiation, returning to MPFL after partial reflection from the detector. Similar maximum focusing power was achieved in this geometry, without notable drops



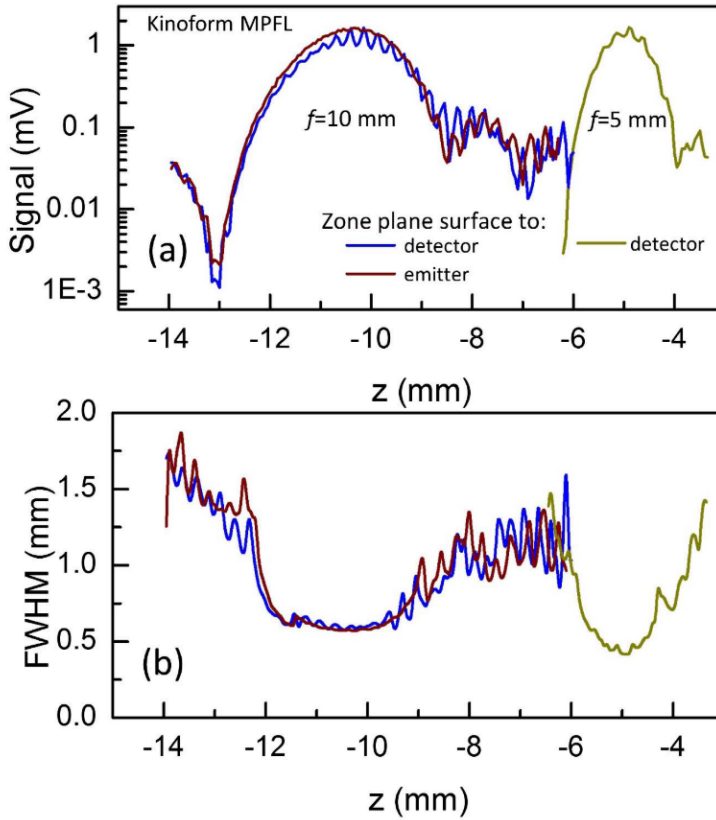


**Figure 4.10:** a) Focused beam intensity and (b) FWHM values along the  $z$  coordinate for the case of kinoform MPFLs with  $f = 5$  mm and 10 mm. The plane silicon surface of a MPFL was facing toward the terahertz detector or emitter as indicated. Adapted after Ref. [P1].

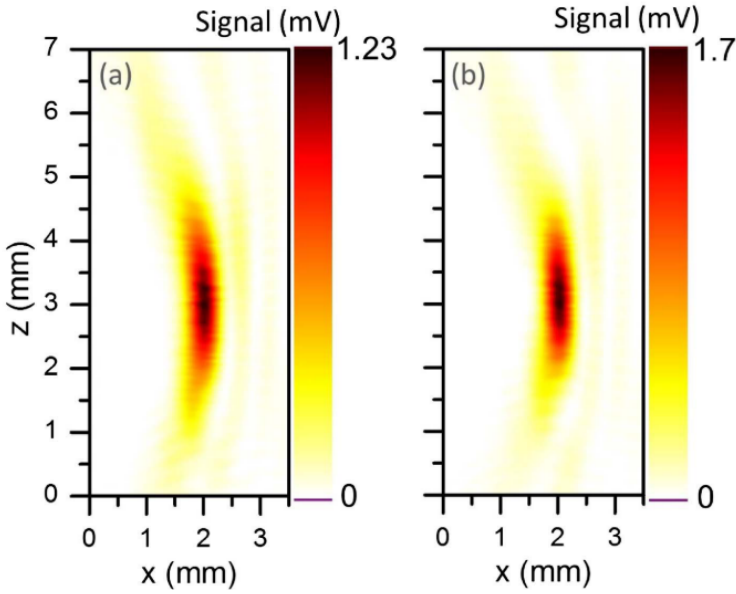


**Figure 4.11:** Experimental 2D beam distribution in the focal depth ( $xz$  direction) measured using a MPFL with eight subzones and  $f = 10$  mm focal length, offset by  $10^\circ$  of optical axis and facing the laser-ablated plane a) to the terahertz detector and b) to the terahertz source. Adapted after Ref. [P1].

in  $z$  direction due to fringes.

In order to check the assumption of standing wave formation, MPFL was rotated  $10^\circ$  around its  $y$  centre axis and  $xz$  scans were performed. Experiments were carried out with the flat surface of the MPFL facing the emitter or the detector. Radiation returning from the detector was expected to scatter by the slanted surface. And indeed when the flat surface faced the detector at  $10^\circ$  much smaller fringes were observed as it is seen in **Fig. 4.11**. Maximum signal at the focused spot was 14% weaker when compared to the geometry of normal incidence THz beam. The drop manifested due to suboptimal orientation of the MPFL zones and possibly increased shadowing of the subzones which had been known to affect the MPFLs in previous works [57, 131]. Significant signal drop was not observed in the case when ablated side of the MPFL was facing the detector at  $10^\circ$  and larger angles. This fact also supports the notion of zone shadowing, as it is demonstrated in **Fig. 4.12**. It is evident from the example that when the slanting is introduced, the shadowing would be more pronounced in the case of MPFL structure facing the emitter. The decline of the focusing performance could also be alleviated by chang-

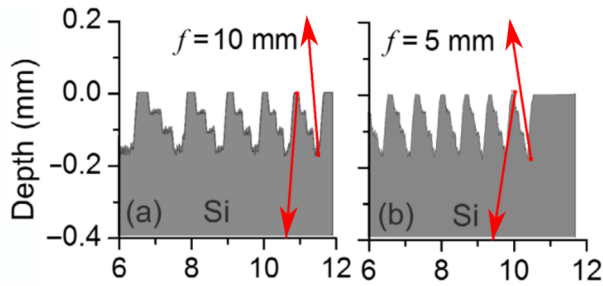


**Figure 4.12:** Illustration of the shadowing effect on the MPFL performance. The secondary waves do not encounter any additional walls in their path when the focal spot is above the sample (illumination from bottom side). The red lines going to the top do not cross the structure. When the focal spot is below the sample (illumination from top side) the secondary waves diffracted from the top part of the MPFL are reflected from the side walls of the zones and decrease the focusing performance. Adapted after Ref. [P2].

ing the design of the MPFL to account for the wafer slanting as diffractive optics can be designed for arbitrary geometries and surfaces.

The absolute value of the focused beam intensity was found to be dependent of the terahertz reflection and absorption losses. Absorption losses were also investigated by measuring the transmittance of a MPFL shown in **Fig. 4.13** In this experiment the collimated THz beam was focused using an OAP mirrors and measured with single pixel detector. The MPFL was placed into the focal spot of the system and raster-scanned in the THz imaging system. Results are shown in **Fig. 4.14**. A round shape of MPFL zones was clearly observed as a low signal area because the diffracted beam was diverted from the optical axis of the system. Absorption losses induced by the patterning was investigated. Average signal of flat ablated area (marked by triangles) was compared to the average signal of an unprocessed sample. Up to 49% reduction of the transmitted signal was observed due to increased optical losses and possible formation of black Si reported with previous research [128,132].

The diffraction efficiency of the terahertz-MPFL was evaluated by integrating the terahertz beam intensity measured at the focal xy-plane and accounting for the absorption losses of the silicon before and after laser ablation. As expected, the MPFLs with  $p > 8$  demonstrated close to 100% diffraction efficiency. A lower efficiency was observed for a MPFL with  $f = 5$  mm due to stronger power dissipation in secondary lobes of

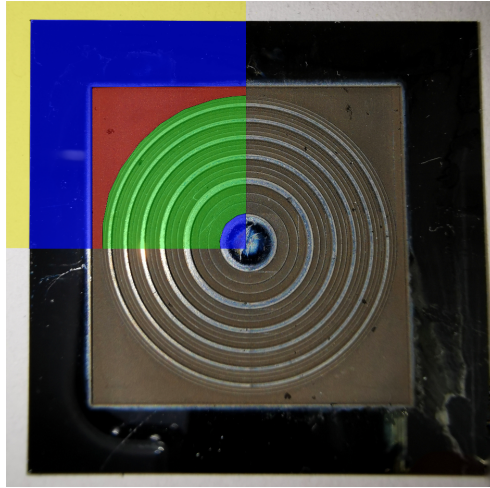


**Figure 4.13:** Optical photo of a sample used for transmission experiment. Blue area marks the unprocessed sample surface (polished silicon), Red is the ablated plane surface, Green is area of MPFL and Yellow is the open area outside of a sample.

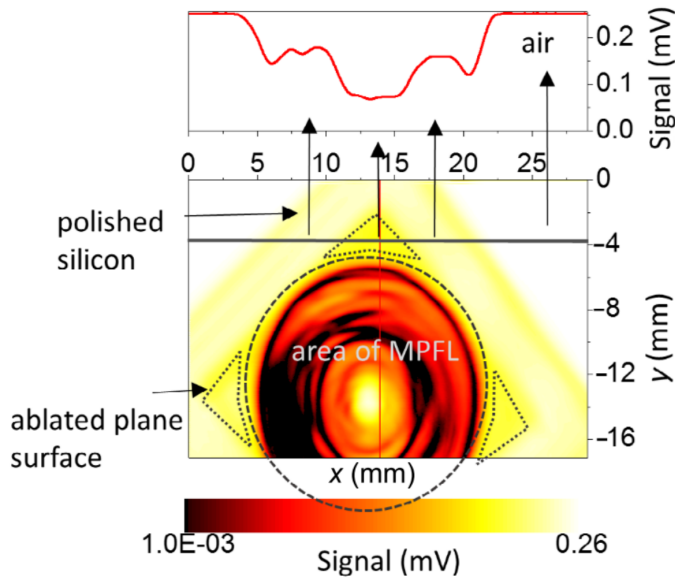


**Figure 4.14:** Transmission imaging of a test MPFL sample with 4 zones and 10 mm focal distance. Top inset shows signal cross section indicated by the line in 2D plot. Adapted after Ref. [P2].

diffraction maxima.

Reflection losses may be minimized by the introduction of laser processed antireflective structures fabricated during the same processing step [9, 75]. Nevertheless, an increase of absorption losses in the processed surface requires additional research and process optimization in order to realise the full potential of laser processed DOEs.

Large area MPFL was also characterised and its performance results are shown in Fig. 4.15. A symmetric Gaussian beam is observed in the  $xy$  scan at the focal spot, with FWHM value of 0.92 mm. Focal spot elongation in the  $z$  direction was observed in the  $xz$  scan similarly to previous MPFLs.

The large area MPFL was used in an imaging experiment. A HDPE lens was used to collimate the radiation from the focal point of MPFL. Collimated beam was then focused to the single pixel detector by an OAP mirror. Targets were attached to 3D translation setup and scanned in the  $xy$  directions within the focal plane of the MPFL. First imaging target was a flat metal foil with several sets of open parallel slits of different width, called the resolution target.

The photos of the targets and imaging results are shown in Fig. 4.16.

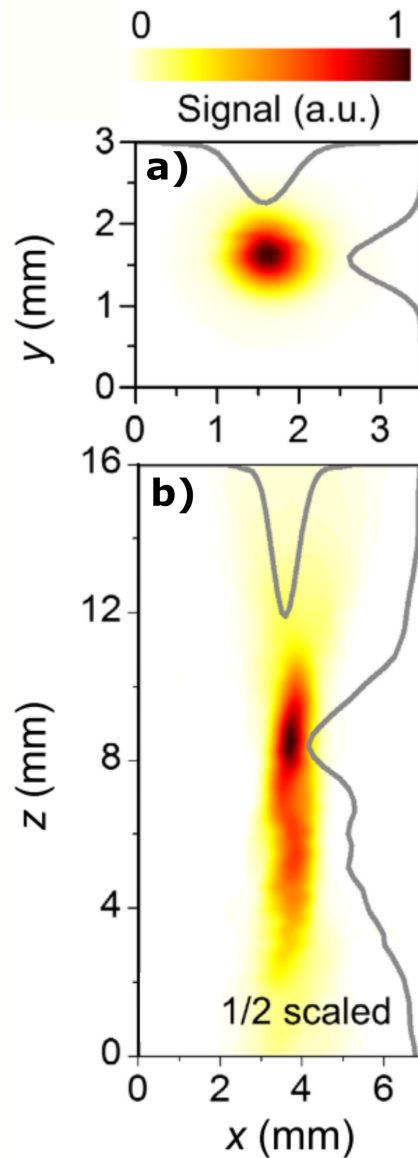


**Figure 4.15:** Focussing performance scans of a Large area MPFL used for imaging experiment. Adapted after Ref. [P2].

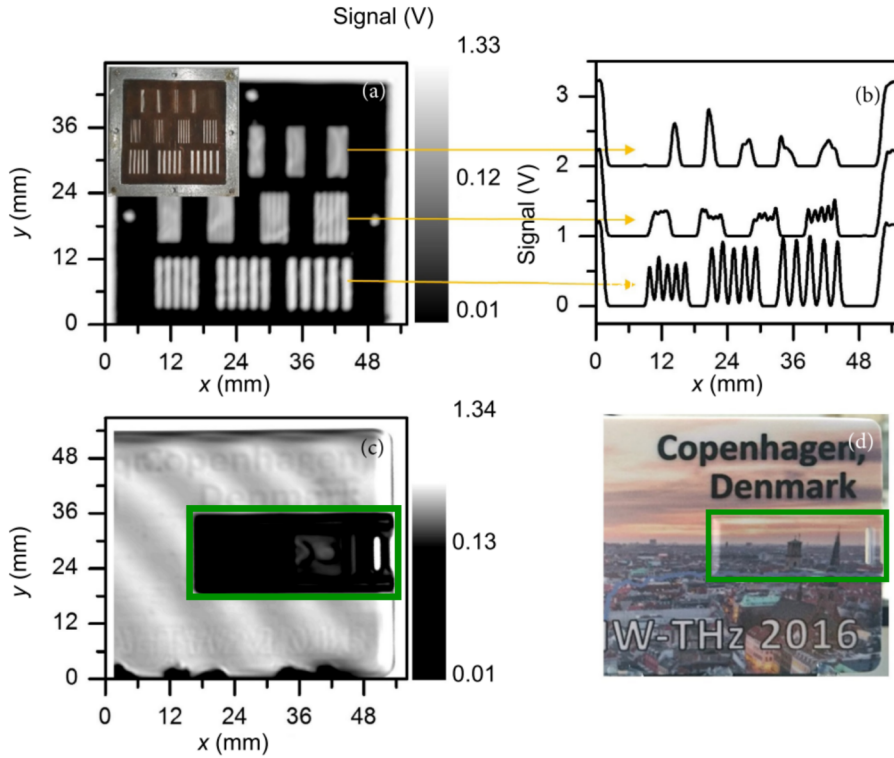


**Figure 4.16:** a) THz image of the resolution target at 580 GHz frequency obtained by a 3 cm focal distance diffractive lens. The pixel size  $0.1 \times 0.1 \text{ mm}^2$ . The image consists of  $590 \times 493$  pixels. Dark colour in the THz images corresponds to the transmittance minimum. The optical photo of the resolution target is shown in the inset. b) Cross sections of the resolution target image stripes with different periodicities. The vertical scale is shifted by 1 V for clarity. Detailed target parameters were described elsewhere [1]. c) THz image of a plastic card containing a "hidden" USB stick. The pixel size  $0.1 \times 0.1 \text{ mm}^2$ . Image consists of  $590 \times 568$  pixels. d) Optical photo of the scanned plastic card. Adapted after Ref. [P2].

Resolution target slits were experimentally observed if the slit widths were above 1 mm. The result is comparable with the one obtained by using commercial OAP mirror system. It was proved, that THz imaging is performed with much smaller and lighter optical element - MPFL, resulting in a compact and lightweight optical system.

The second target was a plastic card with an integrated flash storage. Results are shown in **Fig. 4.16**. Selected sample is interesting for security applications where hidden metallic or electronic components or structures are screened within everyday objects. Another application for shown scenario is the quality control of fabricated items and mate-

rials. Inconsistencies or foreign objects are identified in the products straight on the production line. The scanned image in **Fig. 4.16 c** clearly shows the location of hidden flash card, indicated for clarity by green rectangles. Even more, the difference in THz absorption of the dyes used for the letters shows up clearly in the scan and text from the both sides of the card could be read (interesting for applications in cultural artefact imaging [133]). The ripples observed in the resulting image are caused by standing waves formed between the object and the detector and slight misalignment of the angle of the card.

#### 4.1.5 DOE for 0.6 THz Summary

The focusing performance of all the fabricated MPFLs for 0.6 THz as well as previously reported metal zone plate are shown in **Fig. 4.17**. It can be seen from the shown beam cross sections at the focal plane that the large area MPFL has the highest FWHM of around 1.08 mm. This was caused by the fact that in the experimental geometry with 17 mm beam width and 30 mm focal length, the lens exhibited numerical aperture of 0.27 resulting in Abbe diffraction limit of around 1 mm, indicating optimal performance of the lens in given geometry. In the designed configuration of 50 mm diameter beam the large area lens was expected to have numerical aperture of 0.64 and Abbe diffraction limit around 400  $\mu\text{m}$ .

Values of FWHM for analogous  $p = 16$  PQL MPFL lenses demonstrated in a previous section, with  $f = 10$  mm and 5 mm focal lengths were of 0.57 mm and 0.43 mm with respective beam waists of 0.49 mm and 0.37 mm. The focusing performance of the latter is shown to be analogous to the one obtained for the previously reported metal binary zone plate [P1]. A comparison of all 0.6 THz MPFLs parameters is provided in the table in **Fig. 4.18**.

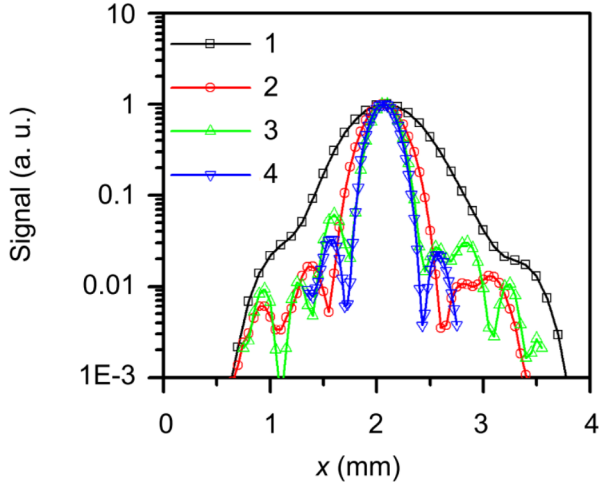


**Figure 4.17:** Comparison of normalised focused beam cross sections for different design diffractive lenses:

1 -  $p = 16$ ;  $f = 30$  mm;  $d = 50$  mm [P2]

2 -  $p = 16$ ;  $f = 10$  mm;  $d = 17$  mm [P2]

3 -  $p = 16$ ;  $f = 5$  mm;  $d = 17$  mm [P2]

4 -  $p = 1$ ;  $f = 5$  mm;  $d = 17$  mm [134]. Adapted after Ref. [P2].

$f$ , mm	NA	$P$	Subzone height, $\mu\text{m}$	$\omega_0$ , mm	$b$ , mm	$E_p$ %
10	0.65	2	139	0.45	2.84	27
		4	56	0.44	2.46	58
		8	25	0.48	3.7	71
		16	13	0.49	3.44	56
		kinoform	0.9	0.48	2.62	72
5	0.86	4	56	0.39	1.42	41
		8	27	0.35	1.18	55
		16	15	0.37	1.32	51
		32	8	0.36	1.14	66
		kinoform	0.9	0.35	1.04	65
30	0.64	16	15	0.92	4.27	93

**Figure 4.18:** Comparison of all MPFLs parameters described in the thesis for the operation in 0.58 THz frequency. NA stands for the designed numerical aperture,  $P$  is the subzone number,  $w_0$  is the achieved beam waist and  $b$  is the focal depth. Adapted after Ref. [P2].



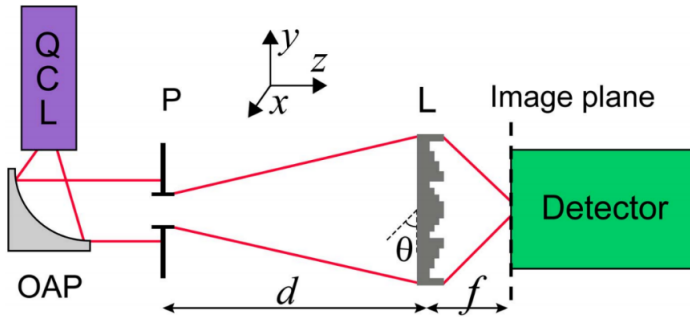


**Figure 4.19:** Schematic representation of the setup used for characterisation of 4.7 THz diffractive optics. Adapted after Ref. [P3].

#### 4.1.6 Performance of the DOEs for 4.7 THz Frequency

The focusing performance of the 4.7 THz lenses was investigated in the setup shown schematically in the **Fig. 4.19**. At the current temperature setting used for lens characterization, the QCL emitted a single mode of 4.745 THz. The iris diaphragm  $P$  was employed for spatial filtering of the QCL emission. The transmitted THz radiation was measured with an uncooled real-time microbolometric camera (pixel size of  $25\ \mu\text{m}$ ) and, alternatively, with a Golay cell detector, if the sensitivity of the camera was not sufficient. A pinhole of 1 mm diameter was used in front of the Golay cell in order to provide an appropriate spatial resolution for the measurements.

The divergence of the beam produced by the QCL was first measured in order to estimate the focusing power of the samples. The dependency of the peak beam intensity on squared reciprocal distance  $d^{-2}$  is shown in **Fig. 4.20**. Gaussian distribution of the beam profile was observed and shown at different positions in the insets of the **Fig. 4.20**. Inset shows the normalised beam profiles at selected distances of 360 and 70 mm. Beam profiles demonstrate good radial symmetry of the focused beam. An optimal position for the Focusing element was found to be at 36 cm from the aperture by investigating the FWHM dependency on the distance  $d$  with an optimal value of FWHM of  $\approx 14$  mm.

The focusing performance for all of the lenses is shown in the **Fig. 4.21**. Good radial symmetry was observed as seen in the inset of the figure with a much smaller diameter as compared to the unfocused beam in **Fig. 4.20**. cross sections of the measured beams were extracted

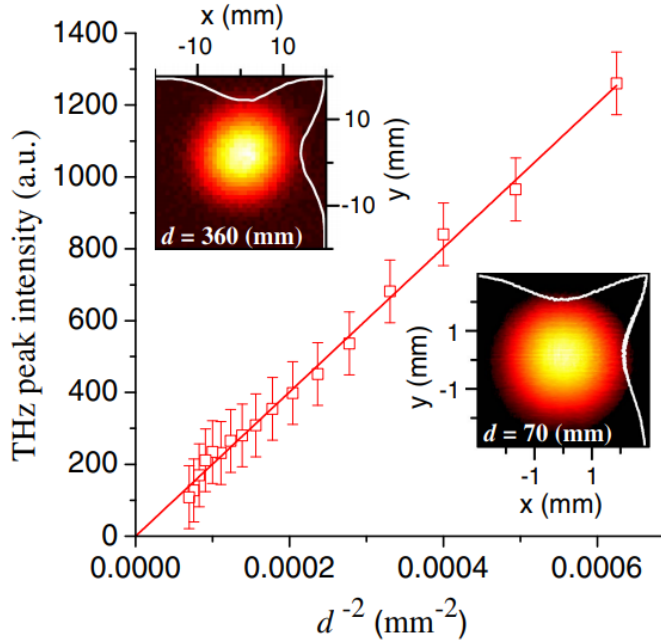


**Figure 4.20:** Beam intensity dependence on the distance after the pinhole ( $P$ ). Inset: beam profile at selected distances to demonstrate a Gaussian radial symmetry. Adapted after Ref. [P3].

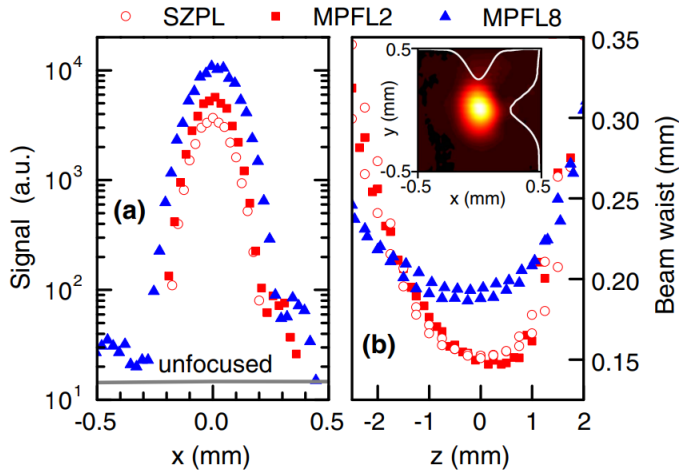


**Figure 4.21:** a) Beam intensity cross sections at the focal plane for different design lenses (b) change of the waist width in direction of the focal depth of different samples. Inset: the beam profile at the MPFL2 focal plane. Adapted after Ref. [P3].

Sample	$f$ [mm]	$G_f$ (Exp.) [dB]	$G_f$ (Theor.) [dB]	Beam waist [mm]
SZPL	56	24	26	0.15
MPFL2	55	25	28	0.15
MPFL8	76	29	32	0.18

**Table 4.1** : Focussing performance parameters listed for the diffractive lenses working at 4.7 THz.

and compared in the **Fig. 4.21 a**. The measured beam intensity distributions allowed to estimate the focusing gain values of 262 (24 dB), 348 (25 dB), and 804 (29 dB) for the SZPL, MPFL2, and MPFL8 samples, respectively. Similar beam widths were observed for ZSP and MPFL2 samples at 0.15 mm, while beamwidth of MPFL8 was slightly larger at 0.18 mm. Focussing parameters of the lenses are summarized in **Table 4.1**. As-measured results are displayed without deduction of possible optical losses of the lenses.

The maximum efficiency of the focusing is known to be around 10% for the Soret zone plates [57]. Nevertheless, these components are interesting for certain applications. In the case of the Soret zone plate with  $f \gg \lambda$ , the theoretical focusing gain can be approximated with an analytical expression [57] as  $G_{SZPL} = N_{OPEN}^2$ . The number of effective zone numbers in SZPL is limited by axial spherical aberrations, which become prominent with an increasing number of zones. The maximum zone number without notable spherical aberrations is given by:  $n_a = (2f/\lambda)^{1/2}$ , giving a value of a maximum of 40 total zones for the investigated design. The fabricated sample had  $n_{OPEN} = 25$  and therefore exhibited some spherical aberrations amounting to 2 dB reduction of the focusing gain. Even taking this into account another 2 dB reduction of focusing gain was observed in the experimental result as compared to the theory.

The discrepancy of experimental SZPL focusing gain was investigated by checking the SZPL dimensions using a calibrated optical microscope. It was found, that the zone radii in the fabricated sample were offset from the designed parameters by an average of  $25 \pm 9 \mu\text{m}$  with the discrepancy of the radii more strongly pronounced for outer-most zones. It is believed that this difference of radii might have led to the observed additional 2 dB reduction of the focusing gain and change of

optimal frequency in accordance to Eq. 2.1. It is speculated that this discrepancy might have happened due to the thermal expansion and deformation of the metal foil during the fabrication process. The optimisation of the fabrication step or sample cooling in a large scale fabrication process would prevent the discrepancy of the zone radii.

This was the first time when viable THz SZPLs were produced out of metal foil for the upper branch of the THz band. Even more, the applicability of direct laser ablation for the fabrication of said elements with good performance was demonstrated. No critical losses associated with the Soret zone plate fabrication process were observed indicating that even higher frequency components might be fabricated using DLA.

In the case of MPFL2 (binary lens) the theoretical maximum efficiency rises to 40%, which is 4 times larger than that of the SZPL. Experimental results show that only 1 dB increase in  $G_f$  was observed for MPFL as compared to the experimental SZPL. This reduction of the gain was attributed to the reduced transmission of laser ablated Si. Transmission reached only 40% at the operational frequency caused by the increased optical absorption Si as well as the reflection due to high refractive index of crystalline Si. Overall optical losses are seen to amount for 4.1 dB reduction in the efficiency which was deduced in the theoretical value represented in the **Table 4.1**. A difference of 3 dB between the experimental and the deduced theoretical result was still observed for both of the MPFL samples. This difference was 1 dB larger than the one observed for the SZPL sample due to the possible shadowing of the zones [57]. A leftover 2 dB difference was attributed to the fabrication imperfections as was in the case of SZPL. Increase of PQLs from 2 to 8 increased the focusing gain by 4 dB. The experimental value of 29 dB ( $\approx 800$  times) was a largest value of experimental focusing gain at the time of publication.[P3] Introduction of additional levels increased the focusing gain around 10 dB as compared to our results reported for Si MPFLs in the previous chapter or TPX [63].

The diameter of the focused spot was in accordance with the theoretical prediction for SZPL and MPFL2 at 0.15 mm. A larger diameter of the spot at 0.18 mm as well as a 20 mm longer focal length (at 70 mm), was observed for the MPFL8 sample. The difference was attributed to the fabrication process of the samples. While in the case of MPFL2 the

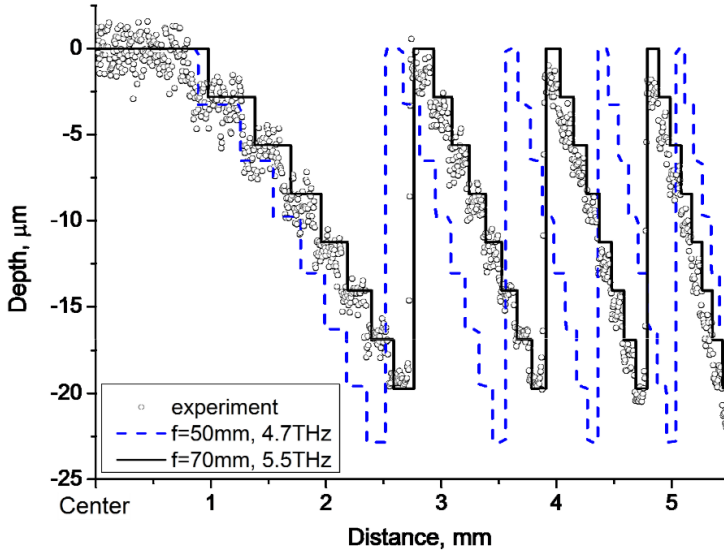


**Figure 4.22:** Depth profile for the MPFL8 sample measured (dots) and calculated at original (dashed line) and modified (solid line) design parameters. Adapted after Ref. [P3].

cross section of the fabricated sample was close to the theoretical design (as can be seen in **Fig. 4.7**), a much larger deviation was observed for MPFL8. The step profiler results and designed profile of MPFL8 sample are shown in the **Fig. 4.22**. In fact, upon closer inspection and subsequent design recalculation, it was found that the experimental sample more closely matches a MPFL design for 5.5 THz frequency and 70 mm focal depth. Nevertheless, the use of DOE with record high efficiency at 4.7 THz frequency was demonstrated.

Finally, in order to demonstrate that the laser fabricated elements are easily applicable in practice, the elements were measured at different tilt angles. The sample was put on a rotation stage; the focusing results are shown in **Fig. 4.23**. The focused signal was integrated in the focal plane and the value normalized to the value of normal incidence plotted in dependence to the tilt angle in order to have a quantitative evaluation of the performance. It was found that the performance was analogous for all of the fabricated samples. The signal did not show a significant drop for angles below  $10^\circ$  with notable 40% drop of integrated signal at  $15^\circ$  angle. The inset in the **Fig. 4.23** shows the maximum signal value on the  $z$  coordinate for different tilt angles of MPFL8, which also supports

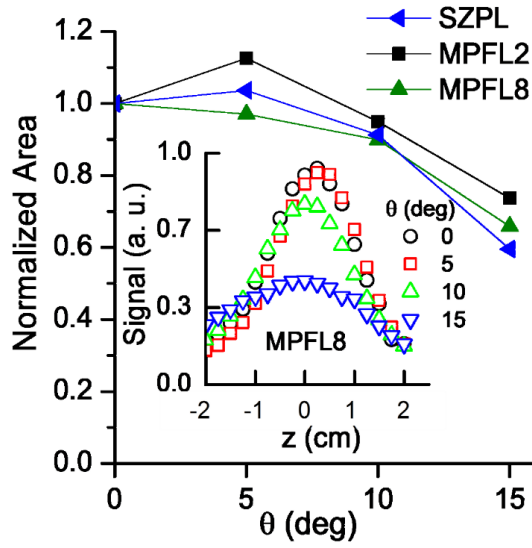


**Figure 4.23:** Normalized area under the curve obtained measuring the intensity dependence along an optical axis (as shown in the inset). Inset: the dependence of the beam amplitude focused with the MPFL8 on the distance at different values of the incident angle. Adapted after Ref. [P3].

the proposition that a tilt angle below  $10^\circ$  does not strongly influence the focusing performance.

## 4.2 Surface Relief Grating Couplers for SPP<sub>h</sub>P Excitation

The process of designing, fabricating and characterizing an optimized SPP<sub>h</sub>P absorber/thermal emitter based on a surface relief grating (SRG) is described in this chapter. The material of choice for the device fabrication was GaN due to its high electrical, mechanical and thermal robustness as well as wide RB region. Due to the limitations of the spectral range of an undoped semiconductor as well as a large amount of research carried out in SPP<sub>h</sub>P in GaN as well as other semiconductors, a highly doped substrate was chosen. The dielectric function and reflectivity spectra of an unpatterned undoped and doped GaN substrate, demonstrating the increase of the operating range of negative real part of dielectric function (region of high reflectivity), are shown in **Fig. 2.13**.

The spectra of an unpatterned sample are first investigated experimentally and used for the fitting of the dielectric function parameters for further SRG calculations. Calculations of surface relief gratings of various geometry were carried out and used to design an SRG coupler for *n*-GaN surface. Selected SRG designs were then used for the calculation of its angular reflectivity behaviour. The selected geometry samples were then fabricated, and the reflectivity at a fixed incidence angle is reported. At the next stage angular reflectivity of all samples was measured and compared to theoretical results. Finally angular emission from thermally excited sample was investigated and the results were used for the estimation of polariton coherence length and emitted power.

### 4.2.1 Surface Relief Grating Samples

Samples were fabricated on highly doped bulk GaN substrate using UV photolithography and a custom design, commercially fabricated photo-mask. The substrate had the doping level of around  $1.55 \times 10^{19} \text{ cm}^{-3}$ . The Surface Relief Grating (SRG) was formed on the surface of the semiconductor itself. A photolithography mask with several different grating areas was designed and commercially fabricated. Processing was carried out in the UNIPRESS using stan-

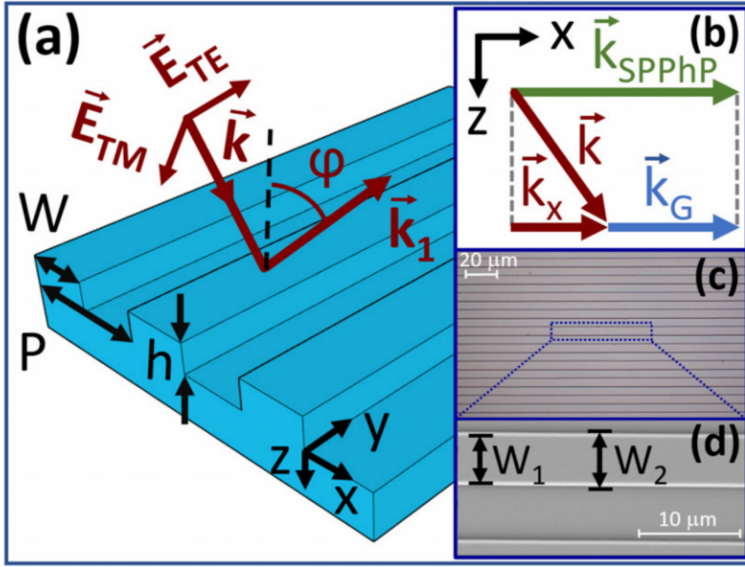


**Figure 4.24:** **a)** The geometry and experimental scheme of SRG coupling experiment.  $W$ ,  $P$  and  $h$  are the geometrical SRG parameters of grating ridge width, period and height respectively.  $k$  and  $k_1$  are the wavevectors of incoming and reflected light, having electric field orientation  $E_{TE}$  in parallel to the grating ridges in TE polarisation and  $E_{TM}$  electric field component lying in the incidence plane (with a component perpendicular to the grating) in TM polarisation. **b)** illustration of the wavevector matching condition according to Eq. 2.35.c) and **d)** SEM images of an experimentally fabricated sample with ridge top width  $W_1$  and ridge bottom width  $W_2$  marked. Adapted after Ref. [P4].

standard UV photolithography and reactive ion etching techniques. The fabrication quality was investigated using profilometry, SEM and AFM measurements. Four SRG designs were chosen for fabrication. These had periodicities  $P$  of 8, 11, 16 and 22  $\mu\text{m}$  and the depth of  $h = 1 \mu\text{m}$ . Three designs were chosen for this work (SRG-1 - SRG-3 in **Table 4.3**), having periodicities  $P = 11, 16$  and 22  $\mu\text{m}$  respectively. All of the samples had the designed filling factors of 50% (with  $W = 5.5, 8$  and 11  $\mu\text{m}$  for SRG-1 SRG-2 and SRG-3, respectively) and the depths of  $h = 1 \mu\text{m}$ .

Surface roughness values were found for the fabricated samples using atomic force microscopy. RMS roughness was around 0.42 and 0.62 nm at the unprocessed and processed surfaces respectively.



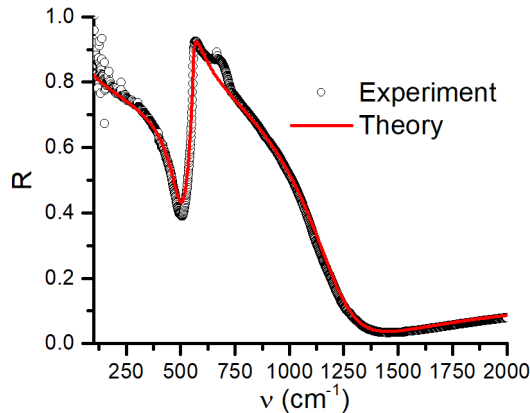


**Figure 4.25:** Experimentally measured and theoretically fitted unpolarised reflectivity spectra of a flat  $n$ -GaN wafer.

#### 4.2.2 $n$ -GaN Substrate Reflectivity

The calculations of the reflectivity spectra were carried out using the RCWA code. Three main layers were simulated in the case of  $n$ -GaN SRG structures, namely  $100\ \mu\text{m}$  thick air,  $h\ \mu\text{m}$  thick grating layer and finally, a  $300\ \mu\text{m}$  thick doped GaN substrate layer. Calculation of the reflectivity spectra of unpatterned sample and fitting of the spectra to the one measured experimentally allowed to evaluate the parameters of the dielectric function of the material. Values of optical phonon damping as well as damping and frequency (doping level) of free carrier plasmons were found. It must be noted that due to strong damping by the free carrier plasmons, the damping of LO phonon was not possible to evaluate, therefore its value was chosen equal to  $\gamma_{TO}$ . Experimental and theoretical unpolarised reflectivity spectra are shown **Fig. 4.25**. Note the excellent agreement between the experimental and fitted results in a wide frequency range, with one small deviation of a reflectivity increase feature of unknown origin in the experimental spectrum. Investigation of the possible nature of this feature in literature did not yield any results, therefore it was not dealt with in further analysis.

Best-fit parameters used in the calculation are listed in the **Table. 4.2**. These parameters corresponded well with the values reported previously in ellipsometry [94] and reflectometry [12, 81] [P4]. Fitted value of the plasmon frequency and the corresponding doping level

Parameter	$\epsilon_\infty$	$\nu_{TO}(\gamma_{TO})$ [cm <sup>-1</sup> ]	$\nu_{LO}(\gamma_{LO})$ [cm <sup>-1</sup> ]	$\nu_P(\gamma_{LO})$ [cm <sup>-1</sup> ]
Best fit value	5.3	557 (7)	739 (7)	1140 (390)

**Table 4.2** : Best fit parameters of the *n*-GaN reflectivity fitting.

of  $1.55 \times 10^{19} \text{ cm}^{-3}$  coincided well with the sample growth protocol supplied by the manufacturer. The plasmon frequency at this level of doping was at around  $1140 \text{ cm}^{-1}$  and allowed to achieve the operational regime of interest, where  $\nu_P > \nu_{LO}$  and overdamping as well as strong increase of the region of negative permittivity of the semiconductor was achieved. Due to large plasmon frequency, the whole region of interest exhibited transmission coefficient of  $T=0$ . It may also be worth noting that the damping of the plasmon ( $390 \text{ cm}^{-1}$ ) is much higher than the one for phonons ( $7 \text{ cm}^{-1}$ ) corresponding to the data in literature, described in the beginning of this chapter. It is also noteworthy, that phonon damping is indicative of the material structure quality, and, damping value of  $7 \text{ cm}^{-1}$  indeed indicates high quality of highly doped *n*-GaN wafer.

### 4.2.3 Design of the SRG Coupler

In the first step of the investigation of SRG coupled *n*-GaN polaritons, the reflectivity spectra dependence on the grating height and period were calculated. With some *a priori* knowledge of several different simulations in *n*-GaN system a starting SRG coupler design was chosen to have around  $1 \mu\text{m}$  depth and around  $10 \mu\text{m}$  periodicity in order to realize SPPPh coupling. A calculation of reflectivity spectra dependence on the geometrical parameters was expected to allow the design to be optimized for optimal SP coupling. A filling factor value of 50% ( $P = 2 \times W$ ) was chosen for the coupler.

In calculating the reflectivity of the *n*-GaN SRG, thirty Fourier expansion orders were, used providing sufficiently good convergence condition. The convergence was tested by calculating the root mean square (RMS) error of the calculated reflectivity against the values obtained by using 50 Fourier orders and finding that the RMS value does not exceed 0.4% in the entire calculation region.

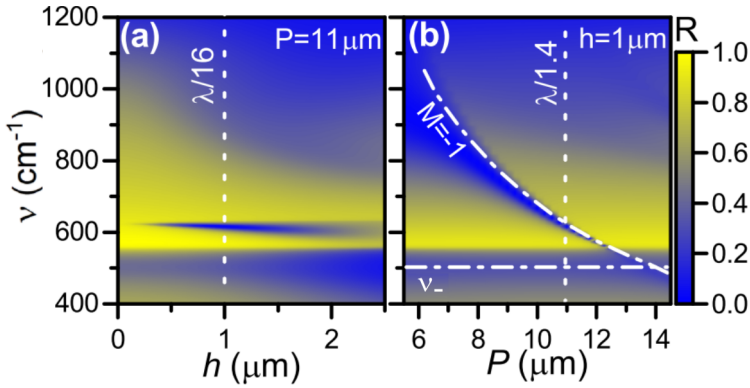


**Figure 4.26:** Calculated reflectivity spectra dependence on the geometrical parameters of the surface relief grating at the incidence angle of  $26^\circ$ . **a)** dependency on grating height  $h$  at fixed period of  $11 \mu\text{m}$ . **b)** dependency on grating period at fixed height of  $1 \mu\text{m}$ . **b)** also shows the frequency of  $\nu_-$  (according to eq. 2.34) and dispersion of SPPHP feature according to the analytical solution of the real part of dispersion equation system. Adapted after Ref. [P4].

The dependence of the reflectivity spectra of  $11 \mu\text{m}$  period grating on its height  $h$  was first calculated at the experimentally important incidence angle of  $26 \text{ Deg}$ . Results of the calculation in the region of  $0 < h < 2.5 \mu\text{m}$  are presented in the **Fig. 4.26 a**. A feature was observed in the results at around  $615 \text{ cm}^{-1}$ , the centre frequency slightly decreasing with the height increase of the grating. Optimum value of  $h$  was found to be at  $1 \mu\text{m}$  (indicated by a line in the figure) as narrow feature with reflectivity dip down to  $\approx 0\%$  was observed. The frequency of the feature corresponded to a wavelength of around  $16 \mu\text{m}$ , therefore indicating subwavelength  $h \approx \lambda/16$  operation regime of the SRG. With  $h$  being below  $1 \mu\text{m}$  the height was insufficient to efficiently diffract the radiation, while increasing  $h$  above  $1 \mu\text{m}$  deteriorated the scattering of the light and degrading SPPHP coupling efficiency.

Upon calculating the dependence of the optimal  $h = 1 \mu\text{m}$  depth SRG reflectivity on its period, strong tuning of the SP feature was observed as predicted by the wavevector matching condition in Eq. 2.35. Calculation results are shown in **Fig. 4.26 b**. Tuning of the feature frequency is predicted in the whole expanded reflectivity region from  $\nu_{TO}$  at  $557 \text{ cm}^{-1}$  to the  $\nu_P$  at around  $1140 \text{ cm}^{-1}$ . Strong reduction of the SP feature width is also observed with the drop of its frequency indicating a strong reduction of the SP damping when closing to the TO phonon. Periodicity of  $P = 11 \mu\text{m}$  (indicated by vertical dashed line) was chosen for the proof

of principle sample design (named SRG-1) due to almost total reflectivity dip of the narrow SP feature at  $615 \text{ cm}^{-1}$ . In order to identify the nature of the observed feature a calculation was carried out by solving the real part of 2.28, 2.33 and 2.35 equations, obtaining the predicted dispersion of  $M = -1$  SPPHP mode (dash dotted line in **Fig. 4.26 b**) following closely the modelled feature. Some shift in the precise frequency of the SPPHP is observed due to the fact that analytical solution did not take into account the damping of oscillations as well as the shape of the SRG.

To conclude, the calculated reflectivity spectra dependence on the geometric grating parameters presented in this section, allowed for the selection of optimal SRG coupler geometry. Proof of principle SRG design was chosen with the height of  $h = 1 \text{ }\mu\text{m}$  and the period of  $P = 11 \text{ }\mu\text{m}$  and named SRG-1. Designed SRG-1 was predicted to exhibit a strong SPPHP feature of  $M = -1$  mode at the designed frequency of  $615 \text{ cm}^{-1}$  and incidence angle of  $\varphi = 26^\circ$ .

#### 4.2.4 Calculation of *n*-GaN SPPHP Dispersion

In order to obtain more insight into the behaviour of SPPHPs full analytical solution of the SP dispersion was implemented. Use of a single material allowed for the analytical calculation of SPPHP dispersion according to the equation system of Eqs. (2.28), (2.33) and (2.35) in addition to rigorous RCWA calculation. Expected frequencies as well as the corresponding losses could be estimated using the analytical solution without rigorous modelling when taking into account the complex nature of permittivity and SPPHP frequency. Nevertheless, reports on this kind of solution are absent due to the complex nature of the dielectric function and either the frequency or wavevector, and only the prediction of the real part of the solution i.e., the plasmon frequencies, are usually estimated.

In the reported calculation, the wavevector was estimated to be real, and the complex frequency  $\omega'(k)$  and damping  $\omega''(k)$  ( $\omega = 2\pi\nu$  being the cyclic frequency) were calculated. Dielectric function parameters based on the fitted results in the **Table 4.2** were used for this calculation. The equation 2.28 i.e. the SP dispersion, forms a third order algebraic

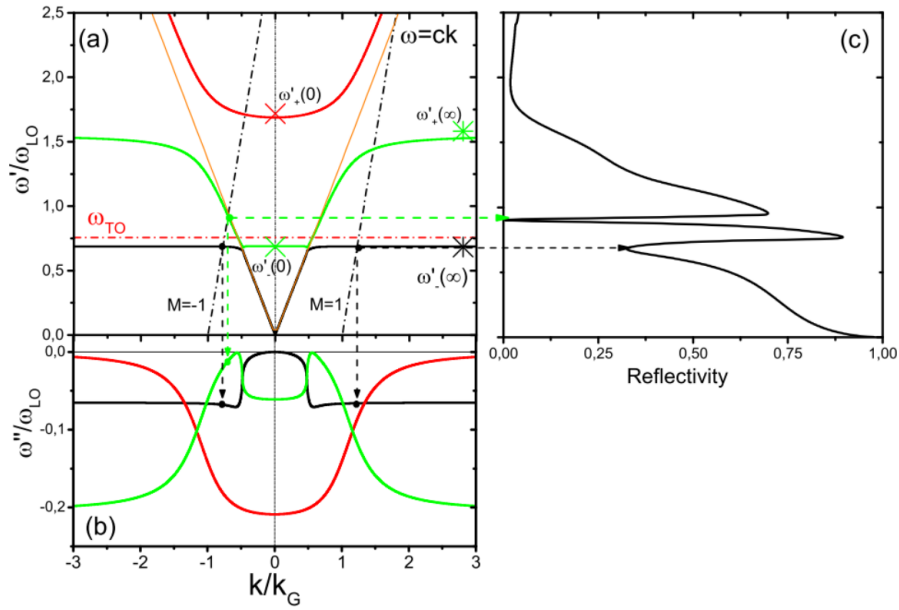


**Figure 4.27:** Dispersion of the SPPPhPs on the surface of *n*-GaN **a)** the dispersion of the SPPPhPs frequency on the wavevector. **b)** calculated damping factor function on the feature frequency. **c)** RCWA calculated sample spectrum with a SRG of 1  $\mu\text{m}$  depth and 10  $\mu\text{m}$  period at the incidence angle of 26 deg. More details are given in Ref. [P5]. Adapted after Ref. [P5].

equation in respect of frequency when the dielectric function of a semiconductor in equation 2.33 is taken into account. Therefore, 3 branches of solutions (modes) are obtained for given wavevector  $k$ . These solutions (branches) are illustrated in the **Fig. 4.27 a)** by red green and black curves. Dimensionless wavevector  $k = k/k_G$ , and frequency  $\omega = \omega/\omega_{LO}$  were chosen for the representation.

For each value of  $k$  of the respective branches, the damping factors were also calculated and shown in the **Fig. 4.27 b)**. Exceptionally small damping resulting in high quality features is expected in the hybrid (green line) SPPPhP branch as well as in the bottom (black line) SPP-like branch. The latter regime of SPP excitation has already been investigated in a recent publication [135]. In this publication, while SPP excitation under the nonequilibrium condition was demonstrated, it was weak and most likely due to the limitations of the experimental setup and nominally sharp feature dampening by the angular aperture.

The hybrid SPPPhP branch (green line) is the most interesting in view of this work with with the excitation of the resonant features at and

above the RB of GaN. With the variation of the wavevector tuning of SPPPhP frequency is seen to be possible in the frequency range of  $\omega_-$  to  $\omega_+$ . The asymptotic frequencies of  $\omega_-$  and  $\omega_+$  also correspond to the anticrossing points of different branches indicating their strong interaction. When taking note of the predicted damping of the hybrid SPPPhP mode it can be seen that with the decrease of the  $k$ , damping value gradually shifts from that of the plasmon down to very low values near the TO phonon, therefore also predicting a strong SPPPhP quality factor dependence on its frequency and a transition from a plasmon polariton like behaviour to the phonon polariton like one.

The radiation coupling (wavevector matching) condition described in Eq. 2.35 is also shown as a dash dotted line with the intercept points giving the polariton frequencies  $\omega'$ . It can be seen that the analytically predicted crossing point coupling frequencies coincide well with a RCWA modelled result in the **Fig. 4.27 c**.

Dispersions of SRG-1, SRG-2 and SRG-3 gratings, calculated using the RCWA method, are demonstrated in reflectivity ( $r = r(\nu, k_x)$ ) and emissivity ( $e = e(\nu, k_x)$ ) dependencies on the  $k_x = k_0 \sin(\varphi)$  wavevector component in **Fig. 4.28**. At  $0^\circ$  incidence angle, corresponding to  $k_x = 0$  and  $k = k_G$  (also corresponding to straight vertical line (not shown) at  $k_G$  wavevector in **Fig. 4.27 a**), the SPPPhP feature is observed at frequencies near respective  $k_g$  values of the SRGs listed in **Table 4.3**. The reflectivity results of different SRGs at a fixed  $0^\circ$  incidence angle therefore represents the tunability of SPPPhPs via the period of SRG. Corresponding feature FWHMs follow the trend predicted by the analytical dispersion calculations in **Fig. 4.27 b** with largest FWHMs (losses) at high frequencies, minimum at around the frequency of TO phonon and once again increased losses below the TO frequency. The FWHM are associated with the quality factor of the resonance  $Q$  as  $Q = Q(\nu_{SPPPhP}, \varphi) = \nu_{SPPPhP} / FWHM$  also listed for the case of 0 deg incidence in **Table 4.3**.

Each of the modes reported in **Table 4.3** splits into a  $M = -1$  and a  $M = +1$  SPPPhP modes upon introduction of  $k_x$  wavevector with the increase of incidence angle. In the **Fig. 4.27 a** this corresponds to increasing incline towards  $k = 0$  ( $M = -1$ ) or  $k = \infty$  ( $M = +1$ ) of the line representing the wavevector matching condition. In the case of SRG-1  $M = -1$  mode covers almost all of the extended RB with SPPPhP linewidth de-

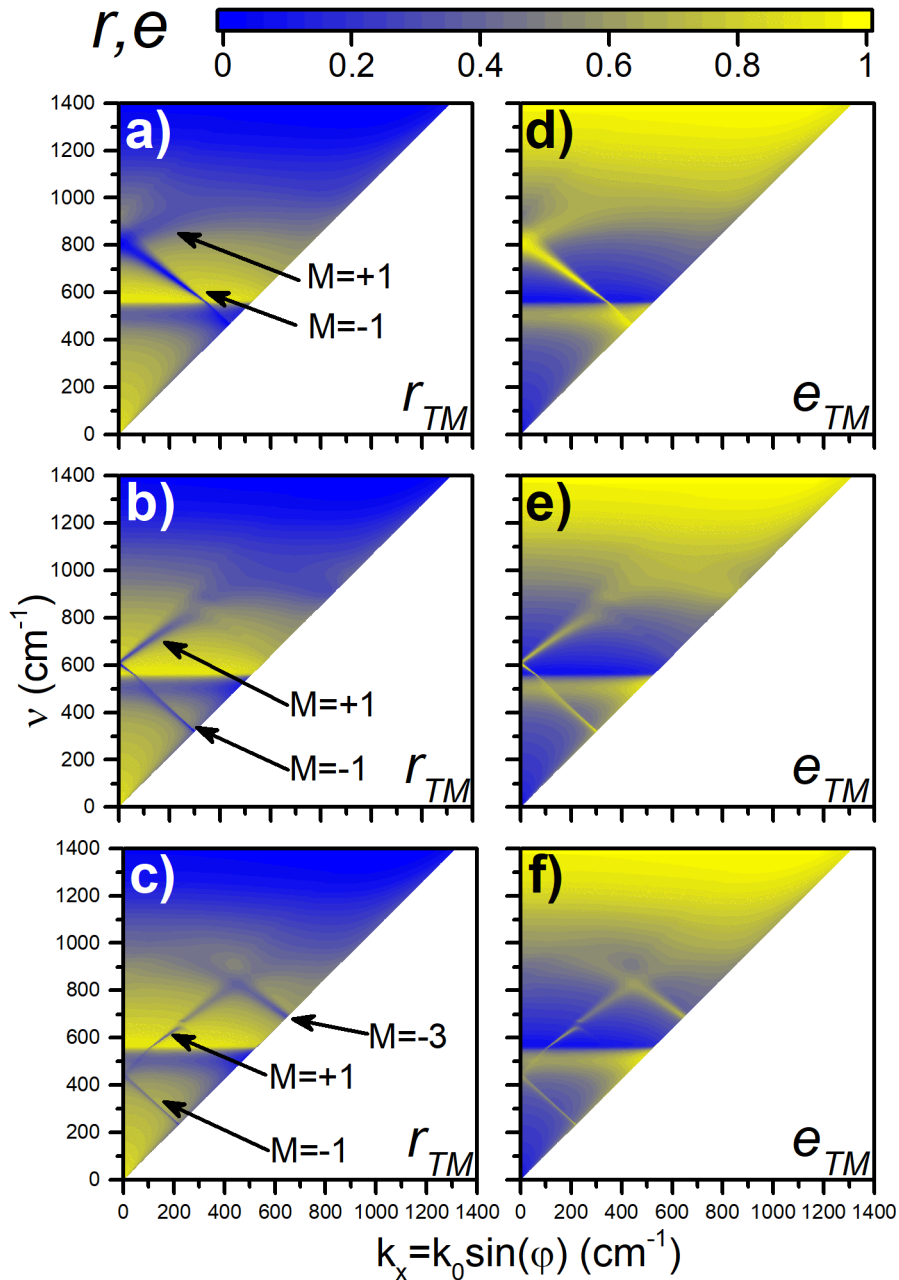


**Figure 4.28:** RCWA calculated, TM polarized, reflectivity (a-c) and emissivity (d-f) dependencies on the in plane component  $k_x$  of the incoming light wavevector  $k_0$  for SRG-1 (a,d), SRG-2 (b,e) and SRG-3 (c-f) structures.

Sample	Period [ $\mu\text{m}$ ]	$k_G$ [ $\text{cm}^{-1}$ ]	$\nu_{\text{SPP}hP}$ [ $\text{cm}^{-1}$ ]	$FWHM$ [ $\text{cm}^{-1}$ ]	$Q$
SRG-1	11	909.1	808	122	6.6
SRG-2	16	625	606	16	37.8
SRG-3	22	455.5	442	32.5	13.6

**Table 4.3 :** SPP $hP$  feature parameters calculated at normal incidence of ( $\varphi = 0^\circ$ ).

creasing monotonically down to the TO frequency. Meanwhile  $M = +1$  mode spans above  $800 \text{ cm}^{-1}$  frequency and is hardly observable in TM polarized spectra in current representation due to low overall reflectivity near the plasmon edge and relatively large linewidth of hybrid SP-PhP mode.

In the case of SRG-2 and SRG-3, both of the  $M = -1$  and  $M = +1$  modes are clearly observable with the SP both in SPP $hP$  regime above TO phonon and SPP regime below it in **Fig. 4.28 b)** and **c)**. It was also noticed that  $M = -2$  is not observed as its excitation is prohibited by the selection rules. An additional anticrossing feature was also observed at the frequency of  $\nu = 844 \text{ cm}^{-1}$  and wavevector value of  $k_x = 306 \text{ cm}^{-1}$  in SRG-2 result. An anticrossing feature indicates existence of hybridized SPP $hP$  interaction with another oscillation mode, nature of which is not known at this point of the research. This unspecified mode is linked with the geometry of the SRG as a respective anticrossing is observed at  $\nu = 655 \text{ cm}^{-1}$  and wavevector value of  $k_x = 230 \text{ cm}^{-1}$  for SRG-3. In this case the anticrossing is observed more clearly due to notably smaller linewidth of an SPP $hP$ . Finally  $M = -3$  mode is also observed in the result of the SRG-3 crossing with  $M = +1$  mode without notable interaction.

#### 4.2.5 SRG-1 Reflectivity at Fixed Incidence Angle

The SRG-1 sample design was chosen for the experimental fabrication of proof of principle sample in order to demonstrate SPP $hP$  excitation. SEM images of a sample fabricated using the RIE procedure are displayed in the **Fig. 4.24 c)** and **d)**. Upon SEM inspection, it was observed that the experimental sample demonstrated a slight incline of the sidewalls, which is a common imperfection in the RIE procedure using a



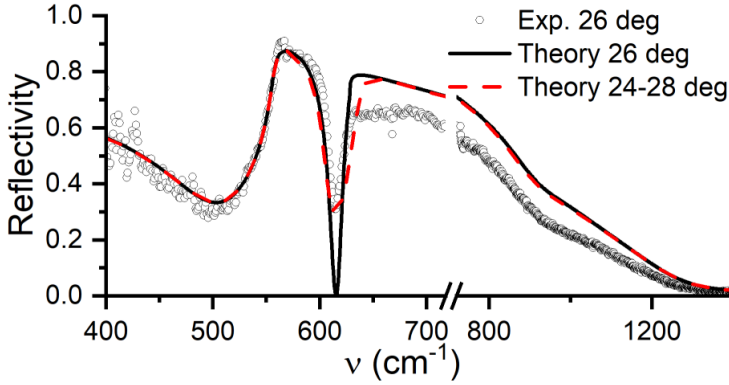


**Figure 4.29:** Measured (dots) and calculated (lines) reflectivity spectra of SRG-1 sample at the incidence angle of  $26^\circ$ . Solid curve represents the calculated spectrum at a discrete incidence angle, while dashed curve represents spectra average between  $24^\circ$  and  $28^\circ$  in  $0.5^\circ$  steps. Adapted after Ref. [P4]

UV photoresist. The SRG ridges were observed to have the top width of  $W_1 = 4.9 \mu\text{m}$  and bottom width of around  $W_2 = 5.7 \mu\text{m}$  and the same width differences were observed for other periodicity gratings. This was taken into account in the calculation by approximating the grating by 5 sub-layers, widths of which were incrementally increased from  $W_1$  to  $W_2$ . Due to the SRG working in the strongly subwavelength regime ( $\lambda/h \approx 16$ ) introduction of the incline only shifts frequency of the feature by roughly  $2 \text{ cm}^{-1}$  with negligible effect to its strength according to calculations. Surface roughness was also shown to be minimal after AFM measurement demonstrating RMS roughness around 0.42 and 0.62 nm at the unprocessed and processed surfaces respectively. Therefore, it was shown that the RIE limitations in the fabrication of SRG-1, and by extension other SRG designs, are not critical.

Reflectivity of a fabricated SRG-1 coupled  $n$ -GaN in TM polarization at a fixed  $26^\circ$  incidence angle is shown in **Fig. 4.29** by circles and line for the experimental and theoretical spectra respectively. As one can immediately notice, there is a strong feature of reflectivity dip in the measured as well as calculated spectra at round  $615 \text{ cm}^{-1}$  in accordance with the feature prediction. A theoretically calculated reflectivity at a discrete  $26^\circ$  incidence angle predicts the reflectivity dip at almost 0%, while the experimental result shows reflectivity dropping to around 30%. This discrepancy was attributed to the existence of an angular aperture in the experimental setup. An angular aperture (range of incidence an-

gles) exists due to the fact that the incident beam is focused on the sample area instead of being collimated. This is done in order collect the maximum signal for measurements by the FTIR spectrometer, and this geometry is schematically illustrated in **Fig. 3.6 b**. The range of angles was limited using a 7 mm diameter circular aperture at around 10 cm optical axis distance from the sample, therefore limiting incident angles to  $\varphi \pm_A \varphi$  to  $26 \pm 2^\circ$  in the case of reflectivity measurement (**Fig. 3.6 b**). As a first order approximation, reflectivity spectra were calculated for incidence angles of  $24^\circ$  to  $28^\circ$  and then averaged resulting in the dashed curve in **Fig. 4.29**. This averaged spectrum is shown to represent the amplitude of the measured feature quite well. It shows that the most probable cause of reflectivity deviation from the predicted result is not some error in sample fabrication or a limitation of operation physics, but the specifics of the experimental setup instead. Therefore, a much stronger reflectivity dip is expected for a large area optical element working with a collimated light beam.

Quality factor  $Q = \nu / FWHM_\nu$  of the SPP<sub>h</sub>P excitation was estimated to be of 27 in the case of experimental and 40 in the theoretical results (with respective feature FWHM values of  $23 \text{ cm}^{-1}$  and  $15 \text{ cm}^{-1}$ ).

An issue of notable reflectivity magnitude decrease at frequencies above the SP feature was observed. Although the reflectivity decrease is not critical and is limited to around 10 %, it is persistent across the whole region above the SP and therefore probably is not related to experiment noise or errors. Most probable reason for such spectral behaviour is the fact that 30 diffraction orders are included in the calculation with all of their diffraction efficiencies summed up. Meanwhile, the experimental spectrum is limited in the view of diffracted orders, due to small angular width of the radiation collection window and higher diffraction order light not being collected. Further investigation is needed in order to check this assumption.

#### 4.2.6 SRG Reflectivity on the Incidence Angle

The dependence of the SRG reflectivity on the incidence angle was investigated experimentally. Bruker Vertex V70 spectrometer was implemented in the experimental investigation of *n*-Ga<sub>N</sub> as described in

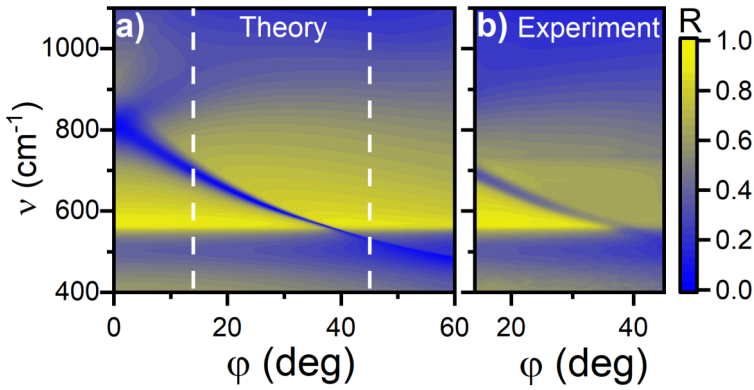


**Figure 4.30:** Theoretical (a) and experimental (b) SRG-1 sample reflectivity spectra dependence on the incidence angle. Vertical dashed lines in the calculated plot corresponds to the angle range of the measurement. Adapted after Ref. [P4].

the section 3.4. The calculated reflectivity results of SRG-1 sample (for TM polarization) as  $r_{TM}$  and measurement result (as reflectance ratio  $R = P_{SR}/P_{OR}$  between respective sample and gold mirror measured spectra) are displayed in **Fig. 4.30 a** and **b** respectively. The experimental range of measured angles is indicated by the vertical dashed lines in **Fig. 4.30 a**. Reflectivity features caused by the phononic processes (increased reflectivity at the  $\nu_{TO}$  of  $559 \text{ cm}^{-1}$  followed by monotonic reflectivity decrease towards  $\nu_+$ ) above  $1000 \text{ cm}^{-1}$  as well as the polaritonic feature (reflectivity dip line at  $800 \text{ cm}^{-1}$  at  $0^\circ$  incidence shifting to  $560 \text{ cm}^{-1}$  at  $37^\circ$  incidence) were observed closely following the calculated TM polarized reflectivity spectra. Additional limiting of the angular aperture was not possible in this setup and therefore slightly weaker experimental feature was observed in the result demonstrated in the **Fig. 4.29**. While reflectivity dip down to 30% was observed at set angle ( $26^\circ$ ) experiment (first experimental setup), dip down to 44% was observed in the angular measurement (second experimental setup), at the same angle. Nevertheless a good agreement between the experimental and theoretical results was obtained in respect of the spectral SPPHP feature position and its angular behaviour. Modelling procedure was therefore validated to be successfully used for designing SPPHP based components.

For the proof of principle sample of SRG-1 at the normal incidence ( $0^\circ$  incidence angle) reflectivity dip to 0% is observed at the frequency

of  $808\text{ cm}^{-1}$  in theoretical spectrum (see **Fig. 4.30 a**). The feature in reflectivity spectrum splits into two  $M = +1$  and  $M = -1$  modes with the introduction of non-zero incidence angle. The modes behave differently with mode frequencies and linewidths increasing and decreasing with the increase of incidence angle for  $M = +1$  and  $M = -1$  modes respectively. The linewidth of SPPPhP mode dropped from  $120\text{ cm}^{-1}$  at  $800\text{ cm}^{-1}$  to  $6\text{ cm}^{-1}$  at  $560\text{ cm}^{-1}$  frequency indicating the change from more plasmon-like SPPPhP to more phonon-like SPPPhP. It should be noted that by combining  $M = -1$  and  $M = +1$  modes, the tuning of SPPPhP position over the whole spectrum region from  $\nu_-$  to  $\nu_+$  frequency is expected with sample rotation, as one can see in **Fig. 4.30 a**.

All in all, the RCWA model represents the feature positions quite well and the feature strength can also be predicted by taking into account the angular aperture of the experiment as in the case of **Fig. 4.29**. Modelling allowed to predict the SPPPhP behaviour in wide angle range, including low as well as high incidence angles where characterization equipment may not work properly. Moreover it was also demonstrated by these results, that SPPPhP feature can be designed at the required frequency and incidence angle by using RCWA and analytical models, both models giving close results in view of the SPPPhP frequency.

#### 4.2.7 Emission from *n*-GaN SRG

According to Kirchoffs law of thermal radiation, a feature of increased absorption (reflectivity dip) translates into a feature in the emission spectrum of a thermally excited material. In theoretical calculations, Kirchoffs law translates into the absorption coefficient being equal to the emissivity ( $a = e$ ). The RCWA method allows one to calculate the diffraction coefficients in the reflected and transmitted diffraction orders, sum of which translates into the coefficients of reflection  $r$  and transmission  $t$ . Due to the fact that in spectrum range of  $0$  to  $\nu_-$  and  $\nu_{TO}$  to  $\nu_+$  the real part of the dielectric function of *n*-GaN is negative (see **Fig. 2.13**), *n*-GaN samples do not transmit radiation resulting in  $t = 0$ . Therefore, emissivity (absorption) was calculated from the energy conservation law, which states that in absence of

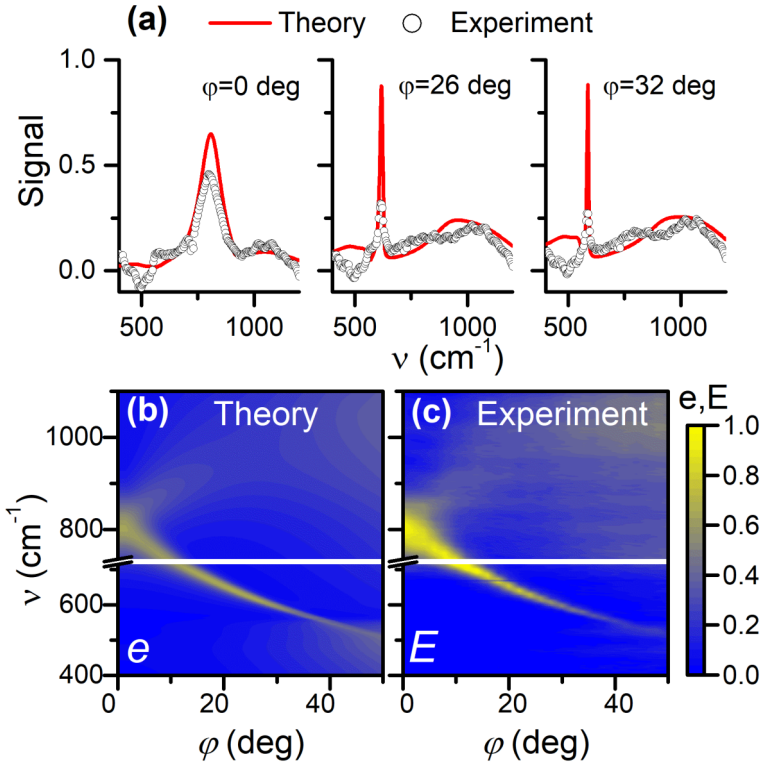


**Figure 4.31:** SRG-1 sample emission results. **a)** The measured emission (black symbols) and calculated emissivity (solid red line) differential spectra (TM-TE) of the  $n$ -GaN grating at various incident angles as indicated. **b)** – The calculated emissivity  $e$  and, **c)**– the measured emission  $E$  dispersions. In the theoretical result averaging over  $2^\circ$  was carried out simulating the influence of the experimental angular aperture. In the experiment, the emission spectra were measured at different angles varying in the range of  $0$ – $50^\circ$  in rotation steps of  $2^\circ$ . Break line corresponds to an absorption line of the polariser. Adapted after Ref. [P4].

scattering  $r + a + t = 1$  and therefore  $a = e = 1 - r$ . Calculated emissivity ( $e$ ) spectra for all samples are presented in **Fig. 4.28 d-f**.

Measured normalized SPP $\phi$ P emission spectra ( $E$ ) of SRG-1 sample at several selected incidence angles (namely  $0^\circ$ ,  $26^\circ$  and  $32^\circ$ ) are displayed in the **Fig. 4.31 a**. Calculated emissivity results are also displayed by red curves. Results are presented as the difference between TM and TE measured (calculated) values, therefore obtaining more pronounced SPP $\phi$ P feature expression. At the normal incidence of  $\phi = 0^\circ$  strong and relatively wide SPP $\phi$ P feature is observed at around  $810\text{ cm}^{-1}$  corresponding well with the reflectivity dip in the **Fig. 4.30**.

It is worth to note that the frequency of  $800\text{ cm}^{-1}$  is outside of the RB of undoped GaN and demonstrates the hybridized nature of SPPPhP mode. The SPhPs alone can not be excited at this frequency without the contribution of collective oscillation of free electrons, i.e. SPPs.

The SPPPhP frequency as well as the linewidth are seen to decrease strongly with an increase of the incident angle, closely following the theoretically calculated emissivity. The measured SPPPhP emission amplitude is seen to be notably reduced with an increase of the incidence angle contrary to the case of calculated emissivity. The measured emission amplitude decrease is associated with the effect of angular aperture described in the analysis of reflectivity measurements. Due to the fact that the theoretical FWHM of the SPPPhP decreases from  $120\text{ cm}^{-1}$  at the frequency of  $800\text{ cm}^{-1}$  to  $6\text{ cm}^{-1}$  at the frequency of around  $560\text{ cm}^{-1}$  SPPPhP amplitude becomes increasingly sensitive to the width of the spectra averaging. This effect was taken into account in calculated angular dependency of the calculated emissivity in **Fig. 4.30 a**. Here, each reflectivity spectrum  $r(\varphi)$  is obtained by averaging 7 adjacent reflectivity spectra in the range from  $r(\varphi - 1.5)$  to  $r(\varphi + 1.5)$  in  $0.5^\circ$  steps therefore simulating an angular aperture of  $3^\circ$ . No increase in the emissivity with the decrease of the frequency was now observed with the result very closely corresponding to normalized emission measurement result in **Fig. 4.30 b**). Another effect contributing to the amplitude loss is associated with the thermal radiation spectrum itself, maximum of which is located around  $1100\text{ cm}^{-1}$  at  $300\text{ C}$  temperature. A 26% decrease of signal to noise ratio (SNR) was estimated due to decrease of BBR intensity by comparing it at  $800$  and  $570\text{ cm}^{-1}$  frequencies, corresponding to observation the SPPPhPs at normal and  $35^\circ$  incidence angles, respectively.

Emissivity in TM polarization was calculated in the angle range of  $0^\circ$ - $70^\circ$  for all of the investigated samples. The results are shown in **Fig. 4.28**. Comparison of calculated emissivity  $e$  and measured emission  $E$  spectra are presented. Emissivity (emission) as difference between  $e_{TM}$  ( $E_{TM}$ ) and  $e_{TE}$  ( $E_{TE}$ ) polarizations were defined. It allowed to observe SPPPhP emission with subtracted broadband thermal radiation of the substrate. Measurement angle ( $k_x$ ) ranges were selected according to the theoretical results for each sample, in order to investigate emission at the regime, where the SPPPhP

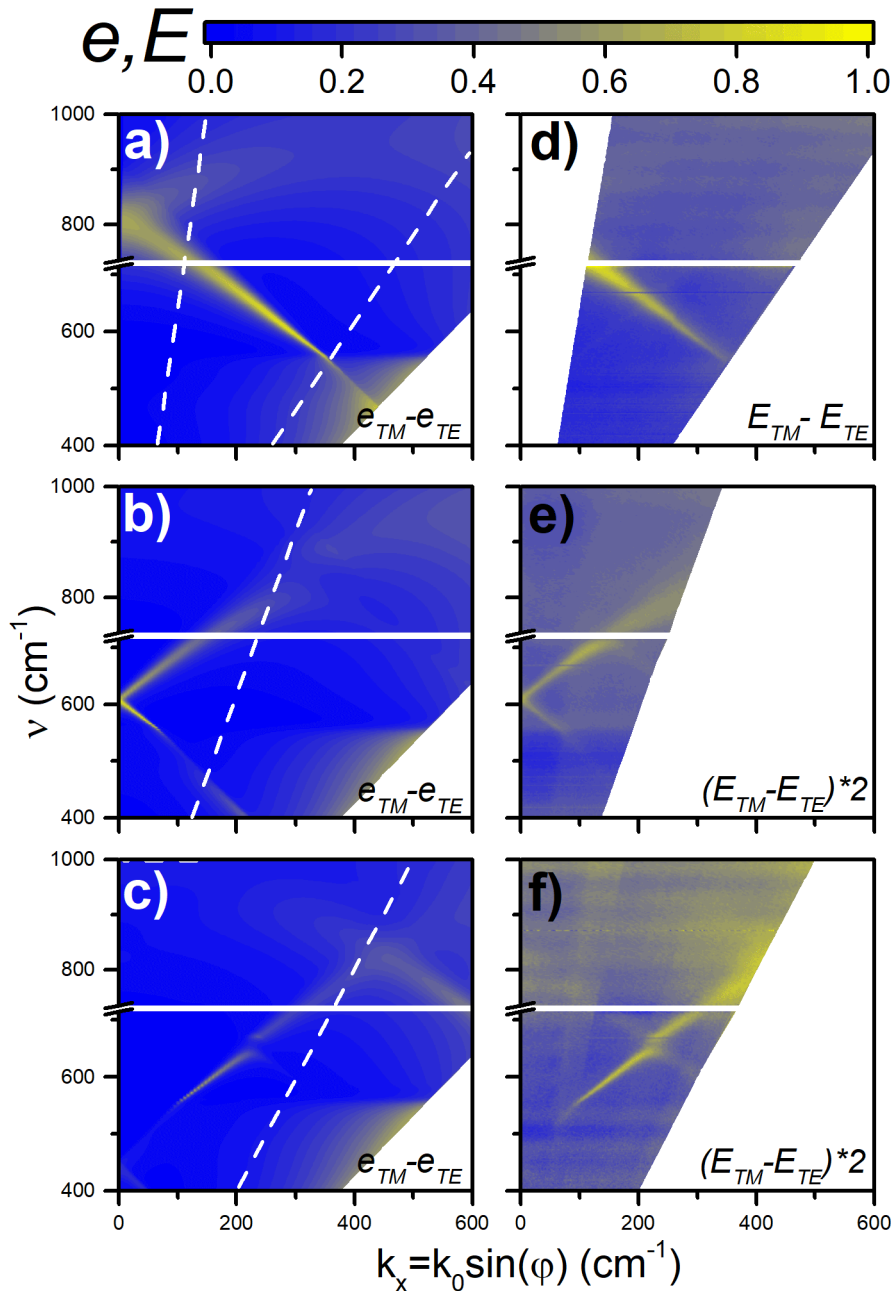


**Figure 4.32:** a)-c) calculated Emissivity and d)-f) measured emission difference (as  $e_{TM} - e_{TE}$  and  $E_{TM} - E_{TE}$ ) dependencies on the incidence angle. Pairs of a) and d), b) and e), c) and f) stand for the results of SRG-1, SRG-2 and SRG-3 samples respectively. White dashed lines in the theoretical spectra show the range of displayed experimental measurements.

crosses the TO phonon frequency resulting in most narrow features. Measurements were carried out in TM polarization with  $0.25^\circ$  steps followed by respective TE polarization measurement and the signal difference when accounting for the polariser transmission is displayed according to section 3.4. Theoretical and experimental results once again showed great accordance in SPPPh emission position as well as relative strength of the features. The results demonstrated tunability of the SPPPh emission via the design of the grating geometry ( $k_g$ ) or the incidence geometry as the SPPPh emission was tuned from above  $1000 \text{ cm}^{-1}$  down to  $540 \text{ cm}^{-1}$ .

By investigating the dependencies of separate SRG structures, it was noted that narrowband emission was stronger at angles closer to the normal incidence. It is expected that a slight increase in grating depth could be needed in order to observe stronger emission further from the normal incidence. As it stands, normal incidence emission was observed for SRG1 and SRG2 samples at respective frequencies of  $810$  and  $620 \text{ cm}^{-1}$ . In the case of SRG-3, normal incidence emission is located at  $460 \text{ cm}^{-1}$  i.e. in the forbidden region of positive dielectric function and therefore not observed. By comparing the emission of all the samples, it was noted that the most powerful emission signal was observed for SRG-1 at normal incidence (note the scale difference between **Fig. 4.32 d** and **e-f**). Meanwhile more narrowband emission signals were observed at near normal incidence for SRG-2 and SRG-3. By closely observing all of the measured spectra, it was noted that the smallest FWHM of SPPPh emission were observed at around  $560\text{-}570 \text{ cm}^{-1}$  for all of the samples. This frequency range acted as an optimal tradeoff between the narrowing linewidth (according to calculation results) and decreasing signal due to the angular aperture and decreasing BBR intensity at lower frequencies.

In the **Table 4.4** the parameters of the measured SPPPh emission at  $570 \text{ cm}^{-1}$  (the frequency of most narrowband experimental emission) for SRG-1 and SRG-2 samples and  $562 \text{ cm}^{-1}$  for SRG-3 sample are listed. The  $\varphi_0$  and  $\Delta\varphi$  here represent the angle of maximum SPPPh emission and angular width (view angle  $\Delta\varphi$ ) of the feature. Finally the SPPPh linewidth (FWHM) the corresponding quality factors  $Q = \nu_0/\text{FWHM}$  are presented. In all of the SRGs high quality factors for the narrowband



Sample	$\nu_0$ [cm <sup>-1</sup> ]	$\varphi_0$ [deg]	<i>FWHM</i> [cm <sup>-1</sup> ]	<i>Q</i>	$\Delta\varphi$ [deg]
SRG-1	570	34.2 (35.6)	14.6 (6)	39 (95)	2.6 (1.44)
SRG-2	570	4 (5.5)	17.3 (5)	33 (114)	2.3 (0.95)
SRG-3	562	11 (11.5)	7.4 (4.9)	78 (116)	1.1 (0.6)

**Table 4.4** : Experimental (theoretical) SPPHP emission feature parameters at the frequency of smallest experimental FWHM value. Parameters were calculated by approximating the measured spectra by Lorentzian functions. Theoretical values were obtained from high definition results calculated at 0.1° angle steps and 1 cm<sup>-1</sup> spectral resolution used in the coherence investigation in next section.

emission are observed, with SRG-3 being near the best reported values for semiconductor gratings on SiC [12]. In the case of SRG-2 existence of  $M = -1$  and  $M = +1$  modes washed out the measured peaks; therefore, a slightly wider emission was observed. Interesting result was obtained in seeing the directivity of emission as the FWHM of emission observation angle ( $\Delta\varphi$ ) reached down to 1° indicating highly directional emission suggesting the existence of spatial coherence described in section 4.2.8. Theoretical SPPHP emission parameters at a corresponding 570 cm<sup>-1</sup> frequency are displayed in brackets of **Table 4.4**. It can be seen that the predicted theoretical resonances are still narrower than their experimental counterparts, nevertheless the tendency of highest quality resonances being observed in SRG-3 is clear in both (theoretical as well as experimental) cases. Differences between theoretical and experimental  $\varphi_0$  values are believed to be caused by the positioning of the sample at the beginning of an experiment and the differences in predicted and measured linewidths are once again believed to be caused by the existence of an angular aperture.

All in all, narrowband tunable thermal emission was demonstrated theoretically and experimentally. Strong correlation was observed between the theoretical and experimental results validating the modeling as well as fabrication technology of custom designed thermal emitters. Resonances with quality factors up to 76 were observed experimentally for SRG-3 structure with theoretically predicted value of around 116.

### 4.2.8 Coherence of *n*-GaN SRG Emission

Spatial coherence was investigated for the fabricated SRGs as it was suggested by the high directivity of observed for SPPHP emission. It was noted that pronounced directivity of a radiation source is associated with the spatial coherence of the emitter surface via Fourier transform [12,96]. Similar relation is known to exist in the linewidth of radiated line with the coherence time (lifetime of the excitation). In literature an approximation of spatial coherence length at emission wavelength  $\lambda_0$  is approximated as  $L_{SC} \approx \lambda_0/\Delta\varphi$  [12,83]. In order to describe the  $L_{SC}$  emission spectra dependencies on the incidence angle were investigated in higher detail. Experimental spectra in the vicinity of highest quality resonances were measured with the angular steps of  $0.2^\circ$  and resolution of  $4\text{ cm}^{-1}$  and theoretical dependencies were calculated in  $0.1^\circ$  steps and  $1\text{ cm}^{-1}$  resolution. Spatial coherence length was calculated for SRG-1 and SRG-3 samples. Signals of adjacent  $M = +1$  and  $M = -1$  modes complicated the extraction of  $\Delta\varphi$  in SRG-2 sample, therefore its coherence is not reported.

The process of  $\Delta\varphi$  extraction from emission spectra is demonstrated in Fig. 4.33. Here, the emission signal at several set frequencies  $\nu_0$  is plotted as a function of observation angle  $\varphi$ . The resulting functions were fitted with Lorentzian waveforms and parameters of centre observation angle  $\varphi_0$  and FWHM of observation angles  $\Delta\varphi$  are obtained.

Experimental spectra were well described by Lorentzian waveforms and the FWHM ( $\Delta\varphi$ ) values were extracted from the fitting procedure. However, the SPPHP features demonstrated an asymmetrical nature in modelled emission, and simple Lorentzian approximation failed to fit the data. Fitted FWHM ( $\Delta\varphi$ ) values were found to deviate from those estimated manually, especially at frequencies below  $\nu_{TO}$  of  $559\text{ cm}^{-1}$ . Therefore, manually estimated values were used for the theoretical  $L_{SC}$  calculation.

Calculated  $L_{SC}$  value dependencies on the  $\varphi_0$  observation angle are displayed for SRG-1 grating in Fig. 4.34. Note that each point corresponds to a specific emission frequency  $\nu_0$ , the angle of maximum emission  $\varphi_0$  and the FWHM of emission observation  $\Delta\varphi$ . It is also worth to note, that proper theoretical calculation resolution must be selected for

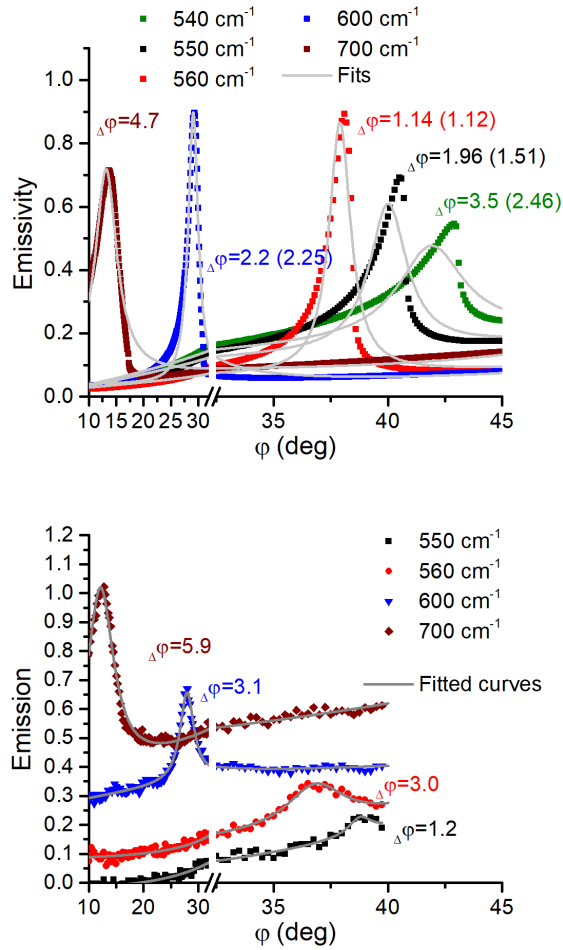


**Figure 4.33:** Example of  $\Delta\phi$  extraction from SRG-1 theoretical emissivity **a)** and experimental emission **b)** spectra at selected frequencies. Numbers represent the extracted  $\Delta\phi$ , with theoretical spectra showing Lorentz fit values (in brackets) and manually estimated values. Experimental spectra are offset by 0.1 for clarity.

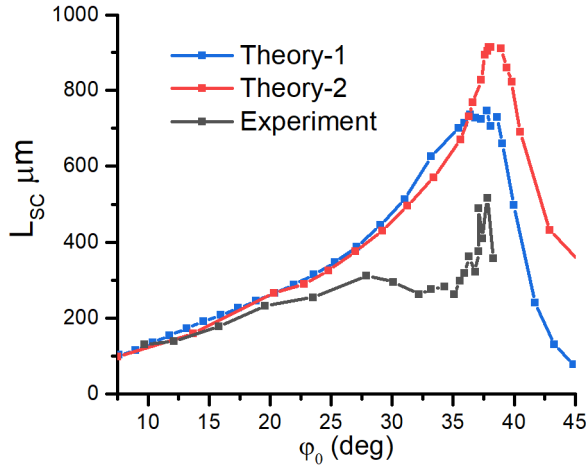


**Figure 4.34:** Coherence length results on the maximum intensity incidence angle ( $\phi_0$ ) for SRG-1 sample. Theory-1 stands for result obtained from the spectra calculation with  $0.5^\circ$  resolution (result adapted after P4). Theory-2 stands for the result obtained from spectra calculation with  $0.1^\circ$  resolution.

an accurate result. This is illustrated in spectra Theory-1 and Theory-2 in Fig. 4.34. The former is calculated using an angular resolution of  $0.5^\circ$  demonstrating predicted coherence length plateau around the maximum coherence condition. Much more pronounced maximum is observed in calculation result with  $0.1^\circ$  resolution.

In the case of SRG-1, maximum coherence was observed at around  $38^\circ$  incidence and  $560\text{ cm}^{-1}$  frequency in theory and at  $37.8^\circ$  incidence and  $555\text{ cm}^{-1}$  frequency in experiment. Above  $38^\circ$  incidence experimental SPPHP emission was not observed. Maximum coherence length values were of  $915\text{ }\mu\text{m}$  theoretically and  $500\text{ }\mu\text{m}$  experimentally, corresponding to  $\approx 50\lambda$  and  $\approx 27\lambda$  respectively. In the case of SRG-3 maximum coherence was observed at around  $11.2^\circ$  in the experiment. Maximum  $L_{SC}$  values were found to be of  $2325\text{ }\mu\text{m}$  in theory and  $921\text{ }\mu\text{m}$  in experiment respectively corresponding to  $167\lambda$  and  $51\lambda$ . The value of theoretical  $L_{SC}$  was 2.5 times larger in the case of SRG-3 as compared to SRG-1 design indicating more optimal SRG operation regime.

In the results of both samples, observed experimental  $L_{SC}$  values were around two times lower than those obtained in theory. Two main possible reasons for this discrepancy are identified. The first one is associated with possible structural defects of surface gratings, which deteriorate the coupler performance and are not incorporated into the model,

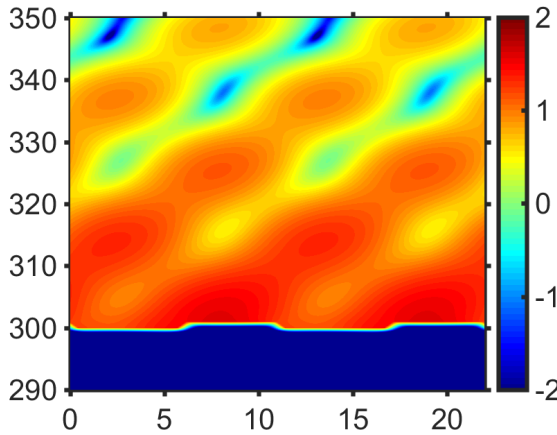


**Figure 4.35:** Field plot of SRG-1 sample SPPHP excitation under 38.1 degree incidence angle and  $561\text{ cm}^{-1}$  excitation frequency. Adapted after Ref. [P4].

even though the SEM and optical measurements did not show notable deviations from design. The second reason is associated with systemic error of the measurement method. More specifically, even when minimised as much as possible, an angular aperture of around  $1.1^\circ$  still existed in the experiment; nevertheless, further investigations of emission with smaller angular apertures or even collimated beams could result in the identification of larger coherence lengths.

Millimetre scale  $L_{SC}$  values suggest possibilities of creating macroscopic locally or even globally coherent SRG based SPPHP emission devices.  $L_{SC}$  values in the range of  $60\lambda$  had been reported for SPPHP emission in undoped SiC structures in previous works [83], here experimental results in a similar scale are demonstrated for *n*-GaN SPPHPs with possible improvement in further experiments. Millimetre scale coherence lengths are also interesting in applications of optical circuitry, where mm scale coherent signal transfer could prove useful in interchip signal transfer or optical logic circuits themselves.

**Fig. 4.35** demonstrates field distribution of SRG-1 structure maximum theoretical coherence condition of  $38^\circ$  incidence and  $560\text{ cm}^{-1}$  frequency. Strong field enhancement at the SRG was observed with low field leakage into the semiconductor. This behaviour is indicative for a SPPHP excitation.

### 4.2.9 Power of *n*-GaN SRG Emission

Measured coherent FTIR emission, suggesting the application of the structures for emitter devices, requires the specification of a possible emitted power. As FTIR measurements were not power calibrated, emission power could not be estimated directly from measured spectra. Use of available wideband power detectors was also prohibited due to the angular nature of emission, needing a measurement of a collimated beam with a negligible angular aperture for correct measurements. A workaround for first order approximation of expected emission power was therefore suggested. Emission power would be estimated from the emissivity spectra multiplied by the black body radiation spectrum (*BB*) defined by the well-known Planck formula (spectrum shown in **Fig.4.36 a**). Obtained spectral power density is then integrated at a certain window around the maximum SPPPh emission frequency and results are displayed in (**Fig.4.36 b**). This geometry was chosen for the investigation as SRG-1 @ 26° the incidence theoretically offers an almost unitary SPPPh emissivity offering largest TM/TE emitted power ratio. Emission power in TM polarization is much larger than in TE, peak emission (emissivity) demonstrating around 8 times difference. At integration window close to the linewidth of SPPPh emission ( $40 \text{ cm}^{-1}$  for SRG-1 shown by the rectangle in **Fig.4.36**) and temperature of 300° C, SPPPh emission power was estimated to be around  $12.4 \text{ W/m}^2 \text{ sr}$ .

One should note that the obtained value is given for one square meter and steradian of power collection as Planck's equation does not differentiate the emission profile. In reality, when using suggested one dimensional emitter the emission angle as well as emitter area are limited. First order approximation of emitted power may be carried out by taking into account known geometric parameters for SRG-1. If one takes into account the emitter area, limited in *x* direction by the OAP mirror spot of around 3 mm and in *y* direction by the coherence length (in the case of SRG-1 at 26° being around 0.35 mm) emission power of  $\approx 13 \mu\text{W/sr}$  is obtained. Further, by including the emission angles as limited to 2.69° by the coherent nature of emission and 28° by the OAP mirror one can approximate the emission angle as 0.023 rad resulting

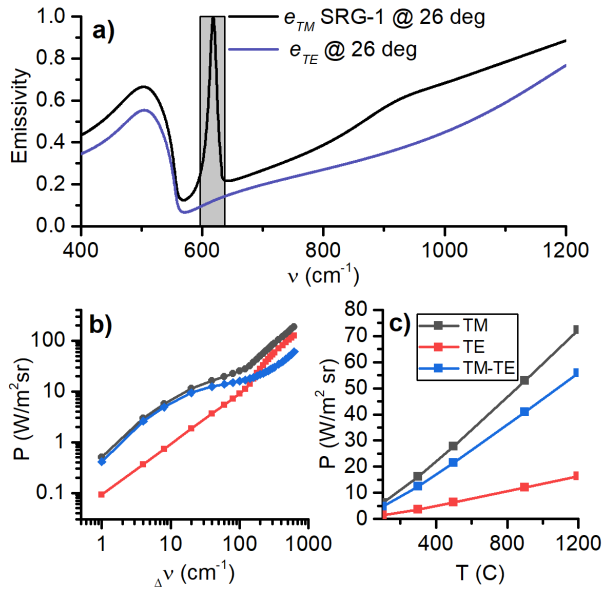


**Figure 4.36:** a) Simulated thermal emission spectra ( $e \times BB$ ) for SRG-1 grating at 26° incidence and 300°C temperature in TM and TE polarisations. b) Dependence of the estimated emitted power on the integration window width  $\Delta\nu$  around the centre frequency of 615 cm<sup>-1</sup> for SRG-1 structure at 26° incidence. c) dependence of estimated emission power on the excitation temperature.

in the estimated coherent SPPHP emission power of around 200 nW for SRG-1 at 26° incidence.

Lastly, due to the high thermal resistance of GaN, high temperature thermal excitation of GaN can be achieved in order to improve the emission power. This is illustrated in **Fig. 4.36 c**. Here, almost linear scaling of emission power with the excitation temperature is predicted in the frequency window of 40 cm<sup>-1</sup>.

### 4.3 Reflectivity of Metal Grating Coupled Heterostructures

The reflectivity investigation of GaN/GaN and SiC/AlN/GaN heterostructures (Sample 1 and Sample 2, respectively), with metal grating coupler (MGC) structures on the surface was carried out theoretically and experimentally. Heterostructures of GaN/SiC are intriguing in their application for polaritonics as they exhibit high reflectivity regions of SiC as well as GaN, effectively broadening the operational SPhP bandwidth as compared to a single undoped material. They also allow for the investigation of polariton formation within the heterostructure, and possibilities of light confinement in the deeper layers of heterostructure. Contrary to the case of GaN, the SRGs application of MGC allowed the sample surface (and the heterostructure) to be unetched (undistorted), therefore preserving its electrical and structural properties.

This section is comprised of the following parts. Experimental spectra of unpatterned samples are first used for fitting of the dielectric function parameters. Theoretically calculated dispersions of the reflectivity spectra on the period of metal grating couplers are then investigated and the behaviour of different SPhP modes described. The calculated dispersions allowed to identify the nature of the observed reflectivity dip lines and demonstrate the tunability of SPhP resonances. Experimental MGC spectra are then reported and the nature of features is described. Finally, the field plots are calculated at selected frequencies in order to investigate/demonstrate light confinement phenomena within the heterostructure layers.

#### 4.3.1 Metal Grating Coupled Heterostructure Samples

MGC-1 and MGC-2 samples consisted of AlGaIn/GaN and AlGaIn/GaN/SiC heterostructures. The sample growth and characterization of HEMT structures has been reported separately [136, 137]. Heterostructures for samples MGC-1 and MGC-2 were grown on bulk *c*-plane GaN and Semi-Insulating (SI) 6H-SiC substrates respectively. The *n*-GaN substrate (from *Ammono S.A.*) was Ga-faced, one side polished, had the thickness of 300  $\mu\text{m}$  and doping level of  $10^{17}\text{cm}^{-3}$ . The



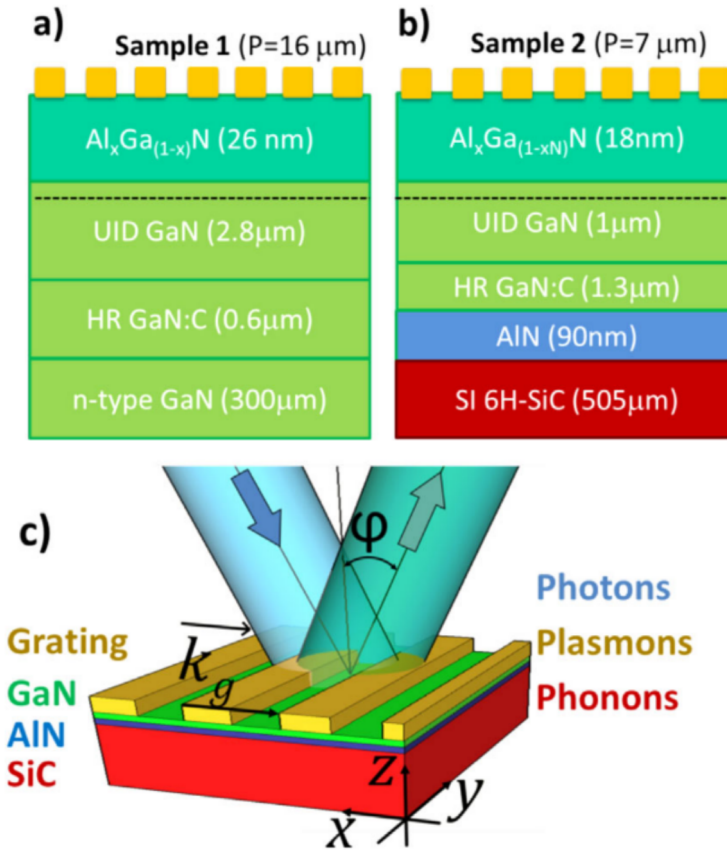


**Figure 4.37:** The heterostructure stacks of **a)** MGC-1 and **b)** MGC-2 samples. Dashed line represents the 2DEG channel at the GaN/AlGaN interface. **c)** representation of the modelled structure as well as the experiment geometry with  $k_g$  representing the grating vector of the metal coupler and  $\varphi$  representing the angle of incidence of radiation in XZ plane. Due to their small optical thickness within the spectral region of interest the AlGaN layer and the 2DEG channel were omitted from the calculations. Adapted after Ref. [P6].

SiC substrate (from *II-VI Advanced Materials*), was both sides polished, had the thickness of 505  $\mu\text{m}$ . The MGC-1 heterostructure consisted of 0.6  $\mu\text{m}$  high resistivity (HR) carbon doped GaN (GaN:C) buffer layer, 2.8  $\mu\text{m}$  unintentionally doped GaN layer and 26 nm AlGaN barrier. The layer structure is illustrated in **Fig. 4.37 a)**. The heterostructure of MGC-2 had a 90 nm AlN nucleation layer, 1.3  $\mu\text{m}$  HR-GaN layer, 1  $\mu\text{m}$  unintentionally doped GaN layer and 18 nm AlGaN barrier [137].

Grating (contact) processing was carried out according to procedures developed at the UNIPRESS for creating Schottky contacts for

Material	$\epsilon_\infty$	$\nu_{TO}(\gamma_{TO})[\text{cm}^{-1}]$	$\nu_{LO}(\gamma_{LO})[\text{cm}^{-1}]$	$\nu_P[\text{cm}^{-1}]$
<b>Sample MGC-1</b>				
Top-GaN	5.3	557 (4)	736 (20)	0
Substr-GaN	5.3	557 (6)	736 (20)	87
<b>Sample MGC-2</b>				
GaN	5.3	557 (4)	736 (4)	0
AlN	4.7	675 (4)	891 (5)	0
SiC	6.6	799 (6)	970 (8)	82

**Table 4.5 :** Parameters used for the calculation of the reflectivity spectra of MGC samples.

2DEG plasmonic HEMT devices [136, 137]. Grating height  $h$  was in the order of 80 nm i.e. much smaller than the characteristic polariton wavelength ( $h \ll \lambda$ ). Specific grating geometry was not investigated in this regime at this point of the research. The included grating parameters were the periodicity, height and filling factor (or metal strip width). MGC-1 and MGC-2 samples had  $1 \times 1$  and  $2 \times 2$  mm<sup>2</sup> area gratings couplers with the periodicities (distances between stripes) of 16 (8), and 7 (2.9)  $\mu\text{m}$ , respectively. Gratings were designed to modulate the dielectric function of the 2DEG channel as well as to couple the light into SPhP modes [138].

### 4.3.2 Unpatterned Sample Reflectivity

Experimentally measured reflectivity spectra of flat samples are shown by dots in **Fig.4.38**. Unpolarised reflectivity of Sample 1 is shown in **Fig.4.38 a**. It is governed mainly by the RB of GaN, without notable inputs of AlGaN or 2-DEG channel. RBs of GaN and SiC are clearly observed in TE polarised Sample 2 spectra in **Fig.4.38 b** and TM polarised spectra of Sample 2. Results are shown in **Fig.4.38 c** Spectral positions of GaN, AlN and SiC phonons are listed in **Table 4.5** and coincide well with those reported in literature [17, 99, 101, 103].

The experimental spectra of pristine sample were used as the reference. Calculated spectra are shown by red lines in **Fig.4.38**. Calculations were carried out using the phonon frequencies in **Table 4.5** and fitting the respective phonon damping factors. The estimated damping of the TO phonons of  $4 \text{ cm}^{-1}$  and  $6 \text{ cm}^{-1}$  for GaN and SiC also corresponded well with the values reported in literature. LO damping

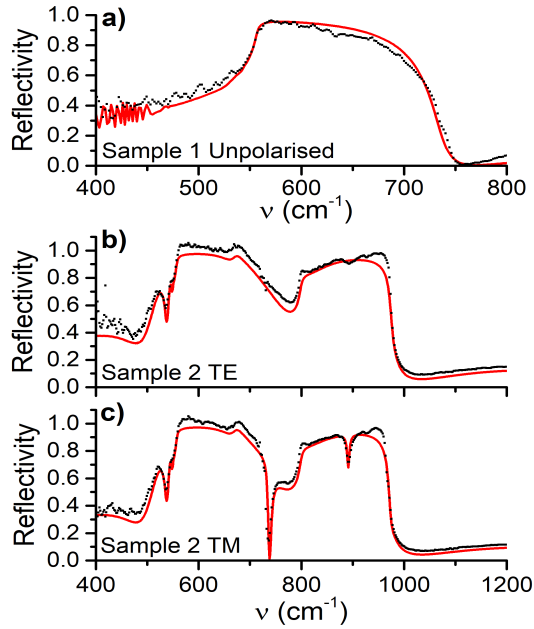


**Figure 4.38:** Measured (black dots) and calculated (red curves) reflectivity spectra of the unprocessed, samples without gratings. **a)** Unpolarised reflectivity spectrum of the Sample 1. **b)** and **c)** TE and TM polarised reflectivity results of the Sample 2. Adapted after Ref. [P6].

was estimated to be comparatively large in the case of Sample 1 with the estimated value of  $20 \text{ cm}^{-1}$  and commonly reported values around  $10 \text{ cm}^{-1}$  [94, 139].

Doping of the substrates was taken into account with the plasmon frequencies listed in **Table 4.5** accounted for in the dielectric function of the Eq. 2.33. A simplified heterostructure was used for RCWA model. Simplified structure contained  $300 \mu\text{m}$  thick doped substrate and a  $3.4 \mu\text{m}$  thick undoped GaN surface layer. The  $20 \text{ nm}$  thick AlGaN layer was not taken into account as notable optical features of this layer were not observed in the experiment. The 2D electron gas channel was not modelled as it was not expected to produce features in the investigated frequency range. Precise definition of 2D electron gas in RCWA model requires additional investigation.

Sample 1 spectrum was fully determined by the RB of GaN. Spectra of Sample 2 displayed additional features. Namely, the small reflectivity dips observable in TE as well as TM polarised spectra at around  $540 \text{ cm}^{-1}$  and  $560 \text{ cm}^{-1}$  are caused by standing Fabry-Perrot waves

within the GaN layer. Small kink in reflectivity at  $670\text{ cm}^{-1}$  in **Fig.4.38 b** and **c** as well as the reflectivity dip line at  $890\text{ cm}^{-1}$  in **Fig.4.38 c** were attributed to AlN phonon modes of AlN nucleation layer. Overall, a very good agreement is observed between the measured and calculated results of the flat sample validating the used model.

### 4.3.3 MGC Reflectivity Dispersion

Reflectivity dispersions  $R$  vs  $\nu$  vs  $k_g$  were calculated for various heterostructures with surface metal gratings using dielectric function parameters described in **Table 4.5**. The grating was included into the model as a 80 nm thick layer of metal with the plasmon frequency at  $80000\text{ cm}^{-1}$  and damping factor of  $6800\text{ cm}^{-1}$ . The grating was optically thin; therefore, its geometry did not influence the spectral features. A coupler was approximated as a single layer rectangular grating with the period and width of metal stripes corresponding to sample geometries. Calculations were carried out for the incidence angle of  $20^\circ$ . The TM and TE polarized spectra were investigated. The results revealed that the SPhP reflectivity features were observed only in the TM polarization. Results obtained for TM polarisation in the grating periodicity range of 5 to 25  $\mu\text{m}$  for various heterostructure stacks are shown in **Fig. 4.39**.

Results for the structure of MGC 1 sample are shown in **Fig. 4.39 a**. In order to compare the polaritonic response, metal grating on the surface of SiC was also calculated. The results are displayed in **Fig. 4.39 b**. High reflectivity RB regions of GaN and SiC are observed in **Fig. 4.39 a** and **b**, respectively. Two polariton lines of  $M = -1$  and  $M = +1$  order were identified by Eq. 2.35. These modes are indicated by dashed lines. Hybridisation of SPs with the LO phonons was observed as the SPhPs (hybrid) reflectivity minima were anti-crossed with the LO phonon modes. The observed modes levelled off asymptotically at around  $700\text{ cm}^{-1}$  and  $950\text{ cm}^{-1}$  frequencies for GaN and SiC based structures respectively.

Much more complex behavior was observed in the results calculated for the MGC-2 sample structure (**Fig. 4.39 c**). Increased reflectivity regions of RB of GaN as well as SiC are observed corresponding to **Fig. 4.38**. Air-GaN interface SPhPs are observed within the RB of GaN

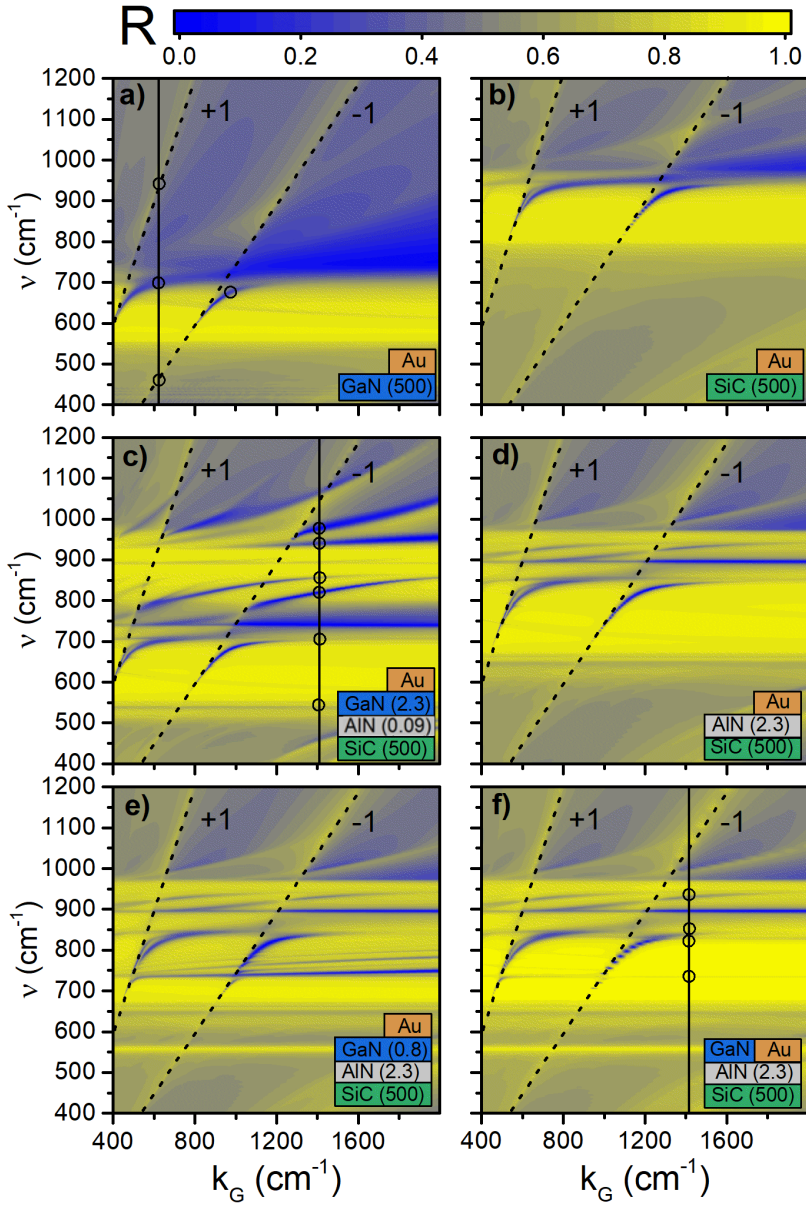


**Figure 4.39:** TM polarised reflectivity spectra of various heterostructures with metal grating couplers. Brackets show the layer thickness. **a)** MGC/GaN (MGC-1 sample). **b)** MGC/SiC. **c)** MGC/GaN/AlN/SiC (MGC-2 sample). **d)** MGC/AlN/SiC. **e)** MGC/GaN/AlN/SiC with inverted layer thicknesses. **f)** MGC-GaN/AlN/SiC. Vertical lines in **a)** and **c)** represent the spectra of the fabricated MGCs. Circles represent the regions of interest for the field plot calculations. The dashed lines correspond to the polariton dispersion lines of order indicated by the numbers beside the lines. **a)** and **c)** were adapted after Ref. [P6].

analogously to **Fig. 4.39 a**. Two modes are observed within the RB of SiC with their positions also tuned by the grating vector of the coupler corresponding to polaritons in GaN-AlN/SiC interface. Several more reflectivity dip lines are observed above  $900\text{ cm}^{-1}$  splitting off from SP dispersion lines. The exact nature of these modes is harder to discern due to interaction of the phonons of different materials and complex heterostructure. Dispersionless features at around  $736$ ,  $890$  and  $940\text{ cm}^{-1}$  frequencies were identified as the LO phonon absorption of GaN, AlN and SiC respectively. The latter one is seen to be shifted from its nominal frequency by its interaction with other modes in its vicinity.

Additional heterostructure dispersions were calculated in order to investigate the influence of different heterostructure stacks to the reflectivity spectra. Grating coupled SiC/AlN heterostructure dispersion is displayed in **Fig. 4.39 d**. In this case a continuous high reflectivity region of combined AlN and SiC RBs is observed. Reflectivity dip lines of AlN SPhPs are observed in the range of  $675$  to  $850\text{ cm}^{-1}$  (RB of AlN) similarly to previous cases of single material wafers. Dispersionless AlN LO line also observed. SiC SPhPs (or ENZ modes) are, in this case, confined, to the range  $900$  to  $970\text{ cm}^{-1}$  i. e. between SiN and SiC LO phonons.

The addition of  $80\text{nm}$  thick GaN layer on top of AlN structure in the **Fig. 4.39 d** was investigated and calculated dispersion is shown in **Fig. 4.39 e**. In this case, instead of continuous GaN RB, a reflectivity increase line is observed at GaN LO frequency and a reflectivity dip line is observed at GaN LO frequency due to the low optical thickness of the layer. Several ENZ modes are also observed as fringes splitting off from the GaN LO line. Additionally, the calculation of a structure with metal grating etched into the surface of heterostructure (simulating ohmic contacts characteristic to HEMT devices) was carried out and displayed in **Fig. 4.39 f**. The results revealed that a thin layer ( $80\text{nm}$ ) of GaN between the metal grating ridges does not cause additional feature formation besides a slight increase in strength at GaN TO and LO lines.

#### 4.3.4 Experimental Investigation of MGC Reflectivity Spectra

The MGCs were deposited on top of the HEMT structures and the reflectivity spectra were investigated. Measured and calculated results

are displayed in **Fig. 4.40**. Calculation results of experimental sample geometries are also marked by black vertical lines in **Fig. 4.39 a** and **c**.

The **Fig. 4.40 a** demonstrates interaction of unpolarised beam with the MGC-1 sample. A signal decrease at the  $700\text{ cm}^{-1}$  frequency is observed in the spectra corresponding to excitation of  $M = +1$  SPhP mode. A reflectivity dip line was observed only in TM polarisation as was expected in the case of polariton excitation. Slight reflectivity level offsets (measured reflectivity level being higher than the calculated one) in the MGC-1 spectra were observed. These were believed to be caused by the measurement imperfections as  $1\times 1\text{ mm}$  area grating required a very small aperture, and the measurement precision was possibly affected. Nevertheless, the qualitative agreement between the calculated and measured results validated the incorporation of the metal grating coupler into the model and confirmed the excitation of SPhPs on the surface of AlGaIn/GaN/GaN HEMTs.

TE and TM polarized spectra of the MGC-2 are shown in the **Fig. 4.40 b** and **c** respectively. Both the TE and TM spectra demonstrated a strong reflectivity modification in comparison to the case of unprocessed sample in **Fig. 4.38**. A wide featureless region of high reflectivity spanning from  $550$  to  $850\text{ cm}^{-1}$  was observed in the TE polarised spectrum. Two features of strong reflectivity dips were observed within the RB of SiC at frequencies of  $890$  and  $960\text{ cm}^{-1}$ . The former of these features was attributed to GaN LO absorption due to its sensitivity to GaN LO phonon position in the calculations while the second one was sensitive to both GaN and SiC LO phonons indicating hybridized nature of absorption at this feature.

RBs of GaN and SiC were still clearly observable in the TM polarized spectra in **Fig. 4.39 d**. The RB of GaN was modified by a reflectivity dip at  $700\text{ cm}^{-1}$  causing a shoulder in overall signal decrease near the GaN LO phonon. This comparatively weak reflectivity dip is attributed to the excitation of the asymptotic line of  $M = -1$  SPhP polariton formed on the surface of GaN. Only the asymptotic "tail" is sampled here due to the large grating vector of the coupler ( $P = 7\text{ }\mu\text{m}$  resulting in  $k_g \approx 1430\text{ cm}^{-1}$ ), which, as seen from the previous case of **Fig. 4.39 a** can only be excited weakly.

Additional reflectivity dip lines were observed in the reflectivity

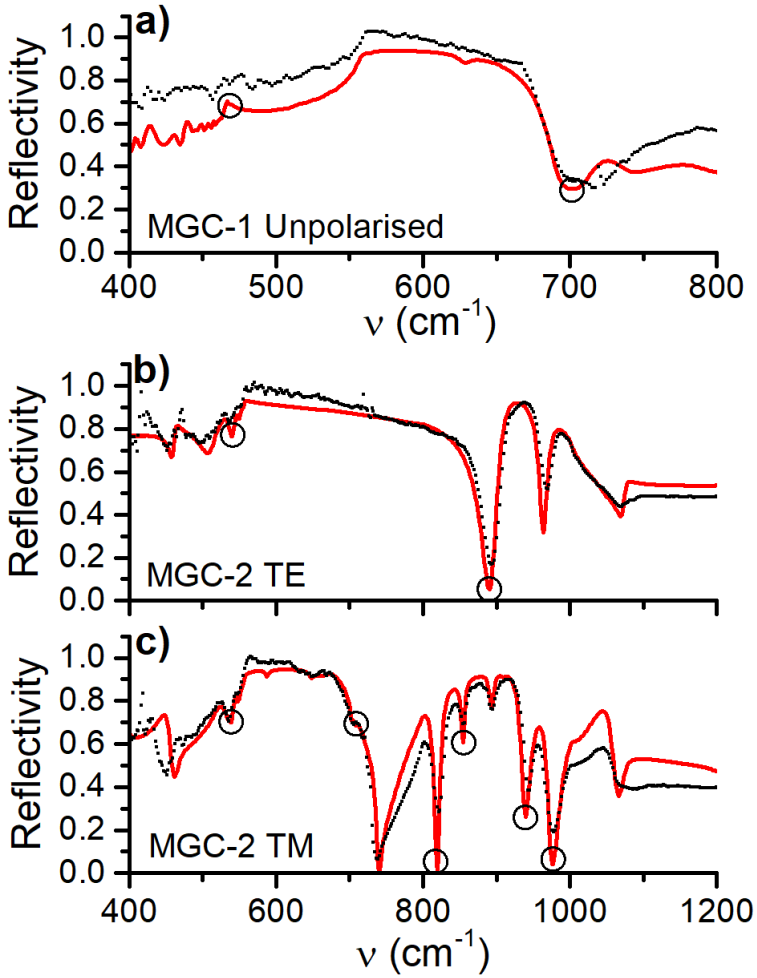


**Figure 4.40:** Measured (Black dots) and calculated (Red curves) reflectivity spectra of experimental samples. **a)** unpolarised reflectivity MGC-1 sample. **b)** and **c)** TE and TM polarised reflectivity of MGC-2 sample. Circles represent frequencies of interest, where field plots were calculated and are presented in next section. Adapted after Ref. [P6].



spectra of MGC-2 within the RB of SiC at the frequencies of 820, 855, 940, 978, and  $1066\text{ cm}^{-1}$ . Almost total absorption was predicted theoretically at the frequencies of 820 and  $970\text{ cm}^{-1}$ , while the experimental spectrum demonstrated the dips to around 20%. This is attributed to the fact that a finite angular aperture was present in the experiment while exact angle was used in the calculations. The existence of a finite aperture comes from the focusing of the probing beam onto the sample surface and subsequent existence of additional angles  $\Delta\varphi$  of incoming radiation in addition to the nominal angle of incidence  $\varphi$ . The presence of an angular aperture suggests that the strongly directional SPhP features (according to Eq. 2.35) exist in a finite frequency range instead of a discrete frequency position. Overall, a good agreement of the measured and calculated results was demonstrated, validating the calculation as well as fabrication procedures for the design and fabrication of SPhP coupling structures.

#### 4.3.5 Field Plots

Magnetic field component plots were calculated in order to investigate the light confinement for different modes of investigated spectra. Magnetic field plots for GaN based structure at frequencies displayed by circles in Fig. 4.39 a and Fig. 4.40 a are shown in Fig. 4.41. Three plots for the grating vector of  $625\text{ cm}^{-1}$  (corresponding to the grating periodicity of  $16\text{ }\mu\text{m}$ ) were calculated at frequencies of  $470\text{ cm}^{-1}$ ,  $698\text{ cm}^{-1}$  and  $958\text{ cm}^{-1}$  are shown in Fig. 4.41 a, b and c, respectively. As could be expected, next to no field localization was observed at the frequencies outside the RB of GaN in Fig. 4.41 a and c. In this case field is seen to penetrate through the heterostructure and deep into the substrate due to the transparency of GaN.

Field plots in the Fig. 4.41 b and d show the excitation of the  $M = -1$  and  $M = +1$  SPhP modes within the RB of GaN at the frequencies of  $685\text{ cm}^{-1}$  and  $698\text{ cm}^{-1}$  by gratings with wavevectors of  $1017\text{ cm}^{-1}$  and  $625\text{ cm}^{-1}$ , respectively. In the case of  $M = -1$  mode, a strong excitation regime is demonstrated with strong field localisation and a symmetric resonance feature. In the case of  $M = +1$  mode at grating vector value of 625 (corresponding to the experimental sample) asymptotic

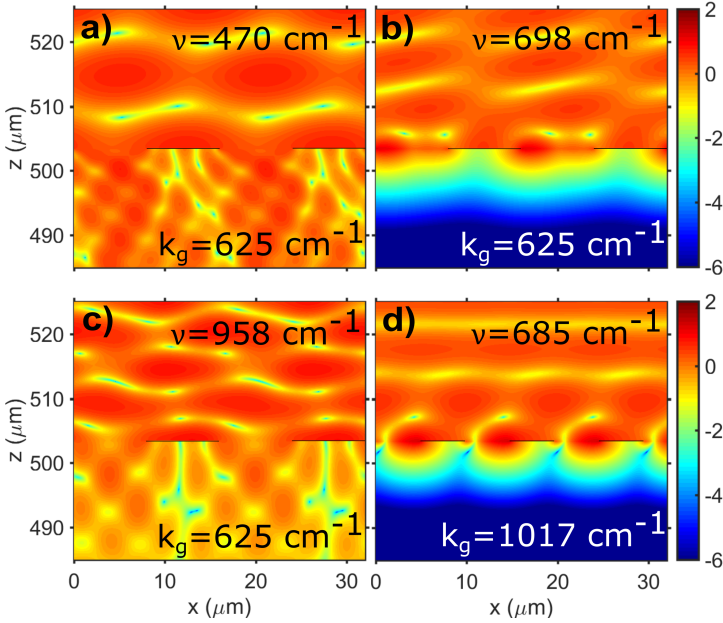


**Figure 4.41:** Field plots of MGC-1 (GaN/GaN) structure at respective frequencies and grating vectors. The spectral positions of the field plots are marked by the circles in the Fig. 4.39. The grating metallization is marked by the black lines as the thickness of the metal was not large enough for observation in given  $z$  scale. The substrate ends at the  $z=500 \mu\text{m}$  and the heterostructure layers as well as the grating are positioned above it. Adapted after Ref. [P6].

case of weaker excitation is sampled demonstrating slightly lower field strength. Close spectral proximity to the asymptotic tail of higher order mode is believed to result in an asymmetric field distribution.

Field plots were also calculated for various modes of interest for MGC-2 structure. Field plots at the frequencies of  $538 \text{ cm}^{-1}$  and  $890 \text{ cm}^{-1}$  in the TE polarization is shown in the Fig. 4.42 a and b respectively (marked by circles in Fig. 4.40 b). Fringes within the GaN layer are clearly observable at  $540 \text{ cm}^{-1}$  frequency. This indicates the standing waves (Fabry-Perrot effect) within the semi transparent GaN, with modulation of its strength in  $x$  direction due to the screening via metal grating. Absorption / field damping is observed only within GaN layer due to transparency of SiC and AlN at this specific frequency. These standing wave fringes could be used to define the thickness of a layer via the fitting of the thickness parameter in the reflectivity spectra calculation. At the frequency of  $890 \text{ cm}^{-1}$  no field localisation is observed indicating that corresponding reflectivity dip is caused by

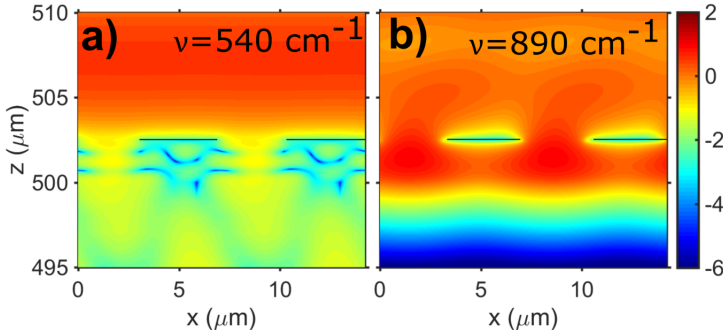


**Figure 4.42:** Field plots for the TE polarisation (electric field component in the  $y$  direction) for the MGC-2 (GaN/AlN/SiC) structure at selected feature frequencies of  $540$  and  $890\text{ cm}^{-1}$  indicated by circles in **Fig. 4.40 b**.

phonon absorption rather than formation of additional modes.

Field plots of the MGC-2 sample structure were calculated at frequencies of interest marked by circles in **Fig. 4.39 c**. The results are displayed in **Fig. 4.43**. Standing wave fringes are observed at  $540\text{ cm}^{-1}$  frequency similarly to the TE polarised case in **Fig. 4.42**. At the frequency of  $708\text{ cm}^{-1}$  weak field localisation is observed at the GaN/Air interface between the MGC "fingers". Field enhancement at the SiC/GaN interface is observed for the  $820\text{ cm}^{-1}$  and  $854\text{ cm}^{-1}$  modes. Optically thin AlN layer did not act as interface itself, instead AlN LO hybridisation with the  $854\text{ cm}^{-1}$  mode was observed as this mode was found to be located at  $878\text{ cm}^{-1}$  in the calculation result without AlN (result not shown). A strong and rather symmetric field maximum was observed at  $820\text{ cm}^{-1}$  corresponding to  $M = -1$  mode while weaker and an field maximum was observed at  $854\text{ cm}^{-1}$  corresponding to  $M = +1$  mode. Similar behaviour was also observed at GaN/Air interface polaritons of respective modes in **Fig. 4.41**. At these frequencies SiC exhibited negative real part of the dielectric function while one for GaN was positive, ensuring the formation of SPhPs.

Last two lines at  $940\text{ cm}^{-1}$  and  $978\text{ cm}^{-1}$  demonstrate field localization within the GaN layer in field plots of **Fig. 4.43 e** and **f**. Modelling of slightly different heterostructure stacks was carried out and sensitivity of these modes to the thickness of GaN was found. Frequencies of these modes are also sensitive to the frequencies of the GaN and SiC LO phonons indicating the coupling between the GaN "cavity" and phonons of substrate, while AlN layer did not strongly influence their

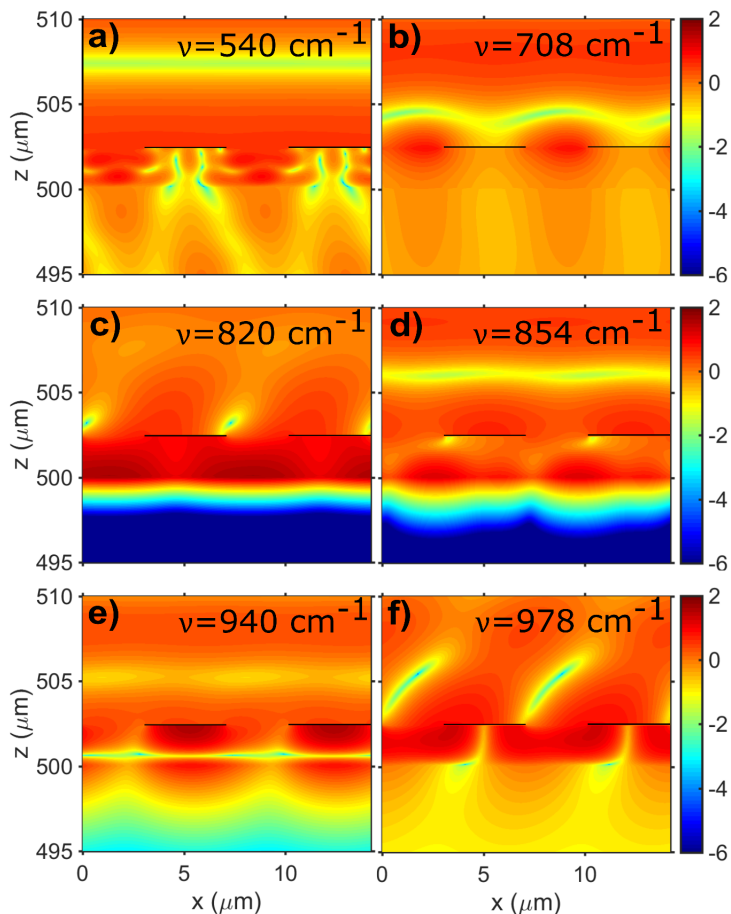


**Figure 4.43:** Field plots for the TM polarisation (magnetic field component in the  $y$  direction) for the MGC-2 (GaN/AlN/SiC) structure at selected feature frequencies of 540, 708, 820, 854, 940 and 978  $\text{cm}^{-1}$ .

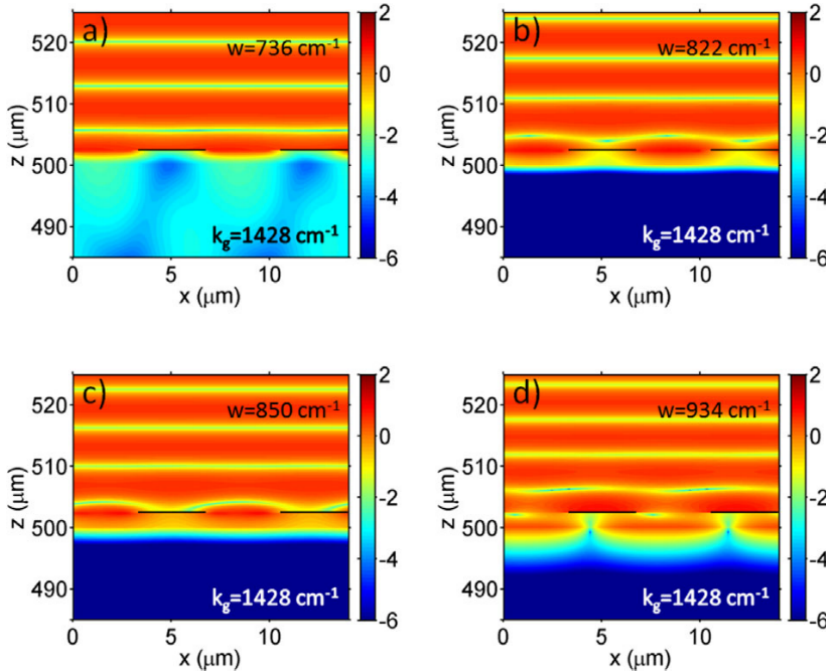


**Figure 4.44:** Field plots for the TM polarisation (magnetic field component in the  $y$  direction) for the MGC-GaN/AlN/SiC structure shown in Fig. 4.39 f) at selected feature frequencies of 736, 822, 850 and 934  $\text{cm}^{-1}$ . Adapted after Ref. [P6].

frequencies.

The field is strongly localized in the case of the 940  $\text{cm}^{-1}$  frequency mode with the maximum being located at the MGC/GaN interface. This indicates that either a guided mode exists in a stead/addition of previously suspected SiC LO absorption or a GaN/Metal surface polariton is excited on the bottom surface of the grating. This mode could be interesting for the application of coupling radiation to a 2DEG channel located very close to the surface of GaN/AlGaIn HEMT structures. In the case of 978  $\text{cm}^{-1}$ , double maximum behaviour of the second guided/polariton mode is observed. This mode also overlaps with the LO frequency of SiC supposedly giving it very high strength (calculated reflectivity dropping almost to 0). Lastly, a weak field enhancement within GaN layer was observed at the frequency of 1066  $\text{cm}^{-1}$  (not shown).

Fig. 4.44 shows field distribution for modes of interest in a slightly different structure. In this case, a heterostructure shown in the inset

of **Fig. 4.39 f** is investigated. Frequencies of interest, at which the field plots were calculated are illustrated by circles in the figure. MGC contacts within in 80 nm GaN thick surface layer are modelled simulating a buried contact geometry.

At the frequency of  $736\text{ cm}^{-1}$  in **Fig. 4.44 a)** field absorption at the GaN layer is observed, with no field localisation and deep field leakage into the transparent AlN and SiC layers. At frequencies of  $822\text{ cm}^{-1}$  and  $850\text{ cm}^{-1}$  in **Fig. 4.44 b)** and **c)** field penetration into GaN layer is observed with almost no leakage into the SiC substrate. Field maximum at the GaN surface is observed in this case, even though strong field enhancement is not observed due to weak asymptotic mode excitation. Lastly, at the frequency of  $934\text{ cm}^{-1}$  polariton mode at SiC/AlN interface, within the heterostructure is observed, even though field enhancement is also not observed.

## 5. MAIN RESULTS AND CONCLUSIONS

1. Multilevel phase corrected Fresnel lenses with different numbers of phase quantisation levels, working at 0.6 THz frequency, were fabricated using the direct laser ablation method. Their focusing properties were investigated, and application in commercially feasible imaging/quality control setup was demonstrated.
2. The Soret zone plate and silicon multilevel phase Fresnel lenses were fabricated using the direct laser ablation method for focusing 4.7 THz frequency radiation with the possibility to apply the direct laser ablation method in the fabrication of higher frequency optical elements.
3. Polariton excitation in *n*-GaN surface relief gratings was investigated theoretically and experimentally in the vicinity of Reststrahlen band of semiconductor. Design was chosen after thorough optimization of grating parameters (including groove height) using the RCWA method. The applicability of polaritonic *n*-GaN elements for tailored narrowband features in the reflectivity spectrum was demonstrated.
4. Directive and polarized emission of thermally excited polaritons in *n*-GaN surface relief gratings was demonstrated for the first time. Tunable emission features with down to  $10 \text{ cm}^{-1}$  ( $6 \text{ cm}^{-1}$ ) linewidths were observed in experiment (theory), demonstrating the spatial coherence length of  $27\lambda$  ( $50\lambda$ ). The applicability of *n*-GaN SRGS in the fields of tailored narrowband thermal emission as well as coherent signal transfer was proposed.
5. Reflectivity spectra of metal grating coupled GaN/GaN and

GaN/AlN/SiC heterostructures were investigated for the first time. Heterostructures were demonstrated to be suitable for broadening the operational range of surface phonon polaritons. A metal grating coupler was successfully applied for the confinement of light within the heterostructure layers.



## 6. SANTRAUKA

### 6.1 Paveikslų Sąrašas

Santraukoje aptariamų paveikslų sąrašas:

**2.3 pav.** Skirtingų tipų lęšių skerspjūviai: a) klasikinis laužiamasis lęšis; b) klasikinis Frenelio lęšis, kurio zonų matmenys nėra susiję su krintančiosios bangos faze; c) Soreto zoninė plokštelė, pagaminta iš koncentrinų folijos žiedų; d) plokščioji dielektrinė zoninė plokštelė; e) fazę apverčianti zoninė plokštelė; f) daugialiptės fazės Frenelio lęšis su  $p = 4$  pazonėmis, kurio zonose išlaikoma krintančiosios bangos fazė; g) tolydus fazinis Frenelio lęšis [43].

**2.8 pav.** Principinė paviršinių poliaritonų nagrinėjimo schema. Toliemojo lauko šviesa, pasižyminti banginiu vektoriumi  $k_0$  (susidedančiu iš  $k_x$  ir  $k_z$  komponentų), krinta į dviejų aplinkų, aprašomų dielektrinėmis funkcijomis  $\varepsilon_1$  ir  $\varepsilon_2$ , ribą kritimo kampų  $\varphi$ .

**2.13 pav.** Naudojantis 6.6 lygtimi ir lentelėje 6.2 pateikiamais parametrais apskaičiuotos dielektrinės funkcijos: a) Reali dielektrinės funkcijos dalis; b) menama dielektrinės funkcijos dalis ir c) remiantis nagrinėjamos dielektrinėmis funkcijomis apskaičiuoti atspindžio spektrai. Skaičiavimai atlikti keliems variantams: 1 – laisviesiems krūvininkams (*Free carriers*) laikant, jog 6.6 lygtyje fononinis narys yra 0. 2 – nelegiruotam puslaidininkui (*Undoped GaN*), laikant jog lygties 6.6 plazmoninis narys yra lygus 0. 3 – legiruotam puslaidininkui (*Doped GaN*) įskaitant abu lygties 6.6 narius.

**3.5 pav.** Vienmačio periodiškumo gardelės, nagrinėjamos RCWA metodu, principinė schema. Nagrinėjamos trys sritys: pirmoji (*Region I*) – atvira erdvė; antroji (*Region II*) – periodinės gardelės sritis; trečioji (*Region III*) – medžiagos padėklo sritis. Krintančioji banga (*Incident*

*wave*), kampu  $\Theta'$  pasiekia gardelę ir difraguoja į skirtingas atspindėtas (*Back diffracted waves*) ir gardelės praleistas (*Forward diffracted waves*) difrakcijos eiles [123].

**3.6 pav.** Principinė eksperimentiniame tyrime naudoto FTIR schema. **a)** Standartinės konfigūracijos *Nicolet 8700* FTIR spektrometro principinė schema, naudojama bandinių pralaidumo spektrų tyrimui. Kolinuotas vidinio šaltinio (paprastai – globaro) spinduliuotės pluoštas naudojamas pralaidumo spektrų tyrimui. **b)** Principinė spektrometro bandinio skyriaus (*sample compartment*) schema atspindžio matavimo geometrijoje. Šiuo atveju spindulys nukreipiamas į bandinį ir atspindėta spinduliuotė surenkama atgal į optinę ašį atspindžio priedėliu (*reflectivity adapter*). Šioje konfigūracijoje, kritimo kampų intervalo sumažinimui, galima naudoti apskritiminę apertūrą *circular aperture*. **c)** Principinė *Bruker V70* spektrometro bandinio skyriaus schema, naudojant atspindžio priklausomybei nuo kritimo kampo tirti skirtą priedėlį. Šiuo atveju du automatizuoti veidrodžiai yra naudojami krintančiajai spinduliuotei nukreipti į bandinį ir surinkti iš jo. **d)** Išorinio šaltinio FTIR matavimo konfigūracija naudota kampinės bandinio spinduliuotės priklausomybės tyrimui. Plyšelio tipo (*slit*) apertūra šiuo atveju naudojama matuojamų spinduliuotės kampų ribojimui (kampinės apertūros sumažinimui).

**4.3 pav.** Pagamintų  $f = 5$  mm fokuso atstumo daugialiptės fazės Frenelio lęšių (MPFL) SEM nuotraukos. **a)** lęšis su  $p = 4$  pazonėmis ir **b)** lęšis su  $p = 32$  pazonėmis. Adaptuota iš [P1].

**4.2 pav.** Profilometru matuoti pagamintų MPFL, kurių fokuso ilgiai  $f = 5$  mm ir  $f = 10$  mm, skerspjūviai. Adaptuota iš [P1].

**4.6 pav.** Pagamintos Soreto zoninės plokštelės nuotraukos.

**4.7 pav.** Pagaminto  $p = 2$  pazonių Si lęšio SEM nuotrauka, kurioje padidintos sritys lęšio centre ir šone. Intarpas paveikslo viršuje rodo lęšio paviršinės morfologijos matavimo profilometru rezultatą ir numatytąjį profilį. Adaptuota iš [P3].

**4.8 pav.** Eksperimentiniai fokusuoto spindulio detektuojamo signalo (*Signal*) profiliai tolydiems (*kinoforn*)  $f=10$  mm ir  $f=5$  mm fokuso atstumo lęšiams. **a)** ir **b)** skenavimo fokuso plokštumoje  $xy$  rezultatai. **c)** ir **d)** skenavimo fokuso gylyje ( $xz$ ) rezultatai. Kiekvieno paveikslo šonuose pateikiami spindulio skerspjūviai maksimalaus signalo koordi-

natėje tiesinėje skalėje. **e)** tiriama išlęšiais fokusuotų spindulių skerspjūvių palyginimas logaritminiu masteliu. Palyginimui pridedamas nefokusuoto (*unfocused*) spindulio signalo lygis. Adaptuota iš [P1].

**4.9 pav.** Maksimalaus eksperimentinio fokusuoto spindulio signalo (*Signal*) priklausomybė nuo lęšio pazonių skaičiaus (pavaizduota taškais). Teorinė lęšio efektyvumo (*Efficiency*) priklausomybė nuo pazonių skaičiaus pavaizduota linija. Adaptuota iš [P1].

**4.10 pav. a)** Fokusuoto spindulio detektuojamo signalo (*Signal*) ir **b)** pločio pusėje aukščio (FWHM) vertės išilgai optinės sistemos ašies. Lęšis pozicionuojamas plokščiaja savo puse link THz jutiklio (*Zone plane surface to: detector*) arba link šaltinio (*Zone plane surface to: emitter*). Adaptuota iš [P1].

**4.15 pav.** Eksperimentiniai 5 cm skersmens ir 3 cm fokuso atstumo MPFL fokusuoto spindulio profiliai *xy* ir *xz* plokštumose. Adaptuota iš [P2].

**4.16 pav. a)** Skiriamajai gebai tirti skirto taikinio terahercinio vaizdinimo, naudojant 0.58 THz dažnio spinduliuotę, rezultatas. Skenavimas atliktas  $0,1 \times 0,1 \text{ mm}^2$  žingsniais. Spinduliuotė fokusuota 3 cm fokuso atstumo lęšiu. Intarpe pateikiama optinė taikinio nuotrauka. **b)** Matuoto signalo skerspjūviai skirtingose taikinio zonose. Atskiros atviros zonos išskiriamos, kai jų matmenys didesni kaip 1 mm. **c)** Kortelės su „paslėpta“ USB laikmena vaizdinimo rezultatas. **d)** Vaizdinimui naudotos kortelės su „paslėpta“ USB laikmena optinė nuotrauka, kurioje žaliai pažymėta laikmenos sritis. Adaptuota iš [P2].

**4.17 pav.** Normuotų skirtingų difracinių lęšių fokusuoto spindulio skerspjūvių palyginimas:  $1 - p = 16; f = 30 \text{ mm}; d = 50 \text{ mm}$  [P2]

$2 - p = 16; f = 10 \text{ mm}; d = 17 \text{ mm}$  [P2]

$3 - p = 16; f = 5 \text{ mm}; d = 17 \text{ mm}$  [P2]

$4 - p = 1; f = 5 \text{ mm}; d = 17 \text{ mm}$  [134] Adaptuota iš [P2].

**4.19 pav.** Stendo, naudoto 4,7 THz skirtingsiems lęšiams charakterizuoti, principinė schema. Adaptuota iš [P3].

**4.21 pav. a)** Skirtingais lęšiais fokusuoto 4,7 THz pluošto intensyvumo skerspjūviai. **b)** Pluošto pločio priklausomybė nuo skenavimo koordinatės *z*. Intarpas rodo MPFL2 lęšio spindulio pasiskirstymą *xy* plokštumoje charakteringą visiems trimis bandiniais. Adaptuota iš [P3].

**4.23 pav.** Normuoto ploto po eksperimentiniu spindulio skerspjū-

viu priklausomybė nuo lęšio kampo su optine sistemos ašimi. Intarpe: MPFL8 lęšiu fokusuoto pluošto skerspjūviai skirtingais lęšio pasukimo kampais. Adaptuota iš: [P3].

**4.24 pav. a)** Principinė bandinio su paviršine gardele (SRG) schema, kurioje pavaizduota spindulio kritimo geometrija. Dydžiai  $W$ ,  $P$  ir  $h$  atitinka gardelės dizaino plotį, periodą ir aukštį.  $k$  and  $k_1$  atitinkamai simbolizuoja krantinčios ir atspindėtos šviesos banginius vektorius, kai elektrinio lauko vektoriai orientuoti bandinio paviršiaus plokštumoje TE poliarizacijos atveju ir spindulio kritimo plokštumoje TM poliarizacijos atveju.  $\varphi$  rodo spindulio kritimo kampą. **b)** Impulso tvermės dėsnio išpildymo schema remiantis 2.35 lygtimi. **c)** ir **d)** pavaizduotos eksperimentiškai pagaminto bandinio SEM nuotraukos.  $W_1$  ir  $W_2$  žymi eksperimentiškai pagamintos gardelės viršutinį bei apatinį pločius. Adaptuota iš [P4].

**4.25 pav.** Eksperimentiškai išmatuotas (*Experiment*) ir teoriškai sumodeliuotas (*Theory*) nepoliarizuotos šviesos atspindžio spektrai netekstūruotam  $n$ -GaN padėklui. Geriausios atitikties dielektrinės funkcijos parametrai, naudoti modeliavimui, išvardinti 6.2 lentelėje.

**4.26 pav.** Modeliuotų TM poliarizacijos atspindžio spektrų priklausomybė nuo geometrinių gardelės pločio **a)** ir periodo **b)** parametru esant  $\varphi = 26^\circ$  kritimo kampui. Fiksuoti parametrai pažymėti atitinkamuose paveiksluose. **b)** dalyje brūkšnine taškine kreive pažymėta analitiškai apskaičiuota SPPHP ypatumo dispersija. Adaptuota iš [P4].

**4.28 Pav.** Modeliuotos TM poliarizacijos atspindžio (**a-c**) ir spinduliuojamosios gebos (**d-f**) koeficientų spektrų priklausomybės nuo krantinčiosios spinduliuotės banginio vektoriaus komponentės  $x$  kryptimi (kritimo kampo) atitinkamai SRG-1, SRG-2 ir SRG-3 bandiniams. Atitinkamų SPPHP ypatumų eilės  $M$  (pagal 2.35 lygtį) pažymėtos paveiksluose.

**4.29 pav.** Matuotas (taškai) ir skaičiuoti (kreivės) SRG-1 bandinio atspindžio (*Reflectivity*) spektrai fiksuoto  $26^\circ$  kritimo kampo geometrijoje. Ištininė kreivė rodo spektrą, skaičiuotą diskrečiam  $26^\circ$  kritimo kampui, o brūkšninė rodo spektrą  $24-28^\circ$  kampų intervale vidurkį, gerai atitinkantį eksperimento rezultatą.

**4.30 pav.** Teoriškai modeliuota (*Theory*) ir eksperimentiškai išmatuota (*Experiment*) atspindžio spektrų priklausomybės nuo spinduliuo-

tės kritimo kampo  $\varphi$ . Vertikalios linijos pateikiant teorinį rezultatą rodo eksperimentinio matavimo režius. Adaptuota iš [P4].

**4.31 pav.** Šiluma žadinamos SRG-1 bandinio spinduliuotės matavimų rezultatai. **a)** Matuoti spinduliuotės (taškai) ir apskaičiuoti spinduliuojamosios gebos (kreivės) spektrai, kai yra skirtingi kritimo kampai. Vaizduojamas skirtumas tarp rezultatų, gautų esant TM ir TE poliarizacijoms, taip stebint stipriau išreikštą SPPHP rezonansą. **b)** ir **c)** atitinkamai visos skaičiuotos spinduliuojamosios gebos koeficiento ir matuotos bandinio spinduliuotės skirtuminių spektrų kampinės priklausomybės. Teoriniame rezultate naudotas vidurkinimas  $2^\circ$  kampinės apertūros intervale. Eksperimento rezultatai matuoti  $2^\circ$  žingsniais. Rezultatų trūkis atitinka naudoto poliarizatoriaus sugerties liniją. Adaptuota iš [P4].

**4.32 pav. a)-c)** Apskaičiuotų spinduliuojamosios gebos ir **d)-f)** matuotų spinduliuotės spektrų priklausomybė nuo krintančiosios spinduliuotės banginio vektoriaus komponentės  $x$  kryptimi SRG-1 (**a,d**), SRG-2 (**b,e**) ir SRG-3 (**c,f**) bandiniams. Brūkšninės linijos teoriniuose rezultatuose iliustruoja eksperimento rezultatų režius.

**4.33 pav.** Spindulio stebėjimo kampo, esant fiksuotiems spinduliuotės dažniams  $\Delta\varphi$ , nustatymo pavyzdžiai **a)** teoriniu modeliuotos spinduliuojamosios gebos (*emisivity*) ir **b)** eksperimentiniu spinduliuotės matavimo (*emission*) atvejais. Skaičiai žymi vertes, nustatytas pagal Lorenco tipo funkcijų (pilkos kreivės) FWHM parametrus. Teorinių rezultatų atveju skliaustuose pateikiamos ypatumų puspločių vertės, nustatytos rankiniu būdu. Eksperimento rezultatai dėl aiškumo tarpusavyje perstumti 0,1 verte.

**4.34 pav.** Erdvinio koherentiškumo ilgio  $L_{SC}$  priklausomybė nuo maksimalios spinduliuotės stebėjimo kampo ( $\varphi_0$ ) SRG-1 bandinio atveju.

**4.37 pav.** Principinės tirtų heterostruktūrų bandinių schemas (**a**) – bandinys MGC-1 ir **b)** – bandinys MGC-2). Brūkšninė linija vaizduoja dvimačių dujų formavimosi sritį GaN/AlGaN sandūroje. **c)** Principinė modeliuotos heterostruktūros, atitinkančios bandinį MGC-2, schema su kartu pavaizduota spinduliuotės kritimo geometrija.  $k_g$  iliustruoja gardelės banginį vektorių,  $\varphi$  – spinduliuotės kritimo kampą  $xz$  spindulio kritimo plokštumoje. Dėl mažų optinių storių tiriamame spektriniame ruože AlGaIn bei dvimačių dujų kanalo sluoksniai į modeliavimą neįt-

raukiami. Adaptuota iš [P6].

**4.38 pav.** Matuoti (taškai) ir modeliuoti (kreivės) netekstūruotų MGC-1 ir MGC-2 bandinių atspindžio spektrai. Geriausios atitikties parametrai, naudoti dielektrinių funkcijų skaičiavimams, išvardyti 6.5 lentelėje. Adaptuota iš [P6].

**4.39 pav.** Modeliuotų TM poliarizacijos,  $20^\circ$  kritimo kampo atspindžio spektrų priklausomybė nuo gardelės periodiškumo skirtingoms heterostruktūroms: **a)** MGC/GaN (MGC-1 bandinys); **b)** MGC/SiC; **c)** MGC/GaN/AlN/SiC (MGC-2 bandinys); **d)** MGC/AlN/SiC; **e)** MGC/GaN/AlN/SiC, kurių viršutinių sluoksnių storiai invertuoti; **f)** MGC-GaN/AlN/SiC. Vertikalios linijos iliustruoja eksperimentinių bandinių spektrus. Apskritimai žymi modas, kurioms buvo apskaičiuoti lauko skirstiniai. Brūkšninės linijos iliustruoja atitinkamas poliaritonų modas. **a)** ir **c)** dalyse. Adaptuota iš [P6].

**4.40 pav.** Matuoti (taškai) ir modeliuoti (kreivės) atspindžio spektrai. **a)** nepoliarizuoti MGC-1 bandinio spektrai. **b)** ir **c)** atitinkamai TE ir TM poliarizuoti MGC-2 bandinio spektrai. Apskritimai žymi modas, kurioms buvo apskaičiuoti lauko pasiskirstymai. Adaptuota iš [P6].

**4.41 pav.** Modeliuoti bandinio MGC-1 magnetinio lauko skirstiniai gardelės aplinkoje. Skaičiavimo dažniai ir gardelės banginiai vektoriai pažymėti paveiksluose. Skirstiniuose vaizduojamos modos taip pat pažymėtos apskritimais **4.39 pav. a)**. Metalinės gardelės padėtis pažymėta juodomis linijomis. Vaizduojant pasirinktu masteliu, padėklas baigiasi ties  $z = 500 \mu\text{m}$  koordinate ir heterostruktūros sluoksniai yra išdėstyti virš jo. Adaptuota iš [P6].

**4.43 pav.** MGC-2 bandinio magnetinio lauko skirstiniai gardelės aplinkoje. Skaičiuojami dažniai pažymėti paveiksluose, taip pat pažymėti apskritimais **4.39 pav. c)** ir **4.40 pav. c)**. Modeliuotos gardelės periodas  $-7 \mu\text{m}$ .

## 6.2 Įvadas

Terahercinių dažnių ruožas (THz), aprėpiantis sritį nuo 0,1 iki 10 THz, šiuo metu yra plačiai tyrinėjamas. Tyrimai yra skatinami daugybės unikalių šio ruožo spinduliuotės savybių ir jų lemiamų pritaikymo galimybių. Dėl itin mažos spinduliuotės kvanto energijos

(nejonizuojančios prigimties) ir daugelio medžiagų skaidrumo šiame dažnių ruože THz spinduliuotė gali pakeisti rentgeno spindulius, pavyzdžiui, medicinoje, skenuojant dantis, navikinius, epiderminius ir kitus audinius [1,2]. Stipri spinduliuotės skvarba leidžia THz sistemas taikyti įvairiose pramoninės gamybos kokybės kontrolės sistemose [3]. Saugumo srityje buvo pademonstruotas THz naudojimas siuntų skenavimui, narkotikų, sprogmenų [4], ir netgi po rūbais paslėptų daiktų identifikavimui oro uostuose ar kitose svarbiose zonose [5]. THz spinduliuotė naudojama astronomijoje, tyrinėjant cheminę objektų sudėtį ir, pavyzdžiui, reliktinę Visatos spinduliuotę [6,7].

Itin svarbus ir sparčiai ryškėjantis THz paremtų sistemų poreikis didelio duomenų srauto komunikacijose. Numatoma, kad dėl eksponentinio visuomenei reikalingo perduodamo duomenų srauto didėjimo netgi dabar vystoma 5G technologija po keleto metų nebegalės patenkinti perduodamo srauto poreikio [4, 8, 9]. Vienas iš šios problemos sprendimo būdų – tai THz technologijomis paremtas duomenų perdavimas, šiuo metu leidžiantis keleto GB/s greičiu perduoti duomenis tiesioginėse *line of sight* sistemose [10].

Visiems minimiems taikymams reikalingi trys pagrindiniai komponentai: siųstuvai, nukreipiančioji optika ir imtuvai. Siekiant plataus sistemų pritaikymo visi šie komponentai turi pasižymėti mažais matmenimis ir lengva bei pigia gamyba. **Pirmojoje šio darbo dalyje** nagrinėjama nukreipiančiosios optikos sritis. Tiriama difrakcinės optikos elementai (DOE), skirti THz pluošteliui energijai koncentruoti erdvėje, konkrečiai – Soreto zonų plokštelės lęšiai (SZPL) ir daugialaiptės fazės Frenelio zonų plokštelės (*multilevel phase Fresnel zone plate*) lęšiai (MPFL), tinkami fokusuoti 0,6 bei 4,7 THz dažnių spinduliuotę. Kuriamas šių elementų dizainas, atliktas fokusavimo savybių modeliavimas, pagaminti numatytų parametrų bandiniai palyginti paprastu, pigiu ir iteraciniam komponentų kūrimui patogiu lazerinės abliacijos (DLA) metodu. Pagamintų bandinių fokusavimo savybės buvo ištirtos eksperimentiškai. Pademonstruotas gamybos proceso tinkamumas elementų kūrimui, taip pat pagamintų elementų panaudojimas eksperimentinėje THz vaizdinimo sistemoje.

**Antrojoje disertacijos dalyje** dėmesys skiriamas aukštesnių dažnių (mažesnio bangos ilgio) spinduliuotei – vidurinei infraraudonajai sri-

čiai (MIR). Šis spektrinis ruožas dažniausiai nagrinėjamas kaip plačiajuostės šiluminės juodų ar „pilku“ kūnų spinduliuotės sritis. Nepaisant išsamaus šios srities aprašymo šiuo metu atrandama vis naujų jos panaudojimo sričių, pavyzdžiui, susijusių su spinduliniu įkaitusių objektų aušinimu dienos metu [12,13]. Pastaruoju metu atsiranda ir gana egzotiškų siūlymų taikyti siaurajuoste spinduliuote pasižyminčius šiluminius šaltinius fotoninių komponentų maitinimui, naudojant, pavyzdžiui, kompiuterių procesorių skleidžiamą šilumą. [14]

Siekiant sukurti siaurajuosčius tam tikro dažnio šiluminius šaltinius, šiame darbe siūloma naudoti paviršinius fonon-polaritonus (SPhP), žadinamus puslaidininkinėse struktūrose [15, 16]. SPhP modos, žadinamos THz ir MIR dažniuose, pasižymi mažais nuostoliais, leidžiančiais pasiekti itin aukštos kokybės rezonansus ir stiprią šviesos lokalizaciją. Jomis paremti šaltiniai spinduliuoja siaurajuostę, derinamo dažnio šviesą puslaidininkio fononų srityje – Reštralo juostoje (RB) [12, 13, 17]. Šiame darbe pasiūlyti du metodai, kuriais galima išplėsti polaritonų darbinę dažnių sritį. Pirmasis – tai hibridinių plazmon-fonon-polaritonų žadinimas stipriai legiruoto GaN paviršiuje, o antrasis – heterostruktūros, sudarytos iš skirtingų polinių puslaidininkių, viena kitą papildančiomis Reštralo juostomis, naudojimas. Atliktas tiek teorinis tiriamų elementų modeliavimas tikslios susietųjų bangų analizės (*Rigorous Coupled Wave Analysis*) metodu, tiek eksperimentinis pagamintų elementų tyrimas. Pirmuoju atveju pademonstruotas paviršinių puslaidininkinių gardelių (SRG), o antruoju – metalinių paviršinių gardelių susiejiklių (MGC) pasitelkimas polaritonų žadinimui ir praktiniam naudojimui.

Abiem atvejais tiek teoriniu modeliavimu, tiek eksperimentiniu atspindžio charakteristikų tyrimu pademonstruotas siaurajuosčių rezonansinių SPPPhP ypatumų sužadinimas. Stebimų ypatumų dažnis esant pasirinktam šviesos kritimo kampui, yra keičiamas parenkant gardelės periodą. Pademonstruotas siaurajuostis (koherentinis) šiluma sužadintas SPPPhP modų spinduliuavimas puslaidininkio Reštralo juostoje. Įvertintas SPPPhP šaltinių erdvinio koherentiškumo ilgis. Tiriant heterostruktūras, stebėtų modų prigimtis paaiškinta naudojantis modeliavimo rezultatais.

Tiek Frenelio optikos, tiek polaritonikos principai yra laisvai deri-



nami dažnių erdvėje, priderinant struktūrų parametrus prie naudojamų polinių puslaidininkinių savybių. Tikimasi, kad ši disertacija padės iš pažiūros skirtingus, tačiau tais pačiais difrakcijos principais paremtus, Soreto ir Frenelio lęšius ir poliaritonikos komponentus bei šaltinius pritaikyti kuriant naujus, integruotus šaltinius ir (ar) nukreipiamosios optikos prietaisus.

### 6.2.1 Darbo tikslas

Difrakcinės optikos ir gardelėmis žadinamos poliaritonikos komponentų kūrimas ir tyrimas spektroskopinio vaizdinimo sistemoms bei taikymui THz-IR dažnių juostoje.

### 6.2.2 Išsikelti uždaviniai

- Ištirti Si bei metaline folija paremtų difrakcinės optikos komponentų veikimą ir taikomumą vaizdinimo sistemose, kurių veikimas paremtas 0,6 ir 4,7 THz dažniais.
- Ištirti paviršinių plazmon-fonon-poliaritonų dispersiją polinių puslaidininkinių Reštralo juostose.
- Ištirti seklių gardelių, suformuotų stipriai legiruoto  $n$ -GaN paviršiuje, tinkamumą generuoti koherentinį šiluminį spinduliavimą.
- Ištirti metalinių gardelių ant AlGaN/GaN/SiC heterostrukturų tinkamumą fonon-poliaritonų modų sužadimui Reštralo juostoje.

### 6.2.3 Naujumas

- Taikant lazerinio abliavimo metodiką, sukurti skirtingais pazonių skaičiais pasižymintys daugialiptės fazės Frenelio zonų lęšiai, skirti 0,6 THz dažniui. Nustatyta šiuo metodu pagamintų lęšių pazonių skaičiaus įtaka lęšio fokusavimo efektyvumui, taip pat pademonstruotas lęšio pritaikymas vaizdinimo sistemoje.
- Lazerinio abliavimo metodika pagamintos neprilaikomos Soreto zoninės plokštelės ir silicio daugialiptės fazės Frenelio zonų lę-

šiai skirti, 4,7 THz dažnio spinduliuotei. Charakterizuotas šių elementų veikimas.

- Atliktas poliaritonų žadinimo stipriai legiruoto  $n$ -GaN paviršinių gardelių struktūrose teorinis bei eksperimentinis tyrimas. Atliktas teorinis modeliavimas, kurio pagrindu parinkti optimalūs struktūrų geometriniai parametrai ir eksperimentiškai pagaminti komponentai. Atlikus atspindžio spektrų priklausomybių nuo gardelės periodo bei šviesos kritimo kampo tyrimą, nustatyta, kad pagaminti komponentai pasižymi teoriniame dizaine nustatytais atspindžio spektrų savybėmis. Taip pademonstruotas tiek modeliavimo, tiek gamybos metodo tinkamumas pasyvių komponentų, pasižyminčių specifinėmis spektrinėmis savybėmis, kūrimui.
- Atliktas šiluma žadinamos  $n$ -GaN paviršinių gardelių plazmon-fonon-poliaritonų spinduliuotės tyrimas. Parodyti siaurajuosčiai, keičiamo dažnio spinduliuotės ypatumai, pasižymintys koherentinėmis savybėmis ir charakterizuojami  $50 \lambda$  eilės erdvinio koherentiškumo ilgiais, taip parodant tiriamų struktūrų tinkamumą keičiamo spektro šiluminės spinduliuotės šaltiniams bei signalų pernašai.
- Atliktas heterostruktūrų su metalinėmis paviršinėmis gardelėmis atspindžio spektrų tyrimas. Parodytas heterostruktūrų panaudojimas fonon-poliaritonų darbinio dažnių ruožo praplatinimui. Modeliavimu pademonstruotas šviesos lokalizavimas vidiniuose heterostruktūros sluoksniuose.

### 6.2.4 Ginamieji teiginiai

- Tiesioginė lazerinė abliacija yra tinkama gaminti daugialaiptės fazės Frenelio zonų lęšius, skirtus 0,6 THz dažniui, o šie komponentai yra tinkami naudoti THz vaizdinimo taikymuose.
- Tiesioginė lazerinė abliacija yra pranaši kuriant metalines Soreto zonines plokšteles bei silicio daugialaiptės fazės Frenelio lęšius, skirtus 4,7 THz ir aukštesnio dažnio spinduliuotei fokusuoti.
- Paviršiniai plazmon-fonon-polaritonai yra optiškai sužadunami sekliose  $n$ -GaN paviršinėse gardelėse, spektriniame  $560\text{--}1000\text{ cm}^{-1}$  ruože, kurį lemia hibridinių plazmon-fononų modų dažniai.
- Paviršiniai plazmon-fonon-polaritonai, termiškai sužadinti  $n$ -GaN paviršinėse gardelėse, demonstruoja koherentinę keičiamo dažnio emisiją spektriniame stipriai legiruoto puslaidininkio Reštrlio juostos ruože.
- Metalinės paviršinės gardelės ant GaN/GaN ir GaN/AlN/SiC heterostrukturų paviršiaus yra tinkamos optiniams infraraudonosios srities komponentams, turintiems pasirinktas atspindžio spektrų savybes kurti.

### 6.2.5 Publikacijos ir asmeninis indėlis

Disertacijoje remiamasi septyniomis publikacijomis, kurių sąrašas pateikiamas 1.7 skyriuje. Sąrašė taip pat nurodomos septynios studijuojant doktorantūroje atspausdintos, tačiau tiesiogiai su disertacijos tema nesusijusios publikacijos. Studijuojant doktorantūroje disertacijos tematika taip pat buvo pristatyta 18 konferencijų pranešimų (išvardyti 1.7 skyriuje) ir 22 pranešimai, tiesiogiai nesusiję su disertacijos tema.

Disertacijos autoriaus **asmeninis indėlis** į pristatomus rezultatus:

Atliktas Frenelio optikos komponentų, skirtų 0,6 THz spinduliuotei fokusuoti, eksperimentinis charakterizavimas, duomenų analizė ir prisidėta ruošiant publikacijas. Paruošti ir atlikti pralaidumo matavimo bei vaizdinimo eksperimentai. Autorius dalyvavo analizuojant ir ruošiant

publikuoti 4,7 THz spinduliuotės fokusavimo elementų charakterizavimo rezultatus.

Teoriškai tiriant poliaritonikos komponentus atliktas pirminio modeliavimo kodo modifikavimas tiriamam spektriniam ruožui ir atlikti visi skaičiavimai tikslios susietųjų bangų analizės metodika. Sukurti  $n$ -GaN poliaritoninių bandinių dizainai, komandiruotės metu atlikta  $n$ -GaN bandinių gamyba. Atliktas išsamus poliaritoninių bandinių eksperimentinis tyrimas, rezultatų analizė, paruoštos publikacijos ir pristatyti konferencijų pranešimai.

### 6.2.6 Dalyvavimas projektuose

Moksliniai tyrimai, atlikti dalyvaujant projektuose:

1. Lietuvos mokslo tarybos projektas „Kompaktiški integriniai THz komponentai ir spektroskopinio THz vaizdinimo sistemos“ (KIT-KAS), LAT-04/2016.
2. Lietuvos mokslo tarybos visuotinė dotacija „Kompaktiški terahercinės spinduliuotės plazmoniniai emiteriai“ (KOTERA-PLAZA), 01.2.2-LMT-K-718-01-0047.
3. Europos kosmoso agentūros projektas „Directive transistor-based THz detectors“ (THzFET), 3500-T41.
4. Lietuvos mokslo tarybos projektas „Terahercinio dažnio plazmoninių bangų nestabilumai GaN/AlGaN nanovielutėse“ (TERAGANWIRE), S-LL-19-1.

## 6.3 Teorinis įvadas

### 6.3.1 Difrakciniai elementai

Klasikiniai optiniai THz ruožo komponentai, kaip antai laužiamieji plastikiniai lęšiai bei atspindintys parabolinės geometrijos (OAP) veidrodžiai, pasižymintys dideliais matmenimis bei svoriu, riboja THz sistemų pritaikomumą modernioje elektronikoje [20]. **Difrakcinės optikos komponentai (DOE)** dėl savo sąlyginai paprastos gamybos, itin mažų matmenų ir masės bei galimybės gaminti lengvai integruojamus Si elementus yra itin patraukli alternatyva THz optoelektronikai formuojant įvairios geometrijos pluoštus [22–24]. Pagrindinis DOE panaudojimą ribojantis veiksnys yra dielektriniai medžiagų parametrai. Kiekvienam konkrečiam dažniui skirti komponentai turi būti gaminami iš kruopščiai parinktos, tinkamo lūžio rodiklio ir maža sugertimi pasižyminčios medžiagos.

Šiuo metu sub-THz sistemos, pasitelkiančios difrakcinius elementus, gaminamus iš plastiko, dažniausiai naudojamos skenuojant objektus saugumo [25] ar kokybės kontrolės [26,27] srityse. Taip pat tikimasi tokius elementus naudoti 6G duomenų perdavimo sistemose. Plastikiniai elementai greitai ir patogiai gaminami šlifavimo [36], 3D spausdinimo [41,42] bei kitais metodais.

THz taikymams spektroskopiniam vaizdinimui [4] ir astronomijai [6] reikalingi komponentai, veikiantys esant dažniams iki kelių THz. Čia susiduriama su gamybos problematika, nes, mažėjant spinduliuotės bangos ilgiui, reikalingos kitos medžiagos dėl per didelės plastikų sugerties ir proporcingai kylančių komponentų kokybės reikalavimų [28].

#### **MPFL dizainas:**

Soreto zoninių plokštelių bei daugialiptės fazės Frenelio lęšių veikimas yra lemiamas šviesos difrakcijos nuo lęši sudarančių koncentrinų žiedų. Charakteringi įvairių komponentų skerspjuviai pateikiami **2.3 pav. c ir f**). Siekiant pagaminti daugialiptį fazinį Frenelio lęšį, reikalingi zonų pločiai ir aukščiai aprašomi atitinkamai lygtimis [57]:

$$b_s = \sqrt{\frac{2s(f + w/2)\lambda_0}{p} + \left(\frac{n\lambda_0}{p}\right)^2} \quad (6.1)$$

ir,

$$t_s = \frac{\lambda_0}{p(n-1)} \quad (6.2)$$

čia  $s$  yra pazonės numeris;  $f$  – elemento fokuso atstumas;  $w$  – plokštelės, iš kurios gaminama, storis;  $\lambda_0$  – darbinis bangos ilgis;  $p$  – pazonių skaičius vienoje Frenelio zonoje;  $n$  – lęšio medžiagos lūžio rodiklis.

### Lęšio parametrai:

Pagrindinis pagaminto lęšio fokusavimo gebos parametras – tai fokusavimo stiprinimo koeficientas  $G_f$  [57]:

$$G_f = \left(\frac{E_f}{E_0}\right)^2 = N_0^2 + 1 = \left(\frac{a_0^2}{\lambda_0 f_1}\right)^2 \quad (6.3)$$

Fokusavimo stiprinimo koeficientas apibrėžiamas kaip elektrinio šviesos lauko intensyvumo  $E_f$  fokuso taške ir nefokusuoto spindulio elektrinio lauko intensyvumo  $E_0$  santykio kvadratas. Teoriškai  $G_f$  taip pat gali būti išreikštas per lęšio spindulį  $a_0$ , darbinį bangos ilgį  $\lambda_0$  ir lęšio fokuso atstumą  $f_1$ .

Fokusavimo efektyvumas  $e_f$  Soreto zoninės plokštelės atveju yra ribotas jos geometrijos bei difrakcijos procesas ir yra lygus  $1/\pi^2 \approx 10\%$ . Daugialaiptės fazės Frenelio lęšio efektyvumas priklauso nuo pazonių skaičiaus ir idealiu tolydaus (*kinoforn*) lęšio atveju siekia 100%. Tolydaus lęšio gamyba yra praktiškai sudėtinga, tad bendru atveju randamas optimalus variantas tarp dizaino sudėtingumo (pazonių skaičiaus  $p$ ) ir fokusavimo efektyvumo. Teorinė fokusavimo efektyvumo priklausomybė nuo laiptelių skaičiaus  $p$  lemiamo fazės žingsnio  $\Delta\Phi = \Phi/p$  yra apibrėžiama kaip [57]:

$$e_f = \frac{\sin^2(\Delta\Phi/2)}{(\Delta\Phi/2)^2} \quad (6.4)$$

Ekspirimentiškai fokusavimo efektyvumas buvo skaičiuojamas

vertinant pagrindinėje fokuso dėmėje integruoto signalo santykį su nefokusuoto spindulio integralu. Vertinant šį santykį taip pat buvo atsižvelgiama į DLA apdirbimo metu atsirandančią sugertį bandinio paviršiuje.

### **DOE gamyba.**

Si pagrindo DOE gamyba THz ruože galima keletu metodų. Mechaniniai gremžimo ar šlifavimo [36] metodai pasižymi nepakankamu tikslumu gaminant THz ar kelių THz eilės dažniams skirtus komponentus. Itin tiksli elementų gamyba galima ultravioletinės fotolitografijos bei reaktyvaus jonų ėsdinimo metodika [28–30, 69]. Nepaisant gamybos metodo tikslumo, daugialaipčių struktūrų gaminimas litografijos būdu reikalauja daugelio litografijos žingsnių, smarkiai didinančių gamybos sudėtingumą ir savikainą [30]. Tai ypač svarbu iteraciniame komponentų vystymo etape, kai tam tikro dizaino vienetinio elemento pagaminimo kaina tampa itin didelė.

Šiame darbe siūloma taikyti lazerine abliacija paremtą MPFL gamybos metodą. Lazerinė abliacija – tai procesas, kurio metu paviršinis apdirbamos medžiagos sluoksnis sugeria itin didelį lazerio spinduliuotės kiekį ir iš kietos būsenos pereina tiesiai į dujinę [72, 73]. Lazerine abliacija pagamintos Soreto zoninės plokštelės buvo pademonstruotos anksčiau tyrimuose [54, 64, 65]. Taip pat jau buvo pademonstruotos DLA pagamintos antirefleksinės SI struktūros [9, 75].

DLA gamybos procesas yra rastrinės prigimties, t.y. skenuojami lazerio impulsai gali būti nukreipiami į bet kurį apdirbamo bandinio paviršiaus tašką. Apdirbamo bandinio dizainas dėl rastrinio apdirbimo gali būti laisvai ir greitai keičiamas vykdant iteracinę elementų gamybos ir charakterizavimo procesą. Unikalaus dizaino vienetinio bandinio, reikalingo iteraciniam komponentų ar prietaisų vystymui, kaina tokiu atveju tampa gerokai mažesnė nei kitais, masinei gamybai pritaikytais, metodais.

### **6.3.2 Poliaritonika**

Paviršiniaisiais plazmon-poliaritonais (SPP) paremta nanofotonika yra plačiai žinoma ir nagrinėjama lokalizuojant UV bei regimojo spektrinio

ruožo šviesą, bangolaidinėse struktūrose ir ir taikant ją kitais atvejais [78]. Nors plazmonikos sritis gana ištyrinėta, net ir šiuo metu atsiranda vis naujų plazmonikos taikymo novatoriškose 2D struktūrose būdų [12, 15]. Paviršiniai fonon-poliaritonai (SPhP) yra SPP atitikmuo THz–MIR spektro ruože. SPhP yra žadinami polinių puslaidininkių paviršiuje, spektrinėje Reštraliio srityje ir pasižymi eile mažesniais charakteringais nuostoliais nei SPP. Maži nuostoliai leidžiančia stebėti siaurus, didelio kokybės faktoriaus rezonansus ir stiprią šviesos lokalizaciją [82, 87].

SPhP paremti keičiamo spinduliuotės spektro prietaisai gali būti taikomi termofotovoltiniams prietaisams, spinduliniam prietaisų ar medžiagų aušinimui dienos metu [88], cheminiams IR jutikliams [89, 90], biojutikliams [91], fotoniniams komponentams [14] ir kt. Visais šiais taikymo atvejais reikalingi siaurajuosčiai, specifinių bangos ilgių šaltiniai, šiuo metu sunkiai realizuojami dabartinėmis šviesos diodų ar kvantinių kaskadinių lazerių technologijomis.

### **Paviršinių poliaritonų dispersija.**

Paviršinių poliaritonų dispersija yra dažnai nagrinėjama 2D sistemoje, kurią sudaro dvi besiribojančios pusiau begalinės sritys, pavaizduotos **2.8 pav.** Šios sritys yra aprašomos dielektrinėmis funkcijomis  $\epsilon_2$  (sritis, iš kurios krinta spinduliuotė, konkrečiu atveju atvira erdvė) ir  $\epsilon_1$  (padėklo, konkrečiu atveju puslaidininkio, dielektrinė funkcija). Tirmoje geometrijoje poliaritono dispersija gali būti aprašoma lygtimi [92]:

$$k_x = k_0 \sqrt{\frac{\epsilon_1 \epsilon_2}{\epsilon_1 + \epsilon_2}} \quad (6.5)$$

čia  $k_x$  yra poliaritono banginis vektorius, o  $k_0$  – krintančios šviesos banginis vektorius. Pagrindiniai poliaritono dispersijos ypatumai yra šie: padėklo dielektrinė funkcija turi būti neigiamos realiosios dalies ir savo moduliui didesnė už viršutinės srities dielektrinės funkcijos realiąją dalį ( $|\epsilon'_1| > |\epsilon'_2| = 1$ ). Ši sąlyga yra tenkinama metalų ir oro sandūroje žemiau paviršinio metalo plazmono dažnio bei poliniuose puslaidininkiuose, spektrinėje Reštraliio juostoje.

Kitas svarbus aspektas yra tas, kad tarp šviesos bangos vektoriaus komponentės  $x$  kryptimi ir poliaritono bangos vektoriaus bendru atveju yra neatitikimas. Šis impulso tvermės dėsnio pažeidimas neleidžia



vykti tolumo lauko šviesos ir poliaritono lygiame medžiagos paviršiuje sąveikai (*coupling*). Impulso tvermės dėsnio išpildymui, naudojami susiejikliai (*couplers*).

### Legiruoto puslaidininkio dielektrinė funkcija

Siekiant aprašyti poliaritonų formavimąsi tam tikros medžiagos paviršiuje, būtina aprašyti tos medžiagos dielektrinę funkciją. Šioje disertacijoje nagrinėjamu atveju legiruoto puslaidininkio dielektrinė funkcija yra aprašoma fononiniu (gardelės svyravimų) ir plazmoniniu (legiruojant įterptų krūvininkų osciliacijų) nariais kaip [94]:

$$\varepsilon_s = \varepsilon_\infty \left( \frac{v_{LO}^2 - v^2 - iv\gamma_{LO}}{v_{TO}^2 - v^2 - iv\gamma_{TO}} - \frac{v_p^2}{v^2 + iv\gamma_p} \right) \quad (6.6)$$

čia  $\varepsilon_\infty$  – aukštadažnė puslaidininkio dielektrinė konstanta;  $v_{TO}$ ,  $v_{LO}$ ,  $v_p$ , ir  $\gamma_{TO}$ ,  $\gamma_{LO}$ ,  $\gamma_p$  – atitinkamai skersinio optinio (TO), išilginio optinio (LO) ir laisvųjų krūvininkų plazmono dažniai bei slopinimo parametrai;  $v$  – dažnis, darbe nusakomas atvirkštiniais centimetrais kaip  $v = 1/\lambda [\text{cm}^{-1}]$ .

Dielektrinės funkcijos realioji ir menamoji dalys, taip pat apskaičiuoti atspindžio spektrai nelegiruotam puslaidininkiiui, laisviesiems krūvininkams ir legiruotam puslaidininkiiui pavaizduoti **2.13 pav.** Šiam skaičiavimui naudoti parametrai, aktualūs disertacijoje, yra išvardyti 6.2. Kaip matyti, neigiama dielektrinės funkcijos sritis nelegiruoto puslaidininkio atveju yra tik Reštralio juostoje tarp TO ir LO fononų. Legiruoto puslaidininkio atveju susiformuoja dvi neigiamos dielektrinės funkcijos sritys: 0–430  $\text{cm}^{-1}$  ir  $v_{TO}$ –1100  $\text{cm}^{-1}$  taip gerokai praplečiant poliaritonų formavimosi diapazoną. Šie dielektrinės funkcijos realiosios dalies nulio kirtimo dažniai yra žinomi kaip  $v_\pm$  modos ir yra aprašomi 2.34 lygtimi.

### Gardelės susiejiklis

Gardelės susiejiklis (*grating coupler*) yra struktūra, skirta 6.5 susidariusiam banginių vektorių neatitikimui panaikinti. Plona paviršine gardele šviesa yra difraguojama į skirtingas difrakcines modas  $M = 0, \pm 1, \pm 2 \dots$  (žiūrėti **3.5 pav.**). Difrakcijos metu prie šviesos bangi-

nio vektoriaus yra pridedamas  $M$ -tosios eilės gardelės vektorius. Tam tikru kritimo kampų  $\varphi$  ir gardelės vektoriaus  $k_G$  verte ši suma tampa lygi paviršinio poliaritono  $k_{SPPhP}$  vertei. Impulso tvermės dėsnis tada užrašomas kaip [92]:

$$k_{SPPhP} = k_0 \sin \varphi + Mk_G \quad (6.7)$$

Lygtis 6.7 kartu su lygtimis 6.5 bei 6.6 sudaro sistemą, nusakančią paviršinių fonon-plazmon-poliaritonų dispersiją. Šios sistemos realiosios dalies analitinis sprendimas leidžia nuspėti SPPhP sužadavimo dažnį [P4,P6]. Menamosios dalies pridėjimas sistemos sprendime gerokai pasunkina uždavinį, tačiau kartu leidžia nuspėti hibridinės SPPhP modos nuostolius esant tam tikram dažniui. [P5]

## 6.4 Metodai

### 6.4.1 Difrakcinė optika

#### Difrakcinės optikos modeliavimas.

Difrakcinės optikos elementų modeliavimui pasitelktas baigtinių skirtumų laiko skyros (FDTD) modeliavimo metodas. Šiuo metodu modeliuojama struktūra yra suskaidoma į aibę taškų baigtiniais tarpusavio atstumais. Kiekvienam taškui priskiriama elektrinio arba magnetinio laukų vertė taip, kad kiekvienas elektrinio lauko taškas būtų apsuptas magnetinio lauko taškais ir atvirkščiai. Taškai taip pat aprašomi medžiagos dielektrinės funkcijos verte esant konkrečiam dažniui. Metodo pagrindas – iteracinis tokios erdvinės sistemos, aprašomos Maksvelo lygtimis, sprendimas [114]. Nuliniu laiko momentu, įjungus tokios sistemos žadinimą, pradedamas iteracinis Maksvelo lygčių sprendimas baigtiniais laiko intervalais. Kiekvieno laiko momento magnetinio lauko vertės nusako sekančio momento elektrinio lauko vertes ir atvirkščiai. Iteracinis sprendimas vyksta tol, kol gaunamas reikiamo tikslumo nuostovusis sprendinys. Nors šis metodas ir reikalauja gana didelių kompiuterinių išteklių, jis plačiai paplitęs modeliuojant prietaisų veikimą, nes juo gaunami itin tikslūs rezultatai su minimaliais modeliuojamų struktūrų geometrijos apribojimais. Disertacijoje aprašomame tyrime naudota komercinė *CST studio*

modeliavimo programa.

### **Difrakcinių lęšių charakterizavimas.**

Difrakciniai lęšiai buvo charakterizuojami stende parodytame **3.3 pav.** THz šaltinis buvo elektroninė Šotkio diodų daugintuvų grandinė. Diverguojanti šaltinio spinduliuotė buvo kolimuojama polietileno lęšiu ir plokščiu veidrodžiu nukreipiama į difrakcinį lęšį (DOE). Fokusuotos spinduliuotės profilis tiriamas skenuojant jį taškiniu detektoriumi, jo signalą registruojant *Lock-in* stiprintuvu [1]. Tikslus detektoriaus pozicionavimas buvo užtikrinamas naudojantis 3D manipuliaciniu stendu.

Terahercinio vaizdinimo eksperimento principinė schema pavaizduota **3.4 pav.** Šiuo atveju naudotas įtvirtintas MPFL elementas, kurio fokuso plokštumoje, ant 2D manipulatoriaus, pozicionuojamas vaizdinimo taikyns. Praėjusi spinduliuotė kolimuojama ir į taškinių detektorių nukreipiama paraboliniiais veidrodžiais.

## **6.4.2 Poliaritonika**

### **Tikslios Susietųjų bangų analizės modeliavimo metodika.**

Poliaritoninių komponentų modeliavimui taikyta tikslios susietųjų bangų analizės *Rigorous coupled wave analysis* modeliavimo metodika (RCWA). Šis metodas leidžia greitai ir tiksliai aprašyti periodinių struktūrų sąveiką su šviesa [119–121]. Šiame darbe nagrinėtos vienmačio periodiškumo paviršinės gardelės, tad naudotas 2D modeliavimo modelis. Jo principinė schema pavaizduota **3.5 pav.** Sistemą sudaro trys pagrindinės sritys: atvira erdvė viršuje, periodinės gardelės sritis viduryje ir padėklo sritis apačioje. Visos šios sritys yra aprašomos dielektrinėmis funkcijomis (puslaidininkio atveju parodytomis 6.6 lygtyje). Sudėtingesnės struktūros yra aprašomos pasitelkus reikiamą kiekį sluoksnių ir pasluoksnių, kurių skirtingos dielektrinės funkcijos, storiai, ar, gardelės srityje, pločiai.

RCWA aprašyme gardelės sritis skleidžiama Furjė skleidiniu ir kartu su *Floquet* sąlyga aprašo gardelę, kaip begalinio periodiškumo sluoksnį. Skleidinio narių skaičius nusako šio metodo tikslumą, nes jį taikant naudojamame Maksvelo lygčių sprendime nėra daroma papildomų su-

paprastinimų. Pasitelkus Furjė skleidinį, kurio narių skaičius baigtinis, ir sutapatinant kraštines sąlygas sluoksnių ribose, begalinė dali- nių išvestinių Maksvelo lygčių sistema yra supaprastinama iki baigti- nės tiesinių lygčių sistemos, gana paprastai išsprendžiamos kompiute- riu [118,122,123]. Sistema sprendžiama esant vienam dažniui pasirink- toje (TM arba TE) poliarizacijoje, ir randami atspindėtų ir praėjusių dif- rakcijos eilių efektyvumai. Jų sumos atspindi struktūros pralaidumo  $t$  bei atspindžio  $r$  koeficientu,  $s$  susijusius su sugerties koeficientu  $a$  kaip  $r + t + a = 1$ . Sprendimą pakartojus dažnių intervale tam tikru pasi- rinktu žingsniu apskaičiuojami struktūros atspindžio bei pralaidumo spektrai.

Pradinis RCWA kodas *Matlab* programai buvo paimtas iš viešai platinamo šaltinio [124], skirto skaičiavimams regimojoje ir artimojoje infraraudonojoje srityse. Kodas buvo papildytas ir pritaikytas atsi- žvelgiant į dielektrines puslaidininkių funkcijas bei tiriamų gardelių geometriją. Modelio tinkamumas patikrintas lyginant modeliuotus ir eksperimentiškai gautus rezultatus.

### **Furjė transformacijos infraraudonoji spektroskopija.**

Eksperimentiniam poliaritoninių bandinių tyrimui buvo pasitelkta Furjė transformacijos infraraudonoji (FTIR) spektroskopija.

Fiksuoto kampo geometrijos atspindžio spektrų matavimai bei  $n$ -GaN SPPPhP spinduliuotės kampinių priklausomybių matavimai atlik- ti komerciniu *Nicolet 8700* spektrometru. Šio spektrometro naudojamo pralaidumo geometrijoje principinė schema pavaizduota **3.6 pav., a**. **3.6 pav., b** pavaizduota spektrometro bandinių skyriaus su fiksuoto kampo atspindžio matavimo priedėliu schema. Šiuo atveju, siekiant sumažinti kampinę į bandinį krintančio pluošto apertūrą,  $n$ -GaN SRG matavimuose, buvo naudojama apskritiminė apertūra. Kad būtų užtikrinta poliari- zacija, naudotas poliarizatorius. **3.6 pav., d** pavaizduota bandinio spin- duliuotės matavimo schema. Bandinys šiuo atveju tvirtintas prie kaiti- nimo ir sukimo stendo spektrometro išorėje ir iš jo sklindantis spindulys nukreiptas į spektrometrą paraboliniu veidrodžiu. Šiuo atveju taip pat naudota plyšio tipo apertūra matuojamų kampų intervalui sumažinti. Kampinių atspindžio spektrų tyrimui naudotas *Bruker V70* spektromet- ras. Jame naudoto kampinio atspindžio matavimo priedėlio, paremto

dviem automatizuotais judinamais veidrodžiais, principinė schema pateikiama **3.6 pav., c.**

FTIR spektrometro veikimas, kaip ir sufleruoja pavadinimas, yra paremtas interferuojančio spindulio Furjė transformacija. Krintantis spindulys spindulio dalikliu yra padalijamas į dvi šakas, kurių vienoje yra stacionarus veidrodis, o kitoje veidrodis, pozicijuotas ant preciziškai valdomos transliacinės ašies. Nuo veidrodžių atspindėti pluoštai, nuėję skirtingus optinius kelius, vėl sujungiami ir nukreipiami pro bandinių kamerą į detektorius. Registruojama interferencinio signalo priklausomybė nuo judinamo veidrodžio koordinatės  $L$ . Interferencijos priklausomybė nuo optinių kelių skirtumo kartu reiškia priklausomybę nuo spinduliuotės bangos ilgio. Atlikus registruoto signalo priklausomybės nuo judinamo veidrodžio koordinatės  $P = P(L)$  Furjė transformaciją, randama pluošto galios dažninė priklausomybė – spektras  $P = P(\nu)$ .

Matuojant atspindžio spektrus bandinio atspindžio spektras randamas matuojamą galios spektrą lyginant su žinomos atspindžio funkcijos, pavyzdžiui, darbe naudoto ir tolygiu beveik 100% atspindžio koeficientu pasižyminčio Au veidrodžio, spektru. Rezultatų analizėje taip pat atsižvelgiama į poliarizatorių pralaidumo funkcijas, pasižyminčias spektriniais ypatumais.

## 6.5 Rezultatai

### 6.5.1 Difrakcinė optika 0,58 THz dažniui

Buvo sukurtas daugialiptės fazės Frenelio lęšių dizainas, atlikta jų gamyba ir charakterizavimas. Gamybai pasirinktas lazerinės abliacijos gamybos metodas. Nuosekli šio gamybos metodo tinkamumo gaminant ir charakterizuojant įvairaus dizaino elementus analizė dar nebuvo pateikta ankstesnėje literatūroje. Gamybai buvo pasirinkti dizainai, pritaikyti 0,58 THz darbinio dažnio (0,517 mm bangos ilgio), 17,5 mm skersmens spinduliuotės pluoštui fokusuoti.

Pagamintos dvi serijos lęšių, skirtų 0,58 THz spinduliuotei fokusuoti atitinkamu  $f = 5$  mm ir  $f = 10$  mm židinio nuotoliu. Kiekvienos serijos elementai tarpusavyje skyrėsi pazonių (Frenelio lęšio diskretizavimo lygių) skaičiumi  $p$ . Pirmojoje  $f = 5$  mm židinio nuotolio serijoje

buvo pagaminti komponentai su  $p = 4, 8, 16, 32$  ir 1643 pazonių. Antrojoje,  $f = 10$  mm židinio nuotolio serijoje buvo komponentai su  $p = 2, 4, 8, 16$  ir 1643 pazonių. Toks serijos elementų pasiskirstymas parinktas siekiant nuosekliai ištirti pazonių skaičiaus įtaką lęšio veikimui nuo binarinės fazinės plokštelės režimo, kai  $p = 2$ , iki beveik tolydaus Frenelio lęšio režimo, kai  $p = 1643$ .

Pagamintų elementų kokybė buvo charakterizuojama SEM (skanuojančiosios elektronų mikroskopijos) ir profilometriniais matavimais. SEM nuotraukose pavaizduotose **4.3 pav.**, matomas pagamintų bandinių vaizdas. Nuotraukose nebuvo pastebėta ryškių nukrypimų nuo numatyto dizaino. Nepaisant to, apdirbtose zonose buvo aptiktas paviršiaus šiurkščio padidėjimas. Apdirbto paviršiaus šiurkštis padidėjo dėl lazerinio abliavimo apdirbimo proceso metu susiformuojančių lazeriu indukuotų periodinių struktūrų (LIPSS), plačiai aptariamų lazerinio apdirbimo tyrimuose. SEM nuotraukose matomos apie 10  $\mu\text{m}$  eilės skersmens cilindrinės / kūginės struktūros bandinio paviršiuje. Nors paviršinių struktūros ir susidarė, jų charakteringi matmenys buvo daug mažesni nei darbinis lęšio bangos ilgis (517  $\mu\text{m}$ ), tad laikoma, kad šios struktūros didelių sklaidos nuostolių nesukėlė.

Bandinių paviršių geometrija buvo tiriama papildomai – matuojama profilometru. Visų pagamintų lęšių profilometrinių matavimų rezultatai yra pavaizduoti **4.2 pav.** Matyti, kad lęšių su 2, 4 ir 8 pazonėmis skerspjūviuose yra dsusidarę pazonių laipteliai, o lęšių, kurių pazonių skaičius didesnis, paviršių reljefas yra tolydus, primenantis klasikinio Frenelio lęšio vaizdą. Pazonių nebematyti dėl to, kad didėjant pazonių skaičiui, jų skersmenys tampa mažesni nei lazerio pluošto plotis (44  $\mu\text{m}$ ).

### **Difrakcinės optikos, skirtos 0,58 THz spinduliuotei fokusuoti, veikimo tyrimas.**

Pagamintų lęšių veikimas buvo tiriamas skenuojant bandinio sufokusuotą dėmę piroelektriniu detektoriumi  $xy$  (fokuso plokštumoje) ir  $xz$  (fokuso gylyje) kryptimis. Pirmasis,  $xy$ , skenavimas buvo atliekamas pozicionuojant detektorių lęšio fokuso plokštumoje  $z_1 = f$ , jo metu gaunama informacija apie fokuso dėmės intensyvumą, simetriją bei plotį. Antrojo,  $xz$ , skenavimo metu detektorius buvo pozicionuojamas

bandinio centre ir tada atliekamas skenavimas į fokuso gylį stebint spinduliuotės konvergavimą į fokuso dėmę.

Skenuoti visi pagaminti bandiniai. Charakteringi rezultatai, gauti tolydiems ( $p = 1643$  pazonių) lęšiams (angl. *kinofilm*), kurių židinio nuotoliai  $f = 5$  mm ir  $f = 10$  mm, parodyti **4.8 pav.** Abiejų lęšių atvejais gauti panašūs, apie 1,7 V detektoriaus signalo siekiantys maksimalūs fokusuotos dėmės intensyvumai, liudijantys vienodą abiejų lęšių fokusavimo efektyvumą. Reikėtų atkreipti dėmesį, kad tiesinėje rezultatų skalėje tiek skenavimo  $xy$  (**4.8 pav., a ir b**), tiek  $xz$  (**c ir d**) kryptimis atvejais gaunamos simetriškos fokuso dėmės, atitinkančios teorinį modelį. Šie rezultatai rodo, kad vyksta signalo bangelių formavimasis, priskiriamas stovinčiųjų bangų lęšio – detektoriaus ertmėje formavimuisi. Logaritminiame fokuso dėmės skerspjūvio  $x$  kryptimi vaizde (**4.8 pav., e**), matyti antriniai *Airy* žiedai, nepasižymintys centrine simetrija. Šis asimetriškumas yra sąlygojamas ne visiškai tiksliai pozicijuoto lęšio bandinio laikiklyje arba nedidelių nuokrypių nuo tikslaus lęšio dizaino gamybos metu. Pademonstruotas 23 dB siekiantis fokusavimo stiprinimas, atitinkantis signalo fokuso plokštumoje padidėjimą apie 170 kartų.

Fokusavimo gebos charakterizavimo matavimai buvo atlikti visiems bandiniams ir kiekvieno matavimo atveju nustatyta maksimali fokusuoto signalo amplitudė. Šis parametras yra proporcingas fokusavimo stiprinimui  $G_f$  (2.4 lygtyje), tad gerai tinka jam įvertinti. Kiekvieno matavimo metu gauta maksimali sufokusuotos dėmės amplitudė pateikta **4.9 pav.** Matyti, kad gauta maksimalaus signalo priklausomybė nuo lęšių pazonių skaičiaus pasižymi asimptotine eiga ir gerai sutampa su normuota teorine priklausomybe. Ši priklausomybė leidžia daryti išvadą, jog lęšių fokusavimo stiprinimas įsisotina ne tik dėl gamybos metu susiliejančių laiptelių, bet ir dėl fundamentinės MPFL lęšio specifikos. Galima teigti, kad optimalaus dizaino lęšis turėtų turėti tarp 8 ir 16 pazonių, taip užtikrinant efektyvų lęšio veikimą nedidinant dizaino sudėtingumo.

Fokusuoto pluošto skerspjūviai  $z$  kryptimi tolydiems lęšiams pateikti **4.10 pav.** Atlikus matavimus skirtingai pozicijuojant lęšį nustatyta, kad optimali pozicija jo veikimui yra kai jo apdirbta pusė yra atsukama link detektoriaus. Šiuo atveju minimizuojamas stovinčiųjų bangų formavimas, išsklaidant nuo detektoriaus atgal į lęšį iš dalies

atspindėtą spinduliuotę. Taip pat kiekvienu  $z$  atstumu apskaičiuoti spindulio pločio ties puse intensyvumo (FWHM) parametrai. Nustatyti minimalūs fokusuotos dėmės pločiai (0,55 ir 0,43 mm) ir fokuso dėmės gyliai (3 mm ir 1,3 mm) atitinkamai 10 cm ir 5 cm fokuso atstumo lęšiams.

### Didelio ploto MPFL lęšio tyrimas.

Buvo pagamintas ir charakterizuotas didelio skersmens Frenelio lęšis siekiant parodyti jo pritaikymą vaizdinimo sistemoms. Šis elementas pasižymėjo 50 mm skersmeniu, optimaliu 16 pazonių skaičiumi ir 30 mm fokuso atstumu. Pagaminto fokusuoto pluošto skenavimo rezultatai pateikiami **4.15 pav.** Matyti, kad  $xy$  skenavimo rezultatas fokuso plokštumoje pasižymi simetriška apskritimine dėme. Skenavimas  $xz$  plokštumoje parodo fokuso dėmės išstetumą už fokuso plokštumos. Šio, anksčiau aprašytų lęšių, kurių pazonių skaičiai yra  $p = 16$ , bei atitinkamos ankstesnėje literatūroje aprašytos metalinės zoninės plokštelės normuoti fokusuotų pluoštų skerspjūviai pateikiami **4.17 Pav.** Matyti kad didelio ploto lęšis pasižymėjo didžiausiu fokuso dėmės pločiu, siekiančiu apie 1 mm. Dėmės skerspjūvio bei ilgio padidėjimas, yra lemtas mažos lęšio skaitinės apertūros (NA) matavimo stende. Pradinio dizaino (50 mm skersmens ir 30 mm fokuso ilgio) elementas turėjo pasižymėti skaitine apertūra lygia 0,64 ir Abės difrakcijos riba (dėmės puspločiu  $d = \lambda/2NA$ ) lygia 0,4 mm. Eksperimentinis stendas pasižymėjo 17 mm spindulio skersmeniu ir atitinkamai skaitine lęšio apertūra, siekiančia 0,27. Tokios apertūros lemiama difrakcijos riba yra apie 0,96 mm, t. y. vertė yra labai panaši į stebėtąją eksperimente. Ši vertė bei 93 % siekiantis elemento efektyvumas rodo itin gerą pagaminto elemento kokybę ir veikimą.

Kitame tyrimo etape buvo pademonstruotas komerciškai svarbus šio lęšio panaudojimas vaizdinimo stende. Lęšis buvo sumontuotas ankstesnėje publikacijoje [1] aprašytame stende, kaip kolimuotą 0,58 THz spindulį fokusuojantis elementas (**3.3 pav.**). Fokuso plokštumoje, ant 2D manipuliacinio stendo, buvo tvirtinamas vienas iš dviejų naudotų vaizdinimo taikinių ir atliekamas jo 2D skenavimas. Kiekvienoje taikinio pozicijoje buvo registruojamas pralaidumo signalas, naudota skenavimo rezoliucija  $0,1 \times 0,1 \text{ mm}^2$ . Pirmasis taikinis buvo THz



spinduliuotei nepralaidi folija su skirtingo pločio juostelių rinkiniais vaizdinimo sistemos rezoliucijos įvertinimui. Antrasis taikiny buvo plastikinė reprezentacinė kortelė su viduje įmontuota (paslėpta) USB laikmena.

Vaizdinimo taikinių nuotraukos ir vaizdinimo rezultatai yra pateikti **4.16 pav.** Rezoliucijos taikinio vaizdinimas (**4.16 pav., a**) parodė, jog ertmės buvo išskiriamos, kai jų plotis buvo 1 mm ir daugiau. Ši vertė gerai atitiko charakterizuojant lęšį įvertintą fokusuotos dėmės pusplotį. Šis rezultatas taip pat atitinka praktikoje naudojamos OAP veidrodžių sistemos rezultatą, tačiau jis pasiekiamas naudojant kur kas kompaktiškesnį ir lengvai pagaminamą elementą. Rezultatai leidžia numatyti, kad naudojant didesnio pločio pluoštus arba trumpesnio židinio nuotolio elementus galima tikėtis apie du kartus geresnės rezoliucijos.

Kortelės vaizdinimo rezultatas (**4.16 pav., b**) – ryškiai matoma USB laikmenos sritis. Metalinės laikmenos struktūros nepralaidžia THz spinduliuotės, todėl matomas itin ryškus pralaidumo signalo kontrastas. Taip pat įdomu, kad laikmenos apipavidalinimo dažų sugertis yra skirtinga ir leidžia vienu pralaidumo matavimu registruoti užrašus esančius abiejose kortelės pusėse. Galiausiai, vaizdinimo rezultato apačioje matomos tamsios zonos yra sąlygojamos skaidrių ir optinėje nuotraukoje neišskiriamų klijų, naudotų kortelei tvirtinti laikiklyje. Toks objekto pralaidumo matavimas ir struktūrų, dažų bei svetimkūnių išskyrimas yra įdomus THz sistemų taikymams tiek saugumo, tiek kokybės kontrolės gamybos metu srityse. Kompaktiškų, lengvų ir paprastai gaminamų elementų taikymas tokiose sistemose leistų greitesnį jų kūrimą bei spartesnį prigrįžimą komerciniuose sprendimuose.

### 6.5.2 Difrakcinė optika 4,7 THz dažniui

Sėkmingai atlikus 0,58 THz skirtų elementų gamybą ir charakterizavimą, buvo siekiama nustatyti, ar lazerinės abliacijos metodas pasižymi pakankamu tikslumu kur kas aukštesnio – 4,7 THz dažnio spinduliuotės fokusavimui. Šis dažnis pasirinktas dėl savo svarbos astronomijoje ir galimybės pagamintus elementus charakterizuoti praktiškai naudojamame stende aprašytame ankstesnėje literatūroje [6]. Tikslus stende naudoto QCL šaltinio dažnis (4,745 THz) atitiko 63,18  $\mu\text{m}$  bangos ilgį, t.

y. buvo tos pačios eilės kaip ankstesnių bandinių analizėje aptikti charakteringi paviršinių nelygumų matmenys. Dėl šios priežasties ir kilo tikslas ištirti, ar lazerinės abliacijos metu gaunami paviršiniai nelygumai kritiškai nesukliudytų elemento veikimui.

Gamybai parinkti trys dizainai. Pirmasis – tai iš metalinės folijos pagamintas Soreto zoninė plokštelės lęšis (SZPL). Metaline folija paremtų elementų veikimas 0.58 THz dažnyje buvo pademonstruotas ankstesnių tyrimų metu [55, 129, 130]. SZPL sudarė koncentriniai, THz spinduliutei nepralaidžios, 16  $\mu\text{m}$  storio Mo folijos žiedai su prilaikomosiomis struktūromis mechaniniam elemento stabilumui. Bandinio vaizdas pateikiamas **4.6 pav.** Šio bandinio gamybai naudotas antrosios harmonikos *Pharos* („Šviesos konversija“) lazerio pluoštas, kurio impulso trukmė 300 fs, pasikartojimo dažnis 100 kHz ir bangos ilgis 515 nm. Impulsai buvo fokusuojami 10 mm atstume į 5,6  $\mu\text{m}$  dydžio dėmę.

Kiti du bandiniai buvo pagaminti lazerinės abliacijos būdu ėsdinant MPFL struktūras 500  $\mu\text{m}$  storio didelės varžos Si plokštelių paviršiuje. Gamybai naudota *Atlantic-6* („Ekspla“) lazeriu paremta sistema. Lazerio impulso trukmė buvo 13 ps, pasikartojimo dažnis 100 kHz ir bangos ilgis 515 nm. Pluoštas buvo fokusuojamas 80 mm atstumu į 28  $\mu\text{m}$  ir 14  $\mu\text{m}$  dydžio dėmes MPFL-8 ir MPFL-2 bandinių gamybai. Šiems bandiniams parinkti dizainai, kurių pazonių skaičiai buvo  $p = 2$  (MPFL-2) ir  $p = 8$  (MPFL-8). Pagaminto MPFL-2 bandinio SEM nuotrauka pavaizduota **4.7 pav.** Dvi zonos parinktos kaip paprasčiausias elementas, siekiant įvertinti paties gamybos proceso galimybes, o aštuonios – kaip kompromisinis variantas tarp gamybos sudėtingumo ir lęšio efektyvumo, remiantis praeito skyrelio rezultatais. Pagamintų bandinių paviršiaus šiuurkščiai siekė apie 500 nm, t. y. buvo apie 120 kartų mažesni nei THz spinduliuotės bangos ilgis, tad laikoma, jog apdirbto paviršiaus sklaidos sukeliama nuostoliai yra nedideli.

Visų bandinių parinkti dizainai pasižymėjo 25 mm skersmeniu ir  $f = 50$  mm fokuso atstumu. Toks dizainas pasižymi skaitine apertūra, siekiančia 0,243, teoriškai modeliuotu fokusuotos dėmės dydžiu – 300  $\mu\text{m}$ , Gausinio pluošto puspločiu – 164  $\mu\text{m}$  ir fokuso gyliu – 1,1 mm. Modeliuojant numatyta fokusavimo geba SZPL bandiniui – 28 dB (630 kartų) ir MPFL-8 bandiniui – 32 dB (daugiau kaip 1500 kartų).

Bandinių charakterizavimas atliktas stende, schemiškai pavaizduo-

tame **4.19 pav.** Pagrindiniai fokusavimo rezultatai yra apžvelgiami **4.21 pav.** Fokusuoto pluošto skerspjūviai  $x$  kryptimi rodo fokusuotos dėmės intensyvumą ir plotį, o skerspjūviai  $z$  kryptimi leidžia nustatyti fokuso atstumą ir gylį. Eksperimentiškai nustatyti fokuso atstumai  $f$ , fokusavimo stiprinimai  $G_f$  ir dėmės pločiai visiems lęšiams pateikiami **6.1 I Lentelėje**. Čia taip pat, palyginimui, pateikiamos teoriškai apskaičiuotos fokusavimo stiprinimo vertės.

SZPL atveju į teorinę  $G_f$  vertę yra įskaitytas 2 dB stiprinimo susilpnėjimas dėl ašinės sferinės aberacijos įtakos. Likęs 2 dB skirtumas tarp teorinės ir eksperimentinės  $G_f$  verčių yra sąlygojamas nedidelio, vidutiniškai apie 25  $\mu\text{m}$ , neatitikimo tarp dizaine nustatytų ir pagamintoje plokštelėje išmatuotų zonų skersmenų. Manoma, kad šis neatitikimas atsirado dėl to, kad gamybos metu bandinys galimai įkaito ir termiškai išsiplėtė. Korecinės komponentų gamybos metu, šį neatitikimą būtų paprasta kompensuoti ir pasiekti artimą 26 dB stiprinimą.

Lęšis MPFL-2 teoriškai pasižymi 4 kartus didesniu stiprinimu nei teorinė SZPL, siekiančiu 34 dB. Rezultatų lentelėje nurodoma vertė, iš kurios yra atmesti 2 dB nuostoliai dėl ašinės – sferinės aberacijos, taip pat 4 dB nuostolių dėl 40 % siekiančio Si pralaidumo dėl galimo anksčiau minėto juodojo Si sluoksnio susidarymo. Eksperimentiškai nustatyta 25 dB vertė vis dar buvo 3 dB mažesnė nei teoriškai apskaičiuotoji. Likęs skirtumas, manoma, yra sąlygojamas zonų šešėliavimo ir gamybos metu atsiradusių neatitikimų.

Pazonių skaičiaus lęšyje padidėjimas iki 8 padidino eksperimentinį stiprinimą iki 29 dB. Šis rezultatas buvo apie 6 dB didesnis nei gautasis 0,58 THz lęšiams praeitame skyrelyje, ir buvo didžiausias, aprašytas literatūroje publikavimo metu. Dar didesnę fokusavimo stiprinimo padidėjimą, manoma, būtų galima pasiekti į MPFL dizainą inkorporuojant antirefleksinę dangą, aprašytą ankstesnėje literatūroje [75], tačiau šis žingsnis reikalauja detalesnių tyrimų ir optimizavimo. Vertinant eksperimentinius bei teorinius MPFL-8 lęšio rezultatus taip pat buvo pastebėta, kad fokusuotos dėmės dydis padidėjo 0.03 mm, o židinio nuotolis pasislinko apie  $\approx 20$  mm, nuo originalaus dizaino. Šie nuokrypiai priskiriami gamybos metu įvykusiai klaidai.

Galiausiai, siekiant pademonstruoti lęšių tinkamumą mechaniškai patvarioms sistemoms, buvo atliktas jų fokusavimo priklausomybės

Bandinys	$f$ [mm]	$G_f$ (eksper.) [dB]	$G_f$ (teor.) [dB]	pluošto plotis [mm]
SZPL	56	24	26	0,15
MPFL2	55	25	28	0,15
MPFL8	76	29	32	0,18

6.1 lentelė. Skirtingų lęšių 4,7 THz dažnio spinduliuotės fokusavimo parametrai.

nuo kampo su optine sistemos ašimi tyrimas. Jo rezultatai pateikiami **4.23 pav.** Iš jo matyti, kad reikšmingo integruoto signalo sumažėjimas lęšiams nėra būdingas iki  $10^\circ$  nuokrypio. Taip parodoma, jog lęšio pozicionavimas nedaro kritinės įtakos jo veikimui ir nedideli mechaniniai optinės sistemos nuokrypiai taip pat būtų toleruoti.

### 6.5.3 $n$ -GaN paviršinių gardelių tyrimas

Atliktas poliaritoninių pasyvių  $n$ -GaN paviršinėmis gardelėmis paremtų elementų modeliavimas, dizainas, gamyba ir charakterizavimas. Elementų kūrimui pasirinkta stipriai legiruoto  $n$ -GaN medžiaga, kurios krūvininkų tankis buvo  $n = 1,55 \times 10^{19} \text{ cm}^{-3}$ . Ši medžiaga pasižymi geru mechaniniu, elektriniu bei šiluminiu atsparumu, taip pat plačia Reštralio juosta (RB), kuri papildomai praplėsta dėl laisvųjų krūvininkų plazmoninės įtakos. Dėl šios įtakos, darbinė poliaritoninių reiškinių formavimosi sritis (ruožas, kuriame reali dielektrinės funkcijos sritis yra mažesnė nei  $-1$ ) praplėsta nuo nelegiruoto GaN RB ( $559 - 736 \text{ cm}^{-1}$ ) iki  $0 - 400$  ir  $559 - 1000 \text{ cm}^{-1}$ .

Tirto dizaino geometrija pavaizduota **4.24 pav.** Tirtas struktūras sudarė vientisas,  $500 \mu\text{m}$  storio legiruoto  $n$ -GaN padėklas, kurio paviršinė gardelė pasižymėjo  $P$  periodo,  $h$  aukščio ir  $W$  pločio. Gardelė atlieka impulso tvermės dėsnio išpildymo funkciją, kai jos banginio vektoriaus  $k_y$  ir krintančios šviesos banginio vektoriaus  $k_x$  suma tampa lygi paviršinio fonon-plazmon-polaritono banginiam vektoriui  $k_{SPPHP}$ . Impulso tvermės dėsnio galiojimo sąlygomis (**4.24 pav., b**) ima vykti paviršinio polaritono ir tolinojo lauko šviesos sąveika (*coupling*). Tokia struktūra vadinama paviršinės gardelės (SRG) susiejikliu (*coupler*). Charakteringa pagaminto bandinio SEM nuotrauka parodyta **4.24 pav., c** ir **d**. Iš čia matyti, jog realiu gamybos metu gaunama ne tikslaus meandro, o tra-

Parametras	$\epsilon_\infty$	$v_{TO}(\gamma_{TO})$ [cm <sup>-1</sup> ]	$v_{LO}(\gamma_{LO})$ [cm <sup>-1</sup> ]	$v_P(\gamma_{LO})$ [cm <sup>-1</sup> ]
Geriausios atitikties vertė	5,3	557 (7)	739 (7)	1140 (390)

6.2 lentelė. Modeliavimuose naudotos geriausios atitikties  $n$ -GaN dielektrinės funkcijos parametų vertės.

pecijos formos gardelė, kurios viršutinės kraštinės plotis  $W_1$ , o apatinės kraštinės plotis  $W_2$ . Nustatyta, kad viršutinė kraštinė, gaminant 1  $\mu\text{m}$  gylio gardeles, gaunama 0,6  $\mu\text{m}$  trumpesnė, o apatinė 0,2  $\mu\text{m}$  ilgesnė nei originalus meandro dizainas. Nors šis neatitikimas yra gerokai mažesnis nei charakteringas tirtos gardelės periodas (11 – 22  $\mu\text{m}$ ) ir stiprios įtakos optiniams spektrams nedarė, į jį buvo atsižvelgta modeliuojant gardeles.

Siekiant teoriškai modeliuoti SPPHP struktūras, buvo reikalingi  $n$ -GaN dielektrinės funkcijos parametrai. Parametų nustatymui pirmiausia buvo atliktas netekstūruoto padėklo atspindžio spektrų matavimas. Tada atliktas netekstūruotos medžiagos atspindžio spektrų modeliavimas, naudojant literatūroje randamus fononų parametrus. Galiausiai parametrai keičiami (*fitting*), kol gaunamas geras atitikimas tarp modeliuoto ir išmatuoto rezultatų. Geriausia spektrų atitiktimi pasižymintys parametrai išvardyti 6.2 lentelėje. Matuotas ir, remiantis geriausios atitikties parametrais, apskaičiuotas spektrai pateikiami 4.25 pav.

Pirminėje poliaritoninių struktūrų teorinio modeliavimo stadijoje buvo apskaičiuotos atspindžio spektrų priklausomybės nuo gardelės periodo, esant fiksuotam gardelės gyliui, ir nuo gardelės gylio, esant fiksuotam periodui. Skaičiavimams pasirinktas 50% gardelės užpildo faktorius ( $P = 2W$ ) ir 26° kritimo kampo geometrija. Pradiniai skaičiavimai atlikti naudojantis *a priori* turėtomis žiniomis ir pasirinktas fiksuotas gardelės gylis – 1  $\mu\text{m}$ , o periodas – 11  $\mu\text{m}$ . Skaičiavimo rezultatai pateikiami 4.26 pav. Iš fiksuoto periodo skaičiavimo rezultatų (4.26 pav.) matyti, kad SPPHP atspindžio kritimo linija formuojasi apie 620 cm<sup>-1</sup> dažnyje. Nustatyta optimalus gardelės gylis SPPHP sužadimui yra  $h = 1$  Šiuo atveju stebima siaura ir beveik nulinį atspindį užtikrinanti  $\nu = 615$  cm<sup>-1</sup> centrinio dažnio SPPHP linija. Modeliuotų atspindžio spektrų priklausomybė nuo gardelės periodo esant fiksuotam optimaliam 1  $\mu\text{m}$  gyliui pateikiama 4.26 pav., b. Šiame

paveiksle taip pat pateikiama analitiškai, pagal 2.35, 2.28, 2.33 formulių sistemos realiosios dalies sprendimą gauta priklausomybė. Matyti, kad priklausomybių eiga sutampa, tačiau yra nedidelis rezultatų nuokrypis mažuose perioduose, nes analitinės formulės neįvertina paviršinės bandinio geometrijos. Paveiksluose brūkšninėmis linijomis taip pat pažymėti parametrai, pasirinkti bandinio (SRG-1), turinčio pademonstruoti veikimo principą gamybai.

Gamybai pasirinktas gardelių gylis  $h = 1 \mu\text{m}$ , daug mažesnis už charakteringus SPPHP sužadavimo bangos ilgus  $10 - 18 \mu\text{m}$  ( $1000 - 560 \text{cm}^{-1}$ ). Gamybai parinkti trys gardelių periodiškumai: 11, 16 ir  $22 \mu\text{m}$ , bandiniai atitinkamai pavadinti SRG-1, SRG-2 ir SRG-3. Disertacijoje daugiausia remiamasi principui pagrįsti skirto bandinio SRG-1 rezultatais. Kiti bandiniai iliustruoja galimybę valdyti atspindžio bei spinduliuotės charakteristikas naudojantis SRG periodiškumu.

Apskaičiuotos visų bandinių atspindžio ( $r$ ) bei spinduliuojamosios gebos ( $e$ ) koeficientų spektrų priklausomybės nuo krintančiosios bangos banginio vektoriaus (kritimo kampo) pavaizduotos **4.28 Pav.** Rezultatai iliustruoja skirtingų  $M$  modų SPPHP sužadimą tiek  $r$ , tiek  $e$  spektruose. Skirtingų šakų padėtis dažnių skalėje valdoma gardelės periodiškumu bei kritimo kampu pagal 2.35 priklausomybę. Pastebėta, jog egzistuoja priklausomybė tarp SPPHP dažnio ir stebimo ypatumo spektrinio pločio. Mažiausio pločio ypatumai gaunami netoli GaN TO fonono dažnio (SPPHP hibridinė moda žadinama esant „fononiniam“ režimui ir aprašoma daugiausia TO slopinimu) ir stipriai didėja artėjant prie plazmono dažnio („plazmoninio“ žadinimo režimo, aprašomo stipriai plazmono slopinimu). SRG-1 atveju skaičiavimo rezultatai rodo, jog  $0^\circ$  kritimo kampu stebimas linijos pusplotis ties  $800 \text{cm}^{-1}$  dažniui buvo  $120 \text{cm}^{-1}$ , sumažėjantis iki  $6 \text{cm}^{-1}$  ties  $37^\circ$  kampu esant  $570 \text{cm}^{-1}$  dažniui. Kampinės SPPHP ypatumų priklausomybės taip pat iliustruoja SPPHP kryptingumą, nes konkretaus dažnio sužadimas vyksta tik siauroje banginio vektoriaus (kritimo kampų) srityje. SRG bandinių periodai, gardelių vektoriai bei SPPHP dažniai, puspločiai ir kokybės faktoriai  $0^\circ$  kritimo kampo geometrijoje yra išvardyti **6.3 lentelėje**.

Išmatuotas ir modeliuoti SRG-1 bandinio atspindžio spektrai esant fiksuotam  $26^\circ$  kritimo kampui pateikti **4.29 pav.** Matyti, kad matuotame rezultate stebimas SPPHP ypatumas yra kur kas silpnesnis ir pla-

Bandinys	P [ $\mu\text{m}$ ]	$k_g$ [ $\text{cm}^{-1}$ ]	$V_{SPP_{hp}}$ [ $\text{cm}^{-1}$ ]	$FWHM$ [ $\text{cm}^{-1}$ ]	$Q$
SRG-1	11	909	808	122	6,6
SRG-2	16	625	606	16	37,8
SRG-3	22	455	442	32,5	13,6

6.3 lentelė. SPP<sub>hp</sub> sužadinių parametrai nulinio kampo ( $\varphi = 0$  deg) kritimo geometrijoje.

tesnis nei modeliuotas diskrečiu  $26^\circ$  kampu (30% minimalus atspindys palyginti su 0% teoriniu rezultatu). Tokia priklausomybė gaunama dėl matavimo stende egzistuojančios baigtinės kampinės apertūros, kai į bandinį krintantis fokusuotas spinduliuotės pluoštas pasižymi ne diskrečiu kritimo kampu, o kritimo kampų intervalu. Nustatyta, kad naudotame stende kritimo kampų intervalas (kampinė apertūra) buvo apie  $4^\circ$ . Į ją atsižvelgus skaičiavimo rezultatuose gautas eksperimentinio ir teorinio SPP<sub>hp</sub> rezultatų sutapimas.

Sumodeliuota atspindžio koeficiento ir išmatuota bandinio SRG-1 atspindžio spektrų kampinės priklausomybės pateikiamos **4.30 pav.** Eksperimentiniame rezultate atspindžio spektrai pateikiami kaip SRG-1 matavimo rezultato santykis su toje pačioje sistemoje matuoto Au veidrodžio atspindžio spektru. Matoma, jog šiuo atveju, matuojant kampinę priklausomybę, nebuvo išvengta kampinės apertūros įtakos, tačiau gautos teorinė bei eksperimentinė priklausomybės atitinka savo eiga. Šis atitikimas iliustruoja modeliavimo metodo tinkamumą kurti SPP<sub>hp</sub> žadinimu paremtų prietaisų dizainus.

### Šiluma žadinamų bandinių poliaritoninė spinduliuotė.

Kitame etape buvo tiriama šiluma žadinamų bandinių spinduliuotė. Remiantis Kirchhofo šiluminės spinduliuotės dėsnium, pusiausvyras kūnas išspinduliuoja tokio paties spektro spinduliuotę kaip ir sugeria. Konkrečiu SRG atveju tai reiškia, jog nuliniu pralaidumu tiriamame ruože pasižyminčio  $n$ -GaN elemento spinduliuojamosios gebos koeficiento spektras yra susijęs su sugerties koeficientu spektru kaip  $e = 1 - r$ . Taigi šiluma sužadinti, ir paviršiumi sklindantys poliaritonai savo energiją gardelės padedami geba išspinduliuoti į tolį lauką. Eksperimentiniam šiluminės spinduliuotės tyrimui buvo pagamintas bandinio kaitinimo ir sukimo stendas, pavaizduotas matavimo schemoje **3.6 pav.**,

d dalyje.

SRG-1 bandinio šiluminės spinduliuotės, bandiniui esant įkaitintam iki 300 °C, matavimo rezultatai pateikiami **4.31 pav.**. Paveikslo **a**) dalyje palyginami matuotos skirtuminės (skirtumo tarp matavimo rezultatų TM ir TE poliarizacijose) spinduliuotės ir modeliuotos spinduliuojamosios gebos (*emisivity*) spektrai 0°, 26° ir 30° matavimo / modeliavimo kampais. Matomas geras matuoto ir modeliuoto ypatumo spektrinės pozicijos atitikimas, taip pat ypatumo puspločio mažėjimo tendencija didėjant spinduliuotės kritimo kampui ir mažėjant dažniui. Verta pažymėti, jog SPPHP 0°kampu yra stebimas ties 810 cm<sup>-1</sup> dažniu, t. y. virš nelegiruoto GaN Reštralio juostos, taip yra iliustruojama hibridinė SPPHP prigimtis, nes esant tokiam dažniui grynai SPP formavimasis nebūtų įmanomas. Išsamus teorinės ir eksperimentinės spinduliuotės spektrų kampinių priklausomybių palyginimas pateikiamas **4.31 pav., b** ir **c** dalyse. Stebimas nuostovus SPPHP sužadavimo dažnio derinimas nuo 810 iki 560 cm<sup>-1</sup> keičiant kritimo kampą nuo 0°iki 37°. Taip pat itin ryškiai matoma SPPHP spinduliuotės linijos pločio dispersija, aprašyta publikacijoje [P5].

Šiluminės spinduliuotės matavimai atlikti ir SRG-2 bei SRG-3 bandiniams. Visas rezultatų rinkinys pateikiamas **4.32 pav.** Visais atvejais rezultatuose matomos tendencijos gerai atitiko modeliavimo rezultatus. Mažiausi SPPHP linijos puspločiai ir kartu didžiausi sužadavimo kokybės faktoriai buvo stebėti netoli GaN TO fonono dažnio. Esant šiame režimui matuoti ir apskaičiuoti SPPHP parametrai apibendrinami **6.4 lentelėje**. Matyti, kad gautos spinduliuotės ypatumo kokybės faktoriaus  $Q$  vertės yra artimos geriausioms SiC paviršinėse struktūrose pademonstruotoms SPhP vertėms [12].

Kitas vertas dėmesio pastebėjimas yra tai, kad, vertinant emisijos signalo priklausomybę nuo stebėjimo kampo esant konkrečiam dažniui, buvo nustatyta stipriai kryptinė priklausomybė. Kryptinės spinduliuotės egzistavimas sufleruoja, kad spinduliuotės mechanizmas pasižymi erdvinio koherentiškumu [83,96]. Šiuo atveju koherentiškumas atsiranda poliaritonui sklindant paviršiumi ir savo energiją iš dalies išspinduliuojant padedamam gardelės tam tikrame bandinio paviršiaus plote (vienmatės gardelės atveju – ilgyje), tam tikru dažniu ir kryptimi. Poliaritono spinduliavimas šiuo atveju panašus į nuostolingos bangos antenos (*le-*



Bandinys	$\nu_0$ [cm <sup>-1</sup> ]	$\varphi_0$ [°]	<i>FWHM</i> [cm <sup>-1</sup> ]	<i>Q</i>	$\Delta\varphi$ [°]
SRG-1	570	34,2 (35,6)	14.6 (6)	39 (95)	3,6 (1,44)
SRG-2	570	4 (5,5)	17,3 (5)	33 (114)	2,3 (0,95)
SRG-3	562	11 (11,5)	7.4 (4,9)	78 (116)	1,1 (0,6)

6.4 lentelė. Eksperimentiniai (teoriniai) SPPHP ypatumų parametrai esant mažiausio ypatumo pusplotio dažniams. Čia  $\nu_0$  – SPPHP dažnis;  $\varphi_0$  spinduliavimo kampas; *FWHM* – ypatumo pusplotis; *Q* – ypatumo kokybės faktorius ir  $\Delta\varphi$  – ypatumo stebėjimo kampas. Eksperimentiniai rezultatai gauti apibendrinant matuotas kreives Lorencio funkcijomis, o teoriniai parametrai gauti apskaičiuojant kampines spektrų priklausomybes 0,1° skiriamąja geba.

*aky wave antenna*) veikimą.

Siekiant įvertinti tiriamo elemento koherentiškumą, buvo surastas SRG-1 ir SRG-3 bandinių **spinduliuotės erdvinio koherentiškumo ilgis**  $L_{SC}$ . Šis parametras yra susijęs su spinduliuotės stebėjimo kampu ( $\Delta\varphi$ ) Furjė transformacijos sąryšiu ir gali būti aprašomas paprasta išraiška:  $L_{SC} \approx \lambda_0 / \Delta\varphi$ . Parametras  $\Delta\varphi$  buvo nustatytas tiek teoriškai, tiek eksperimentiškai atitinkamai tiriant teorinės spinduliuojamosios gebos bei matuotos spinduliuotės spektrų priklausomybes nuo matavimo kampo. Teoriniai spektrai buvo apskaičiuoti kas 0,1°, o eksperimentiniai kas 0,5°, ėmus atitinkamomas 1 cm<sup>-1</sup> ir 4 cm cm<sup>-1</sup> dažnių skiriamąsias gebas. Gautos priklausomybės keliems atrinktiems bangos ilgiams yra pavaizduotos **4.33 pav.** Šis paveikslas iliustruoja parametru radimo procedūrą, kai tam tikram dažniui  $\nu_0$  randamas  $E(\varphi)$  funkcijos ypatumo pusplotis  $\Delta\varphi$  ir centrinis stebėjimo kampas  $\varphi_0$ . Teorinio rezultato atveju šis parametras buvo nustatomas rankiniu būdu, nes dėl funkcijos asimetriškumo jos nebuvo galima pakankamai tiksliai aproksimuoti Lorencio funkcija. Eksperimentinio rezultato atveju buvo stebimos funkcijos, pasižyminčios Lorencio forma, todėl ypatumų pusplotis buvo nustatomas kaip Lorencio funkcijos *FWHM* parametras.

Apskaičiuotos teorinė ir eksperimentinė bandinio SRG-1 erdvinio koherentiškumo ilgio priklausomybės nuo ypatumo kampo  $\varphi$  pavaizduotos **4.34 pav.** Matoma, jog priklausomybių, gautų vertinant teorinius ir eksperimentinius rezultatus, eiga yra panaši, maksimaliu koherentiškumo ilgiu ties 37° kritimo kampu ir atitinkamu 570 cm<sup>-1</sup> dažniu. SRG-1 atveju maksimalus teorinis SPPHP koherentiškumo ilgis buvo apie 900 μm, o eksperimentiškai stebėtas apie 50 % mažesnis –

500  $\mu\text{m}$  koherentiškumo ilgis (atitinkamai apie 50  $\lambda$  ir 27  $\lambda$  vertinant bangos ilgiais). SRG-3 atveju šios vertės siekė atitinkamai apie 2,3 mm bei 920  $\mu\text{m}$  (167  $\lambda$  ir 51  $\lambda$ ).

Teorinių ir eksperimentinių koherentiškumo ilgių rezultatų skirtumas gali būti susidaręs dėl kelių veiksnių, tačiau tiksliai jo prigimtis (realaus eksperimentinio koherentiškumo ilgio skirtumas nuo modeliuotojo ar matavimo sistemos sisteminė paklaida) reikalauja tolimesnių tyrimų. Pirmoji galima priežastis, tai bandinio paviršiuje neišvengiamai susidarantys gamybos netolygumai, pažaidos ar kitos struktūros į kurias modeliuojant nėra atsižvelgiama. Antroji, ir labiau tikėtina, skirtumo prigimtis yra susijusi su matavimo sistemos specifika. Atliekant matavimus sistema pasižymėjo apie 1,5° kampine apertūra, kurios sumažinti nebuvo galima dėl pernelyg žemėjančio signalo lygio. Baigtinė kampinė apertūra gabūt turėjo įtakos kryptingumo matavimo tikslumui. Toliau atliekant SRG koherentiškumo tyrimus, šią prielaidą būtų galima patikrinti atliekant spektroskopinius matavimus kolimuotu pluoštu arba tiesioginius  $L_{SC}$  matavimus žadinimo – zondavimo metodika.

Nepaisant teorinio ir eksperimentinio rezultatų skirtumo, buvo pademonstruotas makroskopinio lygio, milimetro eilės SPPHP koherentiškumo ilgis n-GaN platformoje. Šis rezultatas leidžia teigti, kad paviršinėmis gardelėmis siejami SPPHP gali būti naudojami koherentinės šiluminės spinduliuotės generacijai. Rezultatai taip pat rodo, jog SPPHP struktūros galbūt tinka koherentinei signalų pernašai makroskopiniais atstumais, pavyzdžiui, optinėje kompiuterijoje arba tarplustinėje komunikacijoje.

#### 6.5.4 Heterostruktūrų su paviršinėmis metalinėmis gardelėmis tyrimas

Atliktas metalinėmis paviršinėmis gardelėmis (MGC) susietų (*coupled*) heterostruktūrų atspindžio spektrų tyrimas. Eksperimentinei tyrimo daliai buvo pasirinktos dvi struktūros, pavaizduotos 4.37 pav., a ir b. Pirmoji, GaN/GaN arba bandinio-1 struktūra buvo skirta įvertinti MGC susiejiklio veikimui ir SPhP žadinimui ant vienu puslaidininkiu grįstos struktūros. Antruoju atveju naudota GaN/AlN/SiC arba bandinio-2 heterostruktūra. Ši struktūra buvo įdomi tuo, kad joje

buvo naudojami du pagrindiniai GaN ir SiC sluoksniai, su gretimomis Reštralo juostomis. Šiuo atveju darbinis poliaritono dažnių ruožas teoriškai yra praplečiamas per visą sritį tarp GaN TO ir SiC LO fononų.

**Eksperimentinių bandinių heterostrukūros** turėjo dvejopą paskirtį, t. y. tirti fonon-poliaritonų žadinimą MGC susiejikliu ir moduluoti dielektrinę aplinką AlGaN/GaN sandūroje susiformavusiose 2D elektronų dujose. Šiame tyrime parodyta, jog optiškai plonų AlGaN ir 2D elektronų dujų įtakos atspindžio spektrams nebuvo. Todėl teoriškai modeliuotose struktūrose nebuvo įskaitomas paviršinis AlGaN bei 2D dujų sluoksniai ir dėmesys skiriamas poliaritonų formavimuisi struktūrose. Modeliuoto bandinio su paviršine gardele struktūra pavaizduota **4.37 pav., c** dalyje.

**Metalinės gardelės** buvo gaminamos UV litografijos bei elektronų pluošto metalų garinimo metodu. Metalinių gardelių gamybos procesas aprašytas atskirose publikacijose [136, 137]. Metalo aukštis buvo apie 100 nm eilės, t.y. daug mažesnis už charakteringus bangos ilgus ir anksčiau aprašytą paviršinės gardelės aukštį. Dėl šios priežasties modeliavimo rezultatuose nebuvo atsižvelgiama į tikslią gardelės formą ir ji apibendrinama kaip idealus stačiakampis. Ant bandinio-1 ir bandinio-2 buvo atitinkamai suformuotos  $1 \times 1$  ir  $2 \times 2$  mm<sup>2</sup> pločio gardelės, pavadintos MGC-1 ir MGC-2. MGC-1 gardelė pasižymėjo 16 μm periodu ir 8 μm juostelės pločiu, o MGC-2 gardelė buvo 7 μm periodo su 4,1 μm pločio juostelėmis.

Pirmiausia, siekiant nustatyti puslaidininkių dielektrinių funkcijų parametrus, buvo atliktas **gardele nepadengtų bandinių atspindžio spektrų matavimas**. Kaip ir ankstesniame skyriuje, šie rezultatai buvo naudojami nustatyti struktūrų dielektrinių funkcijų parametrus MGC struktūrų atspindžio modeliavimui. Geriausios atitikties parametrai apibendrinami **6.5 lentelėje**. Metalinėmis gardelėmis nedengtų bandinių matuoti ir modeliuoti spektrai pateikiami **4.38 pav.** Matyti artimas rezultatų atitikimas.

**Skirtingų heterostrukūrų su paviršinėmis metalinėmis gardelė-**

Medžiaga	$\epsilon_\infty$	$v_{TO}(\gamma_{TO})[\text{cm}^{-1}]$	$v_{LO}(\gamma_{LO})[\text{cm}^{-1}]$	$v_P[\text{cm}^{-1}]$
<b>Bandinys 1</b>				
Top-GaN	5,3	557 (4)	736 (20)	0
Substr-GaN	5,3	557 (6)	736 (20)	87
<b>Bandinys 2</b>				
GaN	5,3	557 (4)	736 (4)	0
AlN	4,7	675 (4)	891 (5)	0
SiC	6,6	799 (6)	970 (8)	82

6.5 lentelė. Geriausios atitikties dielektrinės funkcijos parametrai skirtingoms heterostruktūrų medžiagoms, naudoti modeliuojant komponentus.

**mis atspindžio spektrų** priklausomybės nuo gardelės vektoriaus ( $k_g = 1/P$ ) pateikiamos **4.39 pav.** Bandinį MGC-1 atitinkanti struktūra pateikiama **4.39 pav. a** dalyje. Priklausomybėje matyti ryški stipraus atspindžio sritis  $560 - 700 \text{ cm}^{-1}$  dažnių ruože, siejama su GaN Reštralo juosta. Brūkšninėmis linijomis pažymėtos  $M = +1$  ir  $M = -1$  poliaritonų dispersijos linijos. Atspindžio priklausomybėje, priklausomai nuo gardelės banginio vektoriaus, vyksta šias modas atitinkančių paviršinių fonon-poliaritonų žadinimas. Priklausomybė rodo, kad parenkant gardelės vektoriaus vertę (periodą), poliaritonų dažniai yra derinami  $560 - 700 \text{ cm}^{-1}$  dažnių intervale. Priešingai nei  $n$ -GaN SRG atveju, nesant plazmoninės laisvųjų krūvininkų įtakos, stebimas tik nedidelis linijos plėtėjimas didėjant jos dažniui pereinant iš TO slopinimo į LO slopinimą. Juoda vertikali tiesė žymi atspindžio spektrą, atitinkantį eksperimentinį MGC-1 bandinį.

Atitinkama SPhP priklausomybė gauta ir apskaičiavus dispersiją MGC susietam SiC (**4.39 pav., b**). Šiuo atveju esminis skirtumas matomas tik poliaritonų formavimosi dažnių juostoje, kadangi šiuo atveju ji yra lemiama SiC Reštralo juostos ( $799 \text{ cm}^{-1} - 970 \text{ cm}^{-1}$  vietoje  $557 \text{ cm}^{-1} - 736 \text{ cm}^{-1}$  GaN atveju).

Kur kas sudėtingesnė priklausomybė susidaro, tiriant heterostruktūros atitinkančios MGC-2 bandinį, spektrų dispersiją (**4.39 pav., c**). GaN/SiC heterostruktūros spektruose matomos gretimos GaN ir SiC stipraus atspindžio RB sritys. AlN sluoksnis dėl savo mažo optinio storio nesuformuoja vientisos RB, o sąlygoja atspindžio piką ir kritimą atitinkamai ties AlN TO ir LO dažniais. Šios struktūros atspindžio priklausomybėje nuo gardelės vektoriaus matyti tiek SPhP žadinimas GaN/oro

sandūroje (GaN RB dažniuose), tiek SiC paviršinių poliaritonų žadinimas (SiC RB) tiek papildomų modų formavimasis virš SiC LO fonono dažnio. Juoda tiesė šiame paveiksle rodo spektrą atitinkantį eksperimentiškai pagamintą MGC-2 bandinį.

Taip pat atliktas papildomų heterostruktūrų atspindžio spektrų modeliavimas. Tai daryta siekiant teoriškai įvertinti SPhP formavimąsi AlN/SiC Reštralo juostose, ir plonų paviršinių puslaidininkų sluoksnių įtaką atspindžio spektrams. Rezultatais taip pat parodoma, kad naudota skaičiavimo metodika leidžia atlikti pirminį heterostruktūrų spektrų modeliavimą, kuriant optinius elementus, turinčius specifinių spektrinių ypatumų.

**Eksperimentiškai išmatuoti MGC bandinių spektrai** pavaizduoti **4.40 pav.** Teoriškai suskaičiuotos priklausomybės pateikiamos linijomis. MGC-1 bandinio atveju pateikiami nepolarizuoti spektrai, pasižymintys geru atitikimu tarp teorinio ir eksperimentinio rezultato. Stebimas atspindžio kritimo linijos formavimasis  $700\text{ cm}^{-1}$  dažnyje, kuri, remiantis **4.39 pav., a** rezultatais, atitinka  $M = +1$  SPhP modą. MGC-2 bandinio spektrai TE ir TM poliarizacijose pateikiami **4.39 pav., b** ir **c** dalyse. TE poliarizacijos spektre stebėti ypatumai susiję su Fabri – Pero modų formavimusi ( $\approx 540\text{ cm}^{-1}$  bei fononiniais procesais ( $890, 980\text{ cm}^{-1}$ ), nes poliaritonai TE konfigūracijoje nėra žadinami. TM poliarizacijoje pasireiškia kur kas daugiau atspindžio kritimo modų, susijusių su poliaritonų formavimusi. Verta pažymėti, jog net ir sąlyginai sudėtingos struktūros modeliavimo rezultatai rodo, kad ypatumų padėtys itin gerai sutampa su eksperimentiniu rezultatu. Eksperimentiškai nustatytų ypatumų amplitudės kiek mažesnės nei skaičiuotosios dėl spindulio fokusavimo geometrijoje pasireiškiančios kampinės apertūros ir SPhP modų kryptingumo.

Galiausiai, siekiant aprašyti šviesos sąveiką su struktūromis, spektrinių ypatumų dažniuose, buvo paskaičiuoti elektrinio (TE poliarizacijos atvejais) ir magnetinio (TM poliarizacijos atvejais) **laukų skirstiniai gardelės aplinkoje**. Modos, kurių laukų skirstiniai paskaičiuoti, pažymėtos apskritimais **4.39** ir **4.40** paveiksluose. MGC-1 bandinio atveju (**4.41 pav.**) aptiktas lauko stiprinimas SPhP modose GaN paviršiuje,

kaip ir tikimasi įprastinio SPhP sužadavimo atveju. MGC-2 TE poliarizacijos ypatumuose matyti arba Fabri-Pero modų formavimasis, optiškai laidžiamame GaN sluoksnyje, arba spinduliuotės sugertis LO fononais be reikšmingo lauko stiprinimo.

Kur kas įdomesni rezultatai gaunami MGC-2 heterostrukūros ypatumų dažniuose paskaičiuotuose lauko skirstiniuose, pavaizduotuose **4.43 pav.** Šioje struktūroje, esant  $540 \text{ cm}^{-1}$  dažniui, susidaro stovinčioji banga kaip ir TE poliarizacijoje dėl poliarizacijai nejautrios šio proceso prigimties (**4.43 pav., a**). Paviršinio GaN poliaritono formavimasis vyksta esant  $708 \text{ cm}^{-1}$  dažniui, analogiškai MGC-1 bandinio atvejui (**4.43 pav., b**). Įdomūs lauko skirstiniai stebimi  $820$  bei  $854 \text{ cm}^{-1}$  dažniuose, kur formuojasi  $M = -1$  bei  $M = +1$  modos SiC/AlN/GaN sandūroje. Šiame dažnių ruože SiC pasižymi neigiama realia dielektrinės funkcijos dalimi, o GaN – teigiama, todėl galimas SPhP formavimasis panašiai kaip GaN/oro sandūroje MGC-1 struktūroje, tik lauką lokalizuojant jau heterostrukūros viduje (**4.43 pav., c ir d**). SPhP formavimasis yra įdomus poliaritoninių savybių tyrimui, taip pat pasyvių optinių elementų (sugėriklių ar šiluminių šaltinių) kūrimui.

Stiprus lauko lokalizavimasis sluoksnyje po metaline gardele vyksta  $940$  bei  $978 \text{ cm}^{-1}$  dažniuose (**4.43 pav., e ir f**). Tokia lauko lokalizacija tirtose heterostrukūrose būdingose didelio elektronų judrio lauko tranzistoriams, yra įdomi aktyvių optinių komponentų tyrimams. Stipri lauko lokalizacija po susiejiklio, paviršiniuose struktūros sluoksniuose yra svarbi žadinant procesus arti paviršiaus esančiame dvimačių dujų kanale. Varijuojant paviršinių medžiagų sudėtį bei storius, galima derinti šių modų dažnius. Dažnį pritaikius, pavyzdžiui, dvimačių dujų plazmonų dažniui, galimas tokio susiejiklio panaudojimas tiriant plazmoninius procesus, kuriant jutiklius bei šaltinius.

Apibendrinant – pademonstruoti metaline gardele susietų heterostrukūrų atspindžio spektrai. Teorinio modelio ir eksperimentinių rezultatų atitikimas patvirtino tiek modelio tinkamumą spektrams aprašyti, tiek tirtų struktūrų tinkamumą kurti komponentus turinčius specifines spektrines charakteristikas. Modeliuojant pademonstruotos sužadavimų priklausomybės nuo žadinimo poliarizacijos, dažnių derinimas varijuojant gardelės periodą ir heterostrukūros sluoksnių sudėtį. Parodyta, kad teorinės spektrų priklausomybės nuo gardelės

periodo ir apskaičiuoti lauko skirstiniai leidžia nustatyti atskirų modų prigimtį bei vertinti elektromagnetinių laukų lokalizaciją (stiprinimą) ir atskirų modų pritaikymo galimybes. Skaičiavimo metodas leidžia greitai ir iteratyviai kurti naujų, specifinėmis savybėmis pasižyminčių elementų dizainus tolesnei gamybai bei tyrimams.

### 6.5.5 Išvados

- Atlikta daugialaipinės fazės Frenelio zonų lęšių, skirtų 0,6 THz dažnio spinduliuotei ir pasižyminčių skirtingais fazės žingsnių skaičiais, gamyba tiesioginės lazerinės abliacijos metodu. Atliktas pagamintų elementų fokusavimo savybių tyrimas ir pademonstruotas pagaminto elemento taikymas THz vaizdinimo sistemoje.
- Tiesioginės lazerinės abliacijos būdu pagamintos Soreto zoninės plokštelės bei daugialaipinės fazės Frenelio zonų lęšiai skirti 4,7 THz dažnio spinduliuotei. Parodyta, kad gamybos metodas neriboja elementų efektyvumo ir įmanoma gamybos metodą naudoti ir didesnio dažnio komponentų gamybai.
- Atliktas teorinis bei eksperimentinis  $n$ -GaN paviršinių plazmon-fonon-poliaritonų žadinimo tyrimas spektrinėje puslaidininkio Reštrlio juostos aplinkoje. Remiantis tikslios susietųjų bangų analizės metodo modeliavimo rezultatais, nustatyti optimalūs geometriniai bandinių parametrai ir, atsižvelgiant į šiuos rezultatus, atlikta bandinių gamyba bei charakterizavimas. Parodyta galimybė taikyti poliaritoninius sekliomis  $n$ -GaN paviršinėmis gardelėmis paremtus komponentus kuriant siaurajuosčiais, pasirenkamo dažnio atspindžio spektrų ypatumais pasižyminčius optinius elementus.
- Pirmą kartą pademonstruota poliarizuota ir kryptinga šiluma žadinamų  $n$ -GaN paviršinių plazmon-fonon-poliaritonų spinduliuotė. Stebėti keičiamo dažnio spinduliniai ypatumai, pasižymintys nuo  $10 \text{ cm}^{-1}$  ( $6 \text{ cm}^{-1}$ ) spektriniais pločiais eksperimente (teorijoje). Parodyta koherentinė spinduliuotės prigimtis, charakterizuojama  $27\lambda$  ( $50\lambda$ ) erdvinio koherentiškumo ilgiais. Pademonstruotas  $n$ -GaN paviršinių gardelių taikomumas kuriant derinamos siaurajuostės šiluminės spinduliuotės šaltinius bei koherentinio signalo perdavimo sistemas.
- Teoriškai bei eksperimentiškai ištirti GaN/GaN ir GaN/AlN/SiC heterostrukturų su paviršinėmis metalinėmis gardelėmis atspindžio spektrai. Parodyta, jog heterostrukūros naudojimas sėkmin-



gai praplatina darbinį poliaritonų dažnių ruožą ir leidžia šviesą lokalizuoti vidiniuose heterostrukūros sluoksniuose.

## REFERENCES

- [1] I. Kašalynas, R. Venckevičius, L. Minkevičius, A. Sešek, F. Wahaiia, V. Tamošiūnas, B. Voisiat, D. Seliuta, G. Valušis, A. Švigelj, and J. Trontelj, "Spectroscopic terahertz imaging at room temperature employing microbolometer terahertz sensors and its application to the study of carcinoma tissues," *Sensors (Switzerland)*, vol. 16, no. 4, pp. 1–15, 2016.
- [2] S. Sung, S. Selvin, N. Bajwa, S. Chantra, B. Nowroozi, J. Garritano, J. Goell, A. D. Li, S. X. Deng, E. R. Brown, W. S. Grundfest, and Z. D. Taylor, "Thz imaging system for in vivo human cornea," *IEEE Transactions on Terahertz Science and Technology*, vol. 8, no. 1, pp. 27–37, 2018.
- [3] J. P. Guillet, B. Recur, L. Frederique, B. Bousquet, L. Canioni, I. Manek-Hönninger, P. Desbarats, and P. Mounaix, "Review of terahertz tomography techniques," *Journal of Infrared, Millimeter, and Terahertz Waves*, vol. 35, no. 4, pp. 382–411, 2014.
- [4] R. E. Miles, X. C. Zhang, H. Eisele, and A. Krotkus, eds., *Terahertz Frequency Detection and Identification of Materials and Objects*. Dordrecht: Springer, 2007.
- [5] K. B. Cooper, R. J. Dengler, N. Llombart, B. Thomas, G. Chattopadhyay, and P. H. Siegel, "THz imaging radar for standoff personnel screening," *IEEE Transactions on Terahertz Science and Technology*, vol. 1, no. 1, pp. 169–182, 2011.
- [6] H. Richter, M. Wienold, L. Schrottke, K. Biermann, H. T. Grahn, and H. W. Hubers, "4.7-THz Local Oscillator for the GREAT Heterodyne Spectrometer on SOFIA," *IEEE Transactions on Terahertz Science and Technology*, vol. 5, no. 4, pp. 539–545, 2015.
- [7] C. Kulesa, "Terahertz spectroscopy for astronomy: From comets to cosmology," *IEEE Transactions on Terahertz Science and Technology*, vol. 1, no. 1, pp. 232–240, 2011.

- [8] I. Minin and O. V. Minin, *Diffractional Optics of Millimetre Waves*, vol. 20044935 of *Series in Optics and Optoelectronics*. Taylor & Francis, 2004.
- [9] M. Tamošiūnaitė, V. Tamošiūnas, and G. Valušis, “Wireless communications beyond 5G: Uncertainties of terahertz wave attenuation due to rain,” *Lithuanian Journal of Physics*, vol. 58, no. 2, pp. 149–158, 2018.
- [10] K. Nallappan, H. Guerboukha, C. Nerguizian, and M. Skorobogatiy, “Live streaming of uncompressed HD and 4K videos using terahertz wireless links,” *IEEE Access*, vol. 6, pp. 58030–58042, 2018.
- [11] J. M. Chamberlain, M. F. Kimmiti, A. Crompton, M. Havenith, G. Smith, and D. M. Mittleman, “Where optics meets electronics: Recent progress in decreasing the terahertz gap,” *Philosophical Transactions of the Royal Society A: Mathematical, Physical and Engineering Sciences*, vol. 362, no. 1815, pp. 199–213, 2004.
- [12] J. D. Caldwell, L. Lindsay, V. Giannini, I. Vurgaftman, T. L. Reinecke, S. A. Maier, and O. J. Glembocki, “Low-loss, infrared and terahertz nanophotonics using surface phonon polaritons,” *Nanophotonics*, vol. 4, no. 1, pp. 44–68, 2015.
- [13] D. G. Baranov, Y. Xiao, I. A. Nechepurenko, A. Krasnok, A. Alù, and M. A. Kats, “Nanophotonic engineering of far-field thermal emitters,” 2019.
- [14] G. Lu, J. R. Nolen, T. G. Folland, M. J. Tadjer, D. G. Walker, and J. D. Caldwell, “Narrowband Polaritonic Thermal Emitters Driven by Waste Heat,” *ACS Omega*, no. May, 2020.
- [15] P. Törmö and W. L. Barnes, “Strong coupling between surface plasmon polaritons and emitters: A review,” *Reports on Progress in Physics*, vol. 78, no. 1, p. 33, 2015.
- [16] T. G. Folland, L. Nordin, D. Wasserman, and J. D. Caldwell, “Probing polaritons in the mid- to far-infrared,” *Journal of Applied Physics*, vol. 125, no. 19, 2019.
- [17] Y. Chen, Y. Francescato, J. D. Caldwell, V. Giannini, T. W. Ma, O. J. Glembocki, F. J. Bezares, T. Taubner, R. Kasica, M. Hong, and S. A. Maier, “Spectral Tuning of Localized Surface Phonon Polariton Resonators for Low-Loss Mid-IR Applications,” *ACS Photonics*, vol. 1, no. 8, pp. 718–724, 2014.

## REFERENCES

- [18] K. Ohtani, B. Meng, M. Franckić, L. Bosco, C. Ndebeka-Bandou, M. Beck, and J. Faist, “An electrically pumped phonon-polariton laser,” *Science Advances*, vol. 5, no. 7, 2019.
- [19] Wiki, “Satellite systems.” [https://en.wikipedia.org/wiki/Small\\_satellite](https://en.wikipedia.org/wiki/Small_satellite), urldate = 2020-09-02.
- [20] D. Hu, X. Wang, S. Feng, J. Ye, W. Sun, Q. Kan, P. J. Klar, and Y. Zhang, “Ultrathin Terahertz Planar Elements,” *Advanced Optical Materials*, vol. 1, no. 2, pp. 186–191, 2013.
- [21] J. Zdanevicius, D. Cibiraite, K. Ikamas, M. Bauer, J. Matukas, A. Lisauskas, H. Richter, T. Hagelschuer, V. Krozer, H. W. Hubers, and H. G. Roskos, “Field-Effect Transistor Based Detectors for Power Monitoring of THz Quantum Cascade Lasers,” *IEEE Transactions on Terahertz Science and Technology*, vol. 8, no. 6, pp. 613–621, 2018.
- [22] L. Minkevičius, D. Jokubauskis, I. Kašalynas, S. Orlov, A. Urbas, and G. Valušis, “Bessel terahertz imaging with enhanced contrast realized by silicon multi-phase diffractive optics,” *Opt. Express*, vol. 27, pp. 36358–36367, Dec 2019.
- [23] Y. Yu and W. Dou, “Generation of pseudo-Bessel beams at THz frequencies by use of binary axicons,” *Optics Express*, vol. 17, no. 2, p. 888, 2009.
- [24] D. Jokubauskis, L. Minkevičius, M. Karaliūnas, I. Kašalynas, S. Indrišiūnas, G. Račiukaitis, and G. Valušis, “Fibonacci subterahertz imaging: features and applications,” in *Terahertz Emitters, Receivers, and Applications X* (M. Razeghi, A. N. Baranov, and M. S. Vitiello, eds.), vol. 11124, pp. 129 – 132, International Society for Optics and Photonics, SPIE, 2019.
- [25] J. Suszek, A. Siemion, M. S. Bieda, N. Blocki, D. Coquillat, G. Cywinski, E. Czerwinska, M. Doch, A. Kowalczyk, N. Palka, A. Sobczyk, P. Zagrajek, M. Zaremba, A. Kolodziejczyk, W. Knap, and M. Sypek, “3-D-printed flat optics for THz linear scanners,” *IEEE Transactions on Terahertz Science and Technology*, vol. 5, no. 2, pp. 314–316, 2015.
- [26] INO, “THz scanning solutions.” <https://www.ino.ca/en/solutions/thz/>.
- [27] Terasense, “Terasense THz scanner.” <https://terasense.com/products/thz-scanner/>.
- [28] E. D. Walsby, S. Wang, J. Xu, T. Yuan, R. Blaikie, S. M. Durbin, X. C. Zhang, and D. R. Cumming, “Multilevel silicon diffractive optics for terahertz waves,” *Journal of Vacuum Science and Technology B: Microelectronics and Nanometer Structures*, vol. 20, no. 6, pp. 2780–2783, 2002.

- [29] S. Wang, T. Yuan, E. D. Walsby, R. J. Blaikie, S. M. Durbin, D. R. S. Cumming, J. Xu, and X.-C. Zhang, "Characterization of T-ray binary lenses," *Optics Letters*, vol. 27, no. 13, p. 1183, 2002.
- [30] S. C. Saha, C. Li, Y. Ma, J. P. Grant, and D. R. Cumming, "Fabrication of multilevel silicon diffractive lens at terahertz frequency," *IEEE Transactions on Terahertz Science and Technology*, vol. 3, no. 4, pp. 479–485, 2013.
- [31] V. S. Pavelyev, M. S. Komlenok, B. O. Volodkin, B. A. Knyazev, T. V. Kononenko, V. I. Konov, V. A. Soifer, and Y. Y. Choporova, "Fabrication of High-effective Silicon Diffractive Optics for the Terahertz Range by Femtosecond Laser Ablation," *Physics Procedia*, vol. 84, no. July, pp. 170–174, 2016.
- [32] Newport, "Optical materials from Newport." <https://www.newport.com/n/optical-materials>.
- [33] Tydex, "THz materials from Tydex." <http://www.tydexoptics.com/products/thz{ }optics/thz{ }materials/>.
- [34] V. E. Rogalin, I. A. Kaplunov, and G. I. Kropotov, "Optical Materials for the THz Range," *Optics and Spectroscopy*, vol. 125, no. 6, pp. 1053–1064, 2018.
- [35] A. D. Squires, E. Constable, and R. A. Lewis, "3D Printed Terahertz Diffraction Gratings And Lenses," *Journal of Infrared, Millimeter, and Terahertz Waves*, vol. 36, no. 1, pp. 72–80, 2015.
- [36] M. Sypek, M. Makowski, E. Hérault, A. Siemion, A. Siemion, J. Suszek, F. Garet, and J.-L. Coutaz, "Highly efficient broadband double-sided Fresnel lens for THz range," *Optics Letters*, vol. 37, no. 12, p. 2214, 2012.
- [37] S. F. Busch, M. Weidenbach, M. Fey, F. Schäfer, T. Probst, and M. Koch, "Optical Properties of 3D Printable Plastics in the THz Regime and their Application for 3D Printed THz Optics," *Journal of Infrared, Millimeter, and Terahertz Waves*, vol. 35, no. 12, pp. 993–997, 2014.
- [38] S. Banerji and B. Sensale-Rodriguez, "3D-printed diffractive terahertz optical elements through computational design," in *SPIE Defense + Commercial Sensing*, no. May, (baltimore, Maryland, United states), p. 104, 2019.
- [39] F. Machado, P. Zagrajek, V. Ferrando, J. A. Monsoriu, and W. D. Furlan, "Multiplexing THz Vortex Beams With a Single Diffractive 3-D Printed Lens," *IEEE Transactions on Terahertz Science and Technology*, vol. 9, no. 1, pp. 63–66, 2019.

- [40] J. Gospodaric, A. Kuzmenko, A. Pimenov, C. Huber, D. Suess, S. Rotter, and A. Pimenov, "3D-printed phase waveplates for THz beam shaping," *Applied Physics Letters*, vol. 112, no. 22, 2018.
- [41] K. Szkudlarek, M. Sypek, G. Cywiński, J. Suszek, P. Zagrajek, A. Feduniewicz-Żmuda, I. Yahniuk, S. Yatsunenکو, A. Nowakowska-Siwińska, D. Coquillat, D. B. But, M. Rachoń, K. Węgrzyńska, C. Skierbiszewski, and W. Knap, "Terahertz 3D printed diffractive lens matrices for field-effect transistor detector focal plane arrays," *Optics Express*, vol. 24, no. 18, p. 20119, 2016.
- [42] W. D. Furlan, V. Ferrando, J. A. Monsoriu, P. Zagrajek, E. Czerwińska, and M. Szustakowski, "3D printed diffractive terahertz lenses," *Optics Letters*, vol. 41, no. 8, p. 1748, 2016.
- [43] A. Siemion, "Terahertz Diffractive Optics—Smart Control over Radiation," *Journal of Infrared, Millimeter, and Terahertz Waves*, vol. 40, no. 5, pp. 477–499, 2019.
- [44] J. D. Wheeler, B. Koopman, P. Gallardo, P. R. Maloney, S. Brugger, G. Cortes-Medellin, R. Datta, C. D. Dowell, J. Glenn, S. Golwala, C. McKenney, J. J. McMahon, C. D. Munson, M. Niemack, S. Parshley, and G. Stacey, "Antireflection coatings for submillimeter silicon lenses," *Millimeter, Submillimeter, and Far-Infrared Detectors and Instrumentation for Astronomy VII*, vol. 9153, no. 314, p. 91532Z, 2014.
- [45] B. Scherger, M. Scheller, C. Jansen, M. Koch, and K. Wiesauer, "Terahertz lenses made by compression molding of micropowders," *Applied Optics*, vol. 50, no. 15, p. 2256, 2011.
- [46] D. Headland, Y. Monnai, D. Abbott, C. Fumeaux, and W. Withayachumnankul, "Tutorial: Terahertz beamforming, from concepts to realizations," *APL Photonics*, vol. 3, no. 5, p. 51101, 2018.
- [47] D. Seliuta, I. Kasalynas, V. Tamosiunas, S. Balakauskas, Z. Martunas, S. Asmontas, G. Valusis, A. Lisauskas, H. G. Roskos, and K. Kohler, "Silicon lens-coupled bow-tie InGaAs-based broadband terahertz sensor operating at room temperature," *Electronics Letters*, vol. 42, no. 14, p. 825, 2006.
- [48] K. Liebert, M. Rachon, J. Bomba, A. Sobczyk, P. Zagrajek, M. Sypek, J. Suszek, and A. Siemion, "THz diffractive focusing structures for broadband application," *Photonics Letters of Poland*, vol. 10, no. 3, pp. 76–78, 2018.

- [49] B. Morgan, C. M. Waits, J. Krizmanic, and R. Ghodssi, "Development of a Deep Silicon Phase Fresnel Lens Using Gray-Scale Lithography and Deep Reactive Ion Etching," *Journal of Microelectromechanical Systems*, vol. 13, no. 1, pp. 113–120, 2004.
- [50] C. Brückner, G. Notni, and A. Tünnermann, "Optimal arrangement of 90 off-axis parabolic mirrors in THz setups," *Optik*, vol. 121, no. 1, pp. 113–119, 2010.
- [51] J.-Y. Han, "Parametric geometry analysis for circular-aperture off-axis parabolic mirror segment," *Journal of Astronomical Telescopes, Instruments, and Systems*, vol. 5, no. 02, p. 1, 2019.
- [52] Thorlabs, "Thorlabs oap." [https://www.thorlabs.com/newgrouppage9.cfm?objectgroup\[\\_\]id=12395](https://www.thorlabs.com/newgrouppage9.cfm?objectgroup[_]id=12395).
- [53] K. Newman, "OAP tutorial [https://wp.optics.arizona.edu/optomech/wp-content/uploads/sites/53/2016/10/521\\_Tutorial\\_Newman\\_Kevin.pdf](https://wp.optics.arizona.edu/optomech/wp-content/uploads/sites/53/2016/10/521_Tutorial_Newman_Kevin.pdf)," 2013.
- [54] L. Minkevičius, B. Voisiat, A. Mekys, R. Venckevičius, I. Kašalynas, D. Seliuta, G. Valušis, G. Račiukaitis, and V. Tamošiunas, "Terahertz zone plates with integrated laserablated bandpass filters," *Electronics Letters*, vol. 49, no. 1, pp. 49–50, 2013.
- [55] L. Minkevičius, "Terahertz imaging arrays for room temperature operation," p. 48, 2016.
- [56] B. A. Knyazev, G. N. Kulipanov, and N. A. Vinokurov, "Novosibirsk terahertz free electron laser: Instrumentation development and experimental achievements," *Measurement Science and Technology*, vol. 21, no. 5, 2010.
- [57] H. D. Hristov, *Fresnel Zones in Wireless links, Zone Plate lenses and Antennas*. Norwood, MA USA: ARTECH HOUSE, INC., 2000.
- [58] D. Tarrazó-Serrano, S. Pérez-López, P. Candelas, A. Uris, and C. Rubio, "Acoustic Focusing Enhancement In Fresnel Zone Plate Lenses," *Scientific Reports*, vol. 9, no. 1, pp. 1–10, 2019.
- [59] A. R. Parker and Z. Hegedus, "Diffractive optics in spiders," *Journal of Optics A: Pure and Applied Optics*, vol. 5, no. 4, 2003.
- [60] P. Wang, N. Mohammad, and R. Menon, "Chromatic-aberration-corrected diffractive lenses for ultra-broadband focusing," *Scientific Reports*, vol. 6, no. February, pp. 1–7, 2016.

- [61] C. F. Neese, I. R. Medvedev, G. M. Plummer, A. J. Frank, C. D. Ball, and F. C. De Lucia, "Compact submillimeter/terahertz gas sensor with efficient gas collection, preconcentration, and ppt sensitivity," *IEEE Sensors Journal*, vol. 12, no. 8, pp. 2565–2574, 2012.
- [62] X. Tu, L. Kang, C. Wan, L. Xu, Q. Mao, P. Xiao, X. Jia, W. Dou, J. Chen, and P. Wu, "Diffractive microlens integrated into Nb<sub>5N</sub><sub>6</sub> microbolometers for THz detection," *Optics Express*, vol. 23, no. 11, p. 13794, 2015.
- [63] H. D. Hristov, J. M. Rodríguez, and W. Grote, "Broadband reflectarrays made of cells with three coplanar parallel dipoles," *Microwave And Optical Technology Letters*, vol. 56, no. 6, pp. 748–753, 2012.
- [64] L. Minkevičius, V. Tamošiūnas, K. Madeikis, B. Voisiat, I. Kašalynas, and G. Valušis, "On-chip integration of laser-ablated zone plates for detection enhancement of InGaAs bow-tie terahertz detectors," *Electronic Letters*, vol. 50, no. 19, pp. 1367–1369, 2014.
- [65] L. Minkevičius, K. Madeikis, B. Voisiat, I. Kašalynas, R. Venckevičius, G. Račiukaitis, V. Tamošiūnas, and G. Valušis, "Focusing performance of terahertz zone plates with integrated cross-shape apertures," *Journal of Infrared, Millimeter, and Terahertz Waves*, vol. 35, no. 9, pp. 699–702, 2014.
- [66] R. Ivaškevičiūtė-Povilauskienė, L. Minkevičius, D. Jokubauskis, A. Urbanowicz, S. Indrišiūnas, and G. Valušis, "Flexible materials for terahertz optics: advantages of graphite-based structures," *Optical Materials Express*, vol. 9, no. 11, p. 4438, 2019.
- [67] A. Siemion, A. Siemion, M. Makowski, J. Suszek, J. Bomba, A. Czerwiński, F. Garet, J.-L. Coutaz, and M. Sypek, "Diffractive paper lens for terahertz optics," *Optics Letters*, vol. 37, no. 20, p. 4320, 2012.
- [68] E. Minerbi, S. Keren-Zur, and T. Ellenbogen, "Nonlinear Metasurface Fresnel Zone Plates for Terahertz Generation and Manipulation," *Nano Letters*, vol. 19, no. 9, pp. 6072–6077, 2019.
- [69] A. N. Agafonov, B. O. Volodkin, A. K. Kaveev, B. A. Knyazev, G. I. Kropotov, V. S. Pavel'ev, V. A. Soifer, K. N. Tukmakov, E. V. Tsygankova, and Y. Y. Choporova, "Silicon diffractive optical elements for high-power monochromatic terahertz radiation," *Optoelectronics, Instrumentation and Data Processing*, vol. 49, no. 2, pp. 189–195, 2013.
- [70] L. Minkevičius, D. Jokubauskis, V. Janonis, S. Indrišiūnas, G. Račiukaitis, V. Tamošiūnas, I. Kašalynas, and G. Valušis, "High numerical aperture diffractive optics for imaging applications at 0.6



- THz frequency,” in *43rd International conference on infrared, millimeter and terahertz waves (IRMMW THz-2018)*, (Nagoya, Japan), 2018.
- [71] A. Žemaitis, M. Gaidys, P. Gečys, G. Račiukaitis, and M. Gedvilas, “Rapid high-quality 3D micro-machining by optimised efficient ultrashort laser ablation,” *Optics and Lasers in Engineering*, vol. 114, no. November 2018, pp. 83–89, 2019.
- [72] A. Žemaitis, M. Gaidys, M. Brikas, P. Gečys, G. Račiukaitis, and M. Gedvilas, “Advanced laser scanning for highly-efficient ablation and ultrafast surface structuring: experiment and model,” *Scientific Reports*, vol. 8, no. 1, 2018.
- [73] S. Indrisiunas, E. Svirplys, H. Richter, A. Urbanowicz, G. Raciukaitis, T. Hagelschuer, H. W. Hubers, and I. Kasalynas, “Laser-Ablated Silicon in the Frequency Range from 0.1 to 4.7 THz,” *IEEE Transactions on Terahertz Science and Technology*, vol. 9, no. 6, pp. 581–586, 2019.
- [74] V. Stankevič, A. Čermák, S. Mikalauskas, P. Kožmín, S. Indrišiūnas, and G. Račiukaitis, “Processing of ultra-hard materials with picosecond pulses: From research work to industrial applications,” *Journal of Laser Applications*, vol. 30, no. 3, p. 032202, 2018.
- [75] V. Tamosiunas, S. Indrisiunas, M. Tamosiunaite, L. Minkevicius, A. Urbanowicz, G. Raciukaitis, I. Kasalynas, and G. Valusis, “Laser-Ablated Antireflective Structures for Terahertz Radiation Focusing,” *International Conference on Infrared, Millimeter, and Terahertz Waves, IRMMW-THz*, vol. 2018-Septe, pp. 5–6, 2018.
- [76] M. E. Shaheen, J. E. Gagnon, and B. J. Fryer, “Femtosecond laser ablation behavior of gold, crystalline silicon, and fused silica: A comparative study,” *Laser Physics*, vol. 24, no. 10, 2014.
- [77] Y. K. Hsieh, S. C. Chen, W. L. Huang, K. P. Hsu, K. A. V. Gorday, T. Wang, and J. Wang, “Direct micromachining of microfluidic channels on biodegradable materials using laser ablation,” *Polymers*, vol. 9, no. 7, 2017.
- [78] S. A. Maier, *Plasmonics: Fundamentals and Applications*. New York: Springer, 2007.
- [79] H. J. Falge and A. Otto, “Dispersion of Phonon-Like Surface Polaritons on  $\alpha$ - Quartz Observed by Attenuated Total Reflection,” *Physica Status Solidi (B)*, vol. 56, no. 2, pp. 523–534, 1973.

## REFERENCES

- [80] W. Streyer, S. Law, a. Rosenberg, C. Roberts, V. a. Podolskiy, a. J. Hoffman, and D. Wasserman, "Engineering absorption and blackbody radiation in the far-infrared with surface phonon polaritons on gallium phosphide," *Applied Physics Letters*, vol. 104, 2014.
- [81] K. Feng, W. Streyer, S. M. Islam, J. Verma, D. Jena, D. Wasserman, and A. J. Hoffman, "Localized surface phonon polariton resonances in polar gallium nitride," *Applied Physics Letters*, vol. 107, no. 8, 2015.
- [82] J. D. Caldwell, O. J. Glembocki, Y. Francescato, N. Sharac, V. Giannini, F. J. Bezares, J. P. Long, C. Owrutsky, I. Vurgafman, J. G. Tischler, V. D. Wheeler, N. D. Bassim, L. M. Shirey, R. Kasica, and S. a. Maier, "Low-Loss, Extreme Subdiffraction Photon Confinement via Silicon Carbide Localized Surface Phonon Polariton Resonators," *Nano Letters*, vol. 13, pp. 3690–3697, 2013.
- [83] J. J. Greffet, R. Carminati, K. Joulain, J. P. Mulet, S. Mainguy, and Y. Chen, "Coherent emission of light by thermal sources," *Nature*, vol. 416, no. 6876, pp. 61–64, 2002.
- [84] M. A. Huber, F. Mooshammer, M. Plankl, L. Viti, F. Sandner, L. Z. Kastner, T. Frank, J. Fabian, M. S. Vitiello, T. L. Cocker, and R. Huber, "Femtosecond photo-switching of interface polaritons in black phosphorus heterostructures," *Nature Nanotechnology*, vol. 12, no. 3, pp. 207–211, 2017.
- [85] S. Dai, Q. Ma, M. K. Liu, T. Andersen, Z. Fei, M. D. Goldflam, M. Wagner, K. Watanabe, T. Taniguchi, M. Thiemens, F. Keilmann, G. C. Janssen, S. E. Zhu, P. Jarillo-Herrero, M. M. Fogler, and D. N. Basov, "Graphene on hexagonal boron nitride as a tunable hyperbolic metamaterial," *Nature Nanotechnology*, vol. 10, no. 8, pp. 682–686, 2015.
- [86] H. Wang, Y. Yang, and L. Wang, "Infrared Frequency-Tunable Coherent Thermal Sources," *Journal of Optics*, vol. 17, no. 4, pp. 1–6, 2015.
- [87] A. V. Zayats and I. I. Smolyaninov, "Near-field photonics: Surface plasmon polaritons and localized surface plasmons," *Journal of Optics A: Pure and Applied Optics*, vol. 5, no. 4, 2003.
- [88] E. Rephaeli, A. Raman, and S. Fan, "Ultrabroadband photonic structures to achieve high-performance daytime radiative cooling," *Nano Letters*, vol. 13, no. 4, pp. 1457–1461, 2013.
- [89] X. Liu, Z. Li, Z. Wen, M. Wu, J. Lu, X. Chen, X. Zhao, T. Wang, R. Ji, Y. Zhang, L. Sun, B. Zhang, H. Xu, J. Zhou, J. Hao, S. Wang, X. Chen,

- N. Dai, W. Lu, and X. Shen, "Large-area, lithography-free, narrow-band and highly directional thermal emitter," *Nanoscale*, vol. 11, no. 42, pp. 19742–19750, 2019.
- [90] T. Inoue, M. De Zoysa, T. Asano, and S. Noda, "Realization of narrow-band thermal emission with optical nanostructures," *Optica*, vol. 2, no. 1, p. 27, 2015.
- [91] B. Neuner, C. Wu, G. T. Eyck, M. Sinclair, I. Brener, and G. Shvets, "Efficient infrared thermal emitters based on low-albedo polaritonic metasurfaces," *Applied Physics Letters*, vol. 102, no. 21, 2013.
- [92] H. Raether, "Surface plasmons on smooth and rough surfaces and on gratings, Volume 111," p. 136, 1988.
- [93] T. E. Beechem, C. B. Saltonstall, T. Gilbert, J. Matson, F. Ugwu, R. Kasic, F. J. Bezares, J. Valentine, and J. D. Caldwell, "Influence of spatial dispersion on spectral tuning of phonon-polaritons," *Physical Review B*, vol. 100, no. 20, pp. 1–11, 2019.
- [94] A. Kasic, M. Schubert, S. Einfeldt, D. Hommel, and T. E. Tiwald, "Free-carrier and phonon properties of n- and p-type hexagonal GaN films measured by infrared ellipsometry," *Physical Review B - Condensed Matter and Materials Physics*, vol. 62, no. 11, pp. 7365–7377, 2000.
- [95] A. D. Dunkelberger, C. T. Ellis, D. C. Ratchford, A. J. Giles, M. Kim, C. S. Kim, B. T. Spann, I. Vurgaftman, J. G. Tischler, J. P. Long, O. J. Glembocki, J. C. Owrutsky, and J. D. Caldwell, "Active tuning of surface phonon polariton resonances via carrier photoinjection," *Nature Photonics*, vol. 12, no. 1, pp. 50–56, 2018.
- [96] J. Le Gall, M. Olivier, and J. Greffet, "Experimental and theoretical study of reflection and coherent thermal emission by a SiC grating supporting a surface-phonon polariton," *Physical Review B - Condensed Matter and Materials Physics*, vol. 55, no. 15, pp. 10105–10114, 1997.
- [97] F. Gervais and B. Piriou, "Anharmonicity in several-polar-mode crystals: adjusting phonon self-energy of LO and TO modes in Al<sub>2</sub>O<sub>3</sub> and TiO<sub>2</sub> to fit infrared reflectivity," *Journal of Physics C: Solid State Physics*, vol. 7, no. 13, p. 2374, 1974.
- [98] T. Wang, P. Li, D. N. Chigrin, A. J. Giles, F. J. Bezares, O. J. Glembocki, J. D. Caldwell, and T. Taubner, "Phonon-Polaritonic Bowtie Nanoantennas: Controlling Infrared Thermal Radiation at the Nanoscale," *ACS Photonics*, vol. 4, no. 7, pp. 1753–1760, 2017.

## REFERENCES

- [99] M. Schubert, A. Kasic, T. E. Tiwald, J. Off, B. Kuhn, F. Scholz, M. Schubert, A. Kasic, T. E. Tiwald, J. Off, and B. Kuhn, "Optical phonons and free-carrier effects in MOVPE grown Al<sub>x</sub>Ga<sub>1-x</sub>N measured by Infrared Ellipsometry," vol. 4, no. 01, 1999.
- [100] R. Hillenbrand, T. Taubner, and F. Keilmann, "Phonon-enhanced light-matter interaction at the nanometre scale," *Nature*, vol. 418, no. 6894, pp. 159–162, 2002.
- [101] M. Janipour and K. Sendur, "Broadband infrared reflective surfaces using doped and stacked polar dielectric layers," *AIP Advances*, vol. 8, p. 025213, 2018.
- [102] K. Požela, E. Širmulis, I. Kašalynas, A. Šilėnas, J. Požela, and V. Jucienė, "Selective thermal terahertz emission from GaAs and AlGaAs," *Applied Physics Letters*, vol. 105, p. 091601, 2014.
- [103] Y. Ishitani, "Theoretical and experimental study of the optical absorption at longitudinal phonon or phonon-plasmon coupling mode energy: An example of GaN," *Journal of Applied Physics*, vol. 112, no. 6, 2012.
- [104] M. Chafai, A. Jaouhari, A. Torres, R. Antón, E. Martín, J. Jiménez, and W. C. Mitchel, "Raman scattering from LO phonon-plasmon coupled modes and Hall-effect in n-type silicon carbide 4H-SiC," *Journal of Applied Physics*, vol. 90, no. 10, pp. 5211–5215, 2001.
- [105] G. A. Melentev, D. Y. Yaichnikov, V. A. Shalygin, M. Y. Vinnichenko, L. E. Vorobjev, D. A. Firsov, L. Riuttanen, and S. Suihkonen, "Plasmon phonon modes and optical resonances in n-GaN," *Journal of Physics: Conference Series*, vol. 690, p. 012005, 2016.
- [106] J. A. Schuller, T. Taubner, and M. L. Brongersma, "Optical antenna thermal emitters," *Nature Photonics*, vol. 3, no. 11, pp. 658–661, 2009.
- [107] B. Knoll and F. Keilmann, "Near-field probing of vibrational absorption for chemical microscopy," *Nature*, vol. 399, no. 6732, pp. 134–137, 1999.
- [108] A. J. Huber, F. Keilmann, J. Wittborn, J. Aizpurua, and R. Hillenbrand, "Terahertz near-field nanoscopy of mobile carriers in single semiconductor nanodevices," *Nano Letters*, vol. 8, no. 11, pp. 3766–3770, 2008.
- [109] F. Marquier, K. Joulain, J. P. Mulet, R. Carminati, J. J. Greffet, and Y. Chen, "Coherent spontaneous emission of light by thermal sources," *Physical Review B - Condensed Matter and Materials Physics*, vol. 69, no. 15, pp. 1–11, 2004.

- [110] G. A. Melentev, D. Y. Yaichnikov, V. A. Shalygin, M. Y. Vinnichenko, L. E. Vorobjev, D. A. Firsov, L. Riuttanen, and S. Suihkonen, "Plasmon phonon modes and optical resonances in n-GaN," *Journal of Physics: Conference Series*, vol. 690, no. 1, 2016.
- [111] S. Vassant, F. Marquier, J. J. Greffet, F. Pardo, and J. L. Pelouard, "Tailoring GaAs terahertz radiative properties with surface phonons polaritons," *Applied Physics Letters*, vol. 97, no. 2010, pp. 2008–2011, 2010.
- [112] V. A. Shalygin, M. D. Moldavskaya, V. Y. Panevin, A. I. Galimov, G. A. Melentev, A. A. Artemyev, D. A. Firsov, L. E. Vorobjev, G. V. Klimko, A. A. Usikova, T. A. Komissarova, I. V. Sedova, and S. V. Ivanov, "Interaction of surface plasmon–phonon polaritons with terahertz radiation in heavily doped GaAs epilayers," *Journal of Physics: Condensed Matter*, vol. 31, no. 10, p. 105002, 2019.
- [113] V. Janonis, P. Prystawko, K. Gibasiewicz, J. Kacperski, and I. Kašalynas, "Investigation of the reflectivity spectra of n-type GaN semiconductor with surface relief grating," in *44th International Conference on Infrared, Millimeter, and Terahertz Waves (IRMMW-THz)*, (Paris, France), pp. 1–2, 2019.
- [114] A. Taflove and E. Brodwin, "Numerical Solution of Steady-state Electromagnetic Scattering Problems Using the Time-Dependent Maxwell's Equations," *IEEE Transactions on Microwave Theory and Techniques*, vol. MTT-23, no. 8, pp. 623–630, 1975.
- [115] J. B. Schneider, "Conductivity and Perfect Electric Conductors," *Understanding the Finite-Difference Time-Domain Method*, pp. 1–403, 2012.
- [116] D. R. Reid and G. S. Smith, "Design of phase-correcting zone plate antennas for microwave and millimeter-wave applications using a full electromagnetic analysis," *IEEE Antennas and Propagation Society, AP-S International Symposium (Digest)*, vol. 55, no. 8, pp. 1505–1508, 2007.
- [117] B. Zhao and Z. M. Zhang, "Study of magnetic polaritons in deep gratings for thermal emission control," *Journal of Quantitative Spectroscopy and Radiative Transfer*, vol. 135, pp. 81–89, 2014.
- [118] K. M. Han, *Nanotechnology for Solar Module Applications: Zinc Oxide Nanostructures and Anti-Reflective Coating Modeling, Deposition, Analysis, and Model Fitting*. PhD thesis, Oregon State University, 2014.
- [119] M. Laroche, R. Carminati, and J. J. Greffet, "Coherent thermal antenna using a photonic crystal slab," *Physical Review Letters*, vol. 96, no. 12, pp. 2–5, 2006.

## REFERENCES

- [120] P. C. Logofătu, "Rigorous coupled-wave analysis for two-dimensional gratings," in *Advanced Topics in Optoelectronics, Microelectronics, and Nanotechnologies II* (O. Iancu, A. Manea, P. Schiopu, and D. Cojoc, eds.), vol. 5972, pp. 175 – 182, International Society for Optics and Photonics, SPIE, 2005.
- [121] V. Liu and S. Fan, "S4: A free electromagnetic solver for layered periodic structures," *Comput. Phys. Commun.*, vol. 183, pp. 2233–2244, 2012.
- [122] J. Hench and Z. Strakoš, "The RCWA method—a case study with open questions and perspectives of algebraic computations," *Electronic Transactions on Numerical Analysis*, vol. 31, pp. 331–357, 2008.
- [123] T. K. Gaylord, W. E. Baird, and M. G. Moharam, "Zero-reflectivity high spatial-frequency rectangular-groove dielectric surface-relief gratings," *Applied Optics*, vol. 25, no. 24, p. 4562, 1986.
- [124] Z. M. Zhang, "RCWA Matlab Source." <http://zhang-nano.gatech.edu/>.
- [125] B. Voisiat, S. Indrišiūnas, R. Šniaukas, L. Minkevičius, I. Kašalynas, and G. Račiukaitis, "Laser processing for precise fabrication of the THz optics," in *Laser Applications in Microelectronic and Optoelectronic Manufacturing (LAMOM) XXII* (B. Neuenschwander, C. P. Grigoropoulos, T. Makimura, and G. Račiukaitis, eds.), vol. 10091, pp. 66 – 75, International Society for Optics and Photonics, SPIE, 2017.
- [126] J. Zhu, G. Yin, M. Zhao, D. Chen, and L. Zhao, "Evolution of silicon surface microstructures by picosecond and femtosecond laser irradiations," *Applied Surface Science*, vol. 245, no. 1-4, pp. 102–108, 2005.
- [127] C. A. Zuhlke, T. P. Anderson, and D. R. Alexander, "Formation of multiscale surface structures on nickel via above surface growth and below surface growth mechanisms using femtosecond laser pulses," *Optics Express*, vol. 21, no. 7, p. 8460, 2013.
- [128] I. Kašalynas, R. Venckevičius, L. Tumonis, B. Voisiat, D. Seliuta, G. Valušis, and G. Račiukaitis, "Reflective terahertz imaging with the TEM01 mode laser beam," *Applied Optics*, vol. 52, no. 23, pp. 5640–5644, 2013.
- [129] B. Voisiat, G. Račiukaitis, and I. Kašalynas, "Thz components and plasmonic structures fabricated by direct laser patterning of metals," in *2014 39th International Conference on Infrared, Millimeter, and Terahertz waves (IRMMW-THz)*, pp. 1–2, 2014.
- [130] B. Voisiat, A. Biciunas, I. Kašalynas, and G. Račiukaitis, "Band-pass filters for THz spectral range fabricated by laser ablation," *Applied Physics A: Materials Science and Processing*, vol. 104, no. 3, pp. 953–958, 2011.

- [131] S. Indrišiūnas, L. Minkevičius, V. Tamošiūnas, G. Valušis, G. Račiukaitis, and I. Kašalynas, "Laser-processed diffractive optics for terahertz waves," in *2019 IEEE 8th International Conference on Advanced Optoelectronics and Lasers (CAOL)*, pp. 1–4, 2019.
- [132] A. Vorobyev and C. Guo, "Direct creation of black silicon using femtosecond laser pulses," *Applied Surface Science*, vol. 257, no. 16, pp. 7291 – 7294, 2011.
- [133] P. Daukantas, "Cultural artifacts in terahertz light," *Opt. Photon. News*, vol. 29, pp. 28–35, Mar 2018.
- [134] L. Minkevičius, V. Tamošiūnas, I. Kašalynas, R. Venckevičius, K. Madeikis, B. Voisiat, D. Seliuta, G. Račiukaitis, and G. Valušis, "On-chip integration solutions of compact optics and detectors in room-temperature terahertz imaging systems," in *Terahertz Emitters, Receivers, and Applications VI* (M. Razeghi, A. N. Baranov, J. M. Zavada, and D. Pavlidis, eds.), vol. 9585, pp. 104 – 109, International Society for Optics and Photonics, SPIE, 2015.
- [135] G. A. Melentev, V. A. Shalygin, L. E. Vorobjev, V. Y. Panevin, D. A. Firsov, L. Riuttanen, S. Suihkonen, V. V. Korotyeyev, Y. M. Lyaschuk, V. A. Kochelap, and V. N. Poroshin, "Interaction of surface plasmon polaritons in heavily doped GaN microstructures with terahertz radiation," *Journal of Applied Physics*, vol. 119, no. 9, 2016.
- [136] P. Kruszewski, P. Prystawko, I. Kašalynas, A. Nowakowska-Siwinska, M. Krysko, J. Plesiewicz, J. Smalc-Koziorowska, R. Dwilinski, M. Zajac, R. Kucharski, and M. Leszczynski, "AlGaIn/GaN HEMT structures on ammono bulk GaN substrate," *Semiconductor Science and Technology*, vol. 29, no. 7, 2014.
- [137] P. Prystawko, M. Sarzynski, A. Nowakowska-Siwinska, D. Crippa, P. Kruszewski, W. Wojtasiak, and M. Leszczynski, "AlGaIn HEMTs on patterned resistive/conductive SiC templates," *Journal of Crystal Growth*, vol. 464, no. November, pp. 159–163, 2017.
- [138] V. Universitetas, "VYTAUTAS JAKŠTAS KOMPAKTIŠKI AlGaIn / GaN HETEROSANDŪRINIAI ŠALTINIAI IR JUTIKLIAI Daktaro disertacija Fiziniai mokslai , fizika ( 02 P )," 2018.
- [139] V. Janonis, V. Jakštas, I. Kašalynas, P. Prystawko, and P. Kruszewski, "Reflectivity of plasmon–phonon modes in grating-coupled algan/gan heterostructures grown on sic and gan substrates (phys. status solidi b 5/2018)," *physica status solidi (b)*, vol. 255, no. 5, p. 1870118, 2018.

## 7. CURRICULUM VITAE

<b>Date and place of birth</b>	May 12 1990, Biržai, Lithuania
<b>Contact e-mail</b>	vytautas.janonis@ftmc.lt
<b>Phone number</b>	+37062070093
<b>ORCID</b>	0000-0001-8529-3436
<b>SCOPUS ID</b>	57200398337

### **Education:**

Biržų Saulės gymnasium	2009
Vilnius University	2013 Bachelors degree in <i>Applied physics</i>
Vilnius University	2015 Masters degree in <i>Materials science and semiconductor physics</i>

### **Work experience:**

Technician, VU	2011-2012
Student under scholarship, VU	2012–2014
Engineer, FTMC	2014–2017
Junior researcher, FTMC	from 2017

**Publications:** author or coauthor of 20 scientific publications indexed by Clarivate Analytics's Web of Science (WoS).

**Conference presentations:** presented or was a coauthor of 50 thesis in national and international scientific conferences.

**Projects:** participated in 4 scientific projects.

**Grants:** received grants for academic achievements from Research council of Lithuania in 2015 and 2019 and mobility funding in 2017 and 2018.

**Summer schools:** 45th and 46th "Jaszowiec" International School & Conference on the Physics of Semiconductors June 2016 and 2017, Szczyrk, Poland.



**Gimimo data ir vieta** 1990 gegužės 12, Biržai, Lietuva  
**Kontaktinis paštas** vytautas.janonis@ftmc.lt  
**Telefono numeris** +37062070093  
**ORCID** 0000-0001-8529-3436  
**SCOPUS ID** 57200398337

**Išsilavinimas:**

Biržų Saulės gimnazija 2009  
 Vilniaus universitetas 2013 Bakalauras, Taikomoji fizika  
 Vilniaus universitetas 2015 Magistras, Medžiagotyra ir  
 puslaidininkų fizika

**Darbo patirtis:**

Technikas, VU 2011–2012  
 Studentas gaunantis 2012–2014  
 stipendiją, VU  
 Inžinierius, FTMC 2014–2017  
 Jaunesnysis mokslo nuo 2017  
 darbuotojas, FTMC

**Publikacijos:** 20 mokslinių darbų cituojamų Clarivate Analytics's Web of Science (WoS) duomenų bazėse bendraautorius.

**Konferencijų pranešimai:** asmeniškai pristatė arba buvo bendraautorius saraše 50 nacionalinių bei tarptautinių konferencijų pranešimų.

**Projektai:** dalyvavo vykdant 4 mokslinius projektus.

**Parama:** gavo Lietuvos mokslų tarybos paramą doktorantams už akademinis pasiekimus 2015 ir 2019 metais, bei paramą akademinėms išvykoms 2017 ir 2018 metais.

**Vasaros stovyklos:** dalyvavo dviejose vasaros stovyklose: 45-ojoje ir 46-ojoje "Jaszowiec" tarptautinėse Fizikos ir puslaidininkų konferencijose 2016 ir 2017 metų birželio mėnesiais, Szczyrk mieste, Lenkijoje.

# NOTES

# NOTES

Vilniaus universiteto leidykla  
Saulėtekio al. 9, LT-10222 Vilnius

El. p. [info@leidykla.vu.lt](mailto:info@leidykla.vu.lt),  
[www.leidykla.vu.lt](http://www.leidykla.vu.lt)

Tiražas 20 egz.